Towards the study of cold chemical reactions using Zeeman decelerated supersonic beams

Katrin Dulitz

Merton College, University of Oxford

A thesis submitted for the degree of Doctor of Philosophy

Michaelmas Term, 2014

Als nun Zarathustra so den Berg hinanstieg,
gedachte er unterwegs des vielen einsamen Wanderns von Jugend an,
und wie viele Berge und Rücken und Gipfel er schon gestiegen sei.
Ich bin ein Wanderer und ein Bergsteiger, sagte er zu seinem Herzen,
ich liebe die Ebenen nicht und es scheint, ich kann nicht lange still sitzen.

Und noch Eins weiß ich: ich stehe jetzt vor meinem letzten Gipfel
und vor dem, was mir am längsten aufgespart war.

(Friedrich Nietzsche – Also sprach Zarathustra)

Declaration

The research reported within this thesis has been carried out by the author unless otherwise stated. Thoughts taken directly or indirectly from external sources are properly marked as such. The material contained in this thesis has not previously been submitted for a degree at the University of Oxford or any other university.

Contents of Chapters 1, 4 and 5 are published in
[1] Dulitz, K.; Motsch, M.; Vanhaecke, N.; Softley T. P. *J. Chem. Phys.* **2014**, *140*, 104201.

Contents of Chapter 3 are submitted for publication in
[2] Dulitz, K.; Vanhaecke, N.; Softley T. P. *Phys. Rev. A*, *submitted*.

Both publications were written by the author of this thesis.

Oxford, November 24, 2014 Katrin Dulitz

Abstract

Towards the study of cold chemical reactions using Zeeman decelerated supersonic beams

Katrin Dulitz, Merton College

A thesis submitted in partial fulfilment of the requirements for the degree of Doctor of Philosophy of the University of Oxford
Michaelmas Term, 2014

Zeeman deceleration is an experimental technique which allows for the manipulation of open-shell atoms and molecules in a supersonic beam thus producing mK-cold, velocity-tunable beams of particles in selected quantum states. The method relies on the Zeeman interaction between paramagnetic particles and time-varying, inhomogeneous magnetic fields generated by pulsing high currents through an array of solenoid coils.

This thesis describes the construction and implementation of a supersonic beam setup including a 12-stage Zeeman decelerator. The Zeeman decelerator follows an original design that makes it possible to replace individual deceleration coils. Using ground-state hydrogen atoms as a test system, it is shown that the transverse acceptance in a Zeeman decelerator can be significantly increased by generating a rather low, temporally varying quadrupole field in one of the solenoid coils.

An electron-impact source was constructed and optimised enabling, for the first time, the Zeeman deceleration of metastable helium atoms in the 2^3S_1 state, with an up to 40 % decrease in the kinetic energy of the beam. It is shown that the pulse duration for electron-impact excitation needs to be matched to the acceptance of the decelerator in order to attain a good contrast between the decelerated and undecelerated parts of the beam.

Experimental results are rigorously analysed and interpreted using three-dimensional numerical particle trajectory simulations. A phase-space model provides, for the first time, a means to estimate the six-dimensional phase-space acceptance in a Zeeman decelerator and to find optimum parameter sets for improved Zeeman deceleration schemes. The approach also reveals a hitherto unconsidered velocity dependence of the phase stability which is ascribed mainly to the rise and fall times of the current pulses that generate the magnetic fields inside the deceleration coils.

In the future, it is planned to combine the Zeeman decelerator with a source of cold atomic and molecular ions to study chemical collisions at low temperatures. A hybrid magnetic guide consisting of permanent magnet assemblies (Halbach arrays) in hexapole configuration and a set of current-carrying wires is proposed and simulated as an interface between these setups. The design promises very efficient velocity selection, a high degree of quantum-state selection and a nearly complete removal of residual carrier gas. Prospects for using magnetic hexapole focusing in front of the Zeeman decelerator are discussed.

The work represents a major step towards the study and control of chemical reactivity of paramagnetic species in the low-temperature regime and it will help in the testing of fundamental chemical reaction theories.

Acknowledgements

Hereby, I would like to take the chance to thank those who have contributed to the success of this DPhil project.

I would like to express my gratitude to Tim Softley, not just for being a patient and gentle supervisor, for your advice and your good sense of humour, but also for the trust that you have placed in my ideas, and the financial support for the project that came with it.

Many thanks to all the members of the Softley group for their help with this project. I am particularly thankful to Chris Rennick for help with the initial setup of the experiment and to Atreju Tauschinsky for your effort related to the metastable atom experiments. Thanks to Brianna Heazlewood, Sashikesh Ganeshalingam, Eric So, Mark Dethlefsen, James Oldham and Martin Bell for helpful advice. Many thanks to all those that lent their hands to tighten flanges with me (Mike, Chris, Atreju, Alex, Lee, Brianna, Kasra). Cheers to my friend Jess Lam for sharing your ideas and aspirations with me – and for the great year in 7 Manor Place. Nabanita Deb, Lee Harper, Ed Steer, Mike Kohlhoff and Laura Pollum, thank you for bringing a bit of daylight into the lab and the office. Otto Schullian, thanks for adapting your program to work with supersonic beams, even though I could not use it in the end.

I am very grateful to Frédéric Merkt and his group at ETH Zürich for sharing their expert knowledge on Zeeman deceleration with me, and for letting me be a part of the group in summer 2010. I am particularly thankful to Michael Motsch for many discussions about the design of the Zeeman decelerator, and to Hansjürg Schmutz for numerous helpful comments on the decelerator electronics. I am also thankful to Alex Wiederkehr, in particular for help with the trajectory simulations, and to Stephen Hogan.

Nicolas Vanhaecke – without your comments and explanations, I would not have come nearly half as far with this project. Throughout the past three years, you have been an "external postdoc", mentor, motivator, friend and brother for me. Thank you for all the expert

advice, both with respect to theory and the experimental setup. Thank you for pushing when it was needed. Thank you for sharing your excitement about Zeeman deceleration with me, and for letting me share mine with you. Many thanks also to Dongdong Zhang for discussions, and for help with calculations. A special thanks to Bas van de Meerakker for fruitful discussions and thanks to him and his former group in Berlin, especially Janneke Blokland and Christian Schewe, for introducing me to the basics of Stark deceleration and supersonic beams during a summer internship in 2010.

I am grateful to the members of staff from the PTCL workshops, especially to Neville Baker, for devising and building most of the electronics equipment for the experiment, and for your resilience with the decelerator electronics and the coil potting. Andy Green, you did a great job in designing and building the decelerator and the pulsed valve assembly. Thank you to Charlie Jones for finding clever solutions to those tricky problems; and for listening. I am thankful to Howard Lambourne for building the electron gun. Many thanks to Les Hill and Kevin Valentine for squeezing my jobs into the books. Thanks to Phil Hurst, Tim, "the other" Charlie and Dennis for doing all the "small" jobs, and to John Adams for fixing our YAG laser. Many thanks also to the CRL and PTCL lab services, especially to Andy White, Alan Roper, Jude Nettleton and Paul Mitchell.

I would also like to thank the other Physical Chemistry groups in Oxford, who have contributed to this project through the share of equipment and advice. I am particularly grateful to the members of the Brouard group (Ben Winter, Craig Slater, ...) and the Vallance group (Scott Hopkins, Laura Lipciuc, Sara Gardiner). Special thanks to James Bull for a nearly completed electron gun assembly, and for aid with the electron gun electronics. Thanks to members of the Hancock group (Julian Few, Elin McCormack), the Timmel group (Kevin Henbest), the Robinson group (Victor Mikhailov) and John Eland for equipment loans and experimental expertise. Many thanks also to Bob Watkins in Physics for your desperate attempts to polish our fogged BBO crystals.

I am also thankful to my previous group in Mainz (John Crowley, Terry Dillon, Gerhard Schuster, Abraham Horowitz) for teaching me how to deal with frustration, and for show-

ing me how to carry out accurate measurements. Vielen Dank an die PC in Potsdam, vor allem bei Michael Kumke und Professor Löhmannsröben, für das großartige Gruppengefühl, nicht nur auf dem Fußballplatz. Aus meiner Zeit in Potsdam danke ich auch Professor Schmidt und Hubert Motschmann für die Unterstützung bei Bewerbungen; Hubert Motschmann danke ich zudem für gelungenes Mentoring. Meinen Lehrerinnen Frau Winter und Frau Setzer danke ich für ihre besondere Hingabe während der Schulzeit. Meiner Familie danke ich von ganzem Herzen für die Unterstützung. Es tut mir leid, dass ich immer alles auf Englisch schreibe. Anja und Klaus, ab jetzt melde ich mich wieder öfter.

I am indebted to the Chemical Industry Fund (FCI, Germany) for a Kekulé Mobility Fellowship, to Merton College for a Simms Bursary in my final year of studies, and to the EPSRC for financial assistance with the project.

Contents

List of Tables

List of Figures

1 | Introduction

The generation and study of cold molecules is a vibrant research area with applications both in the chemical and physical sciences. There have been a number of review articles and books summarising the advances in this field [1–9], and a complete overview about this research field would fill a DPhil thesis on its own. In this Chapter, I will thus aim at a general summary about the production methods and applications of cold molecules, with a major focus on topics related to my research project, namely cold chemistry in Coulomb crystals, supersonic beam deceleration techniques and Zeeman deceleration in particular. I will then give an overview of my research project and explain the motivation behind the work that is presented in this thesis.

1.1 Production of Cold Molecules

Laser cooling is a common method to generate cold (1 mK $\leq T \leq$ 1 K) and ultracold ($T \leq$ 1 mK) atoms and atomic cations [10–12][a]. Due to their complex energetic structure, molecules and molecular ions cannot be laser cooled in all but a few favourable cases, such as SrF, YO, YbF, CaF, SiO^+, AlH^+ and BH^+ [15–22]. Over the last decade, a number of alternative techniques have been developed to produce cold molecules. Indirect methods like photo- and magnetoassociation [23–27] are based on the bond-formation between two ultracold atoms, but they are usually restricted to alkali and alkaline-earth dimers. These techniques have produced the lowest molecular temperatures to date (in the nK regime), and they allowed the observation of intriguing chemical dynamics (see Section 1.2.2). Direct methods, like buffer-gas cooling and other methods relying on effusive or supersonic molecular beams, start from a room-temperature ensemble of molecules.

[a] Only few anions have bound excited electronic states, so that they are typically not suited for laser cooling. Os^- and La^- ions may be exceptions [13, 14].

Buffer-gas cooling [28] is based on the thermalisation of molecules inside a cryogenic cell that is filled with helium (or neon) gas at a high density, typically around 10^{16} atoms/cm^3. This technique has become particularly valuable in combination with magnetic trapping [29, 30], electrostatic velocity selection [31, 32] or ion trapping [33]. An electrostatic quadrupole guide in itself acts as source of cold polar molecules if it is bent so as to filter out the fast atoms or molecules from an effusive molecular beam source [34].

A supersonic expansion from a high-pressure gas reservoir into a vacuum is a very efficient method to adiabatically cool the translational and rotational degrees of freedom (see Section 2.1). However, as the beam exits the expansion region with a high forward velocity of several hundred meters per second, techniques had to be developed to decrease the translational energy of the beam in the laboratory frame.

Elastic, inelastic and reactive scattering in crossed supersonic beams [35–37] can be used for the production of nearly stationary molecules owing to the transfer of kinetic energy from one collision partner to the other. Near-threshold photodissociation is a related method [38, 39], in which the collision partner is a photon rather than another atomic or molecular species. The cold head of a cryopump [40, 41] and counter-rotating nozzles [42, 43] are useful tools to reduce the temperature of a gas before and during a supersonic expansion, respectively.

Supersonic beam deceleration techniques make use of the interaction between neutral particles and time-dependent, inhomogeneous electromagnetic fields to remove kinetic energy from a supersonic jet [8, 44, 45]. Depending on the type of electromagnetic interaction, these slowing methods can be further subdivided into Stark deceleration, Rydberg Stark deceleration, Zeeman deceleration and optical deceleration. This class of methodologies was pioneered by the Meijer group, which was the first to decelerate beams of polar molecules, such as metastable CO and ND_3, by rapidly switching electric fields of several tens of kV/cm in a Stark decelerator [46, 47]. Over the past decade, several research groups have built Stark decelerators in their laboratories, and the list of decelerated species has grown to an impressive number (see e.g. Hogan et al. [44] for a comprehen-

sive list of decelerated atoms and molecules). Based on this technique, even a synchrotron for neutral polar molecules has been realised [48]. Due to their huge electric dipole moments, atoms and molecules in Rydberg states require much lower electric fields for deceleration [49, 50]. The deceleration of neutral molecules in an optical Stark decelerator is based on the optical dipole force induced by very intense pulsed laser fields [51, 52]. Polar molecules in high-field-seeking quantum states can also be decelerated through their ac Stark shift in a microwave decelerator [53], as shown in a proof-of-principle experiment by Merz et al. [54]. Recently, a technique relying on the centrifugal force on a rotating disk has been developed to decelerate a continuous molecular beam [55].

Zeeman deceleration makes it possible to manipulate the motion of paramagnetic, open-shell atoms and molecules that cannot be addressed with electric fields. The tailoring of a neutron beam using time-varying inhomogeneous magnetic fields was first devised and demonstrated in the 1980s by a group in Vienna [56, 57]. This was done using a travelling magnetic wave setup (see below) by switching off the magnetic fields of two electromagnets (magnetic field amplitude of 0.4 T). However, the achieved acceleration/deceleration was minimal, at an initial beam velocity of 1225 m/s, a mere velocity reduction of 4.5 mm/s was achieved. It was not until 2007 that similar ideas were successfully implemented by the groups of Merkt [58] and Raizen [59] in order to manipulate the motion of atoms and molecules, and that led to the development of electronics equipment capable of switching magnetic fields of about 2 T within a few microseconds. To date, this technique has been successfully used to decelerate supersonic beams of H [58, 60], D [60], metastable Ne [59, 61], metastable Ar [62], O_2 [63, 64], CH_3 [65] and metastable He_2 [66]. Over the course of my DPhil project, I was able to further extend this list. I succeeded - for the first time - to implement the deceleration of metastable He atoms using our 12-stage Zeeman decelerator.

Zeeman deceleration relies on the influence of inhomogeneous magnetic fields on the motion of paramagnetic particles. In a conventional Zeeman decelerator, as built over the course of my DPhil project, these magnetic fields are produced by successively pulsing high currents through an array of solenoid coils. Upon approaching the maximum

magnetic field in the center of a solenoid coil, the Zeeman energy of particles in low-field-seeking quantum states is increased, while their kinetic energy is decreased. To obtain a net loss of kinetic energy, the magnetic field is rapidly switched off before the particles reach the negative slope of the solenoid magnetic field. This process is repeated in subsequent coils until a desired final velocity is reached. The amount of kinetic energy removed depends on the magnetic moment of a quantum state, thus providing a means to manipulate the motion of particles in specific quantum states. Phase stability ensures that a bunch of particles is kept together throughout the deceleration sequence. A detailed description of the underlying deceleration principles is given in Chapters 2 and 3.

The deceleration of thermal atomic beams with laser light also involves inhomogeneous, spatially varying magnetic fields [67], which are often referred to as Zeeman slowers (or even Zeeman decelerators). In this case, the magnetic field is required to keep the atoms resonant with the counter-propagating deceleration laser beam and thereby compensate for the change in Doppler shift owing to the decreasing velocity of the atoms. The magnetic fields are not pulsed, and the design of these devices is entirely different from the Zeeman decelerator for supersonic beams described in this work.

Several factors limit the efficiency of a supersonic beam deceleration experiment. A more detailed overview on particle loss processes in a deceleration experiment is given in Chapter 5. The operation of conventional Stark and Zeeman decelerators is particularly inefficient at low beam velocities, since overfocusing in the transverse beam direction leads to substantial particle losses. In a travelling-wave decelerator, this obstacle is avoided by confining the particles in an electric or magnetic trap that moves along with the supersonic beam, and thereby keeps the particles confined in all three spatial directions. Deceleration or acceleration of the trapped beam packet is then achieved by a modulation of the voltages [68–71] or currents [62] used for trapping. For Zeeman deceleration, a similar effect has also been attained by arranging the coils in anti-Helmholtz pairs, such that the application of current pulses with the temporal shape of half-sine waves translates the magnetic field minimum along the beam axis [72–74]. Using a travelling-wave Stark decelerator, it has been shown that molecules can be efficiently brought to rest in the lab-

oratory frame and electrostatically trapped inside the decelerator [75], thus avoiding additional losses during the transfer to an external trapping geometry. This technique has also proven advantageous in the deceleration of heavy molecules, whose quantum states are only low-field seeking at low electric fields [76]. The improved transverse confinement and the possibility of simultaneous deceleration and trapping thus renders travelling-wave deceleration an ideal technique for applications that require particle trapping. However, conventional Stark and Zeeman decelerators are superior with respect to collision experiments, as they provide a very narrow energy resolution which is beneficial for scattering experiments [77–80].

Except for the microwave decelerator, the deceleration techniques described thus far can only be used for the manipulation of atoms and molecules in low-field-seeking quantum states, since high-field-seekers are transversely deflected towards the electrodes or the coil walls, where they experience the highest field strengths. Alternating gradient (AG) Stark decelerators [81, 82] consist of a system of electrostatic lenses to dynamically focus and defocus polar molecules in high-field-seeking states, and thereby ensure confinement in the transverse direction. This type of Stark decelerator can address molecules in their rotational ground state and heavy molecules, like YbF [83], CaF [84] and benzonitrile [85], which are only low-field-seeking at low electric field strengths. However, the transverse acceptance is generally low. There is a strong coupling between the longitudinal and transverse motion [86, 87] and the design is very critical to misalignments and electrode imperfections [81, 82], so that the overall transmission through an AG decelerator is thus much lower than in a conventional Stark decelerator [84].

The forces acting on the particles in a supersonic beam decelerator are conservative, as they only depend on the particle position. According to Liouville's theorem, phase-space density can therefore not be increased during the deceleration process. Hence, "real" cooling, i.e. an increase in phase-space density, can only take place through elastic and inelastic collisions during the supersonic expansion and dictates the attainable temperature limit of the decelerated particles.

So-called 'bunching' schemes allow for the generation of colder beams, i.e. beams with a narrower longitudinal velocity distribution, but they come at the expense of a wider spatial distribution (to conserve phase-space density). This longitudinal focusing technique has been realised in Stark deceleration experiments by switching electrode pairs in such a manner that the particle distribution is rotated in longitudinal phase-space [88]. The rotation angle is set by the pulse duration of the electric fields and/or the voltage applied to the buncher electrodes [89].

Over the past years, there has been great effort to develop secondary techniques to further increase phase-space density and/or to reach temperatures below 1 mK. Apart from laser cooling [15–19], these approaches include sympathetic cooling, evaporative cooling, optoelectric cooling and trap reloading.

Sympathetic cooling in traps relies on the removal of the particles' kinetic energy through elastic collisons. Owing to the strong charge-charge interaction between ionic species, this technique has found numerous applications in the cooling and co-trapping of atomic and molecular ions in Coulomb crystals, as reviewed by Willitsch [90]. Since mainly the translational degrees of freedom are addressed with this scheme, the rotational and vibrational cooling of Coulomb-crystallised molecular ions requires the application of additional cooling techniques. Rotational cooling of sympathetically cooled MgH^+ and HD^+ ions can be achieved through optical pumping from the vibrational ground state to vibrationally excited states [91, 92]. In an alternative technique, the molecular ions are already prepared in selected rotational levels using threshold-photoionisation [93, 94]. The sympathetic cooling of ions with neutral gases, such as cold He buffer-gas atoms or laser-cooled, ultracold atoms, has been demonstrated in RF multipole traps [95] and in atom-ion hybrid traps [96, 97], respectively. In a two-stage cooling procedure using laser-cooled Ba^+ ions and Ca atoms, Rellergert et al. [98] showed that co-trapped $BaCl^+$ ions can be both translationally and vibrationally cooled (≈ 90 % population in the vibrational ground state). Recently, Hansen et al. [33] demonstrated the rovibrational cooling of MgH^+ ions through collisions with co-trapped laser-cooled Mg^+ ions and a low-density He buffer gas.

The sympathetic cooling of trapped neutral molecules with ultracold atoms has not been demonstrated yet. In order to be successful, the rate of inelastic collisions (leading to trap loss) needs to be much lower than the rate of elastic collisions (allowing thermalisation); typically two orders of magnitude as a rule of thumb. The trapping fields themselves also have a strong influence on the ratio between elastic and inelastic collisions. For example, several trapping geometries have been investigated for the LiH-Li system, and only a microwave trap seems to allow for sympathetic cooling in this case [99]. In a combined theoretical and experimental effort using buffer-gas cooling, it was found that spin-changing collisions between ground-state N atoms was slow over a wide temperature range thus suggesting that N atoms are promising collision partners for sympathetic cooling [100]. These results have inspired theory work on the sympathetic cooling of OH and NH molecules with ultracold ground-state N and H atoms [101–103]. Especially the collisional cooling with H atoms appears to have good prospects even at temperatures of more than 1 K for NH and 250 mK for OH. A detailed overview of the different theoretical studies related to sympathetic cooling can be found in a review by van de Meerakker et al. [8].

Evaporative cooling is a standard route to Bose-Einstein condensation (BEC) in atoms [104]. By slowly lowering the trapping potential, the warmer fraction of the trapped ensemble is ejected, while the remaining particles thermalise to a new, colder equilibrium state. As for sympathetic cooling, the ratio of elastic to inelastic collisions needs to remain high so as to avoid unwanted transitions to untrapped quantum states. By applying microwave pulses to selectively transfer population into an untrapped state, evaporative cooling of molecules has now been experimentally demonstrated for OH molecules in a magnetic trap [105]. Adiabatic cooling of molecules to sub-mK temperatures has also been successful after travelling-wave Stark deceleration and electrostatic trapping of ND_3 molecules [106]. Similarly, adiabatic cooling has been demonstrated for travelling-wave Stark deceleration on a chip. In this case, the trap depth was lowered during the guiding of metastable CO molecules at constant velocity [107].

An optoelectric cooling scheme was devised and experimentally verified by Zeppenfeld et

al. [108]. By repeated optical pumping between rovibrational states that exhibit different energetic splittings in an electric field, they were able to reduce the temperature of CH_3F molecules from 390 mK to 29 mK, corresponding to an increase in phase-space density by a factor of 29.

Trap reloading schemes for NH [109], SO [110] and Br [39, 111] have been proposed as alternative routes to increase phase-space density. Thus far, only the first method has been experimentally demonstrated [112]. For this, NH molecules in the long-lived $a^1\Delta$ state were brought to a standstill using a Stark decelerator, and subsequently optically pumped to the $A^3\Pi$ state which spontaneously decays to the ground state ($X^3\Sigma^-$). NH molecules in the electronic ground state are hardly influenced by electric fields but can be magnetically trapped, therefore enabling trap (re)loading without having to lower the trap depth.

1.2 Applications of Cold Molecules

The generation of cold molecules has stimulated numerous ideas and experiments ranging from precision measurements over cold collision studies to quantum computing and novel quantum phases [1–5, 7–9, 113]. In the following, I will focus on the first two of these applications, with emphasis on supersonic beam experiments, and otherwise refer to the aforementioned review articles for further reading. In addition to that, I will discuss previous work on cold chemistry in Coulomb crystals.

1.2.1 Precision Measurements

It has been long known that supersonic beams provide an outstanding basis for spectroscopic and molecular dynamics applications [114–116]. The beams have very narrow translational velocity distributions, and the rotational and partially the vibrational motion

are cooled during the expansion, while there are no further intermolecular interactions after the expansion is completed. A more detailed description of the physical principles of supersonic expansions is given in Section 2.1. Similar arguments apply to effusive beams emerging from buffer-gas cooled sources, although they are often in a hydrodynamic flow regime, where the forward velocity and the beam intensity are lower than in a supersonic jet [28]. However, buffer-gas-cooled beams can be operated in a continuous mode, thus typically providing a higher overall flux.

Owing to internal cooling and less Doppler broadening, supersonic beams have fewer and narrower spectral features than effusive beams, thus making them an ideal tool for high-resolution spectroscopy. An additional reduction of the forward velocity - as achieved with a decelerator - significantly improves the attainable resolution of a spectrum by increasing the interaction time with the sample and thereby decreasing the transit-time broadening.

This asset has been demonstrated in a measurement of the $^{15}ND_3$ inversion spectrum [117]. By decreasing the beam velocity from 280 m/s to 52 m/s in a Stark decelerator, the time of flight through the successive microwave excitation region was significantly increased so that the hyperfine structure of the transition could thereby be clearly resolved. Similar improvements in spectral resolution were observed in measurements with Stark-decelerated OH molecules [118].

Stark deceleration and subsequent electrostatic trapping (with $1/e$ trapping times of about 1 s for OH molecules [119]) have made it possible to determine the radiative lifetime of metastable CO ($a^3\Pi_1, v = 0, J = 1$) [120] and of vibrationally excited OH molecules in the electronic ground state ($X^2\Pi_{3/2}, v = 1, J = 3/2$) [119]. Radiative lifetimes and electric dipole moments needed for the production of ground-state CO molecules have been quantified with a Stark decelerator in guiding mode [121]. Using microwave Rabi spectroscopy after Stark deceleration, it was even possible to detect magnetic-dipole-allowed transitions in the $A^2\Sigma^+, v = 1 \leftarrow X^2\Pi_{3/2}, v = 0$ band of OH which are more than a factor of 1000 weaker than their electric counterparts [122]. It has also been shown that radiative

lifetimes can be measured in a low-density He buffer-gas environment. In this case, the radiative lifetime of vibrationally excited NH($X^3\Sigma^-$, $v = 1, N = 0$) molecules was determined inside a magnetic trap [123]. The observation times in traps are limited by trap loss due to background gas collisions and, for most polar molecules, excitation due to blackbody radiation [124, 125]. While blackbody optical pumping can be suppressed through cryogenic cooling, collisional trap loss in buffer-gas cells can be efficiently reduced by a rapid pumpout of residual buffer gas. In the latter case, trap lifetimes of more than 20 s have been achieved [126]. Early experiments on Rydberg Stark deceleration and trapping suffered from collisions between the trapped Rydberg atoms and the trailing edges of the supersonic jet [127]. Off-axis trapping significantly eliminated collisional losses and cooling to 125 K helped to reduce effects from blackbody optical pumping [128].

Apart from contributing to a better understanding of molecular structure, as, for example, in Zeeman deceleration experiments of metastable He_2 [66], cold molecules provide an exceptional basis for a number of spectroscopy experiments aiming to test fundamental physics theories. Recently, the Journal of Molecular Spectroscopy has devoted a special issue to this specific topic summarising current progress in this research area [129].

Probably the most prominent example for such a precision measurement is the search for a non-vanishing electric dipole moment of the electron (eEDM), which would indicate a violation of time-reversal symmetry (T-violation) and imply that the Standard Model of particle physics is incomplete. The current upper limit for the eEDM, $|d_e| < 8.7 \cdot 10^{-29}\, e$ cm [130], where e is the electron charge, was determined using buffer-gas cooled ThO molecules. As in the previous best measurement with YbF molecules [131], a polar molecule was chosen owing to its greater polarizability in an electric field resulting in a higher sensitivity to an eEDM as compared to an atom. Although targeted at the (dis)proof of physics theories, the research groups also contributed to progress in the generation of cold molecules along the way. In the course of finding a source of cold YbF molecules, Hinds and co-workers demonstrated AG Stark deceleration and travelling-wave Stark deceleration of YbF molecules [76, 83], and are now considering the use of a laser-cooled fountain of YbF molecules to increase their measurement sensitivity [18].

As an alternative route towards the measurement of an eEDM, molecular ions, like HfF^+ and ThF^+, have been made accessible through the development of a 'rotating bias field' technique. This method makes it possible to apply an electric field to polarise the ions, while keeping them confined within the trap [132].

Owing to the close proximity of opposite parity states, open-shell diatomic molecules and molecular ions with heavy nuclei, such as BaF, RaF, SrF and TlF^+, have been proposed as sensitive probes of parity violation (P-violation) [133–137]. If parity violating effects exist, they would come as a consequence of the weak interaction between electrons and nucleons leading to nuclear spin-dependent effects. As the statistical uncertainty of such an experiment is inversely proportional to the interaction time with the sample [134], work on the travelling-wave Stark deceleration and laser cooling of SrF molecules [138] is aimed at increasing the measuring accuracy. Closed-shell chiral molecules containing heavy atoms constitute a second class of molecules for the study of parity violation [139, 140]. In this case, parity-violating effects would manifest themselves in an energy difference between two enantiomers. Recently, a technique based on Fourier transform microwave spectroscopy (FTWM) has been developed that also allows for enantiomer-specific detection [141–143]. To distinguish between enantiomers, two orthogonally polarised, microwave-timescale electric fields are applied to the molecules. The phase shift of the emitted microwave radiation is then used as a flag of molecular chirality. In combination with a slow supersonic beam, e.g. from an AG Stark decelerator, this technique could be a viable means to observe parity-violating effects in chiral molecules [144].

Research on the variation of fundamental constants, such as the fine-structure constant, α, or the proton-to-electron mass ratio, $\mu = m_p/m_e$, may help to answer astrophysical questions, e.g. whether our universe is expanding on a cosmological timescale [145]. As summarised in a number of review articles [146–149], possible drifts of fundamental constants can be measured in a variety of atomic and molecular systems, both in the laboratory and through astronomical observations. Determining the temporal shift of absorption lines in quasars is a way to observe temporal changes in α and μ through astronomical observations. The current constraints on the temporal variation of α and μ

are $\dot{\alpha}/\alpha$ = (-1.6±2.3)·10^{-17}/yr and $\dot{\mu}/\mu$ = (1.4±1.4)·10^{-17}/yr, respectively [150, 151]. While the current best value for $\dot{\mu}/\mu$ was deduced from radio-astronomical observations of methanol [151], laboratory measurements on the frequency ratio of two different atomic clocks as a function of time provide the most accurate measurement of $\dot{\alpha}/\alpha$ to date [150]. While a change in α can be most accurately measured through electronic transitions in atoms, rotational, vibrational and tunnelling transitions in molecules provide particularly sensitive tests to a temporal variation of μ. The use of cold and controlled molecular beams can further increase the accuracy of such measurements. In ammonia, the inversion splitting frequency is very sensitive to the proton mass, and a molecular fountain for Stark-decelerated ammonia molecules has been proposed as a possible experiment to determine a limit for $\dot{\mu}/\mu$ [152]. Since electrostatic trapping induces a Stark shift of the energy levels of ammonia, and thereby decreases the measuring accuracy of such a precision experiment, recent work on the travelling-wave Stark deceleration of ND_3 showed that – after deceleration to a standstill – switching off the trapping fields and recapturing the molecules after a given time provides a practical way around this problem [106]. Another experiment for the purpose of measuring $\dot{\mu}/\mu$ is currently being setup to carry out two-photon ro-vibrational spectroscopy in a buffer-gas-cooled beam of CF_3H [153].

The techniques for the production of cold molecules offer various possible applications for precision measurements. Among others, there have also been proposals for high-resolution spectroscopy measurements on Zeeman-decelerated hydrogen isotopes [154] and a free-fall gravity experiment using Rydberg-Stark decelerated positronium atoms [155].

1.2.2 Cold und Ultracold Collisions

The study of cold and ultracold collisions paves the way towards the understanding of chemical dynamics in a still vastly unexplored temperature regime where the de Broglie

wavelength becomes comparable to the range of the interparticle interaction so that chemical reactivity will be dominated by quantum effects such as tunnelling, non-classical reflections and resonances. Since only very few quantum states are involved in a low-temperature collision, thermal averaging is avoided, which allows for an accurate interpretation of experimental data and will – through the possibility to calculate improved potential energy surfaces – also lead to a better understanding of collision processes at higher temperatures.

In this Section, I will summarise advances in the fields of crossed- and merged-beam scattering and scattering in traps that have been facilitated owing to the development of methods to produce cold and ultracold molecules. Two recent topical reviews are specifically devoted to collisions in the cold [156] and ultracold [157] temperature regime.

The possibility to manipulate and control supersonic beams has enabled the study of elastic, inelastic and reactive collisions in crossed and merged beam configurations at a previously unattained level of accuracy and/or in temperature regimes that can typically not be reached with established methods. In addition to that, supersonic beam decelerators or other slowing techniques make it possible to perform crossed-beam scattering studies as a function of collision energy using a fixed experimental geometry.

A number of inelastic collision studies near threshold were perfomed by colliding Stark-decelerated OH molecules with rare-gas atoms or D_2 molecules from an ordinary supersonic beam (typical collision energy range: 50 – 500 cm^{-1}) [77, 158–160]. With the introduction of an electrostatic hexapole into the setup, it was possible to further increase the collision-energy resolution (below 13 cm^{-1}) and to control the quantum state of both collision partners, so that inelastic scattering experiments between OH and NO could be carried out with a very high quantum-state purity for both beams (OH: 99.99 %, NO: 99.0 %) [161]. A crossed-beam setup including a Stark decelerator for NO molecules and a velocity-map-imaging system (VMI) allowed for the measurement of state-to-state differential scattering cross sections (DCS) in inelastic collisions with He, Ne and Ar atoms [80, 162]. In these measurements, the energy and angular resolution was so high

that quantum diffraction oscillations, the quantum-mechanical analogon to classical scattering from spherical particles, could be observed. Strebel et al. were able to resolve quantum rainbow scattering effects in elastic collisions between Li atoms from a MOT and rare gas atoms or SF_6 molecules from a supersonic beam, whose velocity was tuned with a fast counter-rotating nozzle [163]. Rainbow scattering can be viewed in analogy to light scattering by raindrops to form an atmospheric rainbow. A classical rainbow singularity is observed as a maximum in the DCS for forward scattering (0°), corresponding to a minimum in the interaction potential. In the measurements, secondary oscillations in the DCS were observed which are due to quantum mechanical interference effects between different partial waves. It is anticipated that crossed-beam experiments with Stark decelerated supersonic beams will also enable the measurement of other resonance effects if the collision energy resolution is sufficiently high [162]. For elastic and inelastic collisions between NH_3 molecules and He atoms, shape resonances, related to tunnelling through the centrifugal barrier, may be seen at low collision energies, while Feshbach resonances should occur at higher collision energies, when excited states of the molecule become energetically accessible [164].

Merged-beam studies are experiments in which the collision angle between two molecular beams is decreased in order to achieve low relative velocities and, hence, low collision energies. Already in the early 1970s, merged-beam scattering between H atoms and Hg atoms led to the observation of orbiting resonances, i.e. the formation of quasibound states of an H-Hg collision complex [165]. Herschbach and co-workers have proposed merged-beam scattering experiments, in which one of the supersonic expansions is coupled to a counter-rotating nozzle to tune the relative flow velocity [166]. Current setups make use of more sophisticated techniques for magnetically and electrostatically guiding a supersonic beam into the path of another as well as very short supersonic beam pulses (from Even-Lavie valves), so that the energy resolution of such collision experiments can be significantly increased [167]. Orbiting resonances have now been observed in merged-beam reactive scattering experiments (Penning ionisation) between magnetically guided metastable He atoms and Ar atoms or H_2 molecules, respectively [168]. Additional mea-

surements with the H_2 isotopologues HD and D_2 illustrated that kinetic isotope effects have a strong influence on the shape and the magnitude of the observed resonances [169]. In contrast to that, no isotope effect was seen for the reaction between magnetically guided metastable Ne atoms and electrically guided NH_3 and ND_3 molecules [170], indicating that the reaction proceeds via the lone pair of the nitrogen atom. Both for the reaction between metastable Ne and NH_3/ND_3 and the reaction between metastable Ne and CH_3F, the authors found that the Langevin capture model for a neutral-neutral reaction does not suffice to describe the observed energy dependence [170, 171]. In addition to that, energy-independent product branching ratios were observed for both reactions; the origin of these effects is still unclear.

Compared to a crossed- or merged-beam setup, much longer interaction times between colliding particles can be achieved in molecular synchrotrons, where storage times of over 13 seconds have been attained, corresponding to a total molecular flight distance of more than one mile [172]. The loading of multiple co- and counter-propagating ND_3 molecular beam pulses has been shown as well, but the data analysis is hampered by additional scattering events outside the detection region of the storage ring. So far, the bimolecular collision signal has been smaller than the statistical error of the measurement [173].

Electrostatic or magnetic trapping is another option to increase the interaction time between two molecular samples, but it does not allow for a discrimination between elastic or inelastic collisions unless product quantum states are detected, thus limiting the interpretation of these data and the comparison with theory. In the following, I will focus on neutral-neutral collisions in traps. Section 1.2.2.1 provides a detailed summary of cold ion-molecule chemistry in Coulomb crystals.

Magnetic trapping has been used in combination with buffer-gas cooling to measure trap loss in atom-diatom systems, e.g. between He and NH [174, 175] and between N and NH [176, 177]. However, buffer-gas cells proved useful for low-temperature inelastic

and reactive collisions studies even without magnetic confinement, as demonstrated by Weinstein and co-workers for He + TiO [178] and Li + CaH [179], respectively.

To measure absolute collision cross sections, Sawyer et al. directed a supersonic beam of He atoms or D_2 into a permanent magnet trap which had been loaded with OH molecules from a Stark decelerator [180]. Theory work related to these results suggests that the observed collision rate was mainly due to elastic scattering, and is influenced by the geometry of the trapping fields [181, 182]. In subsequent measurements, the supersonic beam was replaced by a cryogenic source in combination with a bent electrostatic velocity selector. This allowed for the production of a continuous, quantum-state selected beam of ND_3 molecules and a much lower OH-ND_3 collision energy (3.6 cm^{-1}) [183]. Owing to the dipole-dipole interaction between OH and ND_3, the total cross section was largely increased with respect to previous measurements, and an increase in the reaction rate was seen upon application of an external polarising electric field.

Electric field effects in the *absence* of dipole-dipole interactions were observed in cold Rb-ND_3 collisions, in which samples of ultracold Rb atoms, prepared by laser cooling and magneto-optical trapping, were overlapped with Stark-decelerated and electrostatically trapped ND_3 molecules [184]. Even though atom-dipole collisions were studied, the influence of an electric field caused an increase in the inelastic cross section. This observation was reasoned through non-adiabatic transitions induced by a competing alignment of the polar ND_3 molecule with the electric field axis and the collision axis.

The ability to form ultracold molecules through photoassociation and Feshbach resonances has led to a wealth of studies on alkali-alkali dimer collision processes, starting from inelastic collisions between homoatomic systems (Rb + Rb_2 [185], Na + Na_2 [186], Cs + Cs_2 [187, 188]) to inelastic collisions between heteroatomic systems (Rb/Cs + RbCs [189], Cs/LiCs + LiCs [190, 191]) and association reactions to Cs trimers [192] and Cs tetramers [193]. In the case of KRb + K/Rb/KRb, bimolecular chemical reactions have been observed at temperatures as low as 250 nK [194, 195]. Following these experiments, the Boulder group demonstrated that particle confinement in a two-dimensional

optical lattice in conjunction with quantum-state selection and an external alignment field effectively suppressed head-to-tail collisions, and thereby reduced the reaction rate by two orders of magnitude [196]. These results constitute first steps towards the control of ultracold chemical reaction dynamics using electric or magnetic fields, as envisioned by Krems and others [197, 198].

Cold molecule techniques are also finding applications in the study of molecule-surface interactions, as shown recently in a surface scattering experiment with a Stark-decelerated beam of CO molecules [199]. A chip-based Rydberg Stark decelerator is currently being built in our laboratory to control the velocity of hydrogen atoms in selected Rydberg states as they collide with a surface.

1.2.2.1 Chemical Reactions in Coulomb Crystals

In recent years, major steps have been taken to develop experiments for the study of cold chemical reactions in ion Coulomb crystals, and the advances in this field have been summarised in a number of review articles [90, 200, 201]. A Coulomb crystal is formed upon laser cooling of trapped ions at a temperature of about 10 mK. At this transition temperature, the gaseous ion cloud undergoes a phase transition to form a crystal-like structure in which the ions are repelled by their mutual Coulomb interaction (but confined by the trapping fields). Singly charged alkaline earth metal ions, such as Be^+, Mg^+, Ca^+ and Ba^+, are especially suited for these experiments, since they exhibit (almost) closed-cycle transitions between two energy levels at wavelengths that can be accessed with commercial diode laser systems. As discussed in Section 1.1, sympathetic cooling is the most commonly used technique to cool the translational motion of molecular ions. Depending on the mass ratio between the atomic and the molecular ion, bi-component crystals form, in which the molecular ions either accumulate in the centre of the ion trap if they are lighter than the atomic ions, or they form shells around the laser-cooled atomic ions if they are heavier.

Ions in single-component Coulomb crystals can be readily detected through their laser-induced fluorescence (LIF) emitted during the laser-cooling process. Other detection methods include, e.g. resonant-excitation [202] or ion time-of-flight mass spectrometry techniques [203, 204]. Trapping is usually achieved within a radiofrequency ion trap, such as a linear Paul trap. The magnetic fields used for trapping inside a Penning trap split the energy levels of the ions, and thereby make efficient laser cooling more difficult to implement [205]. However, the formation of Ca^+ Coulomb crystals of various sizes has been demonstrated in these traps as well [205].

Early ion-molecule reactions were observed by leaking in room-temperature gases into the vacuum chamber and observing changes in the shape of the Coulomb crystals imaged with a CCD camera [206–214]. Previous experiments in our group focused on reactions between Coulomb-crystallised Ca^+ ions (or sympathetically cooled ions therein) in a radiofrequency ion trap and cold polar molecules, such as CH_3F, from a bent electric quadrupole guide [201, 215–219]. Due to the broad energy range covered by the quadrupole guide, these reactions were not quantum-state selected and could only be observed at temperatures merely approaching the cold regime ($T \approx 4$ K). Nevertheless, this was an early example of how two sources of cold species could be combined to study cold chemistry, and it illustrated the extra-ordinary sensitivity that is achievable using trapped ions as a collision target. Recently, this experimental setup has been adapted by the group of Hans Schuessler to study a variety of ion-molecule reactions including ND_3, H_2CO and CH_3CN [220]. Current experimental effort in our laboratory is focused on a Stark-decelerator-ion-trap configuration [216, 221] and a setup in which a buffer-gas-cooled, electrostatically deflected molecular beam is directed into an ion trap [32, 222]. Other research groups have successfully combined other sources of cold atomic and molecular sources with ion traps. In a proof-of-principle experiment with 3-aminophenol and Coulomb-cystallised Ca^+ ions, Willitsch, Küpper and co-workers have demonstrated that a combination of an electrostatic deflector with an ion trap can be used to probe the reactivity of specific molecular conformers [223]. A lot of progress has been made in the development of ion-atom hybrid systems, in which radiofrequency ion traps are com-

bined with magneto-optical traps (MOT). In-depth reviews of ion-atom reactions in these hybrid-type setups are given by Willitsch [90, 97] and Härter [96].

1.3 Motivation and Outline of this Thesis

My research project is concerned with the setup, characterisation and optimisation of a supersonic beam apparatus including a 12-stage Zeeman decelerator. This experiment forms part of a wider research programme that is aimed at the study of ion-molecule reactions at mK temperatures.

The manipulation of paramagnetic atoms and molecules in a Zeeman decelerator produces mK-cold ($T \approx 100$ mK), velocity-tunable beams of particles in specific internal quantum states. In contrast to Stark deceleration, a Zeeman decelerator allows for the study of reactions involving open-shell (*radical*) atomic and molecular systems which may not have an electric dipole moment. An ion trap provides a suitable "reaction vessel" in which laser-cooled, Coulomb-crystallised ions can be stored for several hours at a time and, thus, makes it possible to study chemical reactions even at relatively low particle number densities. Such a Zeeman decelerator-ion trap combination should allow for the study of cold ion-atom or ion-molecule processes as a function of collision energy and may reveal quantum effects, e.g. through deviations from the classical Langevin reaction rate. The quantum-state selectivity of the deceleration process will greatly simplify the interpretation of kinetic data, because only certain reaction pathways are possible. Chemical reactions involving these *radical* species are of particular relevance for cold chemistry and the astrophysical medium, since these are fast, often barrierless processes that give rise to rate constants on the order of 10^{-10} cm^3 molecule^{-1} s^{-1}, even at interstellar temperatures of a few Kelvin [224, 225].

Figure 1.1 illustrates a number of reactions involving CO_2^+ and H_3^+ ions that could be studied with a Zeeman decelerator-ion trap configuration. Reactions involving H_3^+ ions are of particular relevance from an astrochemical point of view, since H_3^+ is among the most

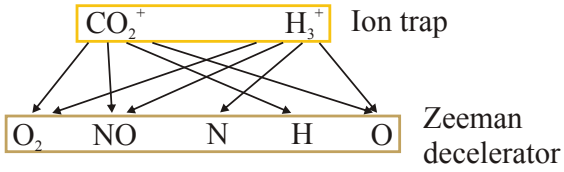

Figure 1.1: Possible ion-molecule reactions for a Zeeman decelerator-ion trap setup. All reactions indicated with arrows have rate constants $\geq 10^{-10}$ cm^3 molecule^{-1} s^{-1} [224]. A (partial) deuteration of the reactants would also allow for the study of isotope effects in these chemical processes.

abundant ions in the interstellar medium [226]. It has been shown that this molecular ion and its isotopomers can be produced and sympathetically cooled with laser-cooled Be^+ ions in a linear Paul trap [209, 210].

The reaction

$$CO_2^+ + H \longrightarrow COH^+ + O \qquad \text{(R 1.1)}$$

is a good test system for such a setup, as the experiments can be carried out with the 12-stage Zeeman decelerator that I have built over the course of my DPhil project. In this case, a Zeeman-decelerated beam of H atoms could be magnetically guided and then directed into a linear Paul trap containing a CO_2^+-Ca^+ bi-component Coulomb crystal (see Chapter 7 for details). Due to their heavier mass, the CO_2^+ ions initially form a non-fluorescent ("dark") shell around the Ca^+ ions. In a CCD camera image, the trap-loading would be indicated by a flattening of the original Ca^+ Coulomb crystal (cf. Figures 1.2 (a) and (b)). As the reaction between CO_2^+ and H proceeds, a dark core of COH^+ is gradually growing in the trap centre while the flattening of the Ca^+ crystal on the outside disappears, as the CO_2^+ reacts away (Figure 1.2 (c) and (d)).

In this context, low H atom number densities are a major obstacle, as they may reduce the reaction rate beyond what is experimentally feasible with this setup. Assuming a bi-molecular rate constant of $4.7{\cdot}10^{-10}$ cm^3 molecule^{-1} s^{-1} (15-300K) [227] for reaction R 1.1, an optimistic H atom number density of $N_H = 10^9$ molecule cm^{-3}, a repetition rate of 10 Hz and a pulse duration of 40 μs for the Zeeman-decelerated atoms, it would take about one hour to observe the formation of an ion image similar to Figure 1.2 (c).

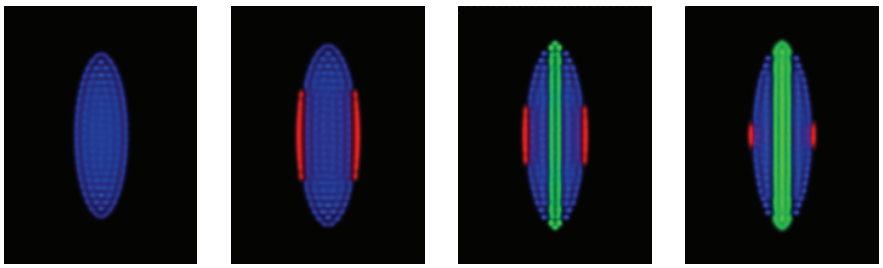

(a) (b) (c) (d)

Figure 1.2: Coulomb crystal images obtained from molecular dynamics simulations [201] at different experimental stages of the reaction between H atoms and CO_2^+ ions in a linear Paul trap (radiofrequency voltage of 300 V, endcap voltage of 4 V). In the experiment, only the laser-induced fluoresence from Ca^+ ions (highlighted in blue colour) would be visible. The CO_2^+ ions (red) and the COH^+ ions (green) are displayed for visual clarity only. (a) Single-component Coulomb crystal of 600 Ca^+ ions. (b) After trap loading with CO_2^+: bi-component Coulomb crystal composed of 600 Ca^+ ions and a shell of 200 CO_2^+ ions. (c) In the course of the reaction with H atoms: formation of a dark core of 100 COH^+ ions. The Ca^+ ions do not react. (d) Further ahead in the reaction: the number of COH^+ ions has grown to 180. Simulated images kindly provided by Alexander Smith.

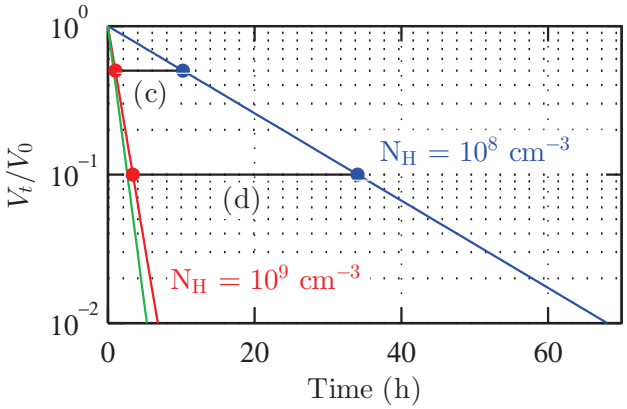

Figure 1.3: Temporal decay of CO_2^+ Coulomb crystal volume, V, in the reaction between H and CO_2^+ at H atom number densities of $N_H = 10^8$ molecule cm^{-3} (blue curve) and 10^9 molecule cm^{-3} (red curve). The background reaction with residual H_2O in the vacuum chamber (see text) is highlighted with a solid, green curve. The black horizontal lines and the dots indicate the estimated times at which ion images similar to Figures 1.2 (c) and (d) would be observed.

If $N_H = 10^8$ molecule cm^{-3}, the same process would take about 10 hours. To decrease experimental uncertainties, i.e. from the comparison between molecular dynamics simulations results and experimental images, even longer reaction times may be required. In addition to that, dark ions in the core of the Coulomb crystal may also be formed through

background reactions, e.g. with residual H_2O and H_2 in the vacuum chamber, and thus bias the observations. For example, if we assume a pressure of $1{\cdot}10^{-10}$ mbar, a 5 % abundancy of H_2O in the chamber and a rate constant of $2{\cdot}10^{-9}$ cm^3 molecule^{-1} s^{-1} [224], we would observe a decay of CO_2^+ (green curve in Figure 1.3) that is comparable to the rate for reaction R 1.1 at high H atom number densities (red curve in Figure 1.3). Additional experimental effort may be needed to discriminate the influence of background reactions, i.e. ion-time-of-flight mass spectrometry. Likewise, a cooling of the ion trap chamber with liquid nitrogen may freeze out contaminants.

This example illustrates that these experiments will be extremely difficult to carry out, and a high flux of decelerated particles through the ion trap will be mandatory to ensure that a significant fraction of reaction products is formed within a short period of time. Since the typical size of an ion crystal is only a few hundred micrometers, focusing of the decelerated particles into the centre of the ion trap would be beneficial as well. Therefore, apart from the design of a compact experimental setup (Chapter 4), I looked at ways to improve particle transmission through the decelerator. One of these approaches involves the use of opposing current directions for the solenoid coils to enhance transverse particle confinement in the decelerator (Chapter 5). I have also assessed the use of a permanent magnetic hexapole system in Halbach array configuration for particle focusing into the Zeeman decelerator and for the magnetic guiding of Zeeman-decelerated H atoms into an ion trap (Chapter 7). In addition to that, I developed a theoretical model to calculate the overall phase-space acceptance in a Zeeman decelerator (Chapter 3). Apart from a better general understanding of the deceleration process, this model also provides a useful tool to evaluate alternative switching schemes for Zeeman deceleration.

The second part of my research project was concerned with the setup of an electron-impact excitation source to produce and decelerate light atoms and molecules in excited, long-lived ("metastable") quantum states, such as He(2^3S_1) N($^2D_{3/2,5/2}$) and $H_2(c^3\Pi_u)$. Chemical processes involving metastable species are important in the Earth's upper atmosphere [228–230], planetary aurora [231], cometary coma [232] and in combustion and plasma processes [233, 234]. The magnetic deceleration of metastable species opens new

avenues for the study of neutral-neutral reactions at mK temperatures. From an experimental point of view, reactions involving metastable atoms and molecules are particularly appealing, since the detection of metastable species and/or reaction products, e.g. ions produced in Penning ionisation processes, is typically straightforward.

Using this setup, I have – for the first time – observed the Zeeman deceleration of metastable He atoms in the 2^3S_1 state. Metastable He also served as a good test system for the characterisation of the electron gun (Chapter 4), and proved useful for the understanding of deceleration data (Chapter 6). There has also been progress towards the deceleration of metastable N atoms, and I will report on the current status of these experiments (Chapter 4).

This thesis is structured as follows. In Chapter 2, I will describe the theoretical framework behind supersonic beams and give an outline of the numerical particle trajectory simulation program that is used to understand the particle motion in a Zeeman decelerator. Chapter 3 contains a detailed summary of the formalism that I have devised to calculate the six-dimensional phase-space acceptance in a Zeeman decelerator, and, using two examples, it is shown that the model can be used to assess the quality of alternative Zeeman deceleration schemes. In Chapter 4, I will provide details about the supersonic beam apparatus and its characterisation. This may serve as a reference for the members of the Softley group, and give guidance to other researchers intending to build a Zeeman decelerator or a supersonic beam experiment in general. In this context, I am listing a lot of technical specifications and figures, as I believe that they will aid in troubleshooting and facilitate the realisation of future experiments.

Chapter 5 summarises Zeeman deceleration experiments on ground-state H atoms demonstrating improved transverse confinement through the use of a reversed current direction for one of the coils. In Chapter 6, results on the Zeeman deceleration of metastable He atoms are presented, and it is shown that metastable production can be significantly increased through an additional discharge-type mechanism. In Chapter 7, I will discuss the prospects of using a permanent magnet assembly (Halbach array) in a hexapole configu-

ration for particle focusing into the decelerator. In view of future ion-molecule reaction experiments, I will propose schemes for a hybrid magnetic guide composed of Halbach arrays and a set of current-carrying wires in order to interface the Zeeman decelerator with an ion trap.

This thesis is full of ideas that have not yet been put into practise (Chapters 3 and 7), and I hope that this manuscript will help to preserve them for the next generation of DPhil students.

2 | Theoretical Background

In the first part of this Chapter, I will give a concise overview on the theoretical framework relevant to this project, with particular emphasis on supersonic beams. Based on these concepts, I will provide a detailed description of the particle trajectory simulations that were carried out to simulate the particle motion in a Zeeman decelerator.

2.1 Supersonic Beams

This Section gives a brief overview on the basic concepts of supersonic beams. It is, for a large part, based on reviews by Miller [235] and Morse [236], and the reader is referred to these texts (and the references therein) for a full account of this subject. An article by Lubman et al. [237] also provides a good reference to most of the relevant equations related to the Mach number.

In general, there are three complementary approaches to describe a supersonic expansion: a molecular approach based on collision theory, a thermodynamical approach, in which the expansion is characterised in the context of pressure, density and temperature, and an approach founded on fluid dynamics.

Depending on the ratio between the nozzle orifice diameter, D, and the mean free path, λ_0, i.e. the distance travelled by a particle in between two successive collisions, we can distinguish between two extreme flow regimes. If $\lambda_0 \gg D$, the particles undergo very few collisions during the expansion, such that the resulting velocity distribution can be described by a Maxwell-Boltzmann distribution whose mean velocity is determined by the temperature of the beam source and the particle mass. Continuous beams emerging from buffer-gas cooled sources are good examples of such effusive atomic or molecular beams. On the other hand, if $\lambda_0 \ll D$, the expansion is characterised by numerous elastic and inelastic collisions leading to a conversion of internal energy into kinetic energy of the

flow. While the beam is moving at very high velocity in the laboratory frame, the velocity spread in the moving frame of reference decreases due to the large number of collisions. Since inelastic collision cross sections are typically much lower than cross sections for elastic collisions, the translational motion (with a temperature $T_{\mathrm{trans}} = T$) is much more effectively cooled than the rotational (with T_{rot}) and the vibrational motion (characterised by T_{vib}), such that the temperatures typically follow the trend $T_{\mathrm{trans}} < T_{\mathrm{rot}} < T_{\mathrm{vib}}$. As a rough guide, Miller [235] assumes that about 10 – 100 collisions are required for the rotational relaxation of a diatomic molecule, while more than 10^4 collisions are needed to cool the vibrational degrees of freedom. Assuming a total number of 10^2 – 10^3 collisions within a supersonic expansion, it becomes obvious that the number of collisions is usually insufficient for vibrational relaxation. The number of two-body collisions is proportional to $p_0 D/T_0$, while three-body collisions scale as $p_0^2 D/T_0^2$, where p_0 and T_0 are the gas pressure and the temperature in the reservoir, respectively. Hence, the collisional cooling in a supersonic expansion mainly results from binary collisions, as they appear much more frequently than three-body collisions. Owing to the pressure dependency, three-body collisions are typically constricted to the region close to the nozzle exit. This type of collisions is responsible for cluster formation, as the third body can carry off excess energy of the collision complex. In the molecular beam setup used in this work, the formation of Xe_2 van der Waals molecules was experimentally observed (see Section 4.6). As the jet expands further, also the number of binary collisions drops rapidly, until the motion is said to be "frozen", i.e. the number of collisions is too low for further cooling. As a rule of thumb, a supersonic expansion is completed after a distance of about 20 – 30 orifice diameters from the nozzle.

Figure 2.1 shows a photograph capturing the supersonic expansion of excited N_2 and N species. The plume of the expanding gas is made visible through fluorescence emitted by the atoms and molecules during electron-impact excitation (100 eV kinetic energy, $U_{\mathrm{bias}} = 250$ V, Section 6.2.2). Light emission is increased by collisional quenching with Ne atoms ($p_0 = 5$ bar, 1/1.5 mixture of Ne in N_2, $T_0 = 93$ K).

In the fluid dynamics approach, an expansion is called supersonic when the average flow

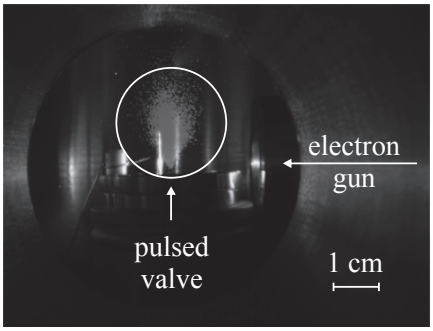

Figure 2.1: Photograph showing the fluorescence of excited N_2 and N species upon electron-impact excitation. Since electron impact occurs close to the nozzle orifice, the plume of the supersonically expanding gas is made visible (inside white circle). Images were taken with a monochrome camera (The Imaging Source, DMK 41AU02), using a 1/23 s exposure time to account for the 10 Hz repetition rate of the pulsed valve. Image processing in MATLAB was carried out to increase the visibility of the light emission. The violet-green fluorescence was also visible by eye.

velocity during the expansion exceeds the local speed of sound, i.e. when the Mach number, M, is greater than one.[a] In this case, the resulting velocity distribution, $f(\vec{v})$, can significantly deviate from Maxwellian. It is often characterised in terms of two Gaussians with a velocity component parallel to the beam axis, v_z, and a perpendicular velocity component, $v_r = \sqrt{v_x^2 + v_y^2}$, [238]

$$f(\vec{v}) = n\sqrt{\frac{m}{2\pi k_B T_z}}\frac{m}{2\pi k_B T_r}\exp\left(-\frac{m}{2k_B T_z}(v_z - v)^2 - \frac{m}{2k_B T_r}v_r^2\right), \tag{2.1}$$

where n is the density, v is the most probable flow velocity, k_B is the Boltzmann constant and m is the particle mass. A longitudinal temperature, T_z, and a transverse temperature, T_r, are attributed to the velocity components v_z and v_r, respectively. The standard deviation is thus $\sigma_{v_z} = \sqrt{k_B T_z/m}$ for the longitudinal velocity component and $\sigma_{v_r} = \sqrt{k_B T_r/m}$ for the transverse velocity component.

The Mach number M is defined as

[a] Analogous to a combat jet travelling at supersonic speed, a supersonic molecular jet is characterised by a shock wave (Mach cone) that is travelling ahead of the expansion.

$$M = \frac{v}{a} = \frac{v}{\sqrt{\frac{\gamma k_B T}{m}}}. \tag{2.2}$$

Here, a is the local speed of sound and $\gamma = C_p/C_V$ is the heat capacity ratio, where C_p is the heat capacity at constant pressure and C_V is the heat capacity at constant volume. In the molecular picture, γ is related to the degrees of freedom of an ideal gas, f, such that $\gamma = (f+2)/f$. Hence, γ = 5/3 for an atom, and γ = 7/5 for a diatomic molecule.

The Mach disk marks the transition zone between subsonic and supersonic flow regimes. The value of the Mach number depends on the distance between Mach disk and nozzle along the beam axis, z_M, and the nozzle diameter, D. Empirically, the relation $z_M/D = 0.67\sqrt{p_0/p}$ has been found [239], where p_0 is the pressure in the reservoir and p is the local pressure in the expansion region. The value of the Mach number changes as a function of z_M/D. To estimate M, an empirical fitting formula was derived,

$$M = A\,(z_M/D - B)^{\gamma-1} - C\,(z_M/D - B)^{-(\gamma-1)}, \tag{2.3}$$

where A = 3.26, B = 0.075 and C = 0.61 for a monoatomic gas, and A = 3.65, B = 0.4 and C = 0.82 for a diatomic gas [239]. The second term in Eq. 2.3 becomes very small at large distances from the nozzle, such that this equation can be simplified to

$$M \approx A\,(z_M/D)^{\gamma-1}. \tag{2.4}$$

For monoatomic gases (except for He), the terminal Mach number, M_∞, i.e. the Mach number at infinite distance from the source, is well approximated by [240, 241]

$$M_\infty = 133 \cdot (p_0^{\mathrm{at}} D^{\mathrm{cm}})^{-(\gamma-1)}. \tag{2.5}$$

In this equation, the source pressure, p_0^{at} and the nozzle diameter, D^{cm}, are given in units of atmospheres and centimeters, respectively. As the nozzle orifice of a pulsed valve is not usually fully open, effective nozzle diameters $D_{\mathrm{eff}} < D$ are sometimes used instead.

From the definition of the Mach number in Eq. 2.2, all relevant thermodynamic quantities can be derived as a function of Mach disk location, among them the flow velocity, v, the local (translational) beam temperature, T, and the local density, n, [242]

$$v = M\sqrt{\frac{\gamma k_{\mathrm{B}} T_0}{m}}\left(1+M^2\frac{\gamma-1}{2}\right)^{-1/2} \tag{2.6}$$

$$T = T_0\left(1+M^2\frac{\gamma-1}{2}\right)^{-1} \tag{2.7}$$

$$n = n_0\left(1+M^2\frac{\gamma-1}{2}\right)^{-1/(\gamma-1)}, \tag{2.8}$$

The parameters T_0 and n_0 denote the source temperature and the source density, respectively. For large z_M/D, the terminal beam velocity, v_∞, is approximated by[b]

$$v_\infty \approx \sqrt{\frac{2k_{\mathrm{B}}T_0}{m}\frac{\gamma}{\gamma-1}}, \tag{2.9}$$

Using typical conditions for the metastable atom experiments in our setup (D = 0.8 mm, nozzle – skimmer distance of 38 mm, T_0 = 302 K, p_0 = 6.0 bar), Eq. 2.3 predicts a Mach number of M = 42 at the location of the skimmer. According to Eq. 2.5, the terminal number is about twice as high as this value (M_∞ = 99), but it would only be attained after a distance of 13.3 cm from the nozzle. Even though this indicates that the expansion is not complete ("frozen") at the skimmer, the calculated beam velocity at this position, v_{skimmer}, is very close to its terminal value, v_∞.

[b] see also reference [243]

Table 2.1: Comparison of experimental and theoretical flow velocities for metastable atoms and molecules from time-of-flight measurements (TOF, T_0 = 302 K and p_0 = 6.0 bar, see Section 6.2.1) and estimates using Eq. 2.9 and Eq. 2.6. Maxwell-Boltzmann distributions were used to extract beam velocities from the TOF profiles, taking into account the finite pulse duration for electron-impact excitation ($\Delta t_e = 50\ \mu$s) and assuming a well-collimated supersonic beam with $v_r \ll v_z$ [244]. The MCP detection method does not allow for a distinction between different metastable states.

Primary Metastable Species [245]	Theory		Experiment
	v_∞ (m/s)	v_{skimmer} (m/s)	v_{exp} (m/s)
$He(2^1S_0)$, $He(2^3S_1)$	1772	1770	1800
$Ne(3^3P_{0,2})$	789	788	840
$N_2(A^3\Sigma_u^+)$[a]	792	784	840
$Ar(4^3P_{0,2})$	561	560	610
$Kr(5^3P_{0,2})$	387	387	430

[a] The internal energy of the metastable $N(^2D)$ and $N(^2P)$ states (2.4 eV and 3.6 eV [246]) is not sufficient to eject electrons from the surface of the MCP detector.

The theoretical values for v_∞ (Eq. 2.9) and v_{skimmer} (Eq. 2.6) are in good agreement with experimentally observed beam velocities, v_{exp} (Table 2.1). In this case, electron-impact excitation was used to excite the particles to metastable states during the expansion (Section 4.3). The experimentally observed velocities are systematically higher than expected from theory, and the values are also consistent with extrapolated H atom velocities from REMPI experiments at high dilution (cf. Figure 2.2b). However, a direct comparison with theoretical values is difficult, since the beam velocities vary depending on the relative timing between electron-impact excitation (or photolysis) and the opening of the pulsed valve (see also Figure 4.4a). This indicates that thermalisation is different in various parts of the beam, and most efficient in the central part of the gas pulse (electron-gun-to-valve delay of 350 μs, velocities in Table 2.1), where the lowest velocities and the coldest translational temperatures are observed. In addition to that, the measured time-of-flight (TOF) spectra in Table 2.1 are convoluted with the finite electron-excitation pulse width [247]

(Δt_e = 50 μs) and need to be corrected for this effect[c]. For MCP detection, the measured longitudinal temperatures for metastable He (T_z = $\approx$ 30 K) are also much higher than for REMPI detection (T_z = 0.7 K), which could be due to the simultaneous detection of several excited species including Rydberg atoms. For H atoms, similar longitudinal temperatures (T_z = 1.1 K for H atoms in a 1/9 NH_3/Kr mixture, Chapter 5) are observed. These values are in good agreement with estimates from Eq. 2.7, which yields a temperature of about T = 0.5 K for a monoatomic supersonic beam. The calculated density, $n = 1{\cdot}10^{16}$ cm^{-3} in the skimmer region (using the ideal gas law to estimate n_0), does not take into account that only a fraction of the beam is excited into a metastable state or photodissociated. For electron-impact excitation, the metastable-to-ground-state fraction is typically 10^{-4} – 10^{-5} [248], so that the maximum achievable metastable densities are on the order of $1{\cdot}10^{11}$ cm^{-3}. An experimental measurement of the absolute beam density was not attempted.

2.1.1 Velocity Slip Effect

In most of the experiments described in this thesis, the valve body is cooled and/or the particles are seeded in a heavier carrier gas in order to decrease the initial velocity for Zeeman deceleration. Experimentally, we have observed that seeded supersonic beams of H atoms ($1^2S_{1/2}$) and metastable He atoms (2^3S_1) do not travel at the expected carrier gas velocity. Figure 2.2 illustrates this effect for different mixing ratios between H atoms (using NH_3 as a precursor) and Ar carrier gas. Although the velocity of the H atoms decreases as the Ar fraction in the mixture is raised, the velocity does neither reach the terminal beam velocity of the Ar gas, v_∞(Ar), nor the experimentally determined metastable Ar beam velocity (Table 2.1), even at the highest dilution of 1/39. For the seeding of metastable He in Ar, similar characteristics were observed, cf. 730 m/s for a 1/6 He/Ar mixture (Section 6.3). The velocity difference is probably due to a velocity (temperature) slip effect, i.e. the insufficient mixing and collisional cooling of a light gas when seeded

[c]However, comparable beam velocities were also obtained for much shorter pulse durations, such as Δt_e = 1 μs, where this effect is negligible.

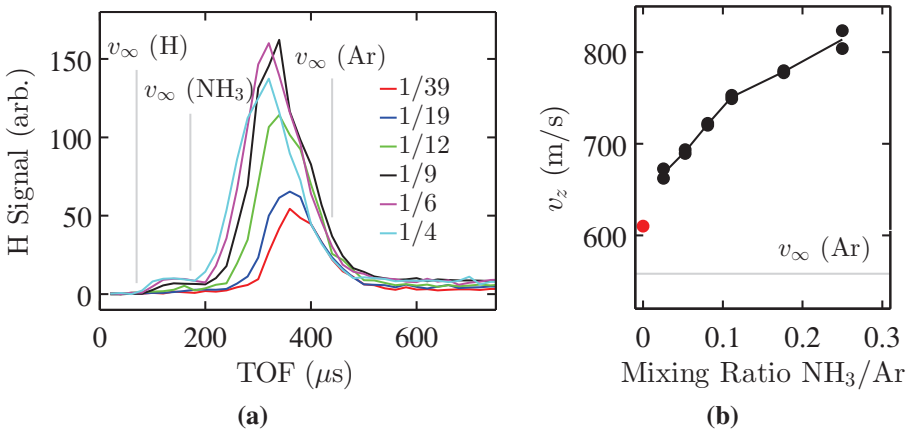

Figure 2.2: (a) Measured H atom time-of-flight profiles (TOF) for different NH_3/Ar mixing ratios (p_0 = 4 bar, T_0 = 299 K) as indicated by the legend. The expected arrival times for unseeded beams of H, NH_3 and Ar, derived from the terminal beam velocity (Eq. 2.9), are indicated with grey lines. (b) Black dots: H atom beam velocities at different NH_3/Ar mixing ratios as determined from the TOF measurements in (a). Grey line: calculated terminal beam velocity for a pure Ar beam, v_∞(Ar). Red dot: Experimentally determined metastable Ar beam velocity (Table 2.1). For H atom deceleration experiments, the valve was cooled to 238 K and a 1/9 NH_3/Kr mixture was used to achieve both good signal intensity and a relatively low beam velocity of 490 m/s.

in a heavy carrier gas. During the expansion, the heavy species may push the lighter gas particles to the outside of the expansion cone [249], and thereby induce both a significant off-axis velocity component to the seed gas and prevent an efficient collisional energy transfer between the carrier and the seed gas. In the case of H atoms, the energy released upon photodissociation of NH_3 produces H atoms with an excess translational energy of $\approx 4500\ \mathrm{cm}^{-1}hc$ [250], which may further contribute to the observed velocity difference between seed and carrier gas.

2.1.2 Influence of the Source Temperature

According to gas kinetic theory, the translational kinetic energy of an atom or molecule is defined as $E_{\mathrm{kin}} = \frac{1}{2}mv^2 = \frac{3}{2}k_{\mathrm{B}}T$. The velocity after cooling (or heating), v_{T}, should therefore scale as

$$v_T = v_{RT}\sqrt{T_T/T_{RT}}, \tag{2.10}$$

where T_{RT} and v_{RT} are the source temperature and the beam velocity for a room-temperature supersonic expansion, and T_T is the temperature of the gas reservoir after cooling (or heating). As shown for NH_3/Ar and He/Ar mixtures in Table 2.2, this relationship is indeed observed in the experiment, even though – owing to a velocity-slip effect (see previous Section) – the initial room-temperature velocity after seeding is much higher than predicted by theory.

Table 2.2: Experimentally measured flow velocities, v_{exp}, of H atoms ($1^2S_{1/2}$) and metastable He atoms (2^3S_1) after seeding of He and NH_3 precursor gas in Ar (mixing ratio shown in brackets) at different source temperatures; see Sections 4.1.1 and 4.1.2 for experimental details. The data are compared to predictions of the terminal carrier gas velocity, v_∞, and the expected velocity after cooling, v_T, as calculated from v_{exp} at room temperature using Eq. 2.10.

	v_∞ (m/s)	v_{exp} (m/s)	v_T (m/s)
NH_3/Ar (1/9)			
T_{RT} = 300 K	559	748	–
T_T = 238 K	498	661	666
He/Ar (1/3)			
T_{RT} = 301 K	560	812	–
T_T = 143 K	386	540	560

2.2 Simulation of the Particle Motion in a Zeeman Decelerator

As the particle motion in a Zeeman decelerator cannot be understood intuitively, numerical three-dimensional particle trajectory simulations were carried out to facilitate the interpretation of time-of-flight data (see 5.3.1). This Section provides a general idea of the trajectory program that I have written in MATLAB. A C++ code by the Merkt group (Yves Salathé [251]) served as a key reference and guidance for this work, and the

implementation of the C++ program is summarised in the theses by Salathé [251] and Wiederkehr [252].

Figure 2.3 shows a simplified outline of the particle trajectory program, which consists of two main subroutines: the generation of the switching sequence for Zeeman deceleration, and the actual three-dimensional particle trajectory simulation. Both subprograms share common principles, such as the generation of a time-dependent current, the calculation of magnetic field components and gradients to obtain the force exerted on the particles, and the numerical integration of the particle motion. However, the practical implementation of the subroutines is very different, since the pulse generation subprogram requires multiple iterations over time to find an accurate switching sequence for deceleration. In addition to that, this part of the program is calculated only for a single, on-axis particle with $v_r = 0$ so that the evaluation of the magnetic field contribution is less complicated than in the three-dimensional simulation of an entire particle ensemble.

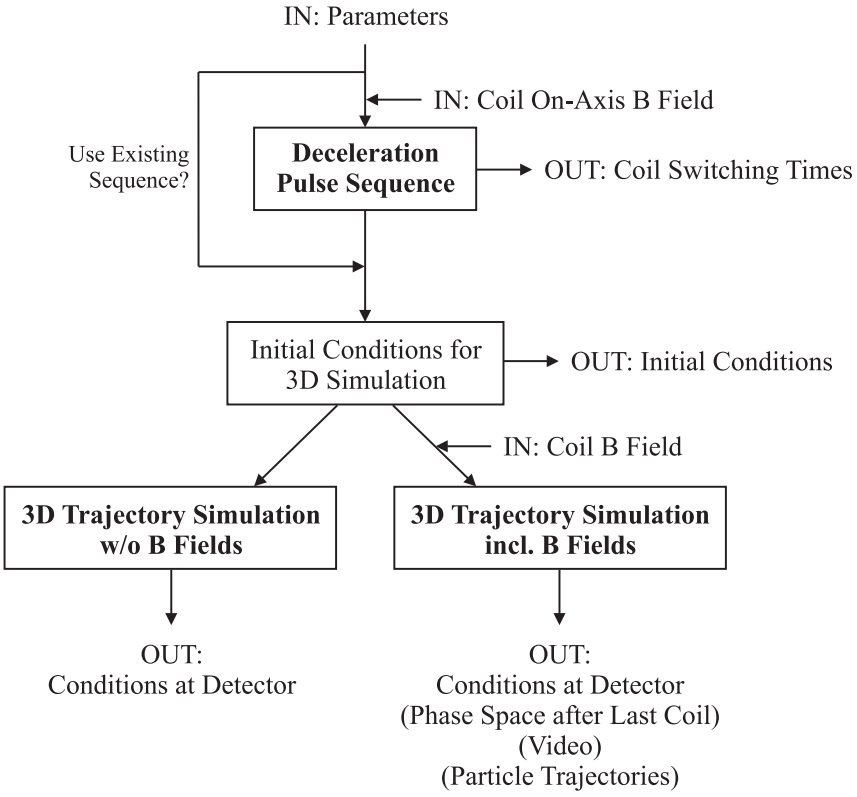

Figure 2.3: Flowchart of the Zeeman deceleration particle trajectory program.

2.2.1 Deceleration Pulse Sequence

Zeeman deceleration relies on phase stability, which implies that only a specific particle ensemble ("bunch") with a certain range of relative velocities and spatial positions will be decelerated by the solenoid magnetic fields. Chapter 3 of this thesis is particularly devoted this topic, and therefore, only a brief outline is given here.

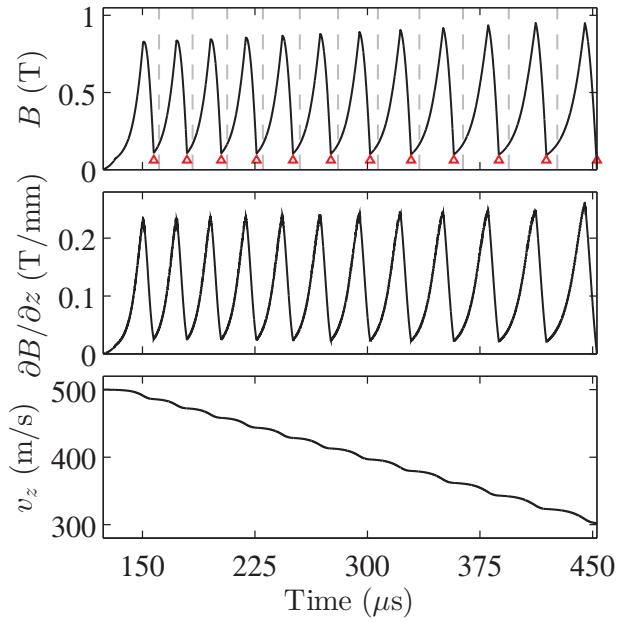

Figure 2.4: Magnetic field magnitude (top) and longitudinal gradient (middle) experienced by a synchronous particle as a function of time after photolysis. Bottom: Longitudinal velocity of the particle. The deceleration pulse sequence ($\bar{a}_z/\bar{a}_{z,m}$ = -0.8) from v_0 = 500 m/s to a final velocity of 300 m/s was calculated for a ground-state H atom in the M_F = 1 state. Top figure: red triangles mark the switch-off times corresponding to κ_0, dashed lines indicate the time at which the centre of an active coil is reached.

For phase-stable deceleration, an imaginary on-axis ("synchronous") particle with velocities $v_z = v_0$ and $v_x = v_y = 0$ is picked from the velocity distribution of the supersonic beam. To maximise the transmission through the decelerator, v_0 is often chosen such that it corresponds to the mean flow velocity of the beam, v. As shown in Figure 2.4, the currents are switched so that this particle experiences a periodic magnetic field pattern. In a simple picture with infinitely short rise and fall times of the currents, the synchronous particle always moves exactly one coil distance, d, in between deceleration stages to achieve this

periodicity. As the particle's velocity changes during its passage through the decelerator, the switching period of the coils increases (decreases) as the particle is decelerated (accelerated), and must be determined in a one-dimensional trajectory simulation. For this, the particle position relative to an active coil is defined by a parameter $\kappa = (z - z_0)/d$, where z_0 is the coil centre and d is the coil-to-coil distance. The particle position at which each coil is switched off is then set by the reduced position κ_0. At vanishing rise and fall times, κ_0 = const. However, as detailed in Chapter 3, the finite switching times of the currents require the use of a variable κ_0 in order to achieve the same amount of deceleration per coil. Alternatively, the normalised mean acceleration, $\bar{a}_z/\bar{a}_{z,m}$, where $\bar{a}_{z,m}$ is the maximum mean longitudinal acceleration, can be used to define the switch-off position within a coil.

For the chosen amount of deceleration in Figure 2.4, $\bar{a}_z/\bar{a}_{z,m}$ = -0.8, the coils are turned off (red triangles) before the synchronous particle reaches the coil centre (grey dashed lines). Therefore, the gradient $\partial B_z/\partial z$ remains positive throughout the deceleration pulse sequence (middle panel), i.e. the particle is continuously being decelerated (bottom panel) even though the magnetic field strength decreases before κ_0 is reached (top panel).

In practise, the simulation is started with an initial guess of the switching times. The position and velocity of the synchronous particle are numerically integrated (see Section 2.2.5) until the switch-off time of the active coil is reached, and the particle position at that time is compared to the on-axis position corresponding to κ_0. Depending on the position relative to κ_0, the switching times of the coil are shifted, and the simulation is reiterated until the two positions coincide. If this is the case, the same procedure is performed for the next active coil.

2.2.2 Three-Dimensional Particle Trajectory Simulation

Numerical three-dimensional particle trajectory simulations are carried out with and without the magnetic fields of the solenoid coils. In the field-free case, the particle velocities

do not change and numerical integration of the motion is not necessary. However, this simulation provides a good cross check with the other trajectory calculations, especially when changes to the boundary conditions are applied.

Initially, a particle matrix of up to 500,000 particles with randomised initial positions and velocities is created within the expected envelope of the beam (see Section 2.2.3), and a comparison step ensures that particles are selected only if they pass through the aperture of the skimmer. To simulate more than 500,000 particles, the program is automatically re-initialised with a different set of initial conditions once the previous run has been completed. If currents are applied to the coils, the resulting magnetic field and magnetic field gradients are evaluated in order to determine the magnetic force, and thus the acceleration of the particles (see Section 2.2.4), which is used for numerical integration of the particle motion (see Section 2.2.5). Particles are removed from the simulation either if their transverse position is larger than the inner radius of a deceleration coil or if they have passed through a detection area spanned by the xy plane at a given position z behind the decelerator. The finite volume of a detection laser beam is typically taken into account in the post-analysis of the trajectory data.

2.2.3 Initial Particle Positions and Velocities

The three-dimensional trajectory program relies on the random sampling of initial particle positions and velocities from the expected distribution for the beam. In this Monte Carlo-type approach, the Mersenne Twister [253] (MATLAB built in) is chosen as the pseudorandom number generating algorithm. It is seeded with a fixed value so that the same random numbers are produced for repeated executions of the code.

To generate numerical results that match experimental conditions, the initial conditions in the program resemble the given experimental geometry in the source region. In the experiments with ground-state hydrogen atoms, the particles are expanded through a quartz capillary (see Section 4.1.1) to increase the number of thermalising collisions after laser

photolysis. The particle positions in the simulation are therefore uniformly random distributed inside a cylinder with dimensions determined by the length and the inner diameter of the quartz capillary (1 mm diameter, 15 mm length). To model the electron-beam excitation region, initial positions are randomly chosen from a cylindrical volume in the x direction (2 mm diameter) located at the valve exit; the extent in the x direction is limited to -1 mm $\leq x \leq$ 1 mm with respect to the pulsed valve, as only those particles are likely to pass through the skimmer. To account for the duration of the electron excitation pulse, the particles are randomly assigned an initial time such that the time distribution of the simulated particle ensemble matches either a square pulse or an experimental pulse shape, given by the temporal characteristics of the electron current (see Figure 4.8a).

In accordance with theory (see Section 2.1), normal distributions with velocity spreads σ_{v_z} and σ_{v_r} are chosen for both the longitudinal and the transverse velocity components v_z and $v_r = \sqrt{v_x^2 + v_y^2}$. Bivariate normal distributions of off-axis random velocities, v_x and v_y, centred at zero and with the velocity spreads $\sigma_{v_r} = \sigma_{v_x} = \sigma_{v_y}$ are generated using MATLAB's built-in function 'mvnrnd'. For transverse velocity distributions peaked at $v_r > 0$, e.g. to simulate the displacement of H atoms by Kr carrier gas (see velocity slip in Section 2.1), a uniform distribution of random numbers is created inside a cuboid (see Figure 2.5). The random points inside the cuboid, $\{v_{x,i}, v_{y,i}, h_i\}$ with $0 \leq h \leq 1$, are evaluated using a shape function

$$f(v_r) = f(v_x, v_y) = \exp\left(\frac{-(v_{r,i} - \bar{v}_r)^2}{2\sigma_{v_r}^{\star\,2}}\right) \tag{2.11}$$

with a velocity spread, $\sigma_{v_r}^{\star}$ and a maximum at $\bar{v}_r$. Only those points are kept that meet the condition $h_i \leq f(v_{r,i})$. This subroutine is repeated until the desired number of random velocities is generated. However, for data analysis in this thesis, only bivariate normal distributions are used to describe the off-axis motion.

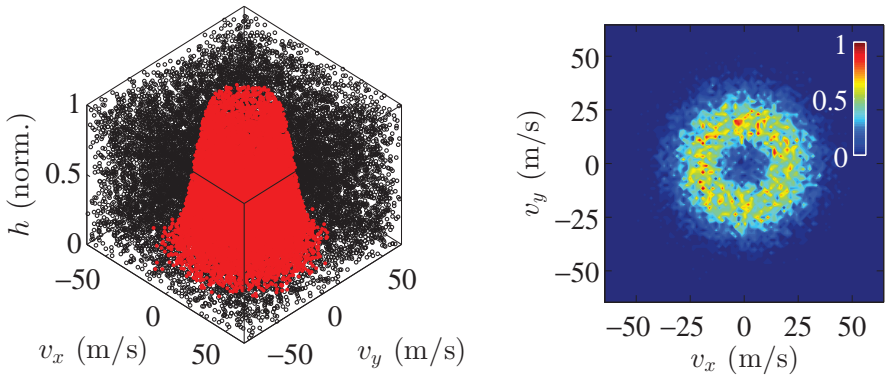

Figure 2.5: Generation of off-axis random velocity distributions centred at $v_r > 0$. (a) Cuboid containing the random points, $\{v_{x,i}, v_{y,i}, h_i\}$ (red and black dots), to be evaluated. Red dots correspond to values which fall below the cutoff set by the shape funtion $f(v_r)$ with a maximum at $\bar{v}_r = 20$ m/s and a velocity spread of $\sigma^{\star}_{v_r} = 9$ m/s. While these points are kept in the simulation, the points in black colour are excluded from the selection process. (b) Density plot of the obtained bivariate velocity distribution (3 D histogram of red-coloured points in (a)).

2.2.4 Evaluation of the Magnetic Fields

In cylindrical coordinates, the magnitude of the magnetic field, B, reads

$$B = |\vec{B}| = \sqrt{B_r^2 + B_\phi^2 + B_z^2}. \tag{2.12}$$

From this, the derivative vector of B, $\vec{\nabla}B$, where $\vec{\nabla} = \left(\frac{\partial}{\partial r}, \frac{1}{r}\frac{\partial}{\partial \phi}, \frac{\partial}{\partial z}\right)^T$, can be obtained as

$$\vec{\nabla}B = \frac{B_r\vec{\nabla}B_r + B_\phi\vec{\nabla}B_\phi + B_z\vec{\nabla}B_z}{B}.^{\text{d}} \tag{2.13}$$

The magnetic field components B_z and B_r of a solenoid coil at a given current level, I_{sim}, are pre-calculated using the analytic formulas of Bergeman et al. [254] and loaded into the program as lookup tables. Owing to the cylindrical symmetry of the solenoid

[d] In cartesian coordinates, $B = |\vec{B}| = \sqrt{B_x^2 + B_y^2 + B_z^2}$ and $\vec{\nabla} = \left(\frac{\partial}{\partial x}, \frac{\partial}{\partial y}, \frac{\partial}{\partial z}\right)^T$, so that $\vec{\nabla}B = \frac{B_x\vec{\nabla}B_x + B_y\vec{\nabla}B_y + B_z\vec{\nabla}B_z}{B}$.

magnetic field about the z axis, the B_ϕ component vanishes, and the field components and partial derivatives can be obtained by bilinear interpolation from the B_z and B_r grid nodes, which requires less computational effort than trilinear interpolation in cartesian coordinates [255]. The practical implementation is explained in depth by Salathé [251] and Wiederkehr [252]. An additional hexapole field, where $B_\phi \neq 0$, can be included analytically (see Chapter 7).

The calculation of the deceleration pulse sequence only requires linear interpolation, since $B_r = 0$ on the z axis and $B_\phi = 0$. Here, the magnitude of the magnetic field, B, simplifies to $B = B_z$ and the derivative vector of B, $\vec{\nabla}B$, becomes

$$\vec{\nabla}B = \vec{\nabla}B_z = \begin{pmatrix} 0 \\ 0 \\ \frac{\partial B_z}{\partial z} \end{pmatrix}. \tag{2.14}$$

The temporal characteristics of the currents (see Figure 4.13) are taken into account through scaling to I_{sim}, and the time overlap between adjacent coils is included by adding the scaled magnetic field components and partial derivatives of single coils *before* calculation of B and $\vec{\nabla}B$.

The acceleration of a paramagnetic particle in a magnetic field, $\vec{a}$, is given by

$$\vec{a} = \frac{F_{\mathrm{mag}}}{m} = -\frac{1}{m}\vec{\nabla}B\frac{\mathrm{d}(\Delta E_{\mathrm{Z}})}{\mathrm{d}B}, \tag{2.15}$$

where F_{mag} is the force exerted by the magnetic field, m is the particle mass and ΔE_{Z} is the Zeeman shift in a magnetic field.

Using Eq. 2.13, the acceleration vector is of the form $\vec{a} = \left(a_r, a_\phi, a_z\right)^T$. As the motion is calculated in cartesian coordinates with $\vec{a} = (a_x, a_y, a_z)^T$, a coordinate transformation is required to obtain a_x and a_y,

$$\begin{pmatrix} a_x \\ a_y \end{pmatrix} = \frac{a_r}{r} \begin{pmatrix} x \\ y \end{pmatrix} + \frac{a_\phi}{r} \begin{pmatrix} -y \\ x \end{pmatrix}. \tag{2.16}$$

In the calculation of the deceleration pulse sequence, only the a_z component of the acceleration vector is non-zero.

The Zeeman effect describes the splitting of atomic and molecular energy levels in the presence of an external magnetic field. The Zeeman shifts for H($1^2S_{1/2}$), He(2^3S_1) and N($^2D_{3/2,5/2}$) take simple forms and are thus used analytically in the trajectory simulation. In metastable He, the two electron spins couple to give a total angular momentum with a quantum number $J = 1$. As the nuclear spin is $I = 0$ (^{4}He), there is no hyperfine interaction [256], and the Zeeman shift can be expressed in terms of M_J. The nuclear spin of ^{14}N is $I = 1$, but the hyperfine interaction and the coupling between the N(^{2}D) spin-orbit states can be neglected [257]. Hence, both for metastable He atoms and metastable N atoms, the Zeeman effect is a linear function of the magnetic field with $\Delta E_Z = M_J g_J \mu_B B$, where M_J is the projection of the total angular momentum J onto the local magnetic field axis, g_J denotes the Landé factor and μ_B is the Bohr magneton. Here, $g_J = 2.00$ in the case of He(2^3S_1) [258]; $g_J = 0.80$ and $g_J = 1.20$ for N($^2D_{3/2}$) and N($^2D_{5/2}$), respectively [259].

In the case of ground-state atomic hydrogen ($1^2S_{1/2}$), the hyperfine interaction between the electron spin ($S = 1/2$) and the nuclear spin ($I = 1/2$) is not negligible. At zero magnetic field, the spins couple to give a total angular momentum with a quantum number F, with a singlet ($F = 0$) and a triplet ($F = 1$) component. In the presence of an external magnetic field, the Hamiltonian for the magnetic interaction can be written as

$$\hat{H}_{\text{mag}} = -g_J \mu_B \hat{\vec{J}} \vec{B} - g_I \mu_B \hat{\vec{I}} \vec{B} + ha \hat{\vec{J}} \hat{\vec{I}}. \tag{2.17}$$

The first two terms describe the interaction of the electron and the nuclear spin with the external magnetic field $\vec{B}$, respectively. The third term is the hyperfine interaction, i.e. the

magnetic interaction between the electron angular momentum $\vec{J}$ and the nuclear spin $\vec{I}$. The constant $a = 2\pi A/\hbar$ is related to the hyperfine splitting A = 1420.406 MHz in ground-state atomic hydrogen, $h = 2\pi\hbar$ is the Planck constant and g_I is the nuclear g factor. Since the orbital angular momentum of the electron is zero (1s orbital), $\hat{\vec{J}} = \hat{\vec{S}}$ and $g_J = g_e$, where g_e is the g factor of the electron. Diagonalisation of the Hamiltonian matrix [260, 261], and assuming that the nuclear magneton $\mu_N \ll \mu_B$, yields two low-field-seeking states with eigenenergies

$$\Delta E_{Z_1} = a\hbar^2/4 + \mu_B B \tag{2.18}$$

$$\Delta E_{Z_2} = -a\hbar^2/4 + \sqrt{(a\hbar^2/2)^2 + (\mu_B B)^2} \tag{2.19}$$

and two high-field-seeking states with eigenenergies

$$\Delta E_{Z_3} = a\hbar^2/4 - \mu_B B \tag{2.20}$$

$$\Delta E_{Z_4} = -a\hbar^2/4 - \sqrt{(a\hbar^2/2)^2 + (\mu_B B)^2}. \tag{2.21}$$

At the magnetic field strengths in the experiment, the gradient $\mathrm{d}(\Delta E_Z)/\mathrm{d}B$ is almost identical for the two low-field-seeking (high-field-seeking) states, and particles in both states will be similarly affected by the Zeeman deceleration sequence.

Zeeman diagrams for (a) H($1^2S_{1/2}$), (b) He(2^3S_1) and (c) N($^2D_{3/2,5/2}$) are shown in Figure 2.6. The deceleration pulse sequences were always obtained for the low-field-seeking state with the largest Zeeman shift, or, in the case of H atoms, the Zeeman substate with a linear Zeeman shift at all magnetic field strengths (red curves in Figures 2.6 (a)–(c)). In the three-dimensional trajectory simulation, it is assumed that all magnetic sublevels of a

spin-orbit state are equally populated initially, since there is no evidence that the experimental schemes for photodissociation, electron-impact excitation and REMPI detection favour a particular magnetic substate.

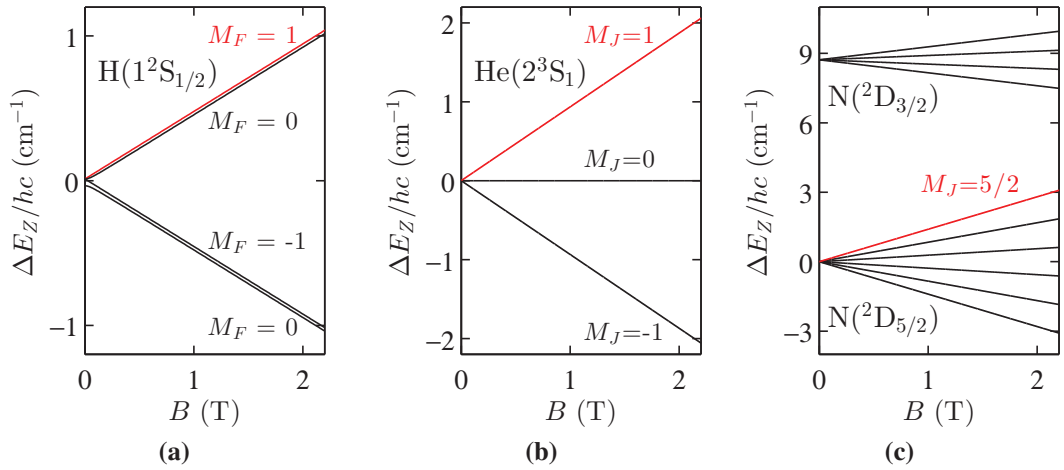

Figure 2.6: Zeeman diagrams for (a) $H(1^2S_{1/2})$, (b) $He(2^3S_1)$ and (c) $N(^2D_{3/2,5/2})$. The Zeeman sublevels used for the calculation of the deceleration pulse sequence are plotted in red colour. The Zeeman shift for $N(^2D_{3/2})$ is offset by the energy difference with respect to the $^2D_{5/2}$ state. Note the change in the vertical scale between (a)-(c).

2.2.5 Numerical Integration of the Particle Motion

The particle velocities, $\vec{v} = (v_x, v_y, v_z)^T$, and positions, $\vec{s} = (x, y, z)^T$, are updated using the Velocity Verlet algorithm [262, 263] which is a symplectic (phase-space conserving) and time-reversible method for numerical integration (truncation error $\mathscr{O}\left(\Delta t^4\right)$). It is typically implemented as a two-step process:

Step 1: The acceleration at time t, $\vec{a}(\vec{s}[t])$, is required to update the particle positions, $\vec{s}(t+\Delta t)$ and to determine the velocity half-step, $\vec{v}(t+0.5\,\Delta t)$,

$$\vec{v}(t+0.5\,\Delta t) = \vec{v}(t) + 0.5\,\vec{a}(t)\,\Delta t \tag{2.22}$$

$$\begin{aligned}\vec{s}(t+\Delta t) &= \vec{s}(t) + \vec{v}(t)\,\Delta t + 0.5\,\vec{a}(t)\,\Delta t^2 \\ &= \vec{s}(t) + \vec{v}(t+0.5\,\Delta t)\,\Delta t.\end{aligned} \tag{2.23}$$

Step 2: The acceleration at time $t+\Delta t$ for the new particle position, $\vec{a}\,(\vec{s}[t+\Delta t])$, is then used to update the particle velocities $\vec{v}\,(t+\Delta t)$,

$$\vec{v}\,(t+\Delta t) = \vec{v}\,(t+0.5\,\Delta t) + 0.5\,\vec{a}\,(t+\Delta t)\,\Delta t. \tag{2.24}$$

This procedure can be shortened to a single-step procedure by performing Step 1 at t_0, and then replacing Eq. 2.22 with

$$\vec{v}\,(t+0.5\,\Delta t) = \vec{v}\,(t) + \vec{a}\,(t)\,\Delta t \tag{2.25}$$

at $t > t_0$. Although the velocities lag behind by $0.5\,\Delta t$, this difference is usually negligible for the time steps (Δt = 100 ns) and accuracies needed for comparison with experimental deceleration data. If $\vec{a}\,(t)$ = 0 at time t_0, the numerical integration scheme turns into an Euler-Cromer algorithm (truncation error $\mathscr{O}\left(\Delta t^2\right)$).

2.2.6 Majorana Transitions

When the magnetic field direction is rapidly reversed, e.g. when the current through a solenoid coil is quickly ramped through zero, the electron spin may not be able to adiabatically follow the change in field direction causing a transition into another Zeeman substate. These non-adiabatic transitions, often referred to as Majorana transitions, can lead to a population redistribution among the Zeeman sublevels and induce particle losses in a Zeeman decelerator [60]. It is therefore important to know about the contribution from Majorana transitions in the experiment, and, if necessary, to find measures to prevent them. In the following, I will describe the approach that we used to estimate non-adiabatic transitions in the Zeeman deceleration of ground-state hydrogen atoms, but the scheme can, in principle, be adapted to any other paramagnetic species.

For ground-state hydrogen atoms, state-to-state Majorana transition probabilities were derived from a numerical solution of the time-dependent Schrödinger equation (including hyperfine structure) as a function of slew rate through a zero magnetic field (calculation by N. Vanhaecke). In this calculation, the B_z component is linearly ramped through zero as a function of time.

An estimate of the Earth's magnetic field [264] is used to define the magnetic field components in all three spatial dimensions giving rise to non-zero off-axis diagonal elements. In Figure 2.7, the state character after the field reversal is shown as a function of slew rate for the low-field-seeking $M_F = 1$ and $M_F = 0$ states, respectively. In the case of $M_F = 1$, which experiences a linear Zeeman shift in a magnetic field (Figure 2.6a), the state character after field reversal gradually changes from low-field-seeking ($M_F = 1$) to high-field-seeking ($M_F = -1$) as the slew rate is increased. At rates > 0.1 T/μs, a state with almost pure $M_F = -1$ character is produced. The reverse process is observed for the $M_F = -1$ state (not shown). For the low-field-seeking $M_F = 0$ state, a different behaviour is observed. While a state with mixed character is formed at intermediate slew rates, e.g. 50 % $M_F = 1$ and 50 % $M_F = -1$ at $6{\cdot}10^{-3}$ T/μs, the state is again almost a pure low-field-seeking $M_F = 0$ state at rates > 0.1 T/μs. Owing to the hyperfine splitting, the high-field-seeking $M_F = 0$ state was found not to undergo any state-changing transitions (not shown). In the experiment, rise and fall times of about 8 μs are observed for currents of 243 A, resulting in a slew rate of 0.2 T/μs (grey vertical lines in Figure 2.7). Under these conditions, there is a near-unit probability for $M_F = 1 \leftrightarrow M_F = -1$ transitions, while the other Zeeman states are not affected.

Results from previous studies suggest that an undershoot of the solenoid current during the switch-off process is the main cause of non-adiabatic transitions [60, 61]. However, this effect is difficult to quantify experimentally (oscillations of the current probe signal, see Figure 4.13), and it was therefore not directly included in the simulated current profiles (see Figure 5.6). Instead, a critical magnetic field, B_{crit}, was introduced in the trajectory program, which may be thought of as the maximum magnetic field strength reached during the current undershoot. Since the program cannot handle quantum states

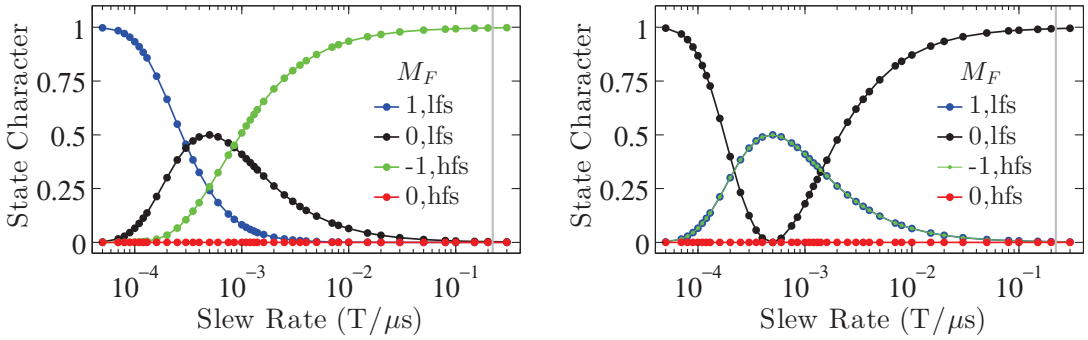

Figure 2.7: Quantum-state character of the Zeeman sublevels in H($1^2S_{1/2}$) as a function of slew rate through a zero magnetic field, starting with a pure low-field-seeking (a) $M_F = 1$ and (b) $M_F = 0$ state. In the legend, 'lfs' ('hfs') denotes a low (high)-field-seeking quantum state.

with mixed quantum-state character, the results from the above Majorana calculations are treated in terms of a 'spin-flip probability'. This is implemented by choosing particles, which satisfy $B < B_{\text{crit}}$ at the time at which the current reaches zero, and weighting the random assignment of a new quantum state with the spin-flip probability.

Taking into account the rapid slew rate in the experiment, the calculation could be further simplified by assuming that particles in $M_F = 1$ are *always* transferred into $M_F = -1$ and vice versa, while other particles remain in their original quantum states. However, the current approach was chosen to provide a more general treatment of Majorana transitions in a Zeeman decelerator. A simple model for Majorana transitions in a Zeeman decelerator was also devised by the group in Zürich [60], but the probabilities used in these calculations are statistical estimates only without an underlying quantum mechanical treatment.

3 | Model for the Overall Phase-Space Acceptance in a Zeeman Decelerator

3.1 Introduction

Both Stark and Zeeman deceleration are based on the concept of phase stability which was originally devised for charged-particle acceleration in synchrotrons [265, 266]. Phase stability explains why particles within a limited range of positions and velocities are kept together throughout the deceleration process. The characteristics of a decelerated beam, e.g. particle transmission and velocity spread, are widely governed by phase-space acceptance, and a thorough understanding of this concept is needed for the design of improved deceleration sequences and experimental setups. Phase-space acceptance in a Stark decelerator was first described by Bethlem et al. [267, 268], and the model was extended by van de Meerakker et al. to explain the influence of the transverse motion on the deceleration process [269]. The group also demonstrated that the periodicity of the electric fields leads to additional phase-stable regions inside a Stark decelerator [270]. Based on these ideas, they built a Stark decelerator with an improved overall performance if operated in a higher-order mode ($s = 3$) [271]. Particle motion in a multistage Zeeman decelerator and a moving-trap Zeeman decelerator has thus far been pictured through one-dimensional models, and via numerical three-dimensional particle-trajectory simulations [74, 272].

In this Chapter, I will present a model that allows for a more general understanding of the longitudinal and transverse acceptance as well as the overall six-dimensional phase-space acceptance in a Zeeman decelerator. It thus provides a useful means to find conditions for the phase-stable operation of a Zeeman decelerator without the need of having to run large sets of trajectory simulations in a multi-parameter space. The output of the model suggests that, for a given switch-off position inside a solenoid coil, κ_0 (defined below), the phase-space acceptance in a multistage Zeeman decelerator is dependent on the particle velocity, and on the time overlap of the current pulses between neighbouring coils. In

order to remain in the same phase-stable region throughout the deceleration process, I will suggest the use of an adaptive κ_0 which follows the change in the mean longitudinal acceleration as the particle velocity is decreased.

Using the model, it is possible to explain the origin of unfilled regions in phase space that have been predicted by theoretical and experimental studies [61, 272], and that are also obtained using numerical three-dimensional particle trajectory simulations. To overcome this decrease in phase stability, I will assess the efficiency of two alternative schemes for Zeeman deceleration that are similar to those used for the switching of electric fields in Stark decelerator experiments [46, 270, 271]. Furthermore, I will outline a new mode of operation for a Zeeman decelerator that is based upon the alternation between Zeeman acceleration and deceleration. This scheme only relies on changes in the computed deceleration pulse sequence thus facilitating its experimental implementation. The improved performance of a Zeeman decelerator in this operating mode is evaluated with the aid of numerical particle trajectory simulations.

3.2 Phase-Space Model

Phase stability ensures that particles within a certain range of relative positions and velocities with respect to a so-called synchronous particle remain together during the successive switching of several deceleration coils. The synchronous particle is an imaginary on-axis particle which experiences precisely those magnetic fields that are calculated for a pulse sequence to achieve a given amount of deceleration or acceleration. In order to achieve phase stability, the solenoid magnetic fields in a multistage Zeeman decelerator are switched in a periodic manner, so that the synchronous particle always moves exactly one coil distance, d, before the active coil is turned off. The particle position relative to the centre of a deceleration coil can be described by a dimensionless parameter $\kappa = (z - z_0)/d$ which is related to the particle position on the beam axis, z, the centre of the active coil, z_0, and the centre-to-centre coil distance, d. The change in kinetic

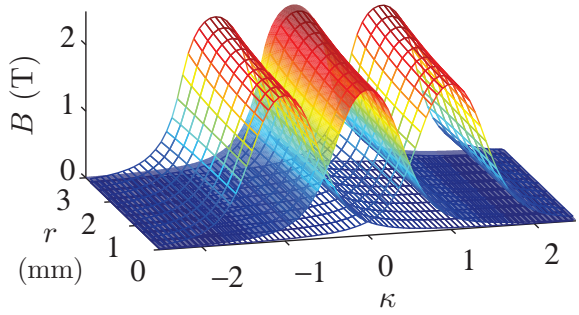

Figure 3.1: Three-dimensional magnetic field of a solenoid coil for Zeeman deceleration at a current of 300 A (shaded surface). Mesh plots indicate the magnetic fields of neighbouring coils. The magnetic fields of the individual coils are not added up vectorially. The coil specifications and positions are the same as in the experiment (Section 4.4).

energy is determined by the position of the synchronous particle at the switch-off time, κ_0. For infinitely short rise and fall times, phase-stable deceleration is achieved when κ_0 is chosen such that each solenoid coil is switched off before the synchronous particle reaches the coil centre ($\kappa_0 < 0$, see Figure 3.1). In this case, more kinetic energy will be removed from particles that are further ahead in the decelerator, while particles lagging behind the synchronous particle will be decelerated less, as they experience a lower average magnetic field gradient. If the positions and velocities of these 'non-synchronous' particles are within a certain range relative to the synchronous particle, an oscillatory motion results which is maintained throughout the deceleration process. Wiederkehr et al. [272] have devised a one-dimensional model for phase stability that reliably captures this oscillatory behaviour.

An accurate description of phase stability becomes more complex if the finite switching times of the current pulses are taken into account. Based on the mean acceleration for each deceleration period, I will present an approach to calculate phase stability in a Zeeman decelerator that can cope with arbitrary current pulse shapes. Besides predictions for the longitudinal and the transverse phase stabilities, the model gives an estimate of the overall, six-dimensional phase-space acceptance for each switch-off position κ_0. This allows for an evaluation of Zeeman-deceleration sequences within a wide parameter range that is complementary to trajectory simulations.

3.2.1 Longitudinal and Transverse Phase-Space Acceptance

The approach given here builds up on a number of ideas that were previously used to describe the longitudinal and transverse motion in a Stark decelerator [268, 269]. Assuming that the longitudinal and the transverse dynamics take place on very different time scales, the longitudinal and the transverse motion can be treated as independent entities. Longitudinal and transverse accelerations, $\bar{a}_z$ and $\bar{a}_r$, are obtained by numerical integration over one period in time, T, which is equivalent to the track of the synchronous particle across one coil distance, d, at constant particle velocity:

$$\begin{aligned} \bar{a}_i(\kappa, r, v_z) &= \frac{1}{T}\int_0^T a_i(z(v_z,t), r, t)\,\mathrm{d}t \\ &\approx \frac{1}{d}\int_{(\kappa-1)d+z_0}^{\kappa d+z_0} a_i(z(v_z,t), r, t)\,\mathrm{d}z \end{aligned} \tag{3.1}$$

where $i = z, r$. It is assumed that the longitudinal and transverse particle velocities, v_z and v_r, and the transverse positions, r, do not change during this interval. Such an approximation is valid for particles with a small magnetic-moment-to-mass ratio and/or for sufficiently high particle velocities. The transverse positions and velocities can be treated as constant for one deceleration period, since off-axis velocities are typically small ($\leq$ 20 m/s) and the transverse magnetic field gradients are significantly less than those in the longitudinal direction (see Figure 3.1). Changes in the mean longitudinal acceleration as a function of r are less than 20 % (between r = 0 mm and r = 3 mm) for the coil dimensions shown in Figure 3.1.

All calculations presented here were carried out for nitrogen atoms in the metastable $^2D_{5/2}$, M_J = 5/2 state. The Zeeman shift, ΔE_Z, for this state [257] can be linearly approximated by $\Delta E_Z = M_J g_J \mu_B B$, where $M_J = 5/2$ is the projection of the total angular momentum J onto the local magnetic field axis, g_J = 1.20 [259] is the Landé factor, μ_B denotes the Bohr magneton and B is the magnetic field magnitude. Although the results shown are valid for

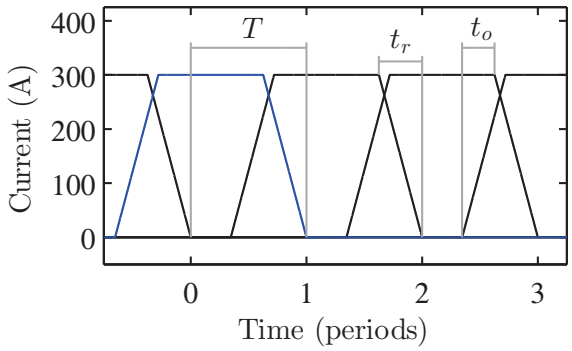

Figure 3.2: Temporal profiles of the current pulses for five consecutive deceleration coils as used in the model. The pulse shape for one coil is shown in blue colour for clarity. Time is scaled to the period T, i.e. the time required for the passage of one coil distance. The rise and fall times are denoted with t_r, and the time overlap between adjacent pulses, defined as shown in the figure, is referred to as t_o.

this specific quantum state only, they can be scaled to any other atom or molecule with a linear Zeeman shift. Metastable nitrogen is chosen due to its relatively small magnetic-moment-to-mass ratio, so that the validity conditions of the model are met.

For the calculations, distances and coil dimensions from the experiment are used (Section 4.4), e.g. d = 10.7 mm. Figure 3.2 illustrates the temporal characteristics of the current pulses. The rise and fall times (assuming equal values in both cases), t_r, and the time overlap, t_o, are shown on a scale that is related to the time period T. Here, t_r = 8 μs, t_o = 6 μs and a current of 300 A are used for each coil, resulting in a maximum mean longitudinal acceleration, $\bar{a}_{z,m}$, of $2.3{\cdot}10^5$ m/s^2 on the beam axis. Mutual inductance effects, which induce additional cusps in the current profiles, were not taken into account for reasons of simplicity. However, in principle, the numerical integration allows for the implementation of any arbitrary time profile, e.g. experimental waveforms.

The cylindrical symmetry of solenoid magnetic fields reduces the complexity of phase-space calculations, since the angular momentum of the particles about the molecular beam axis is conserved, so that the dimensionality of the problem is reduced by two. To obtain information on longitudinal phase stability, the relative mean accelerations

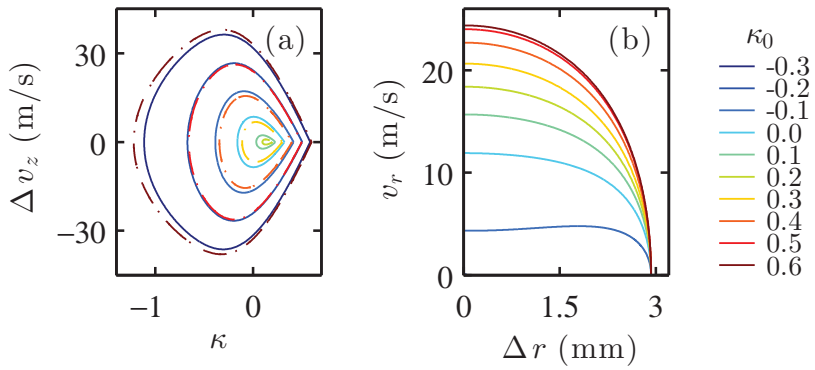

Figure 3.3: Separatrices in (a) longitudinal and (b) transverse phase space for the Zeeman deceleration of nitrogen atoms in the $^2D_{5/2}$, M_J = 5/2 state at different κ_0 and at a longitudinal velocity of 500 m/s. Particles inside the separatrix revolve in stable orbits around the synchronous particle. Transverse trajectories at $\kappa_0 <$ -0.1 are not phase stable. There are longitudinal separatrices for $\kappa_0 > 0.1$ (dashed lines in (a)), because the deceleration pulse sequence, applied to achieve a given final velocity, addresses particles in the same phase space as for a lower value of κ_0, e.g. an identical separatrix centred at κ = -0.1 exists both for κ_0 = -0.1 and κ_0 = 0.4.

$$\Delta\bar{a}_z(\Delta\kappa, 0, v_z) = \bar{a}_z(\kappa, 0, v_z) - \bar{a}_z(\kappa_0, 0, v_z), \tag{3.2}$$

where $\Delta\kappa = \kappa - \kappa_0$, at $r = 0$ and v_z = const. are used to calculate the relative longitudinal positions and velocities of 'non-synchronous' particles with respect to the synchronous particle. Trajectories of non-synchronous particles are determined for -4 $\leq \Delta\kappa \leq$ 4 using numerical integration. The separatrix is then given by the largest stable orbit around the synchronous particle within this $\Delta\kappa$-interval. Trajectories in the transverse direction at a given longitudinal velocity, v_z, are obtained in a similar manner for each switch-off position κ_0:

$$\Delta\bar{a}_r(\kappa_0, \Delta r, v_z) = \bar{a}_r(\kappa_0, r, v_z) - \bar{a}_r(\kappa_0, 0, v_z). \tag{3.3}$$

Due to the cylindrical symmetry, the transverse forces on the beam axis ($r = 0$) vanish, and hence $\bar{a}_r(\kappa_0, 0, v_z) = 0$.

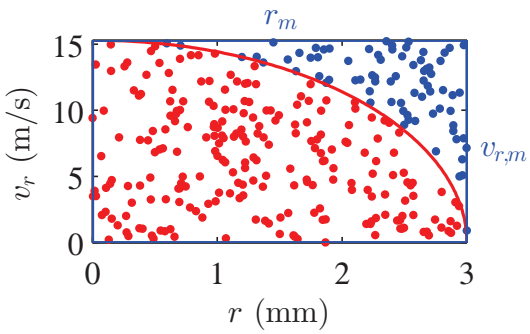

Figure 3.4: Schematic illustration of the Monte Carlo numerical integration algorithm used for the calculation of the four-dimensional transverse acceptance. The separatrix (red curve) is enclosed by a rectangle (in blue colour). The side lengths of the rectangle, r_m and $v_{r,m}$, are determined by the point of origin and the amplitudes of the transverse position and the transverse velocity, respectively.

Separatrices, as in Figure 3.3, mark the boundaries between stable and unstable trajectories around the synchronous particle. Only trajectories inside a separatrix are phase stable. In Figure 3.3, opposite trends are seen for the longitudinal and the transverse stability as κ_0 is increased. The longitudinal acceptance decreases as κ_0 is increased from -0.3 to 0.1, i.e. the more kinetic energy is removed during a deceleration step. Figure 3.3 (a) also shows an increase in the longitudinal acceptance for $\kappa_0 > 0.1$. In this case, the deceleration pulse sequence, applied to achieve a given amount of deceleration, is effectively the same as for a bunch of particles that revolve around a synchronous particle located at a lower κ. For example, at $\kappa_0 = 0.4$, a separatrix exists which is centred at $\kappa = -0.1$. The change in transverse acceptance can be explained through a change in the shape of the magnetic field (see Figure 3.1) from defocusing outside the coil to focusing inside the coil. Hence, the transverse motion is unstable at more negative κ_0, but increasingly stable the further a particle moves into a coil during one period. The maximum transverse position relative to the beam axis is determined by the distance to the coil walls ($r = 3$ mm).

Quantitative information on phase-space acceptance can be drawn from the volume that is enclosed within each separatrix. The two-dimensional longitudinal acceptance for each parameter set (κ_0, v_z) is obtained by trapezoidal numerical integration of the points that form the separatrix in longitudinal phase space (see Figure 3.3 (a)). The transverse phase-

space volume, V_r, is given by

$$V_r = \int\int\int\int r v_r \mathrm{d}r\mathrm{d}\theta\mathrm{d}v_r\mathrm{d}\theta_v. \tag{3.4}$$

The angles θ and θ_v are integrated from 0 to 2π owing to the cylindrical symmetries of the sought four-dimensional volume. The integrals over r and v_r are taken over the two-dimensional transverse stability region shown within the separatrix in Figure 3.4.

V_r is evaluated numerically in a Monte-Carlo approach. For this, a uniform random distribution of points $p = r_p, v_{r,p}$ (all points in Figure 3.4) is drawn within the two-dimensional volume $\mathscr{N}$ given by the distances from the point of origin to the maximum values for the transverse position, r_m, and the transverse velocity, $v_{r,m}$. The volume $\mathscr{N}$ entirely encompasses the two-dimensional transverse stability region $\mathscr{M}$ (red points in Figure 3.4). The sought evaluation of V_r therefore reads

$$V_r \approx (\pi r_m v_{r,m})^2 \frac{4\pi^2 \sum_{p\in\mathscr{M}} r_p v_{r,p}}{4\pi^2 \sum_{p\in\mathscr{N}} r_p v_{r,p}}. \tag{3.5}$$

In the calculation, each point p is given a weight $r_p v_{r,p}$ to account for the elementary volume in cylindrical coordinates, while the normalisation pre-factor originates from the analytically known volume $\mathscr{N}$.

Figures 3.5 and 3.6 show maps of the longitudinal and transverse acceptances for N(^{2}D$_{5/2}$, M_J = 5/2) as a function of the beam velocity, v_z, and the switch-off positions of the synchronous particle, κ_0, respectively. The black lines indicate the contours of constant mean longitudinal acceleration, $\bar{a}_z$, on the beam axis. For each beam velocity, the variation of the acceptance as a function of κ_0 is in accordance with the change in the area covered by the separatrices in Figure 3.3. However, as the beam velocity decreases, the acceptance profile is shifted to lower values of κ_0. Both for the longitudinal and the transverse acceptance, this displacement is approximately parallel with the lines of constant longitudinal

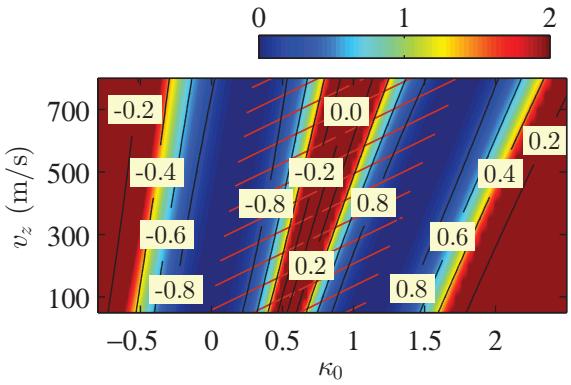

Figure 3.5: Density plot: longitudinal phase-space acceptance (in m^2/s) for Zeeman deceleration/acceleration of $N(^2D_{5/2}, M_J = 5/2)$. Black contour lines: normalised mean longitudinal acceleration $\bar{a}_z/\bar{a}_{z,m}$ along the beam axis, where $\bar{a}_{z,m}$ is the maximum mean longitudinal acceleration. White boxes give values of $\bar{a}_z/\bar{a}_{z,m}$ for selected contour curves. In the calculation, a cut-off was implemented for acceptances > 2 m^2/s, as stable longitudinal orbits can extend beyond -4 <= $\Delta\kappa$ <= 4. Red hashes mark regions in which longitudinal phase stability is observed only because the deceleration/acceleration pulse pattern addresses the same particles as in another phase-stable region (no hashes) with the same $\bar{a}_z$, and thus effectively corresponds to a different adaptive κ_0.

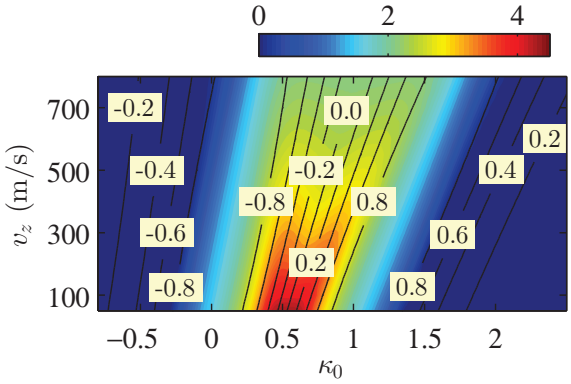

Figure 3.6: Density plot: transverse phase-space acceptance (in 10^{-2} m^4/s^2) for Zeeman deceleration/acceleration of $N(^2D_{5/2}, M_J = 5/2)$. As in Figure, 3.5, the normalised mean longitudinal acceleration $\bar{a}_z/\bar{a}_{z,m}$ along the beam axis is marked with black contour lines.

acceleration. Hence, operating the decelerator at constant mean longitudinal acceleration will ensure that the phase-space acceptance remains nearly unchanged as the beam velocity decreases.

The velocity dependence of the mean longitudinal acceleration is due to an explicit time dependence of the solenoid magnetic fields caused by the finite rise and fall times for the switching. In the deceleration pulse sequence, the time period, T, is increased as the beam velocity decreases to ensure that the synchronous particle always travels one coil distance at each deceleration step. For current pulses such as in Figure 3.2 with $t_r = 8$ μs, the rise and fall times account for a significant fraction of the time period at high velocities causing reduced acceleration. For example, while $T = 54$ μs $\approx 7t_r$ at 200 m/s, T is as short as 15 μs $\approx 2t_r$ at 700 m/s. Thus, if κ_0 is kept constant, a synchronous particle experiences much less acceleration at high velocities than at low velocities. At very low beam velocities, the average amount of deceleration approaches the value that is expected for vanishing rise and fall times. While the longitudinal phase-space acceptance does not markedly change as a function of beam velocity (Figure 3.5) along a line of constant acceleration, there is a significant decrease in the transverse acceptance (Figure 3.6) towards higher velocities. This change is a consequence of the fall times which reduce the transverse particle focusing inside a coil during each deceleration period.

The influence of the beam velocity can be eliminated by linking the experimental rise and fall times to the change in the period, for example, by successively lowering the voltage for the kick interval [61] as the particle velocity is decreased. Alternatively, deceleration sequences can be calculated such that the switch-off position κ_0 follows the change in $\bar{a}_z$ as a function of velocity. The practicality of this scheme is demonstrated in the trajectory simulations below. In addition to that, the use of $\bar{a}_z$ is superior to κ_0 in the evaluation of alternative Zeeman deceleration schemes (Section 3.3), as it provides a direct means of comparison between different operating modes.

In Zeeman deceleration experiments, where the switch-off position inside a coil is defined by a phase angle $\phi_0 = \pi\,(\kappa_0 + 1/2 - vt_r/d)$, the beginning and the end of each period in

Figure 3.2 is shifted by $-t_r$, i.e. the end of each period is defined as the time at which the current to the coil is switched off [60]. Due to the time overlap between adjacent current pulses, the current for the active coil is then almost constant throughout the interval T, and the effect of the rise and fall times from adjacent coils is less. However, the velocity dependence of the phase-space acceptance remains significant irrespective of the definition of the switch-off position, especially at shorter time overlaps and for advanced deceleration schemes (see Section 3.3).

3.2.2 Overall Phase-Space Acceptance

The overall phase-space acceptance is *a priori* a complex volume in a six-dimensional phase space, and cannot be correctly evaluated by the product of the longitudinal and transverse acceptances, as shown in Figures 3.5 and 3.6. Instead, in order to evaluate the overall phase-space acceptance, assumptions on the dynamics of the three-dimensional particle motion are required. Here, it is assumed that the time for one revolution in transverse phase space, τ_r, is much longer than the time needed for one orbit in longitudinal phase space, τ_z (adiabatic approximation). In this case, the trajectories of non-synchronous particles in longitudinal phase space can be calculated, and the phase-space volume covered by two adjacent trajectories can be multiplied with the average transverse acceptance that the particles experience during one revolution in longitudinal phase space. The overall six-dimensional phase-space acceptance for each value of v_z and κ_0 is then obtained by summation over all these sub-volumes.

The model is compared with numerical three-dimensional particle trajectory simulations (Section 2.2) for a total of 137 deceleration coils. For the computation of a deceleration pulse sequence, an iso-contour line of $\bar{a}_z$ is chosen according to the desired amount of deceleration or acceleration, and the switch-off position κ_0 is varied as a function of the beam velocity (to follow the contour line of constant $\bar{a}_z$). To circumvent deviations from periodicity, the 3 D trajectory simulation starts after the switch-off for the first coil, and it stops when the current of the second to last coil has decayed to zero. An initial

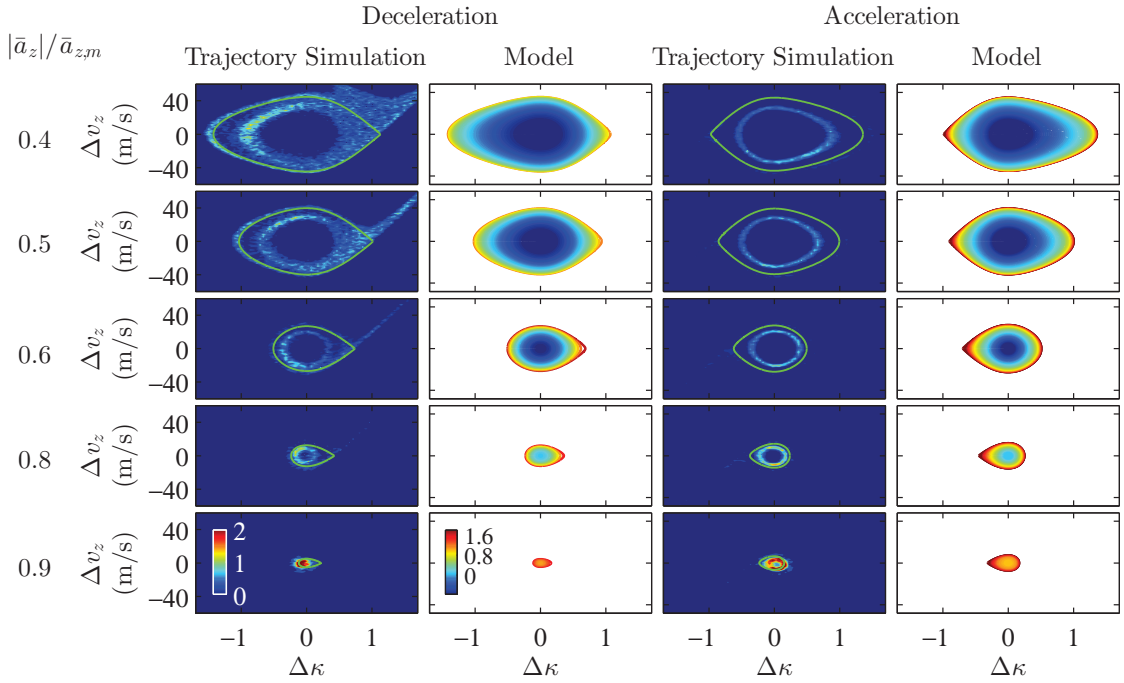

Figure 3.7: Longitudinal phase-space distributions of N(^{2}D$_{5/2}$, M_J = 5/2) inside the decelerator at different mean longitudinal accelerations, $\bar{a}_z$, that result from 3 D trajectory simulations and from the phase-space model. To account for the different number of initial particles in the trajectory simulations, the results for deceleration and acceleration are normalised to the number of particles in the phase-space window at $\bar{a}_z/\bar{a}_{z,m}$ = -0.6 and 0.6, respectively. Under these conditions, the number of unstable particles remaining in the phase-stable region is expected to be small (see text). The separatrices in longitudinal phase space, as obtained from the model, are shown in the results from trajectory simulations (green curves) for comparison. The colour scales are referenced to the (scaled) number of particles from the simulation and the transverse acceptance (in 10^{-2} m^4/s^2) from the model, respectively.

velocity of v_z = 800 m/s is chosen for deceleration sequences, such that the final velocity for the maximum amount of deceleration is 200 m/s. Likewise, an initial velocity of v_z = 200 m/s is used for acceleration pulse sequences. Due to the larger beam divergence at low velocities, the program iterates over 15 million metastable nitrogen atoms in the ^{2}D$_{5/2}$, M_J = 5/2 state for deceleration, and 105 million particles for acceleration. For a quantitative analysis, uniform random distributions for both the initial particle positions and their velocities are chosen in a range that is larger than the maximum extent of the longitudinal and transverse separatrices (Figure 3.3), i.e. $|\Delta\kappa| \leq 2.3$, $|\Delta v_z| \leq 50$ m/s, $r \leq 3$ mm and $|v_r| \leq 25$ m/s.

Figure 3.7 contrasts longitudinal phase-space distributions obtained from the model and from 3 D trajectory simulations. As detailed before, the longitudinal phase-space volume decreases as the mean longitudinal acceleration, $\bar{a}_z$, is increased. The trajectory simulations suggest that the longitudinal separatrices are not uniformly filled for all but the largest amount of deceleration and acceleration ($|\bar{a}_z| / \bar{a}_{z,m} = 0.9$ in the figure). Instead, there are two unfilled regions in the longitudinal phase-space diagram, located close to the synchronous particle and near the separatrix. Similar effects were seen by van de Meerakker et al. for a Stark decelerator [269] and by Wiederkehr et al. for a Zeeman decelerator of variable length (56 – 80 deceleration stages) [272]. The model confirms their interpretation of the unfilled region close to the synchronous particle, since comparison with the model input parameters implies that the convex shape of the magnetic fields outside of a solenoid coil (Figure 3.1) leads to a net transverse defocusing of low-field-seeking particles over the course of one longitudinal revolution in phase space. Non-synchronous particles at large distances relative to the synchronous particle, $\Delta\kappa$, move further into a coil during a longitudinal orbit which compensates for the transverse defocusing and thus explains the ring of phase-stable trajectories in Figure 3.7.

As these trajectory simulations mimic the motion through a much longer Zeeman decelerator, the empty phase-space region close to the separatrix ('halo') is much more prominent than in Wiederkehr et al. [272]. Following the explanations given for a Stark decelerator [269], it was assumed that resonant coupling processes lead to unstable trajectories in transverse phase space, and thus induce particle loss during the deceleration process. I also believe that the unfilled phase-space regions in Figure 3.7 are due to such resonant couplings which can occur whenever the times for a longitudinal and a transverse revolution in phase space, τ_r and τ_z, become very similar. Figure 3.8 shows that τ_r and τ_z can indeed become comparable under certain conditions for $\Delta\kappa$ and κ_0. The model is unable to capture these effects, because it explicitly assumes adiabatic behaviour, i.e. $\tau_r \gg \tau_z$ (see above). It is very likely that the unfilled phase-space regions close to the separatrix in Figure 3.7 can be explained through such a mechanism.

Figure 3.9 shows the overall phase-space acceptance that is obtained from the model at

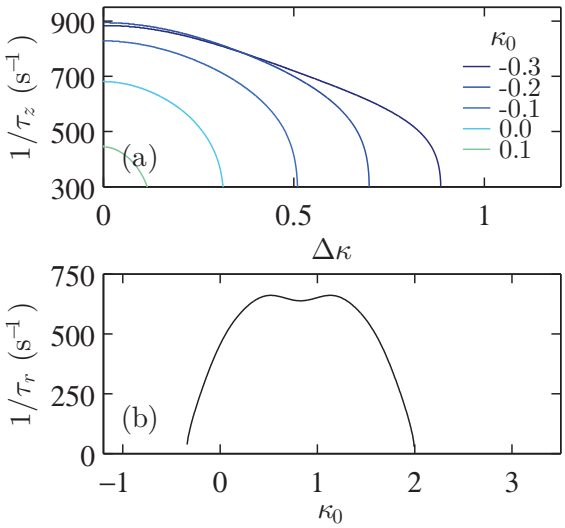

Figure 3.8: (a) Inverse time needed for one orbit in longitudinal phase space versus the maximum relative position, $\Delta\kappa$, of non-synchronous particles at different switch-off positions, κ_0. (b) Inverse time for one revolution in transverse phase space as a function of κ_0 for a particle moving close to the beam axis ($\Delta r \to 0$ mm). The data are calculated for the Zeeman deceleration of nitrogen atoms in the $^2D_{5/2}$, $M_J = 5/2$ state at $v_z = 500$ m/s.

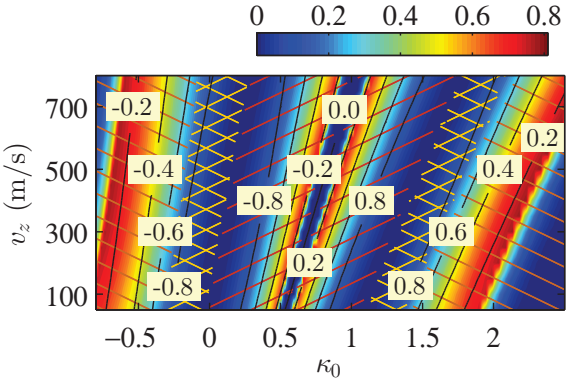

Figure 3.9: Density plot: overall phase-space acceptance (in 10^{-2} m^6/s^3) for Zeeman deceleration/acceleration of N($^2D_{5/2}$, $M_J = 5/2$). As in Figures 3.5 and 3.6, the normalised mean longitudinal acceleration $\bar{a}_z/\bar{a}_{z,m}$ along the beam axis is marked with black contour lines. Brown hashes: regions in which only particles with very high longitudinal velocities or large displacements with respect to the synchronous particle are phase stable. Orange crossed hashes: particle motion close to the synchronous particle is phase stable. Red hashes: regions in which phase stability is observed owing to a deceleration/acceleration pulse sequence which addresses particles in the same phase space as for the same value of $\bar{a}_z$ in a region marked with brown or orange hashes, respectively.

different beam velocities, v_z, using the same conditions as above. In agreement with Figures 3.5 and 3.6, there is an explicit velocity dependency of the overall acceptance in terms of $\bar{a}_z$. However, following any contour line of constant mean longitudinal acceleration, the overall acceptance does not markedly change as a function of beam velocity.

The phase-space acceptance highlighted with red hashes in Figure 3.9 is a reflection of the phase stability for the same $\bar{a}_z$ that is already observed in the regions highlighted with orange and brown hashes, since the applied deceleration pulse sequence effectively addresses particles in the same phase-space volume. Neglecting this 'fake' additional phase-space acceptance, there is only a limited parameter range for Zeeman deceleration and acceleration, where the overall six-dimensional phase-space acceptance is non-zero. This is in accordance with the partial overlap between the regions of maximum longitudinal and transverse acceptance (cf. Figures 3.5 and 3.6). Phase stability close to the synchronous particle is seen in an even smaller region (orange crossed hashes in Figure 3.9).

For experiments in which the transmitted beam is used to study collisions, these results imply that Zeeman deceleration and acceleration should ideally be carried out at $0.8 \leq |\bar{a}_z| / \bar{a}_{z,m} \leq 1.0$ (orange crossed-hatched regions in Figure 3.9) to obtain a superior kinetic energy resolution while maintaining an almost uniform distribution in phase space. If maximum transmission is the major goal, e.g. for trapping experiments, a lower mean longitudinal acceleration would be more advantageous (brown-hatched regions in Figure 3.9). The maximum overall acceptance is obtained at a mean longitudinal acceleration of $|\bar{a}_z| / \bar{a}_{z,m} = 0.3$, but it comes at the expense of a large spread in relative particle positions and velocities with respect to the synchronous particle.

Considering the limited validity of the model, no quantitative agreement between the output of the model and results from trajectory simulations is expected. However, Figure 3.10 shows that the general trends for the model and the simulation are very similar, e.g. the position of the maximum in phase-space acceptance in terms of $\bar{a}_z$ and the decrease in acceptance towards larger values of the mean longitudinal acceleration. Despite the

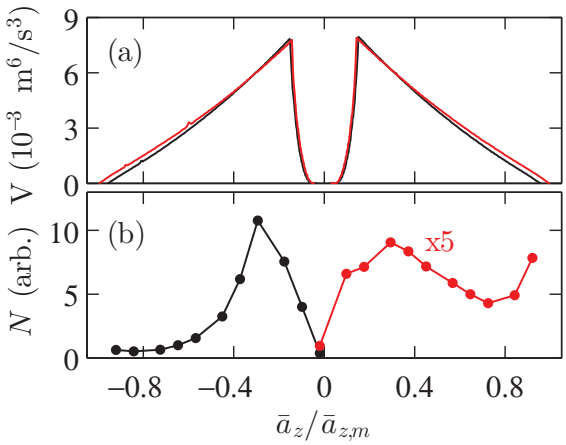

Figure 3.10: (a) Overall phase-space acceptance, V, obtained from the phase-space model and (b) number of transmitted particles, N, in the trajectory simulation (dots) versus normalised mean longitudinal acceleration, $\bar{a}_z/\bar{a}_{z,m}$. V is proportional to N, since the trajectory simulation was carried out with uniform initial position and velocity distributions. Red traces and black traces in (a) correspond to the overall acceptance at $v_z = 200$ m/s and 800 m/s, respectively. The number of decelerated (accelerated) particles in (b) is derived from the number of particles in the phase-space windows shown in Figure 3.9; the solid lines are a guide to the eye only. The number of accelerated particles (red dots) is upscaled for visibility.

limitations of the model, I am confident that it can provide an order-of-magnitude estimate of the overall phase-space acceptance in a Zeeman decelerator.

Again, Figure 3.10 (a) illustrates that the six-dimensional phase-space volume does not notably change between $v_z = 200$ m/s (red lines) and 800 m/s (black lines). In this representation, it also becomes obvious that, for any given value of $|\bar{a}_z|/\bar{a}_{z,m}$, the overall phase-space acceptance is the same for Zeeman deceleration and acceleration. However, from the trajectory simulations (Figures 3.7 and 3.10), it can be seen that a lot more particles are transmitted during the deceleration sequence than during acceleration. In the case of Zeeman deceleration, a significant number of particles is captured within the phase-stable region, even though their trajectories are not phase-stable, especially at low $\bar{a}_z$. This effect is also apparent in the distinct tail of particles outside the longitudinal separatrix (Figure 3.7) indicating that particles are leaving the phase-stable region even after having passed more than a hundred deceleration stages. As the initial velocity for acceleration is much lower than for deceleration – 200 m/s as compared to 800 m/s – non-synchronous parti-

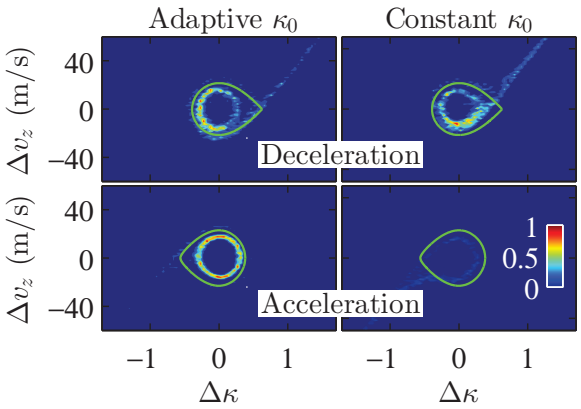

Figure 3.11: Longitudinal phase-space distributions for Zeeman deceleration (upper panel) and acceleration (lower panel) of N($^2D_{5/2}$, M_J = 5/2), respectively. Results are obtained from particle trajectory simulations using an adaptive (left column) and a constant (right column) switch-off position, κ_0. In the case of an adaptive κ_0, a mean longitudinal acceleration of $|\bar{a}_z|/\bar{a}_{z,m}$= 0.7 is used. The constant values for κ_0 are chosen such that the final velocities are the same in both modes of operation, i.e. κ_0 = -0.1 for deceleration (800 m/s $\rightarrow$ = 410 m/s) and κ_0 = 1.8 for acceleration (200 m/s$\rightarrow$ 710 m/s). Normalisation is the same as in Figure 3.7, but the colour scale is adjusted to increase the contrast. For comparison, longitudinal separatrices from the model are shown as green curves.

cles, that do not meet the conditions for phase-space acceptance, have much more time to leave the phase-stable region or to hit the walls during the acceleration process.

Various experimental studies have demonstrated that the intensity of the decelerated signal changes according to the amount of deceleration [59, 61, 63, 272, 273]. Due to the different experimental arrangements, a direct comparison with the model results is difficult. Although phase-space acceptance is not pronounced in our short 12-stage Zeeman decelerator in Oxford, the experimental results on ground-state hydrogen atoms (Chapter 5) clearly show a signal decrease by about a factor of two from κ_0 = -1 to κ_0 = 0 which is what would be expected from the model.

The consequences of using a constant switch-off position, κ_0, i.e. successively increasing $|\bar{a}_z|$ during a Zeeman deceleration or acceleration sequence, are two-fold. The upper (lower) panel in Figure 3.11 shows results from trajectory simulations in which an adaptive and a constant κ_0 value are chosen for Zeeman deceleration (acceleration), such that the final velocity is the same. In the case of Zeeman acceleration, a dramatic decrease

in the number of phase-stable particles in the constant κ_0 mode of operation is observed while there is little change in the phase-space distribution for Zeeman deceleration. The behaviour shown for both Zeeman deceleration and acceleration at constant κ_0 can be attributed to a change from a larger to a smaller phase-space volume meaning that particles originally located in a phase-stable region will find themselves in an unstable region at the end of a deceleration or acceleration sequence (cf. Figure 3.7). Likewise, a lot of particles are ejected from the decelerator at the beginning of a deceleration or acceleration sequence although their trajectories would be phase stable at a later point in time. However, in the acceleration process, the more pronounced velocity dependence along with the greater velocity change (Δv_z = -390 m/s for deceleration, Δv_z = 510 m/s for acceleration) causes a stronger decrease in phase-space acceptance, and results in less particle transmission through the decelerator. In this specific case, the results of applying an adaptive κ_0 (a constant $\bar{a}_z$) only imply a significant advantage for Zeeman acceleration, and little advantage for deceleration. However, the use of this procedure generally simplifies data interpretation in terms of phase-space acceptance, and it helps to find improved deceleration schemes, as demonstrated in Section 3.3.

3.2.3 Influence of the Time Overlap

Thus far, the effect of the time overlap between the current pulses of adjacent coils, t_o, was neglected, and a constant value of t_o = 6 μs was used. However, following the same arguments as for the rise and fall times, a constant time overlap will have a greater impact at higher beam velocities, and its influence will be negligible at low velocities. As the particles are typically quite far away from the centre of the neighbouring coil at the time it is switched on, the velocity dependence of $\bar{a}_z$ will not be as strong as for the rise and fall times, t_r. The influence of the time overlap on the overall phase-space acceptance is shown in Figure 3.12 for $t_r = 0$. In this idealised case, the acceptance only depends on changes in the time overlap. Furthermore, a coupling of the time overlap to the period ($t_o \propto T$) eliminates the velocity dependence of $\bar{a}_z$. Figure 3.12 illustrates that

the overall acceptance steadily increases as the time overlap becomes a larger fraction of the time period. The increase is small (about 20 % from $t_o = 0$ to $t_o = T/2$) and the maximum phase-space acceptance is shifted to higher mean longitudinal accelerations, equally for Zeeman deceleration and acceleration. A similar effect is observed when both the switching times and the time overlap are linked to the time period, e.g. $t_r = t_o = T/2$. In this case, however, the overall acceptance is lower due to the contribution of the rise and fall times. With regard to Figures 3.9 and 3.10, the time overlap ensures that the magnitude of the overall acceptance is nearly constant at all beam velocities. Without this contribution, the rise and fall times cause a gradual decrease in acceptance towards higher velocities (not shown). The increase in overall acceptance as a function of the time overlap is mainly a longitudinal effect. In fact, as t_r is increased, the transverse acceptance decreases due to the larger contribution from transversely defocusing magnetic fields outside of a coil. In contrast to that, the additional magnetic field from the adjacent coil raises the potential hill in the longitudinal direction, so that particles with a position further ahead in the decelerator will still be captured in longitudinal phase space. As the contribution is small and the heating of solenoid coils during operation is generally a major concern, I do not think that an excessive increase in overlap times will contribute much to the success of future deceleration experiments. However, this effect should be kept in mind when considering alternative switching schemes. In addition to that, a time overlap between neighbouring coils also guarantees a residual magnetic field to prevent Majorana spin-flip transitions [58, 273].

3.3 Applications of the Model to Advanced Deceleration Schemes

In the previous Section, I have demonstrated that the model can provide a better understanding of phase stability in a Zeeman decelerator. As shown, there are a number of limitations to the normal operating mode, especially the empty regions in phase space and the large variation of the overall acceptance as a function of the mean longitudinal acceleration. Alternative Zeeman deceleration schemes may resolve these problems. In the

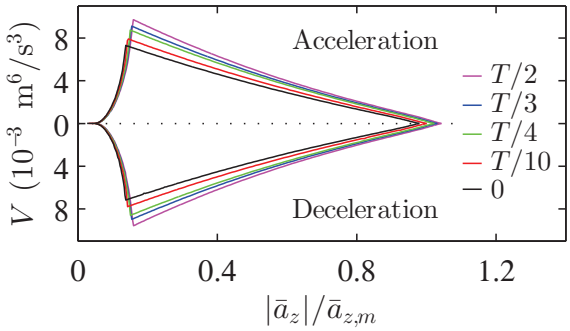

Figure 3.12: Overall phase-space acceptance, V, as a function of normalised mean longitudinal acceleration, $|\bar{a}_z|/\bar{a}_{z,m}$, for Zeeman deceleration (bottom) and acceleration (top) of N(^{2}D$_{5/2}$, M_J = 5/2) at different overlap times between adjacent coils, as indicated in the legend. Overlap times are linked to the time period, T. Infinitely fast rise and fall times are assumed.

following, the model is used to evaluate the feasibility of two advanced operating modes that are inspired by schemes developed for Stark deceleration. Thereby, it is demonstrated that the model can serve as a valuable tool to assess the performance of different Zeeman deceleration sequences. In Section 3.3.2, I will present a switching scheme for Zeeman deceleration that makes more effective use of the phase-space characteristics in the normal deceleration mode, and I will show that this approach provides superior phase-space characteristics that are especially well suited for collision experiments.

3.3.1 Mimicking Stark Deceleration Sequences

There are a lot of parallels between Stark and Zeeman deceleration, and a number of authors have already compared the two techniques in detail [8, 44, 272]. Differences arise from technical restrictions, for example, inductance and the resistive heating of solenoid coils in a Zeeman decelerator thereby limiting the switching times and the overall duration of a current pulse, respectively. In addition, the longitudinal and transverse properties of electric and magnetic fields are dissimilar, so that a switching scheme may work reliably in one deceleration technique but not in the other.

In a Stark decelerator, alternating deceleration stages are electrically connected. Thus,

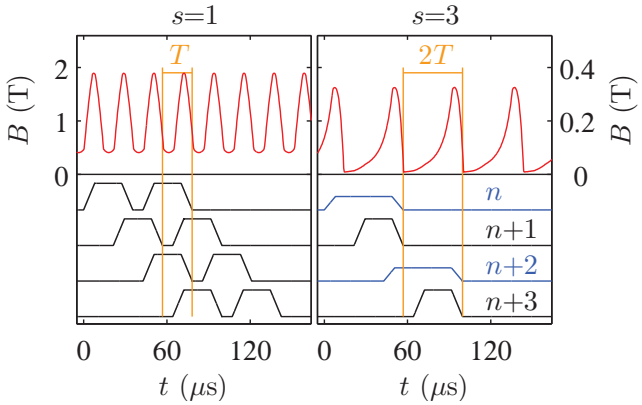

Figure 3.13: Zeeman deceleration sequences imitating the $s = 1$ (left column) and $s = 3$ (right column) operating modes of a Stark decelerator. The lower traces schematically indicate the switching times of four consecutive deceleration coils, and the red lines in the upper panel illustrate the magnetic field experienced by the synchronous particle (initial velocity of 500 m/s). A guiding sequence ($\bar{a}_z = 0$) is chosen for the $s = 1$ mode. In the $s = 3$ sequence, $\bar{a}_z/\bar{a}_{z,m}$= -0.14 and a current of 150 A is applied to every focusing coil (blue curves). All other coils are operated at 300 A. The horizontal bars indicate the time periods T and $2T$ that are used to obtain the mean longitudinal acceleration, $\bar{a}_z$.

when the electric field stages are successively switched between a high voltage and a low voltage (or ground) configuration, a potential hill is created at both sides of the synchronous particle. In the $s = 1$ mode of operation, the switching takes place as soon as the synchronous particle has travelled exactly one electrode-to-electrode distance, d, while in the $s = 3$ configuration, the electrodes are switched after the particles have covered a distance of $3d$, so that the particles have to surmount an additional potential hill during each deceleration step. The latter mode of operation provides additional transverse confinement, and it effectively decouples the longitudinal and the transverse dynamics. The $s = 1$ scheme enables guiding, i.e. an equal amount of acceleration and deceleration per switching stage ($\bar{a}_z = 0$), so that the actual beam velocity is not changed during the switching sequence. Guiding can prove useful in the initial characterisation of a supersonic beam. However, as shown in Section 3.2, switching in the normal Zeeman deceleration mode does not result in phase-stable motion at $\bar{a}_z = 0$.

In the following, both the $s = 1$ and the $s = 3$ mode will be mimicked but, in view of ohmic heating, the switching will be restricted so that each coil is turned on for a maxi-

mum duration of two periods, T, as compared to the normal mode of operation. Figure 3.13 shows schematic pulse sequences for both schemes (lower panel), and it illustrates the corresponding magnetic field experienced by the synchronous particle under these conditions (upper panel). The $s = 1$ mode is not very different from the normal mode of operation, except that each coil is turned on again after a break of one period, T. The duration of the second pulse is synchronised with the other switching times, so that its duration is also of time T. In the $s = 3$ sequence, every second coil is turned on for a duration of two periods (blue curves), while every other coil is switched as usual. In contrast to the $s = 3$ sequence in a Stark decelerator, every coil represents one potential hill, so that the $s = 3$ mode shown here is essentially $s = 2$. To study focusing in the transverse direction, one configuration is chosen in which all coils are operated at 300 A, and another in which a current of 150 A is applied to those coils with an extended pulse duration of $2T$ (blue curves, 'focusing coils'). Similar $s = 3$ Zeeman deceleration schemes have been described by Wiederkehr et al. [272], but either every second coil was not switched, or the coils were placed at larger distances with respect to each other. From the arguments in Section 3.2.2, it seems reasonable to keep the particles within the active coil for as much time as possible to increase transverse focusing. Therefore, the coil configuration with respect to the normal mode of operation was not changed.

The implementation of the $s = 1$ and $s = 3$ sequences in the model is analogous to what has been described for the normal mode of operation, but care must be taken in the determination of the mean longitudinal acceleration, $\bar{a}_z$. While averaging $\bar{a}_z$ over one period is sufficient in the $s = 1$ scheme, two periods ($2T$ or $2d$) must be taken into account in the $s = 3$ mode, because the pulse patterns for two adjacent coils differ (cf. Figure 3.13). Again, the results of the model are compared with trajectory simulations. In this case, an initial velocity of 500 m/s is chosen for the guiding, deceleration or acceleration of 10 million nitrogen atoms in the $^2D_{5/2}$, $M_J = 5/2$ state through a 137-stage Zeeman decelerator (configuration as in Section 3.2.2).

Selected longitudinal phase-space distributions obtained from model and trajectory calculations are highlighted in Figure 3.14. There is very good agreement for the extent of

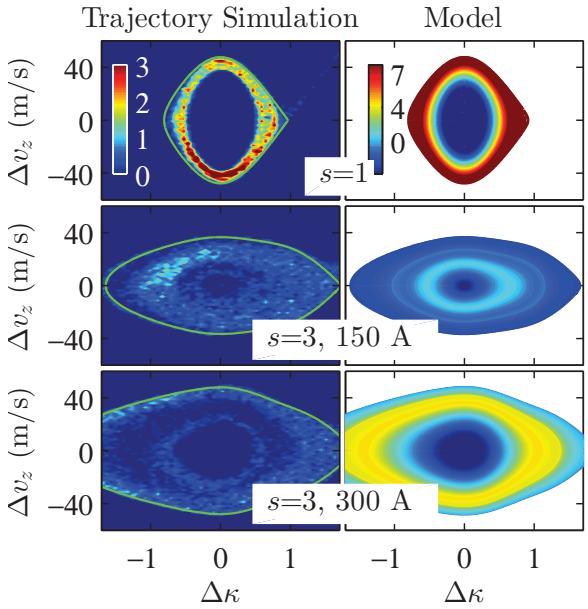

Figure 3.14: Longitudinal phase-space distributions for Zeeman guiding and deceleration of N(^{2}D$_{5/2}$, M_J = 5/2) in the s = 1 (top) and s = 3 (middle and bottom) modes of operation, respectively. The focusing coils in the middle panel are operated at 150 A. Otherwise, a current of 300 A is applied to the coils. The mean longitudinal acceleration is $\bar{a}_z/\bar{a}_{z,m}$= 0 (s = 1, top), -0.21 (s = 3, 150 A, middle) and -0.23 (s = 3, 300 A, bottom). Trajectory results and longitudinal separatrices from the model (green curves) are shown in the left column. The output from the model is displayed in the right column. The colour scales are referenced to the number of particles from the simulation and the transverse acceptance (in 10^{-3} m^4/s^2) from the model, respectively. For the sake of clarity, the colour code is matched to the maximum value among the three plots in each column.

the longitudinal phase space, and the empty phase-space region in the centre of the phase space is well reproduced by the model. As expected for guiding in the $s = 1$ mode, the longitudinal phase space is mirror-symmetric with respect to the v_z-axis, which indicates that the potential hills both in front and behind the synchronous particle are of similar shape. Due to the vectorial addition of the magnetic fields, the region in between two coils is even more transversely defocusing than in the normal mode of operation thus explaining the large depleted phase space in the centre of the distribution. Similar features are also observed for deceleration and acceleration pulse sequences. Unfilled central regions are less of a problem in the $s = 3$ schemes. As seen for the normal mode of operation, the trajectory data reveal unfilled regions in phase space, e.g. for $s = 3$, 300 A in Figure 3.14, that differ from the model predictions. Again, it is likely that these regions are dominated by motion that cannot be described within the adiabatic approximation of the model. The longitudinal phase space is much more evenly filled when a current of 150 A is applied to the focusing coils (also at other mean longitudinal accelerations that are not shown here). This indicates that the longitudinal and the transverse dynamics may be uncoupled more effectively if the currents used for deceleration and for transverse confinement are not the same.

As in the normal mode of operation, a distinct velocity dependence of the phase-space acceptance is observed in all three alternative switching schemes (not shown). Figure 3.15 illustrates that there is a very good correlation between model and trajectory simulation results concerning the overall phase-space acceptance as a function of $\bar{a}_z$. The overall acceptance for the $s = 3$ schemes is highest at $|\bar{a}_z| / \bar{a}_{z,m} = 0.2 - 0.3$, with the 150 A data reaching the maximum at lower mean longitudinal acceleration. For the $s = 1$ mode, the acceptance peaks at $\bar{a}_z = 0$, with a significantly higher phase-space acceptance than in the normal mode of operation. Unfortunately, the acceptance decays quickly towards higher mean longitudinal accelerations, especially in the trajectory simulations. As for the normal mode of operation, there are recurring regions of phase-space acceptance for the same value of $\bar{a}_z$ (not shown in Figure 3.15). In the $s = 1$ mode, there are other acceptance regions for deceleration and acceleration in addition to that. To access these regions, the

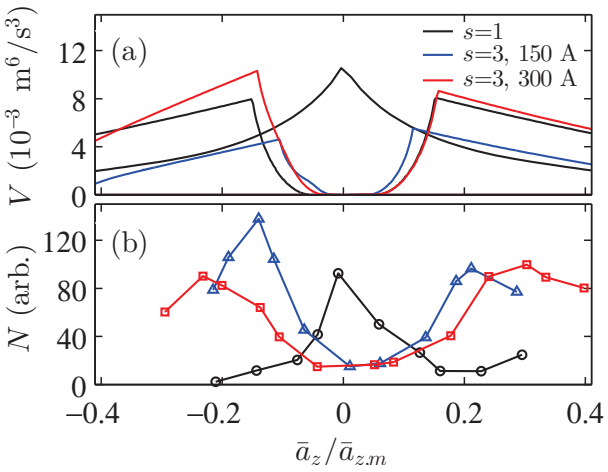

Figure 3.15: (a) Overall phase-space acceptance, V, for the s = 1 and s = 3 modes as a function of the normalised mean longitudinal acceleration, $\bar{a}_z/\bar{a}_{z,m}$, calculated using the model for phase stability; see legend for assignments. (b) Number of transmitted particles, N, for the same modes of operation (colour code as in (a)) versus $\bar{a}_z/\bar{a}_{z,m}$ that is obtained from the trajectory simulation (initial velocity of 500 m/s) by counting the number of particles in the phase-space window (cf. Figure 3.14). The solid lines are a guide to the eye only. The scaling of the trajectory data is not the same as in Figure 3.10. Here, a value of N = 10 corresponds to a transmission of 100 phase-stable particles per 1 million initial particles. The final velocities are within a range of 240 – 690 m/s for the s = 3, 300 A mode.

pulse sequences are chosen such that the reswitching of each coil has no effect on the particles. The magnetic fields in these sequences then effectively correspond to those in the normal mode of operation thus explaining why the maximum acceptance is the same as in Figure 3.10. In this case, however, the use of an $s = 1$ mode proves unnecessary.

In general, due to the low overall acceptance beyond $\bar{a}_z = 0$ and the unfilled regions in phase space, the $s = 1$ mode does not seem suitable for deceleration or acceleration experiments. However, owing to the very high acceptance at $\bar{a}_z = 0$, the guiding mode may still be useful in the characterisation of a supersonic beam. The $s = 3$ scheme seems to be promising for Zeeman deceleration at low $\bar{a}_z$, especially for a focusing current of 150 A, because the longitudinal phase space is more uniformly filled. The main disadvantage of this approach is the much smaller maximum amount of deceleration/acceleration that can be attained in comparison to the normal mode of operation. Essentially twice as many coils are needed, since every second coil is used for transverse focusing instead of deceleration.

3.3.2 Acceleration-Deceleration Switching Scheme

In Section 3.2, it was demonstrated that the phase-space acceptance in a Zeeman decelerator varies as a function of the mean longitudinal acceleration, $\bar{a}_z$. Particularly at low $\bar{a}_z$, the extent of the phase-stable region in $(\Delta\kappa, v_z)$-space is huge compared to higher amounts of acceleration; and above all, the 6 D phase-space volume is not evenly filled. These phase-space characteristics are not practical for collision experiments, where ideally, the phase-space volume should stay constant as the kinetic energy of the beam is changed. In the following, I will describe an approach that makes it possible to tune the final velocity of a supersonic beam over a wide range while keeping the phase-space volume nearly constant. This scheme, which is based upon the switching between Zeeman acceleration and deceleration, is also very easy to implement in existing Zeeman decelerator experiments as it only relies on changes in the computed deceleration pulse sequence.

The analysis of the normal mode of operation (Section 3.2.2) shows that the occupied phase-stable regions for Zeeman deceleration and acceleration are mirror-symmetric (Figure 3.7) if the amount of acceleration is equal to the amount of deceleration ($+\bar{a}_z = -\bar{a}_z$). Equally, for a given $|\bar{a}_z|$, the overall acceptance in the model is virtually the same for deceleration and acceleration (Figure 3.10). Assuming that the experiment consists of a set number of coils, m, a specific mean longitudinal acceleration, $|\bar{a}_z|$, can be chosen, for which the first n stages are used for Zeeman acceleration and the remaining $m-n$ coils for deceleration. Tuning of the final beam velocity is then achieved solely by changing the relative number of coils for acceleration and deceleration, n and $m-n$, respectively. The minimum (maximum) velocity is given by the final velocity that can be attained if all coils are used for deceleration (acceleration). This scheme does not only allow for efficient deceleration and acceleration at low or zero effective mean acceleration, $\bar{a}_{z,e}$, but it also makes it possible to stay within the same phase-stable region throughout the acceleration-deceleration sequence. In the trajectory simulations for this scheme, all acceleration steps are carried out before switching over to the deceleration mode. The two coils at the changeover between the acceleration and deceleration stages are not operated to allow for the synchronous particle to travel one coil distance within a period, T. The experimental arrangement for the simulations is the same as in Section 3.2.2 (137 stages). In each numerical calculation, 10 million N($^2D_{5/2}$, M_J = 5/2) atoms with an initial velocity of 500 m/s are propagated from the switch-off of the first coil until the current of the second to last coil has reached zero.

Figure 3.16 highlights trajectory simulation results obtained for the acceleration-deceleration switching scheme at four different $|\bar{a}_z|$ values. The relative number of phase-stable trajectories is shown as a function of the effective mean acceleration averaged over the acceleration and deceleration sequences. It can be seen that this operating mode indeed allows for a wide tuning range in terms of the final beam velocity, including acceleration, deceleration and guiding. For $|\bar{a}_z|/\bar{a}_{z,m}$= 0.4, the transmitted particle numbers in the phase-stable region are comparable to the s = 1 and s = 3 modes of operation (Figure 3.16 (a)). However, the obtained particle velocity distributions are very broad and not

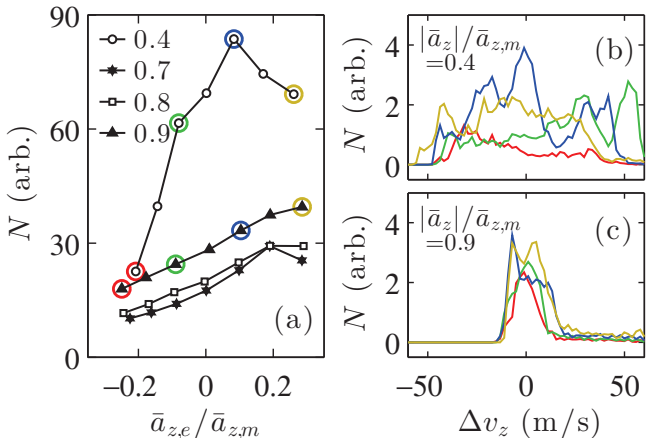

Figure 3.16: (a) Trajectory simulation results for Zeeman deceleration of N($^2D_{5/2}$, M_J = 5/2) in the acceleration-deceleration mode using $|\bar{a}_z|/\bar{a}_{z,m}$= 0.4, 0.7, 0.8 and 0.9 as indicated in the legend. The particle numbers within the phase-space window (cf. Figure 3.7), N, are plotted against the normalised effective mean acceleration, $\bar{a}_{z,e}/\bar{a}_{z,m}$, where $\bar{a}_{z,e}/\bar{a}_{z,m}$ = 0 corresponds to a velocity of 500 m/s. The solid lines are a guide to the eye only. The scaling of the trajectory data is the same as in Figure 3.15. (b) and (c) Velocity distributions, Δv_z, for $|\bar{a}_z|/\bar{a}_{z,m}$= 0.4 and 0.9 at different $\bar{a}_{z,e}/\bar{a}_{z,m}$, respectively. The line colours in (b) and (c) correspond to the coloured circles in (a).

uniform (Figure 3.16 (b)). In contrast to that, switching at a higher mean longitudinal acceleration of $|\bar{a}_z|/\bar{a}_{z,m}$= 0.9 (Figure 3.16 (c)) yields a very narrow velocity distribution which is centred near zero. In addition to that, the number of transmitted particles for $|\bar{a}_z|/\bar{a}_{z,m}$= 0.7 – 0.9 changes only by a maximum factor of two between the minimum and the maximum final velocities considered, which is much smaller than in any other operating mode presented in this Chapter (cf. Figures 3.10 and 3.15). Owing to the small and almost constant velocity spread, switching at $|\bar{a}_z|/\bar{a}_{z,m}$= 0.9 would clearly be the method of choice for collision experiments.

The output of the simulation can be understood from the corresponding phase-space distributions in the normal mode of operation (see Figure 3.7) which predicts higher particle numbers and broader velocity distributions at low values of $|\bar{a}_z|$. It is somewhat surprising to see that more particles are transmitted at $|\bar{a}_z|/\bar{a}_{z,m}$= 0.9 than in the intermediate regime (red and green curves in Figure 3.16). This may be related to the more uniform phase-space distribution at high mean accelerations which helps to match the phase-space distributions for acceleration and deceleration.

3.4 Conclusions

In this Chapter, I have introduced a formalism to calculate the longitudinal, transverse and overall phase-space acceptance in a Zeeman decelerator. Due to the finite rise and fall times of the current pulses, the phase-space acceptance depends upon the beam velocity if the switch-off position of the synchronous particle, κ_0, is kept constant. I have demonstrated that the velocity dependence can be eliminated by varying κ_0 according to the mean longitudinal acceleration while the beam velocity is changed. Despite the inherent limitations of the model, good agreement was found in comparison with numerical three-dimensional particle trajectory simulations. In view of the restricted phase-space acceptance in the normal mode of operation, I have also examined alternative schemes for Zeeman deceleration. Switching modes adapted from Stark deceleration may, for example, find applications in the characterisation of the initial beam velocity. An acceleration-deceleration switching scheme appears to be a promising method for experiments in which a well-defined energy resolution is required.

Since the particle motion in a Zeeman decelerator is widely governed by phase stability, the model contributes to a better understanding of the underlying mechanisms that stipulate the number of decelerated particles and the final velocity distributions. I believe that this work does not only provide a useful recipe for determining the phase-space acceptance in a Zeeman decelerator, but that it will also trigger ideas for advanced switching sequences and thereby aid in the development of improved Zeeman deceleration experiments.

4 | Experimental Setup

4.1 General Setup

A schematic illustration of the experimental setup, which I have designed and constructed over the course of the past four years, is shown in Figure 4.1; a CAD drawing and a photograph are given in Figure 4.2. The molecular beam apparatus consists of two chambers: a source chamber for the generation of supersonic beams, and a detection chamber containing both the Zeeman decelerator and a time-of-flight (TOF) detection system. The chambers are separated by a skimmer (Beam Dynamics, 2.0 mm orifice diameter), and differential pumping is achieved using two turbo pumps (TURBOVAC SL 700, Oerlikon Leybold, 690 l/s for N_2 [274][a]). During experiments, the pressures are typically at $1{\cdot}10^{-5}$ mbar in the source chamber and at $4{\cdot}10^{-8}$ mbar in the detection chamber. Without a gas load, pressures of 2–$5{\cdot}10^{-9}$ mbar are reached in both chambers. The experimental arrangement for the studies with metastable species is similar to the setup used for hydrogen atom deceleration experiments (see Figure 4.1), with the main differences being the use of different radical production methods, the distances between the pulsed valve and skimmer, and the laser wavelengths for detection.

4.1.1 Experiments with Hydrogen Atoms

In the experiments with ground-state hydrogen atoms, a supersonic beam is generated by expanding a mixture of NH_3 and Kr through a pulsed valve (NH_3/Kr mixing ratio of 1/9, p_0 = 4 bar, T_0 = 238 K) into the vacuum. Ammonia was chosen as a precursor for H atoms owing to its high absorption cross section at 193 nm ($6.4{\cdot}10^{-18}$ cm^2 [276]) and its relative ease in handling compared to other possible precursor species like HI, H_2S or

[a] Owing to a failure of the bearings, the turbo pump for the source chamber has been replaced by a TURBOVAC 600 C (Leybold, 560 l/s for N_2 [275]) for the metastable atom experiments. The vacuum conditions attained with this pump are comparable to before.

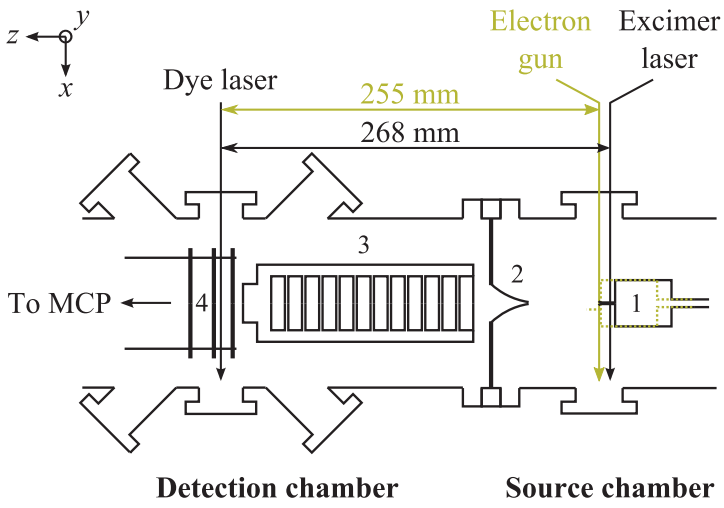

Figure 4.1: Sketch of the experimental setup, not to scale. 1: Pulsed valve, 2: Skimmer, 3: Zeeman decelerator, 4: Extraction plates.

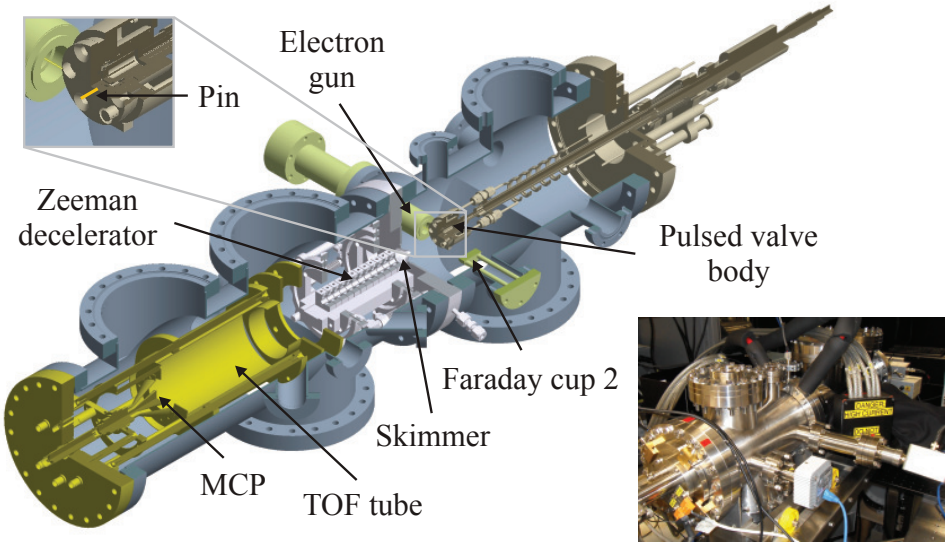

Figure 4.2: CAD drawing of the experimental assembly with the electron-impact excitation source, and a photograph of the setup in the laboratory.

PH_3. NH_3 molecules are photolysed using an ArF excimer laser (Neweks, PSX-100-2) inside a quartz capillary (1 mm inner diameter, 15 mm length, conically widened at the exit) that is attached to the front of the valve. The 193 nm laser beam, with a square area of about 4 mm^2 and a typical energy of 2 mJ/pulse, is focused into the capillary close to the valve orifice using a cylindrical lens (f = 350 mm). Light scattering off the capillary indicates the vertical alignment of the excimer laser beam. The atoms pass through a skimmer that is placed at a distance of 50 mm from the nozzle. Thereafter, they are

subject to the solenoid magnetic fields of the decelerator (first coil 85 mm from the valve). A detailed description of the Zeeman decelerator is given in Section 4.4. After Zeeman deceleration, the H atoms are photoionised in a (2+1) resonance-enhanced multiphoton ionisation (REMPI) scheme via the $2s\ ^2S_{1/2}$ state and the resulting ions are detected in a Wiley-McLaren-type TOF mass spectrometer. The extraction plates are turned on after the detection laser pulse to prevent losses from electric-field-induced mixing between the $^2S_{1/2}$ and the $^2P_{1/2}$ states, which considerably shortens the lifetime of the resonant state, i.e. from 122 ms for the field-free $^2S_{1/2}$ state into the ns-regime for the coupled state [277–279]. For the REMPI process, laser radiation at 243.13 nm is generated by frequency-doubling the 10 mJ/pulse output of a pulsed dye laser (Quanta-Ray PDL-3, Spectra-Physics, Coumarin 480 dye) pumped by the third harmonic of a Nd:YAG laser (Quanta-Ray GCR-290, Spectra-Physics, 235 mJ/pulse at 355 nm in front of the dye laser). The 1.2 mJ/pulse output energy (elliptical beam with major and minor axes of $\approx$ 2 mm and 1 mm) is tightly focused into the chamber (f = 150 mm) to increase the number of hydrogen ions produced.

4.1.2 Experiments with Metastable Atoms

For the generation of metastable species, an electron-impact excitation source is mounted perpendicular to the pulsed valve and aimed close to the valve orifice (distance of $\approx$ 1 mm, see Figure 2.1) to increase metastable production. Cross sections for metastable excitation are highest just above threshold ($\leq 10^{-17}$ cm^2) and level off towards higher electron energies [280]. However, we found optimum working conditions for metastable generation at kinetic energies of 100 eV (the maximum kinetic energy for this source) due to considerably higher electron emission currents under these conditions. For deceleration experiments, the electron gun is pulsed for a duration of either 20 μs or 50 μs. A 10 mm long metal pin (1 mm diameter) is mounted on the valve plate along the axis of the electron beam (see inset of Figure 4.1). Positive biasing of the pin (U_{bias} = 150 V) leads to an avalanche of secondary electrons in Ar, Kr and N_2 gas which have sufficient kinetic

energy to enhance metastable formation (see Section 6.2.2).

For metastable He deceleration experiments, supersonic beams with an initial velocity of 520 m/s are generated by seeding He in Ar carrier gas (He/Ar mixing ratio of 1/3, p_0 = 4.5 bar) and cooling the valve body to a temperature of 143 K. With the electron-impact excitation setup, supersonic beams of metastable N atoms are now routinely generated. However, a proof-of-principle deceleration experiment with our 12-stage Zeeman decelerator requires a very low initial beam velocity ($\approx$ 450 m/s) to observe a clear change in N($^2D_{5/2}$) velocity. Seeding in Kr is not an option, as it leads to broad and very noisy TOF signals. To date, the most promising route is via the use of a N_2/Ne gas mixture, which is pre-cooled with dry ice, and supersonically expanded at a valve temperature of 92 K. Condensation of the N_2 gas at this temperature has thus far prevented any Zeeman deceleration measurements.

For all metastable atom experiments, the distance between the centre of the electron beam and the skimmer is set at 37 mm, such that the distance between the valve and the first deceleration coil is reduced to 72 mm. Zeeman-decelerated metastable atoms are state-selectively detected using REMPI detection schemes, since metastable formation in both the seed and carrier gas leads to electron emission from the MCP surface. In addition to that, the 2.4 eV excited-state energy of metastable N(^{2}D) is below the Fermi level of most metals, thus precluding the ejection of electrons from the MCP surface. Detection of He atoms in the $1s2s\ ^3S_1$ is attained in a (1+1) REMPI process using the strong transition at 388.97 nm via the $1s3p\ ^3P_{0,1,2}$ state [281]. Approximately 10 mJ/pulse of laser light at this wavelength is produced by pumping a pulsed dye laser system (Quanta-Ray PDL-3, Spectra-Physics, Exalite 389 dye[b]) with 355 nm light from of a Nd:YAG laser (Quanta-Ray GCR-290, Spectra-Physics, 235 mJ/pulse in front of the dye laser). N atoms in the $2s^22p^3\ ^2D_{5/2}$ and the $2s^22p^3\ ^2D_{3/2}$ spin-orbit states are detected in a (2+1) REMPI scheme using two photons at 268.97 nm for resonant excitation to the $2s^22p^2(^3P)3p\ ^2S_{1/2}$ state, and an additional photon at this wavelength for ionisation. Here, the Nd:YAG laser

[b]Laser energy was found to drop very quickly with this dye, with a 50 % decrease in laser energy within one day of use.

is used to pump Coumarin 540A dye to produce a 538 nm laser beam with an energy of about 10 mJ/pulse. Second-harmonic generation at 268.97 nm is attained inside an Inrad Autotracker II system (2.5 mJ/pulse[c]). For all metastable atom experiments, a lens (f = 150 mm) is used to focus the detection laser beam into the vacuum chamber. In contrast to the experiments with H atoms, a continuous voltage is applied to the extraction plates to prevent the impingement of ions, produced by the electron-impact excitation process, onto the MCPs.

4.2 Pulsed Valve

The pulsed valve (General Valve Series 99, Parker, 0.8 mm orifice diameter, 12 V DC with Cu gasket seal allowing for cryogenic cooling of the valve) is mounted on a translation stage, whose design has been adapted from the Stark deceleration experiments carried out by the Meijer group in Berlin. The translator allows for an external adjustment of the pressure on the valve poppet, and a three-dimensional alignment of the valve position. The valve body can be cooled with a flow of gaseous nitrogen through a liquid-nitrogen reservoir, and temperature control (to an accuracy within 3 K) is achieved through a feedback loop with a PID-driven air-process heater (CAL 9500P). For room-temperature experiments with metastable atoms, nitrogen gas is continuously flown through the valve body to prevent a rise in valve temperature caused by the increased temperature of the electron-gun filament.

4.2.1 Distance between Pulsed Valve and Skimmer

Figure 4.3 shows H atom time-of-flight (TOF) spectra measured using different distances between the pulsed valve and the skimmer (T_0 = 300 K, $p_0 \approx$ 3.5 bar); the location of the excimer laser beam was adjusted to dissociate NH_3 at a constant distance from the valve.

[c]The higher output energy with respect to the H atom experiments was attained through the use of a new BBO crystal (Sirah, SHG-250-T).

A long, increasing tail appears in the TOF distribution as the valve is moved closer to the skimmer. This observation can be attributed to skimmer interference effects [282], i.e. a deflection of gas particles from the walls of the skimmer leading to an interaction with the supersonic beam. Therefore, a valve-to-skimmer distance of 50 mm was chosen to avoid this interference. Such interference effects were not observed in the experiments with metastable atoms, and it seems likely that the effective valve-to-skimmer distance in the H atom experiments was shortened due to the 15 mm long quartz capillary attached to the valve orifice.

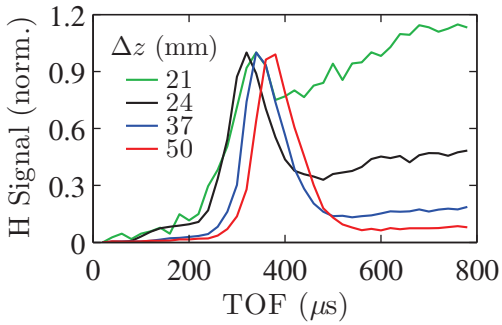

Figure 4.3: H atom TOF spectra at different distances, Δz, between pulsed valve ($\hat{=}$ position of excimer laser beam) and skimmer, as indicated in the legend.

4.2.2 Valve Opening Time

In order to determine the opening time of the pulsed valve, H atom TOF spectra (He/Ar mixing ratio of 1/9, T_0 = 300 K, $p_0 \approx 3.2$ bar) were taken at different trigger delays between the pulsed valve and the excimer laser. To account for fluctuations in laser energy and drifts of the laser frequency, the data were normalised to a reference measurement after each scan. Figure 4.4a illustrates that maximum signal intensities are obtained for delays between 300 μs and 450 μs. Furthermore, an early TOF peak is observed in the spectra at short and at long excimer-to-valve delays, indicating that collisional cooling with the Ar carrier gas is not as effective in the tails of the gas pulse as in the centre, where the particle number densities are much higher.

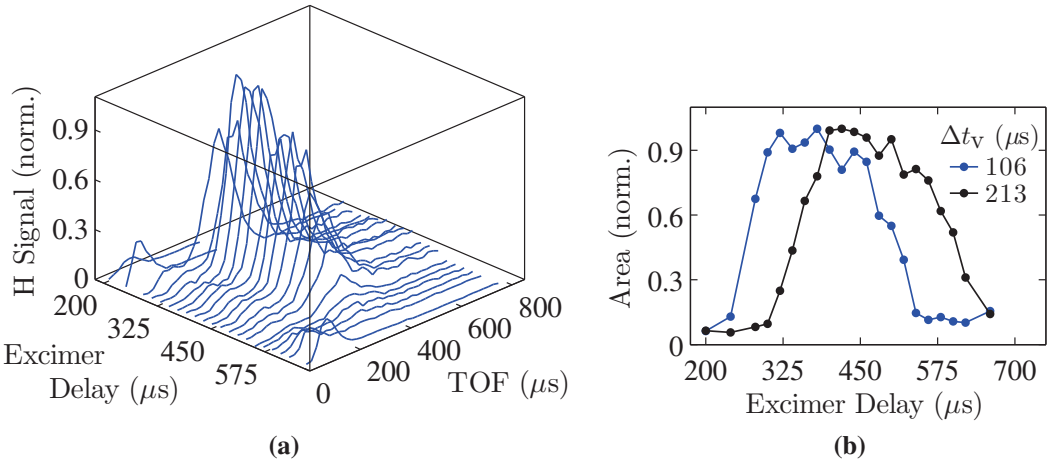

Figure 4.4: (a) H atom TOF profiles at different excimer-to-valve trigger delays. (b) Integrated H atom TOF signal as a function of excimer delay for two valve settings. For the blue data points, a trigger width Δt_v = 106 μs (1.0) and a driving voltage U_v = 200 V are applied to the valve (same settings as in (a)). For the black points, Δt_v = 213 μs (3.0) and U_v = 80 V.

Integration of the TOF signal intensities at every excimer laser delay yields intensity profiles as given in Figure 4.4b. Here, results for two different trigger widths to the valve driver electronics, Δt_v = 106 μs and 213 μs, are contrasted. For the shorter trigger width, the valve driving voltage, U_v, had to be increased to 200 V in order to obtain a comparable H atom signal intensity, indicating that the valve would otherwise not fully open. If we assume an RL circuit for the solenoid coil inside the pulsed valve, the higher voltage also means a shorter initial rise time for the current. Consequently, the current level required to induce a release of the poppet is reached earlier in time explaining why the integrated H atom TOF signal in Figure 4.4b is shifted by about 85 μs when Δt_v is decreased to 106 μs (and U_v increased to 200 V). However, the full width at half maximum opening time (FWHM; from parabola fits of the profiles in Figure 4.4b), is very similar in both cases, i.e. FWHM = 230 μs at Δt_v = 106 μs and FWHM = 254 μs at Δt_v = 213 μs. This implies that the opening time of the valve cannot be significantly altered through a variation of the valver driver setting. A different type of pulsed valve, such as an Even-Lavie valve [283], an Amsterdam piezovalve [284] or a Nijmegen pulsed valve [285], would be required to obtain much shorter opening times. For the day-to-day operation of the valve, Δt_v = 106 μs (1.0) and U_v = 150 V were found to give reliable and reproducible working

conditions.

Compared to the optimum H atom valve-to-excimer laser delay of 390 μs at room temperature, metastable He intensities are highest at a delay of 350 μs. This shift may be related to a change in the valve opening characteristics owing to the use of different gas mixtures, or it may be attributed to the quenching of metastable He atoms in the main part of the gas pulse.

4.2.3 Valve Characteristics at Different Temperatures

Both in experiments with H atoms and metastable species, the maximum signal intensity is shifted to shorter valve-to-excimer laser (electron gun) trigger delays when the valve temperature is decreased, e.g. from 390 μs at room temperature to 350 μs at 238 K for H atoms. For experiments with metastable He atoms, the valve is cooled to a temperature of 143 K, resulting in a 100 μs decrease of the optimum delay with respect to the room-temperature setting (top panel in Figure 4.5). While similar delay characteristics are observed for both REMPI and direct metastable detection on the MCPs (not shown), the maximum electron current at the pin[d] is consistently offset to longer valve-to-electron gun delays. We anticipate that this deviation is related to the detection of secondary electrons which are produced during electron-impact excitation. The optimum trigger delay between the electron gun and the pulsed valve is therefore not directly related to the maximum electron current at the pin, and the latter should therefore not be used for optimisation purposes.

Figure 4.5 also illustrates that the decrease in valve temperature leads to an increase in signal intensity, both for REMPI and pin detection. The gain of about a factor of 1.5–2 is consistent with the increase in particle density, n_0, that is predicted by the ideal gas law for these experimental conditions. The higher signal intensities for an electron gun pulse

[d]Here, the pin is used both as a Faraday-cup-type detector and to increase metastable signal intensity.

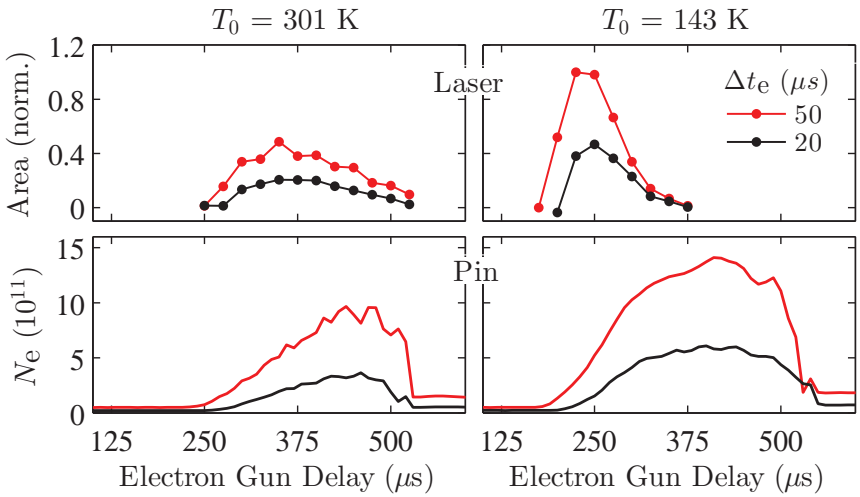

Figure 4.5: Top panel: integrated metastable He atom TOF signal as a function of valve-to-electron gun trigger delay at valve temperatures of 301 K and 143 K and pressures of 5.9 bar and 4.5 bar, respectively. Measurements were done at pulse durations, Δt_e, of 20 μs (black data points) and 50 μs (red data points) for the electron gun. Bottom panel: number of electrons, N_e, deduced from the electron current at the pin over the duration of the electron pulse (same experimental conditions as in the top panel). The measurements at different temperatures were done with 1/3 He/Ar gas mixtures, comparable laser energies (8 mJ/pulse) and similar electron currents at the pin at zero delay.

duration of 50 μs, as compared to a pulse duration of 20 μs, are in accordance with other measurements (see Section 4.3.1 for details).

4.3 Electron Gun

To extend the range of species amenable to Zeeman deceleration with this experimental setup, we decided to implement an electron gun as a source of metastable atoms and molecules. We opted for an electron-impact excitation setup owing to its well-defined electron energy distribution and low energy spread as compared to a discharge source. The design of the electron gun is based on a commercially available electron source (ELS 100, PSP Vacuum Technology), and was drafted by James Bull, a postdoc in the Vallance group. A photograph of the electron source is shown in Figure 4.6.

A scale drawing of the electron gun, including an assignment of the electrodes, is given

Figure 4.6: Photograph of the electron gun assembly. The mu-metal tube for magnetic shielding (top left) has been removed so that the different electrostatic lenses can be seen.

in Figure 4.7. An yttria-coated iridium filament (ES-526, Kimball Physics) is used as a thermionic electron emitter. According to the data sheet, it provides a high emission current of 3–5 mA and is suitable for relatively poor vacuum conditions (up to $1{\cdot}10^{-4}$ mbar), as observed close to the pulsed valve. An energy spread of approximately 0.6 eV can be expected. Magnetic shielding with a mu-metal tube around the electrostatic lenses and the reduction of stray magnetic fields – through a replacement of the existing pressure gauges (PENNINGVAC PTR 90, Leybold Oerlikon) by active ion gauges (Edwards, AIGX) – were crucial for the realisation of an intense electron beam. A mu-metal cup can also be fitted to the front of the valve body to prevent a distortion of the electron beam by the solenoid magnetic fields of the pulsed valve. However, by the time of writing this thesis, the shielding has not yet been put into place.

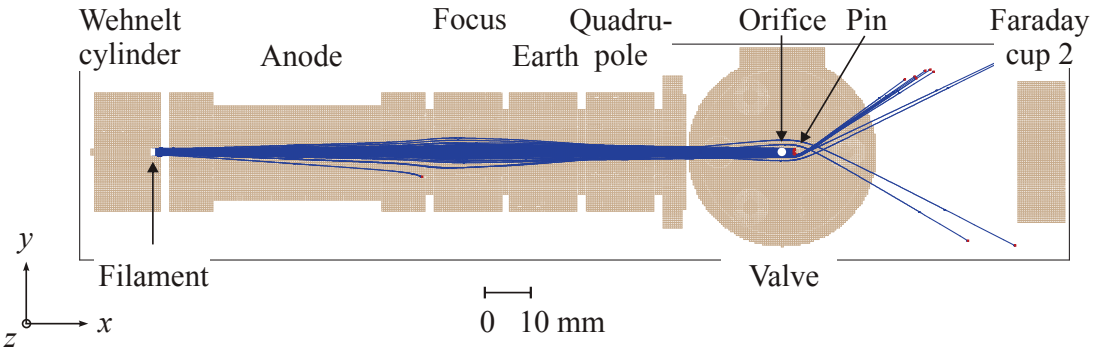

Figure 4.7: Scale drawing of the electron gun setup in SIMION and a subset of electron trajectories (in blue colour) simulated in the program using the experimental voltages given in Table 4.1.

The electronics are implemented such that the electron source can be operated at kinetic energies between 0 eV and 100 eV. However, in practise, hardly any electron emission is observed below 10 eV. Some of the voltage ranges for the electrostatic lenses (anode, fo-

Table 4.1: Typical voltages applied to the elements of the electron gun to produce a high-intensity electron beam with a kinetic energy of 100 eV. Typically, a filament current of 3.90 A (86.6 %) is used.

Electrode	Potentiometer setting (%)	Voltage (V)
Filament	95.0	-100.1
Wehnelt cylinder	16.4	-4.7 (+48) [a]
Anode	74.8	746.6 [a]
Focus	50.3	145.6 [a]
X deflectors	57.7	
X1 (left)		4.3
X2 (right)		-8.6
Y deflectors	61.2	
Y1 (bottom)		6.4
Y2 (top)		-12.8
Pin		150

[a] Voltage referenced to the filament. Value in brackets denotes the voltage applied to the Wehnelt cylinder for pulsing.

cus, X and Y deflectors) have been increased with respect to the commercial design, since they yielded higher electron beam currents and increased metastable signal intensities. Typical settings for the individual elements of the electron gun system are summarised in Table 4.1.

4.3.1 Pulsed Operation

Initially, a picoammeter (Keithley 6487) was required to detect the low, continuous electron current at the Faraday cup. Operation of the electron gun in pulsed mode resulted in a several orders of magnitude gain in beam current. The current released during such a short time interval is significantly larger than the overall continuous current of an electron gun, which is probably owing to the influence of patch fields on continuous electron

emission [286]. In addition, pulsed electron beams provide a well-defined phase-space window that is advantageous for Zeeman deceleration experiments (see Section 6.3).

Pulsing of the electron emission is achieved by negatively biasing the Wehnelt cylinder with respect to the filament and applying a positive voltage pulse (up to +48 V) of duration Δt_e to the Wehnelt cylinder, which rapidly releases a dense electron beam into the other parts of the system. Beam current is detected on a graphite-coated Cu surface ('Faraday cup', 8 mm diameter conical cavity in a 30 mm diameter Cu cylinder, Figure 4.2) which is located opposite to the electron gun and biased with a positive voltage, U_{bias}, to prevent electron back-scattering off the surface and to suppress secondary electron emission. Likewise, beam current can be detected on a positively biased metal pin (1 mm diameter, 10 mm length) that is mounted on the valve body to increase the electron density near the valve orifice. Signal from the Faraday cup or the pin is amplified and monitored with an oscilloscope (1 mV corresponds to 0.5 μA). Despite the smaller detection area, much higher beam currents are measured at the pin, indicating that stray fields cause a significant deflection of the electron beam on the additional 47 mm beam path to the Faraday cup. The electron collection efficiency also depends on the surface geometry, the electronics equipment and the collector material [287] (see also Section 6.2.2). A calibration of the current detectors was not carried out. Since the collection efficiency is < 1, the measured values provide a lower estimate of the actual electron beam current.

Figure 4.8a shows typical temporal profiles of the electron current for pulse durations, Δt_e, of 20 μs and 50 μs. When the pulsed valve is not operated (or set to a zero valve-to-electron trigger delay), the detected electron current shows a nearly rectangular shape for both pulse durations, with 5 μs rise and fall times. In the presence of a supersonic beam, the measured intensity profile can be significantly different from that, as highlighted for a 1/3 He/Ar mixture in Figure 4.8a. We attribute this to the detection of secondary electrons produced during the electron-impact excitation process (see Section 6.2.2).

Longer pulse durations also result in an increased production of metastable species (see Table 2.1 for a list of quantum states of the detected species), which is in accordance with

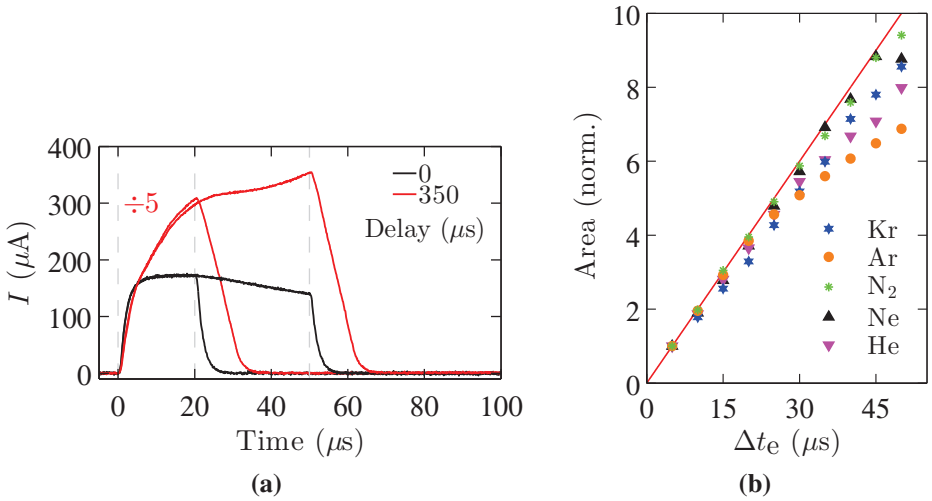

Figure 4.8: (a) Electron current, I, detected at the pin as a function of time for a 1/3 He/Ar mixture (p_0 = 6 bar, T_0 = 301 K, U_{bias} = 150 V) at two different valve-to-electron gun trigger delays, as specified in the legend. Traces were recorded for electron gun pulse durations Δt_e = 20 μs and 50 μs. Triggers to the electron gun pulser are indicated with grey dashed lines. Signals recorded at a delay of 350 μs are scaled down by a factor of 5 for visibility. (b) Change of integrated TOF signal intensity as a function of electron gun pulse duration for different gases (see legend, p_0 = 6 bar, T_0 = 302 K, U_{bias} = 150 V). TOF traces are measured via electron emission from the MCP surface. Integrated TOF traces are normalised to the integrated signal at Δt_e = 5 μs. A tentative proportional dependence between pulse duration and signal intensity is shown as a red line.

the higher number of emitted electrons. As can be seen from Figure 4.8b, there is an almost linear dependence of metastable signal intensity on pulse duration for most atomic and molecular species studied.

4.4 Zeeman Decelerator

The inhomogeneous magnetic fields for Zeeman deceleration are generated in a set of 12 solenoid coils. A maximum on-axis magnetic field of 2.5 T is sufficient to entirely remove the initial kinetic energy of a Kr-seeded, supersonic beam of hydrogen atoms that exits the nozzle with a forward velocity of about 500 m/s (corresponding to 11 $cm^{-1}hc$ of kinetic energy). The electronic modules for the fast switching of the magnetic fields are based

on the original circuit diagrams from the Merkt group [61] and the mechanical design was, to some extent, inspired by the Merkt and Raizen group setups [61, 288]. Both the mechanical parts and the electronics for the Zeeman decelerator were built in-house in Oxford.

Concerning the mechanical construction, we opted for a different type of modular design that allows us to both shape and to replace each coil individually, and hence to change quickly between different coil configurations, e.g. single coils with more turns, other radii or lengths. Due to the rather extreme demands on the coils from high-current pulsing, ease of exchangeability is also beneficial from an experimental point of view. Furthermore, every coil is connected to its own independent driver electronics, so that different sets of electronics can be used to operate the decelerator. For the focusing experiments presented in Chapter 5, we took advantage of this feature in particular.

4.4.1 Coil Design and Fabrication

The technical specifications of the decelerator coils are similar to those used by the Merkt group but the mechanical implementation is entirely different. Each decelerator coil consists of 70 turns of Kapton-insulated copper wire (Goodfellow, 400 μm diameter, 25 μm insulation thickness) which are wound in 4 layers around a PEEK bobbin (6 mm inner diameter, 500 μm wall thickness) using a hand-operated winding machine and cast into an aluminium shell using thermally conductive epoxy resin (LewVac A-H77, Epoxy Technology). Using an LHC bridge, we measured a resistance of $R = 0.29\ \Omega$ and an inductance of $L = 26\ \mu$H which is in accordance with calculations. Notches are cut into the aluminium housing to suppress eddy currents. A schematic cross section of such a coil block is illustrated in Figure 4.9a. To the right, a photograph of a cross-section cut through a coil is shown.

To obtain a uniform coil, free from air bubbles and with good thermal contact to the aluminium housing, a specific coil fabrication procedure was developed. Details of the

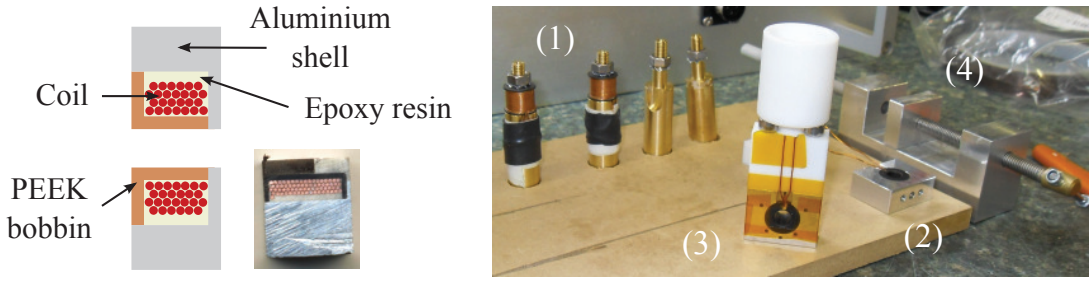

(a) (b)

Figure 4.9: (a) Schematic cross section of a coil block and a photograph of a cross-section cut through a coil. (b) Photograph illustrating details of the coil potting procedure: (1) coils after curing of the applied epoxy, (2) coil block after insertion of a coil, (3) coil block after preparation for casting including funnel, (4) miniature vice to clamp the coil blocks for casting and degassing in vacuum. The figures show an early version of the coils in which TECAPEEK is used as a material for the bobbins. This material was dismissed, as it was found to wear away the insulation of the Cu wire during the winding process.

potting procedure are illustrated in Figure 4.9b. Already during the winding process, thin layers of epoxy are applied to the turns. After impregnation in an oven, the coil is inserted into the aluminium housing and firmly clamped in a miniature vice for casting and repeated degassing of the epoxy (in a vacuum-pumped desiccator). The aluminium blocks are wrapped into Kapton foil to prevent an undesired coating with epoxy that is difficult to remove. A PTFE rod is put into the inside of the bobbin for the same purpose (not shown). Finally, the epoxy is hardened in a two-step cure at 373 K (1 hr) and 393 K (2 hrs).

We had serious problems with partial discharges of enamelled Cu wire caused by mechanical stress and a breakdown of the insulation material from the rapid high-current switching [289]. We therefore opted for Kapton-insulated wire owing to its increased durability[e]. An additional layer of insulation (Figure 4.10a) was put onto the exiting wires for the same purpose. The insulation resistance of each coil was checked at a DC voltage of 2 kV.

[e]The Kapton insulation was so durable that the ends had to be burned off to achieve a good electrical contact with the connectors.

4.4.2 Decelerator Assembly

The coils are mounted onto a water-cooled aluminium base plate to attain cooling inside the vacuum chamber, as shown in the photograph in Figure 4.10a. Vacuum-compatible, thermally conductive grease (Apiezon H) increases the thermal contact between the base plate and the aluminium blocks. A closed-cycle chiller system (ICS, Cygnus Tech, CY 031, water flow rate of 0.2 l/s), operating with an ethylene glycol/water mixture to prevent corrosion of the base plate, keeps the coils at temperatures below 315 K even when pulsed at a 10 Hz repetition rate with currents of 300 A. Coil temperature and water flow through the decelerator are continuously monitored with an interlock system that automatically turns off the electronics in the event of a fault. The decelerator is mounted onto a supporting structure with screws for precise alignment in the *xy* dimension (Figure 4.10b). Base plates for additional deceleration stages can be added to the current setup to allow for the deceleration of particles with a smaller magnetic-moment-to-mass ratio than atomic hydrogen.

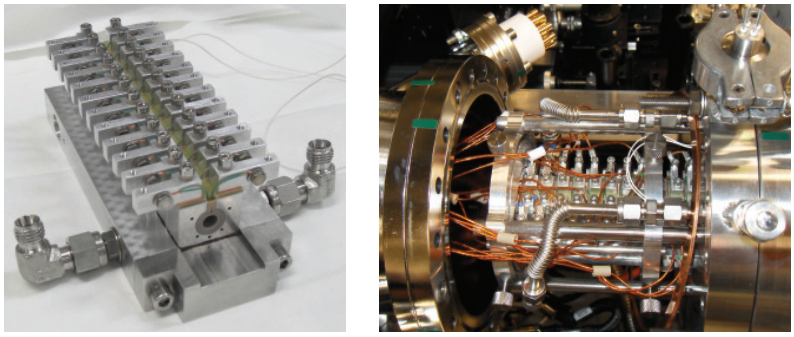

(a) **(b)**

Figure 4.10: (a) Photograph of the Zeeman decelerator on a bench. Swagelok elbow pieces mark the inlet and the outlet of the cooling water. (b) Picture of the complete decelerator assembly before joining the two vacuum chambers.

The solenoid coils are connected to two 12-pin power feedthroughs (LewVac, 5 kV, 50 A DC, temperatures up to 723 K) with 1 mm diameter, Kapton-insulated Cu wires which are labelled with coloured wire beads for identification (Figure 4.11a). Home-built spacers are used to prevent bending of the feedthrough pins and PTFE heat-shrink tubing provides electrical insulation between the wire push-on connectors. On the air side of the chamber,

closed housings ensure secure and firm support of the cables leading to the decelerator electronics equipment (Figure 4.11b). The design is arranged such that the feedthroughs and the wires are left in place if the decelerator is taken out of the chamber. The label code for the wires and cables can be found in Appendix 8.

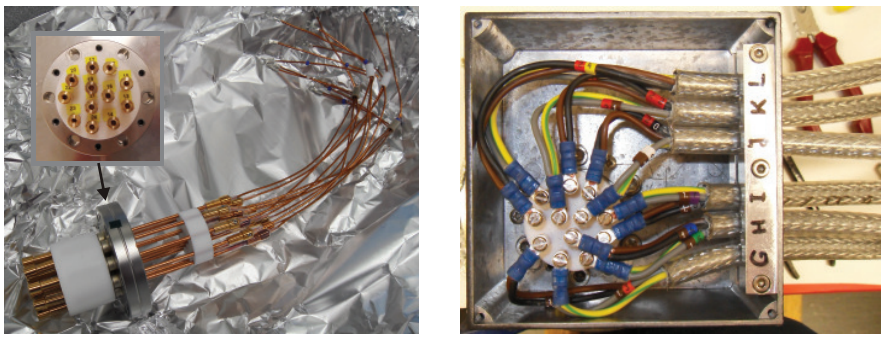

(a) (b)

Figure 4.11: Photographs of the electrical connections to the feedthroughs (a) showing the Cu wires into the vacuum chamber and (b) illustrating the mounted support of the air-side cables. All wires are labelled either through coloured wire beads (inside the vacuum) or numbers from 1–24. The cables to the electronics are given letters from A–L.

4.4.3 Static and Pulsed Magnetic Field Characteristics

We determined the real on-axis magnetic fields using a Hall probe sensor (Honeywell, SS59ET) that was moved through the decelerator assembly with a high-precision linear translation stage. To obtain magnetic field profiles, as shown in Figure 4.12, a static current of 6 A DC was applied to one coil at a time while the translation stage was shifted. The results are consistent with the nominal centre-to-centre coil distance d of 10.7 mm (with a root-mean-square deviation of 90 μm). The experimental data for all 12 coils are accurately matched by the analytic solution [254] to a 70-turn coil of 8.5 mm length, 7 mm inner diameter and 10.6 mm outer diameter. As illustrated by the residuals in Figure 4.12, the agreement between theory and experiment is so good that we can rule out any influence of the entering and exiting wires on the shape of the solenoid magnetic fields.

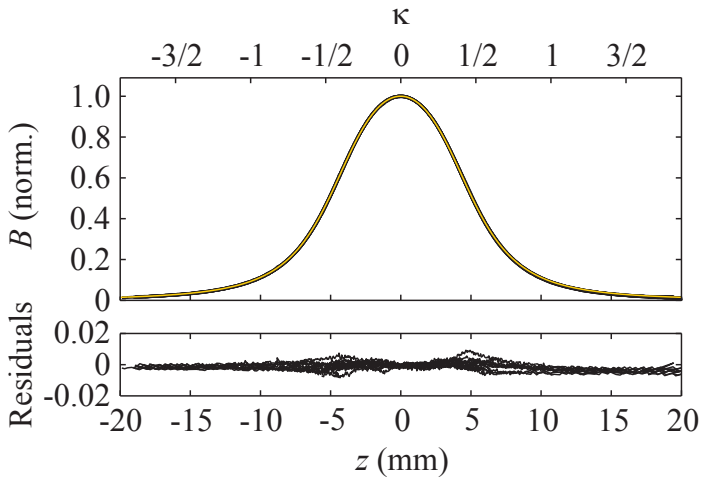

Figure 4.12: Top: On-axis magnetic field of each solenoid coil in the experiment measured with a Hall probe sensor (black curves) at 6 A DC. The analytical solution is shown as a yellow curve. The data are normalised and centred to the maximum magnetic field of each coil along the beam axis z. The abscissa on top of the graph gives a scale in terms of the reduced position κ which is used to define the switch-off time of a coil for Zeeman deceleration. Bottom: Residuals between measured data and theory.

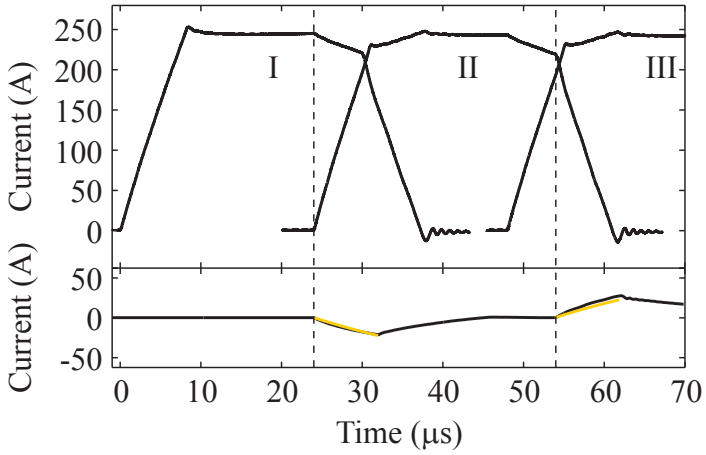

Figure 4.13: Temporal characteristics of the pulsed currents through coils I, II and III as measured with a current probe. Coil I is the first coil after the skimmer. Due to mutual inductance effects, the current through a coil is decreased when it is temporally overlapped with an adjacent coil. The oscillation at the end of each pulse is an artefact of the current-probe measurement [61]. The black curve in the lower part of the figure shows the current induced in coil I when coil II is pulsed (all other coils turned off). The induced current can be explained through RL circuit theory, as illustrated by the yellow curves.

As described by Wiederkehr et al. [61], the fast switching of currents is achieved with an electronic circuitry based on insulated-gate bipolar transistors (IGBT). Briefly, a high-

voltage power supply is used to obtain a rapid increase/decrease of the current (kick interval), while a constant current level is maintained via a low-voltage supply until the coil is switched off again (hold interval). The end of the kick phase and the current through a coil during the hold interval are determined by a comparator circuit which correlates the voltage drop through a shunt resistor with a preset value. In the experiments described in this thesis, we worked at a kick voltage of 800 V and a hold voltage of 110 V, giving rise to decelerator currents of $I = 243$ A during the hold interval and rise and fall times of 8 μs during the kick phase, as measured with a current probe (LeCroy CP500). Current pulses of adjacent coils were overlapped by 6 μs to prevent Majorana spin-flip transitions [60] during the deceleration process (see Section 5.3). Under these conditions, we observe additional cusps in the current profile that are caused by mutual inductance effects (see Figure 4.13). Using an LHC bridge, we measured a mutual inductance of $M = 2.8$ μH which is in accordance with the output of finite-elements calculations (FEMM 4.2 [290]). The lower part of Figure 4.13 shows the current induced in coil I when coil II is switched; the temporal behaviour of the induced current matches the switching times for coil II, as indicated by the dashed vertical lines. The induced current in coil I can be approximated by RL-circuit theory, thus yielding an exponential growth (yellow curves in Figure 4.13) with a characteristic time L/R and an amplitude MI/Rt_r, where t_r is the rise time.

Mutual inductance effects are intrinsic to every setup that consists of coils in close proximity whose currents are rapidly changed. The influence of mutual inductance can be reduced by increasing the coil distance, e.g. $M \approx 0.4$ μH at a centre-to-centre coil distance of 2 d. However, this would require longer switching times for the coils to prevent losses from Majorana transitions and cause a redistribution in phase space due to free flight, and it would also come at the expense of a much longer apparatus. Nonetheless, mutual inductance effects do not pose a major limitation on Zeeman deceleration. The cusps in the current profiles can be taken into account both in the generation of the pulse sequence for Zeeman deceleration and in the three-dimensional particle trajectory simulations. For a 6 μs pulse overlap, the current through a coil is about 10 % higher than its preset value, because it is still rising when the comparator circuit switches from the kick

to the hold interval. The change in current can be accounted for in the generation of the pulse sequences for Zeeman deceleration. Likewise, it is possible to adjust the reference voltage for each comparator to the output of a current probe, such that the current during the hold interval matches the current of the other coils.

4.5 Laser System

Sections 4.1.1 and 4.1.2 already give an account of the laser systems used for H atom and metastable atom deceleration experiments, respectively. In this Section, I will give a general overview of the atomic and molecular transitions observed with this experimental setup over the past four years, as they may become useful for future experiments. I have used these data for a calibration of the PDL-3 dye laser grating position to enable a more reliable search for other spectral features. I will also discuss the influence of laser energy on the observed spectral linewidths.

4.5.1 Observed Atomic and Molecular Transitions

Using REMPI spectroscopy, we were able to observe atomic and molecular transitions in ground-state H, Xe, Xe_2 and NH_3 as well as transitions originating from metastable states of He, N and Ar. Technical details of these measurements are summarised in Table 4.2.

Table 4.2: Observed atomic and molecular transitions and corresponding PDL-3 dye laser grating positions. In the Table, $\tilde{\nu}$ is the transition energy expressed in cm^{-1}, λ_{PDL3} denotes the PDL-3 dye laser fundamental wavelength (in vacuum) and g is the grating position.

Transition	$\tilde{\nu}$ (cm^{-1})	REMPI	λ_{PDL3} (nm)	g
$H(2s\ ^2S_{1/2} \leftarrow 1s\ ^2S_{1/2})$	82258.95 [246]	(2+1)[a]	486.27	24316.7
$Xe(5p^5(^2P^o_{3/2})6p,\ ^2[3/2],\ J=2$				

Continued on next page

Table 4.2 – continued

Transition	$\tilde{\nu}$ (cm^{-1})	REMPI	λ_{PDL3} (nm)	g
$\leftarrow 5p^6\ ^1\mathrm{S}_0$)	79212.47 [246]	(2+1)[a]	504.97	25254.0
Xe($5p^5(^2\mathrm{P}^{\mathrm{o}}_{3/2})6p$, $^2[1/2]$, $J=0$				
$\leftarrow 5p^6\ ^1\mathrm{S}_0$)	80118.96 [246]	(2+1)[a]	499.26	24967.2
$\mathrm{Xe}_2(0^+_g, v'=0 \leftarrow 0^+_g, v''=0)$	80046.14 [291][b]	(2+1)[a]	499.71	24990.3
$\mathrm{Xe}_2(0^+_g, v'=1 \leftarrow 0^+_g, v''=0)$	80064.39 [291][b]	(2+1)[a]	499.60	24984.4
$\mathrm{Xe}_2(0^+_g, v'=2 \leftarrow 0^+_g, v''=0)$	80081.64 [291][b]	(2+1)[a]	499.49	24978.7
$\mathrm{Xe}_2(0^+_g, v'=3 \leftarrow 0^+_g, v''=0)$	80099.11 [291][b]	(2+1)[a]	499.38	24973.6
$\mathrm{NH}_3^+(\tilde{\mathrm{X}}^2A''_2\ nf(0100)(1,0))$				
$\leftarrow \mathrm{NH}_3(\mathrm{X}^1A'_1(0000)(0,0))$	82320.0 [292]	(2+ai)[a,d]	485.91	24298.8
Ar($3s^23p^5(^2\mathrm{P}^{\mathrm{o}}_{3/2})5s$, $^2[3/2]^{\mathrm{o}}$, $J=1$				
$\leftarrow 3s^23p^5(^2\mathrm{P}^{\mathrm{o}}_{3/2})4s$, $^2[3/2]^{\mathrm{o}}$, $J=2$)	20499.50 [246]	(1+1)	487.82	24395.1
N($2s^22p^2(^3\mathrm{P})3p\ ^2\mathrm{S}^{\mathrm{o}}_{1/2}$				
$\leftarrow 2s^22p^3\ ^2\mathrm{D}^{\mathrm{o}}_{5/2}$)	74357.09 [246]	(2+1)[a]	537.94	26903.0
N($2s^22p^2(^3\mathrm{P})3p\ ^2\mathrm{S}^{\mathrm{o}}_{1/2}$				
$\leftarrow 2s^22p^3\ ^2\mathrm{D}^{\mathrm{o}}_{3/2}$)	74348.37 [246]	(2+1)[a]	538.01	26906.4
He($1s3p\ ^3\mathrm{P}^{\mathrm{o}}_{0,1,2} \leftarrow 1s2s\ ^3\mathrm{S}_1$)	25708.69 [246][c]	(1+1)	388.97	27237.1

[a] Frequency doubling of the dye laser output required.
[b] Transition frequencies are given as average values of the isotopomers observed by Dimov et. al. [291].
[c] Transition frequency is given as the average value of the three J states.
[d] ai = autoionisation.

Two-photon transitions in Xe and Xe_2 were used for an initial calibration of the dye laser grating position, and this calibration enabled a quick and efficient search for H atom REMPI signal at 243.13 nm. Earlier attempts with a pulsed wavemeter (WA-4500, Burleigh) were not successful, and it turned out that the calibration of the wavemeter was off by -0.32 nm at the dye laser fundamental wavelength of 486.27 nm.

To allow for a quick referencing of spectral lines and the corresponding grating positions, I have made a calibration using all the observed transitions listed in Table 4.2. As illustrated

in Figure 4.14, the laser wavelength follows a linear dependence on grating position over the entire wavelength range between 389 nm and 538 nm. Considering the larger deviation from the fit at 389 nm, linear regression to a smaller wavelength interval will give more accurate estimates of the grating position, especially between 486 nm and 505 nm.

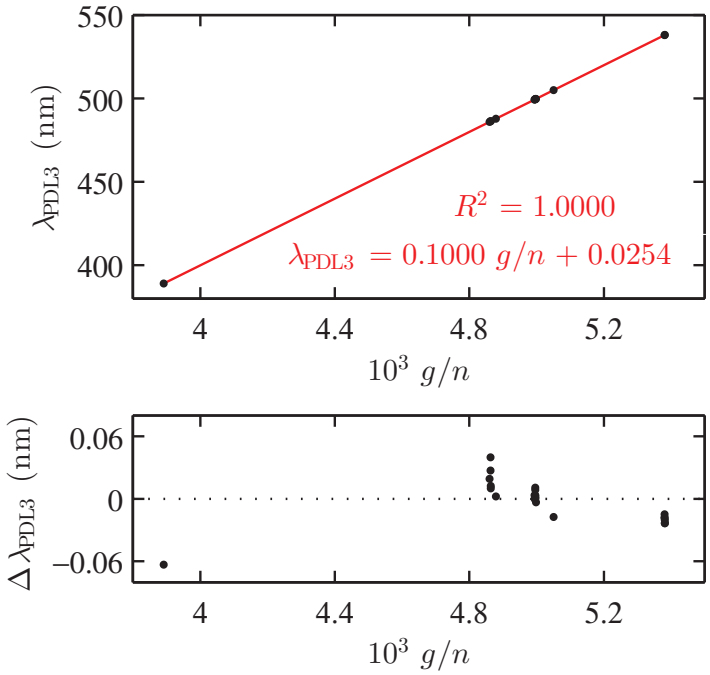

Figure 4.14: Calibration of the PDL-3 dye laser grating using the atomic and molecular transitions listed in Table 4.2. Top: PDL-3 dye laser fundamental wavelength, λ_{PDL3}, as a function of the ratio g/n, where g is the grating position and n is the grating order. A linear fit to the data is shown in red colour. Bottom: deviation of the observed PDL-3 dye laser wavelength from the linear fit.

4.5.2 Transition Linewidths

Figure 4.15a shows a two-photon spectrum of the $2s\ ^2\mathrm{S}_{1/2} \leftarrow 1s\ ^2\mathrm{S}_{1/2}$ transition in atomic hydrogen at 243.13 nm measured at a laser energy of 1.2 mJ/pulse. The relative laser frequencies were determined with a Burleigh WA-4500 wavemeter and the wavelength tuning was micro-stepper motor driven. In general, the implementation of a micro-stepper motor was crucial for the optimisation of signal intensity, since the scale on the grating wheel (0.2) is only accurate by 0.57 cm^{-1}, which is larger than the observed 0.44 cm^{-1}

full width at half maximum (FWHM) linewidth for this transition. Compared to that, one micro-step corresponds to a change of $3{\cdot}10^{-3}$ cm^{-1} and thus allows for a much more accurate positioning of the grating.

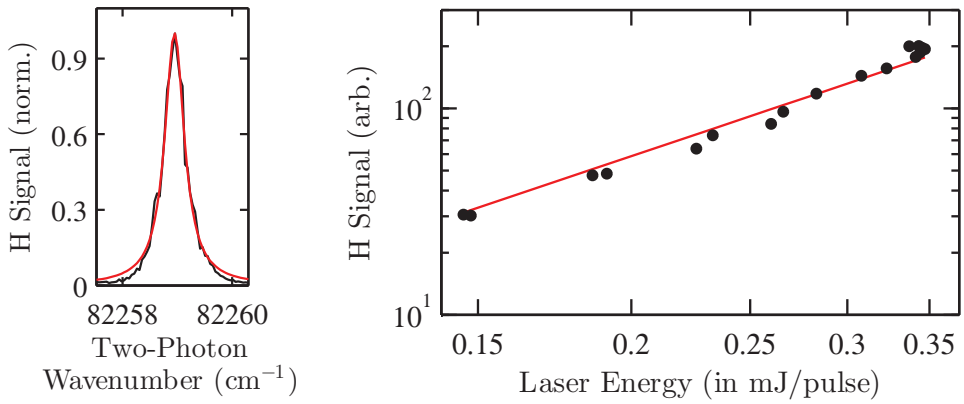

Figure 4.15: (a) Measured (2+1) REMPI spectrum of H($1^2S_{1/2}$) (black curve) at a laser energy of about 1.2 mJ/pulse and fit to a Lorentzian function (red curve). The use of a Lorentzian can be rationalised in terms of power broadening. (b) Log-log plot of the H atom signal intensity as a function of laser energy. The data are fit to a quadratic dependence on laser energy (red line).

The measured FWHM linewidth of the H line is many orders of magnitude broader than the natural linewidth of the transition (8.3 Hz) which is probably a consequence of several factors: power broadening caused by relatively high laser energies and tight focusing of the beam (f = 150 mm), the contribution of (broadband) amplified spontaneous emission (ASE) and the dye laser bandwidth. According to the instruction manual, the PDL-3 laser has a bandwidth of 0.05 cm^{-1} at λ = 500 nm [293], corresponding to approximately 0.21 cm^{-1} at 122 nm, while the contribution of ASE should, under these conditions, be less than 0.4 %. In the experiment, we typically see that ASE makes up about 1/3 of the 15 mJ/pulse dye laser energy and there is a fair chance that not all of the ASE is eliminated by frequency doubling. The observed REMPI spectrum is best fit with a Lorentzian function, which is the characteristic lineshape for power broadening [294].

Figure 4.15b shows results from an experiment, in which the energy dependence of the REMPI signal intensity was investigated. For this, the laser energy, E, was varied by

changing the Q-switch delay (maximum signal intensity at a Q-switch delay of 180 μs) and measured with an energy meter (Gentec-EO, QE12SP-S-MB-D0) after passage of the laser beam through the chamber. While an E^3 relationship would be expected for a two-photon resonant, three-photon ionisation scheme, the quadratic laser energy dependence, as shown with a red line in Figure 4.15b, implies that the ionisation step is already saturated under these experimental conditions [295, 296].

In the case of He(2^3S_1), measurements at two different laser energies clearly reveal the influence of power broadening on the transition linewidth. Here, a lowering of the laser energy from 8.0 mJ/pulse to 0.9 mJ/pulse goes along with an eightfold decrease in FWHM linewidth (from 47 cm^{-1} to about 6 cm^{-1}). Even at the lower laser energy, the linewidth of the He spectrum is much broader than in the H atom REMPI measurements. Similar observations were made by other authors [297–299] and ascribed to power broadening, resulting from the very strong one-photon transition to the 3^3P state (absorption cross section of $8.7 \cdot 10^{-18} cm^2 \approx \lambda^2$ [281]), and the fine-structure splitting of the resonant state. We also think that the contribution from broadband ASE is much more severe than in the case of atomic hydrogen, since there is no nonlinear crystal involved that could act as an efficient filter for the ASE noise.

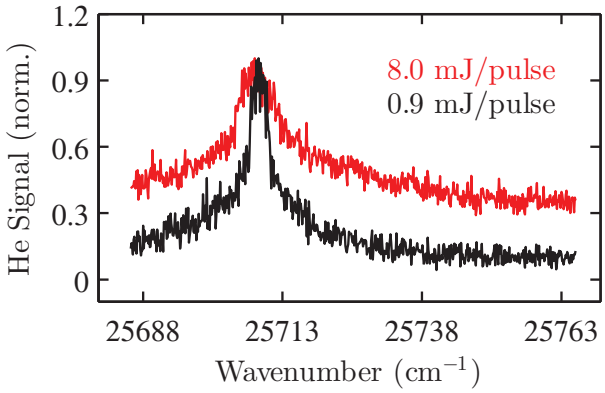

Figure 4.16: (1+1) REMPI spectrum of He(2^3S_1) at different laser energies as indicated in the legend.

The REMPI spectra for the two spin-orbit states of N(^{2}D) exhibit an asymmetric shape (Figure 4.17), whose origin is yet unclear, but could be related to an AC Stark shift in-

duced by the laser radiation [300]. If fit to Lorentzian functions, FWHM linewidths of about 0.7 cm^{-1} are obtained. The peak positions do not quite match with the literature data [246], which is probably due to the rough wavelength calibration to other atomic and molecular transitions observed with this laser system (see Section 4.5.1). A more accurate wavelength calibration could, for example, be achieved by referencing to an iodine vapour cell [301].

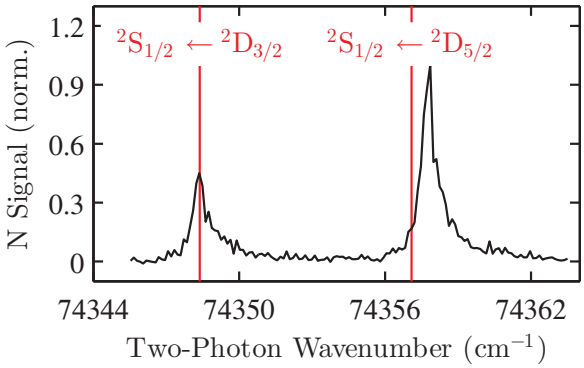

Figure 4.17: (2+1) REMPI spectrum of N($^2D_{3/2}$) and N($^2D_{5/2}$) at a laser energy of about 2.5 mJ/pulse (T_0 = 301 K, p_0 = 6.0 bar, U_{bias} = 150 V). Red vertical lines indicate literature line positions.

4.6 Ion Time-of-Flight Mass Spectrometer

For mass-selective ion detection, the already existing extraction stack has been extended to a Wiley-McLaren-type ion time-of-flight (TOF) mass spectrometer [302], consisting of three extraction plates (repeller, extractor and a grounded electrode) and an ion drift tube. A schematic drawing of the ion TOF spectrometer, along with dimensions and typical voltages used for the extraction plates and the MCP setup, is shown in Figure 4.18b.

The applied voltages have been adjusted to yield a strong ion signal and a good mass resolution. The anode is positively biased at 250 V to collect the electron avalanche from the MCP stack (Photonis, Chevron configuration, 25 mm working diameter). The MCPs can be gated with a home-built push-pull switch (maximum voltage difference of

1.5 kV) to suppress the amplification of unwanted laser light or ion signal[f]. MCP signal is increased with a fast bootstrap amplifier which allows for the detection of ion TOF traces with a FWHM as short as 5 ns. For the detection of metastable atoms and molecules, a charge amplifier is used instead. The electronics for both the charge amplifier and the MCP gating switch were devised by Hansjürg Schmutz (ETH Zürich).

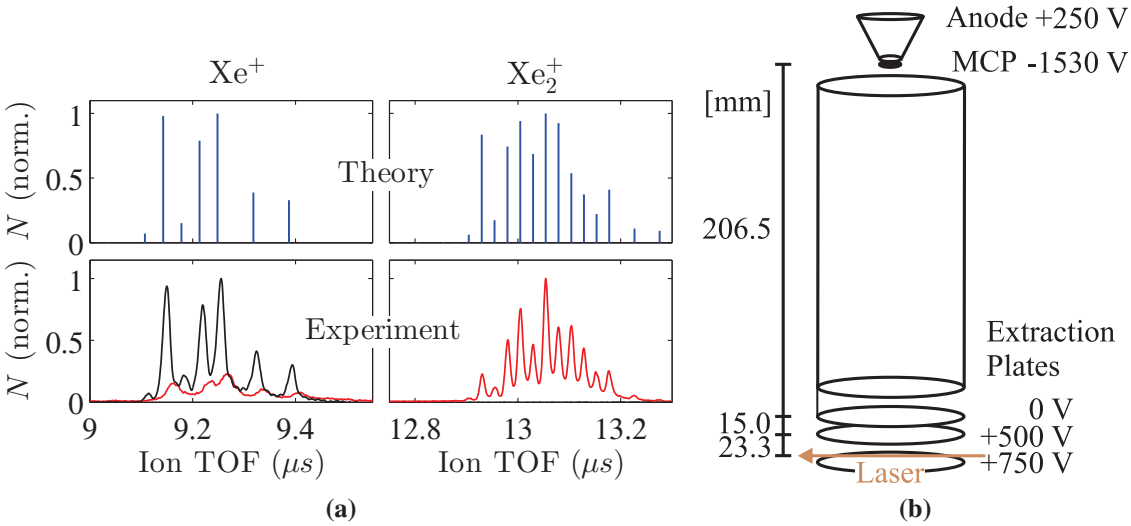

Figure 4.18: (a) Theoretical (top panel) and measured (bottom panel) ion TOF spectra of Xe^+ and Xe_2^+. The black (red) traces in the bottom panel were obtained by (2+1) REMPI detection of Xe (Xe_2) using the two-photon resonant transition at 80118.96 cm^{-1} (80081.64 cm^{-1}). (b) Schematic drawing of the ion TOF spectrometer (not to scale) including dimensions and typical voltages applied to the extraction plates and the MCP setup.

Figure 4.18a contrasts experimental Xe^+ and Xe_2^+ ion TOF traces (pure Xe, p_0 = 3 bar, T_0 = 302 K) with theoretical values obtained using the analytical formulas by Wiley and McLaren [302]. Xe_2 abundancies were calculated assuming natural abundancies for the different Xe isotopes [303] in the reservoir and equal binding energies for all the Xe_2 dimers, irrespective of their constituent isotope masses. Different transition and ionisation probabilities for the dimers are also disregarded. The Figure illustrates that the different Xe isotope and Xe_2 isotopomer ions are clearly resolved with this setup. The ion TOF positions are in excellent agreement with theory and, in the case of Xe^+, the ion peak

[f] A low-pass filter, connected to the MCP front plate for noise reduction, needs to be removed for this purpose.

intensities match the natural abundance of the Xe isotopes. The ion peak intensities for Xe_2^+ are somewhat different than expected from theory, which is likely due to the assumptions made in the calculation (see above). In the (2+1) REMPI detection of Xe_2, we also monitor Xe^+ monomers in the ion TOF traces (bottom left, red curve in Figure 4.18a). It is likely that excited states of Xe_2 dissociate to Xe monomers and are subsequently ionised [291]. This would also explain why the arrival times for these Xe^+ ions are delayed with respect to ion TOF traces for REMPI detection of Xe monomers (bottom left, black curve in Figure 4.18a).

Measured TOF data for other ions are also in perfect agreement with theory (Table 4.3). However, pulsing of the extraction plates appears to induce an additional delay of 100 ns, cf. Ar^+ data for continuous and pulsed extraction. The data presented here are also in good accordance with ion TOF calculations in SIMION 8.0 (not shown).

Table 4.3: Comparison of measured ion TOF data with theoretical values calculated using the formulas by Wiley and McLaren[302].

	Theory	Experiment	
Ion Species	TOF (μs)		Extraction Mode
He^+	1.63	1.61	continuous
N^+	3.04	3.01	continuous
Ar^+	5.13	5.09	continuous
Ar^+	5.23	5.09	pulsed
NH_3^+	3.45	3.32	pulsed
H^+	0.93	0.81	pulsed

4.7 Experiment Control and Data Acquisition

Since individual deceleration coils need to be addressed separately, a large number of trigger pulses is required to operate the experiment. While the Nd:YAG laser is triggered separately to ensure a constant 10 Hz repetition rate, a user-programmable pulse generator (PulseBlaster, SpinCore, PB24-100-32k) is used to control the timing of

- the pulsed valve
- the excimer laser / the electron gun pulser
- the digital oscilloscope
- the individual deceleration coils
- the extraction plate pulser
- the MCP gating and
- the microstepper motor for the PDL-3 grating.

A detailed trigger scheme for the experiment is given in Appendix 9. In short, an arbitrary waveform generator (RIGOL, DG1022) is used as a master clock to address an SRS DG535 pulse generator[g]. The DG535 sets the timing of the Nd:YAG laser flashlamps and Q-switch, and it serves as an external trigger to the PulseBlaster. Signals are acquired with an oscilloscope (LeCroy, Waverunner-2, LT262) that is either triggered by the PulseBlaster or by a fast photodiode (Thorlabs, DET10A/M) which detects stray light from the PDL-3 dye laser beam. To minimise jitter in the detected ion TOF traces, triggering by the PulseBlaster (photodiode) is used when the extraction plates are pulsed (running in a continuous mode). A graphical user interface (GUI, see Appendix 9) in MATLAB is used both for programming the PulseBlaster board and for data acquisition. GUI default settings (found in the file 'set_default_settings.m') are loaded at each start-up. Oscilloscope traces and settings as well as the GUI input parameters are saved with each output file (in .mat format).

[g] An irreparable electrical fault in this DG535 unit causes jitter between the output channels if triggered internally.

5 | Transverse Focusing Effects in the Zeeman Deceleration of H Atoms

5.1 Introduction

Research on cold chemistry and cold collisions would benefit from high number densities, as these would make experiments easier and less time-consuming to carry out. However, due to several different loss processes, the particle densities of decelerated beams are rather low, typically on the order of 10^9 molecules cm^{-3} or less [78]. The principal factors limiting the density are two-fold. First, a rapid reversal of the magnetic or electric field direction can cause Majorana transitions to high-field-seeking quantum states that are not decelerated [58, 273, 304, 305]. For Zeeman deceleration, these losses can be suppressed by temporally overlapping the current pulses of adjacent coils [273]. In a Stark decelerator, transitions to high-field-seeking states were circumvented by switching the decelerator electrodes between a high and a low electric field configuration, as opposed to turning off the electric field of an electrode pair after each deceleration step [304]. Nonadiabatic transitions in a chip-based Stark decelerator were reduced by applying a static offset magnetic field perpendicular to the electric field such that the energetic splitting between the hyperfine states at zero electric field was increased [305].

Second, longitudinal and transverse effects can reduce the phase space acceptance of a decelerator. Van de Meerakker and co-workers showed that an interplay between the longitudinal and transverse motion set limits to the efficiency of Stark deceleration [269]. Transverse effects, such as overfocusing, defocusing and insufficient transverse confinement, represent other important loss processes [269, 272]. Several strategies have been proposed and pursued to increase the particle flux. The transverse confinement was enhanced using novel types of decelerators that rely on co-moving magnetic or electric traps to confine and decelerate the particles [62, 70, 71, 74]. There has also been a proposal for

a quadrupole-guiding Stark decelerator, in which the longitudinal and the transverse motion are decoupled through the use of additional electrodes for transverse focusing [306]. Other approaches involve the use of higher-order modes for deceleration or the application of optimised pulse sequences based on evolutionary algorithms [269, 272]. There are also other losses related to mechanical heating [305] or the imperfect mechanical alignment of the deceleration stages [75], but those are specific to each decelerator setup.

In this Chapter, experiments are described demonstrating that the transverse confinement inside a Zeeman decelerator is increased by applying a low, anti-parallel magnetic field to one of the coils. Since the Zeeman deceleration of hydrogen atoms has been successfully demonstrated in previous studies [58, 60, 273, 307], this atomic species is chosen as a test system to elucidate these effects. The results are compared to three-dimensional numerical particle trajectory simulations, which also facilitate a more general understanding of the experimental findings.

5.2 Experimental

5.2.1 Transverse Focusing Experiments

In the experiments described here, eleven coils were operated with the decelerator electronics. One coil was disconnected from the decelerator circuitry and driven by another set of electronics that provided a comparably low current for an extended period of time ("quasi-static" operation). In the following, this coil will be referred to as the "focusing coil". For these electronics, the temporal current profile is described by an RL circuit with $R = 0.95\ \Omega$ for experiments with pulse durations of 600 μs, and $R = 3.15\ \Omega$ for measurements in which the delay of the focusing coil was scanned (pulse duration of 100 μs). The current rises/decays exponentially, with a characteristic time L/R and a current amplitude $I_{\mathrm{max}} \leq 60$ A. The higher resistance in the latter set of experiments was used to decrease the length of the trailing edges of the current pulse.

Most of the data were taken with coil VI for focusing, but coils I and XII were also used for comparison in a number of additional experiments (labelling the coils from I to XII in the order in which the beam passes through them). Typically, the current direction was the same for all coils. However, for some measurements, the direction of the quasi-static current was reversed, as denoted with a negative sign for the current of this coil.

All data were taken at a 10 Hz repetition rate and time-of-flight traces with and without magnetic fields were compared by alternating the applied field on and off on a shot-by-shot basis. For experiments with the focusing coil, a three-shot sequence was used to get a reference measurement in which current was only applied to the deceleration coils. The reference was recorded using the same time sequence for Zeeman deceleration to avoid changes in the TOF profile due to secondary effects caused by a change in decelerator timings.

In general, the data are very reproducible and have little noise. A complete TOF scan, as shown for example in Figure 5.3 (a), was usually completed within 20 minutes. Each data point typically corresponds to an average of 50 laser shots.

5.3 Results and Discussion

5.3.1 Interpretation of TOF Data

The operation of a Zeeman decelerator is based on phase stability, and the principles are similar to other supersonic beam deceleration techniques. Detailed descriptions of phase stability are, for example, given by Bethlem et al. [267] for Stark deceleration, and by Hogan et al. [60], Wiederkehr et al. [272] and in Chapter 3 of this thesis for Zeeman deceleration. Therefore, only a brief summary of the basic ideas and differences with respect to previous definitions are given here.

Zeeman deceleration exploits the interaction of paramagnetic atoms and molecules with time-varying, inhomogeneous magnetic fields. By successively switching high currents inside an array of solenoid coils, kinetic energy is converted into Zeeman energy, and permanently removed when a coil is switched off. The coil switching times are chosen such that a so-called "synchronous particle" has always moved by exactly one coil distance d in the time interval between one coil and the next being switched off. A range of other (non-synchronous) particles, which are further ahead or behind the synchronous particle, are decelerated as well. Faster particles move further into the solenoid magnetic field, and are therefore more strongly decelerated, while slower particles are decelerated less. Non-synchronous particles oscillate about the position and velocity of the synchronous particle, provided that they are within the phase-stable region of the decelerator.

By analogy with Stark deceleration and particle acceleration schemes, a reduced position $\kappa = z/d$ is used to describe the position of the synchronous particle relative to the centre of a coil (see Figure 4.12). The reduced position of the synchronous particle after the switch-off, i.e. when the decreasing current reaches zero, is denoted as κ_0. In previous studies on Stark and Zeeman deceleration, a phase angle ϕ_0 has been used to describe the operation of the decelerator, as in e.g. Wiederkehr et al. [272]. However, this notation is rather misleading in terms of Zeeman deceleration, because the shape of the on-axis potentials is not periodic thus resulting in non-zero deceleration at $\phi_0 = 0$ and counter-intuitive phase angles (< 0 or $> 2\ \pi$). The conversion between κ_0 and ϕ_0 is given by $\kappa_0 = \phi_0/\pi + vt_r/d - 1/2$. Due to the non-zero ramp time t_r, there is an explicit dependency on the velocity v of the synchronous particle. Hence, deceleration at constant κ_0 is not equivalent to operation at a constant phase angle ϕ_0. The phase-space model in Chapter 3 was developed after the experiments described here. Hence, all data in this Chapter were acquired using a constant κ_0.

The applied deceleration pulse sequence is calculated in a one-dimensional numerical trajectory simulation using the positions and velocities of the synchronous particle. In our case, this synchronous particle is a ground-state hydrogen atom in the low-field-seeking $M_F = 1$ Zeeman sublevel, where M_F denotes the projection of the total angular momentum

F onto the local magnetic field axis. The influence of the magnetic fields on the particles is monitored by their time of flight (TOF) through the apparatus. In the experiments, the time of flight of the hydrogen atoms is defined by the relative temporal delay between the excimer laser pulse for photolysis and the pulsed UV laser beam for photoionisation.

The TOF data are interpreted using numerical three-dimensional particle trajectory simulations. In the code, written in MATLAB and based on similar concepts to other programs [251], the geometry, timings and magnetic fields are matched as closely as possible to those in the experiment. A Monte-Carlo approach is used to select the initial positions and velocities of four million trajectories, with the particles equally distributed amongst the four Zeeman states (two high-field seeking and two low-field seeking) of H($1^2S_{1/2}$).

The hydrogen atom beam can be modeled as a supersonic jet with a Gaussian velocity distribution centred at an initial longitudinal velocity of 490 m/s. The beam velocity was derived by comparing peak positions of simulated and experimental TOF profiles for Zeeman deceleration at different switching times. Note that the mean velocity of the beam can be different from the selected initial velocity of the synchronous particle, v_0, that is used for the generation of the pulse sequence; for example, a below-average initial velocity may be selected to achieve a lower final velocity after deceleration. For the experiments described here, v_0 = 500 m/s is used. The transverse velocity distribution of the beam is modeled as a bivariate normal distribution centred at zero. The widths of the distributions are inferred from the longitudinal beam temperature, T_z, and the transverse beam temperature, T_r; neither of these temperatures were measured experimentally. However, the width of the TOF profiles gives a good estimate for T_z and, owing to the selectivity of the skimmer, the simulated TOF profiles are not markedly sensitive to T_r, even when the transverse temperature at the source is increased from 10 mK to 150 mK. In the simulations for these experiments, T_z = 1.1 K and T_r = 10 mK are used.

At a source temperature of 238 K, the initial beam velocity is about 150 m/s higher than the velocity of a pure supersonic jet of krypton atoms [243]. This indicates that, probably due to the large mismatch in mass between H and the Kr carrier gas, the excess

translational energy of the H atoms after 193 nm laser photolysis ($\approx$ 4500 cm^{-1}hc on average [250]) does not fully thermalise through collisions during the supersonic expansion. Related to that, the experimental TOF data could only be matched in simulations by assuming that the initial particle positions were uniformly distributed over a region equal to the length of the capillary, even though the photolysis laser beam is only 2.5 mm in diameter. The evolution of the supersonic expansion is also seen in a time delay after photolysis, which was experimentally determined as 31 μs, before the atoms emerge from the capillary.

The pulsed magnetic fields of the decelerator are modeled using analytical approximations to the observed current profiles and static magnetic fields (Figures 4.12 and 4.13). Particle positions and velocities are integrated at a numerical time step of 100 ns using the Velocity Verlet algorithm [262, 263]. Simulations at a 10 ns time step give very similar results, but come at the expense of computational time.

In Figure 5.1, the output of a three-dimensional numerical trajectory simulation for Zeeman deceleration from 500 m/s to 240 m/s at $\kappa_0 = 0$ is shown. The time-of-flight traces for deceleration are compared with the experimental data at the top of the figure, and have a rather complicated structure which is due to the complex particle motion inside the decelerator. The plots in (a) and (b) show the distributions of final and initial longitudinal velocities that lead to the time-of-flight signal above, respectively. As shown in (a), the peak at around 500 μs is due mainly to particles that are accelerated from 500 m/s to 600 m/s; the TOF signal at 680 μs originates from particles that are partly decelerated from 460 m/s to 370 m/s. Only the peak at an arrival time of 780 μs can be attributed to the particles fully decelerated to 240 m/s, with a minor contribution of particles travelling at a velocity of 370 m/s. The velocity distribution of the decelerated atoms is very narrow, with a half-width of approximately 20 m/s. As shown in (b), the fully decelerated particles originate almost exclusively from a velocity distribution of low-field-seeking particles centred at the selected velocity for the synchronous particle (500 m/s).

At the right-hand side of panel (a), the velocity distributions of particles in low-field-

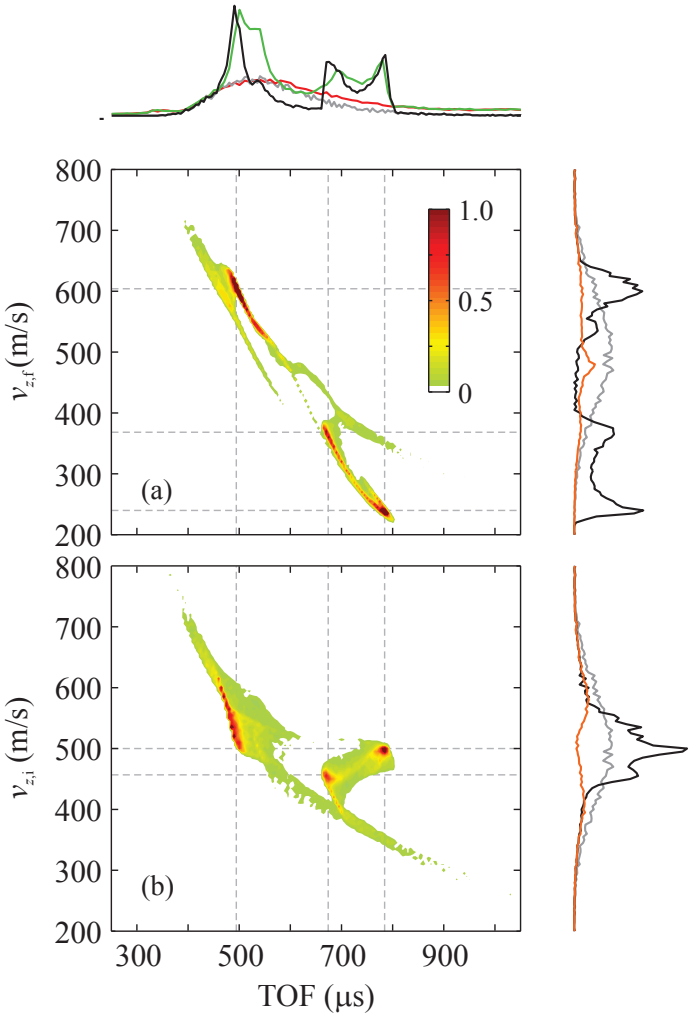

Figure 5.1: Zeeman deceleration of H($1^2S_{1/2}$) from 500 m/s to 240 m/s at $\kappa_0 = 0$. The focusing coil (coil VI) is not switched. Top: Experimental (green trace) and simulated (black trace) TOF profiles. Measured and calculated TOF traces without the influence of the decelerator magnetic fields are shown as red and grey curves, respectively. Density plot (a): simulated longitudinal particle velocities after deceleration, $v_{z,f}$, versus arrival time. Density plot (b): simulated initial longitudinal particle velocities of those trajectories arriving at a given TOF, $v_{z,i}$, versus TOF. Density scale for (a) and (b) in arbitrary units. Right: Distribution of longitudinal particle velocities before (bottom right) and after (top right) Zeeman deceleration subdivided into particles in low-field-seeking (black curves) and high-field-seeking states (orange curves). The particle velocity distributions without magnetic fields are given as grey curves for comparison. All plots are scaled with respect to the maximum TOF signal without deceleration (grey curve at the top). Note that only the velocities and arrival times of particles in the focus of the detection laser are taken into account.

seeking quantum states and high-field-seeking quantum states are plotted as black and orange curves, respectively. In the experiment, we cannot spectroscopically distinguish between the different quantum states, but the results from trajectory simulations strongly suggest that the number of transmitted high-field seekers is very small, confirming the good quantum-state selectivity of the deceleration process. Particles in high-field-seeking states are subject to forces opposite to those experienced by low-field seekers. Hence, their motion is not phase stable, and they are deflected towards the even-higher off-axis magnetic fields.

The agreement between theoretical and experimental TOF traces is very good. However, a higher signal level is measured in between the main peaks (from about 550 μs to 650 μs) than predicted by the simulation. This increase in signal could be a sign of population redistribution among the Zeeman sublevels, induced by Majorana spin-flip transitions [60]. Majorana losses are caused by a rapid reversal of the magnetic field direction, and may be driven by a current undershoot during the switch-off of a deceleration coil [61]. This argument is further supported by trajectory simulations in which state-to-state transition probabilities are included as a rough estimate of the contribution from Majorana spin-flip transitions during deceleration. As detailed in Section 2.2.6, the number of Majorana transitions in the simulation program depends both on the slew rate of the currents and the magnetic field undershoot, B_{crit}. From the rise and fall times of 8 μs at a current of 243 A, a slew rate of 0.2 T/μs can be derived. Under these conditions, a magnetic field undershoot of $\approx$ 75 mT was estimated from a measurement with a Hall probe sensor.

Figure 5.2 demonstrates that the signal intensity in between TOF peaks indeed increases if spin flips are taken into account, but the value B_{crit} = 300 mT, required to see a good agreement with experimental data (cf. 5.3 (g)), is much higher than the Hall probe estimate of 75 mT. In general, the overall fit to the TOF profiles was not improved, e.g. the additional peak at 600 μs is not observed in the experiment. The mismatch may be related to the inherent approximations in the spin-flip modelling and its implementation in the trajectory code. In any case, as detailed in Section 5.3.2, Majorana transitions do not appear to have a significant influence on the experimental results on transverse focusing

that are presented here, and the spin flip estimate was not used for data analysis to avoid any artifical bias.

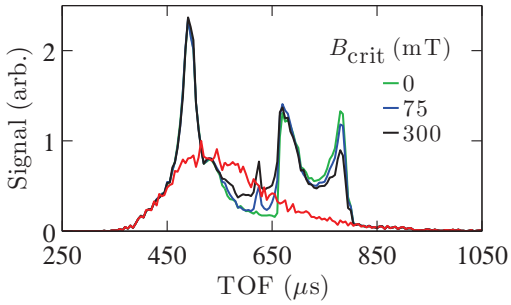

Figure 5.2: Simulated effect of Majorana transitions on the TOF profiles for Zeeman deceleration from 500 m/s to 240 m/s (κ_0 = 0) using 11 deceleration coils (coil VI not operated). The signal in between TOF peaks increases as the magnetic field undershoot, B_{crit}, is increased (see legend). The red curve show a trace in which no magnetic fields are applied to the decelerator.

The final velocity of the hydrogen atoms after Zeeman deceleration can be tuned by changing κ_0, as illustrated in Figure 5.3. As κ_0 is increased from -1 to 0, the decelerated peak is shifted to later arrival times which also corresponds to a decrease in final particle velocity from 490 m/s at κ_0 = -1 to 240 m/s at κ_0 = 0. At large positive κ_0, it is also possible to increase the particle velocity, e.g. at κ_0 = 2. In this case, an accelerating force is exerted onto the particles as they pass through the decreasing magnetic field of a coil (Figure 4.12).

The comparison between experiment and simulation in Figure 5.3 generally shows good agreement in terms of the positions, widths and relative intensities of peaks in the time-of-flight spectrum.

5.3.2 Transverse Focusing Experiments

In this Section, it is demonstrated that the transverse particle confinement in a Zeeman decelerator can be improved by applying a negative, quasi-static current to a coil that would otherwise be used for deceleration. This effect was studied using various experimental

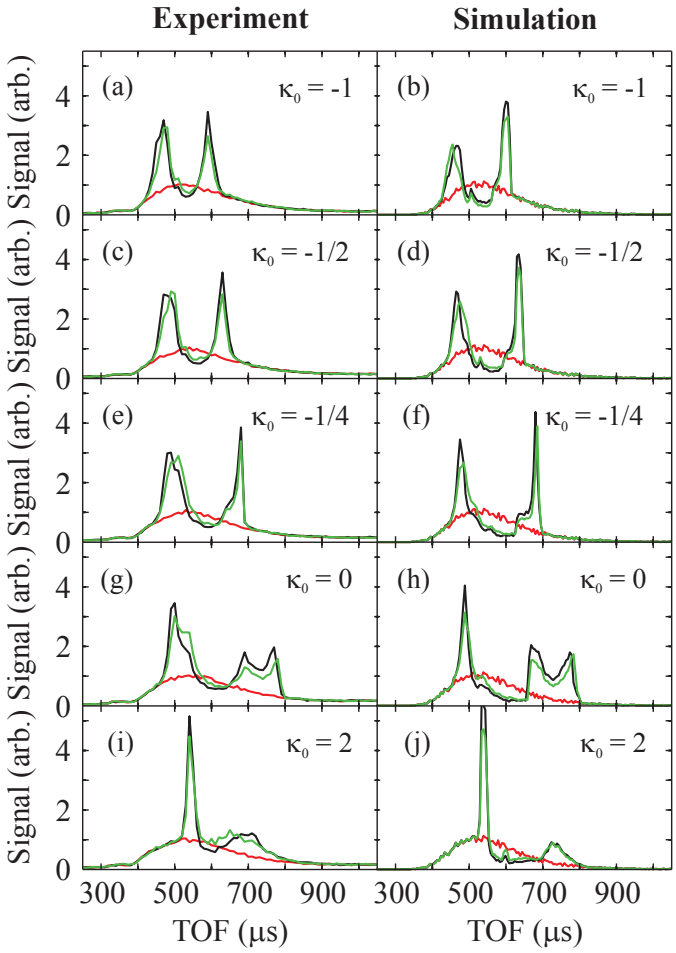

Figure 5.3: Experimental (left column) and simulated (right column) TOF profiles for Zeeman deceleration/acceleration of H($1^2S_{1/2}$) from 500 m/s to a range of different final velocities of the synchronous particle. In the green traces, only the deceleration coils are switched. For the TOF profiles in black colour, an additional current of -30 A is applied to the focusing coil (coil VI). The red curves correspond to traces in which no magnetic fields are present. The final velocities are: (a) and (b) 490 m/s (κ_0 = -1), (c) and (d) 440 m/s (κ_0 = -1/2), (e) and (f) 350 m/s (κ_0 = -1/4), (g) and (h) 240 m/s (κ_0 = 0), (i) and (j) 590 m/s (κ_0 = 2).

settings. In the following, the dependency of the signal enhancement on κ_0 and the influence of the magnitude and the direction of the applied quasi-static current is analysed. By varying the position and the switch-on time of the focusing coil, it is shown that the observed effects are indeed related to the action of this specific coil only.

As illustrated in Figure 5.3, there is an increase in signal intensity for all peaks in the TOF trace – typically 10–30 % of peak height – when a quasi-static current of -30 A

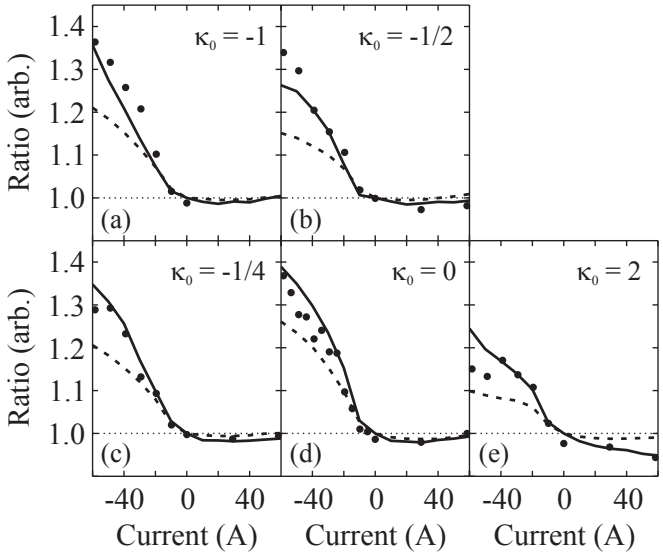

Figure 5.4: Change in decelerated hydrogen atom signal as a function of current applied to the focusing coil (coil VI). The ratio is derived from a comparison between the integrated signal with and without current through the focusing coil. Experimental data are shown as dots. Results from trajectory simulations are shown as solid and dashed lines. For the dashed lines, the ratio is obtained by counting all particles that pass through an imaginary detection area spanned by the *xy* plane perpendicular to the beam axis. For the solid lines, only particles in the focus of the laser beam (a cylinder of 0.5 mm diameter assumed) are taked into account.

is applied to coil VI (black traces). This effect is observed for all values of κ_0, and it is well reproduced by particle trajectory simulations. The signal increase becomes even more apparent in Figure 5.4, where currents of up to $\pm$60 A were used. For the largest negative values of the current, the integrated signal enhancement is 30–40 % for all κ_0 values in the range -1 to 0. In this figure, a signal ratio is plotted as a function of current applied to the focusing coil. The ratio is derived by comparing, on a shot-by-shot basis, the integrated signal within a specified time gate encompassing the decelerated peak in the TOF (see Figure 5.3) with and without current applied to coil VI. The outcome was checked using different widths and positions of the arrival-time gates for integration, and results were obtained that are very similar to those shown in Figure 5.4. Measurements were also carried out at zero current for the focusing coil, in which case we would expect a ratio of unity as the current is the same for both measurements. The observed deviation from 1.0 therefore gives a good estimate of the statistical error in the experiment.

Figure 5.4 illustrates that the spatial extent of the detection laser beam needs to be taken into account in the data analysis (solid lines) in order to see good agreement between experiment and simulation. The ratios obtained by taking into account all decelerated particles passing beyond the final stage of the decelerator (dashed lines) are too small to explain the signal gain observed in the experiment. Thus, the observed boost in signal has two origins: an increase in the overall number of decelerated particles transmitted through the decelerator, typically about 15–25 % at -60 A; and a stronger focusing of particles into the detection laser volume, which accounts for another 10–15 % increase in signal.

In general, the signal ratio increases as the magnitude of the negative current through coil VI is raised. On the other hand, there is no increase in signal if the current direction for the focusing coil is the same as for the deceleration coils. The observed trends can be explained by a change in the shape of the transverse magnetic field between coil VI and the adjacent deceleration coils. The anti-parallel currents generate quadrupole-like magnetic fields between coils V and VI and between coils VI and VII (see right column in Figure 5.6), which are more strongly focusing in the transverse beam direction than in the case of two deceleration coils with parallel currents. The quadrupole-like field is not generated if a positive current is applied to coil VI, hence there is no additional transverse confinement and no signal enhancement.

The complex interplay between the magnetic fields and the motion of the particles in the Zeeman decelerator makes it difficult to find simple physical explanations for differences in the signal ratios for the different values of κ_0 shown in Figure 5.4. Much smaller ratios are observed for acceleration (κ_0 = 2), even though the average longitudinal and transverse confinement is comparable to other reduced positions, e.g. to deceleration at κ_0 = -1/2. The differences might be related to the different mode of operation (coil switched off when the synchronous particle is moving down the potential hill) which makes the transverse focusing with coil VI more effective for deceleration than for acceleration.

Time-of-flight profiles were also obtained when coils I and XII, rather than VI, were used for transverse focusing. At a focusing current of -30 A, an increase in the decelerated

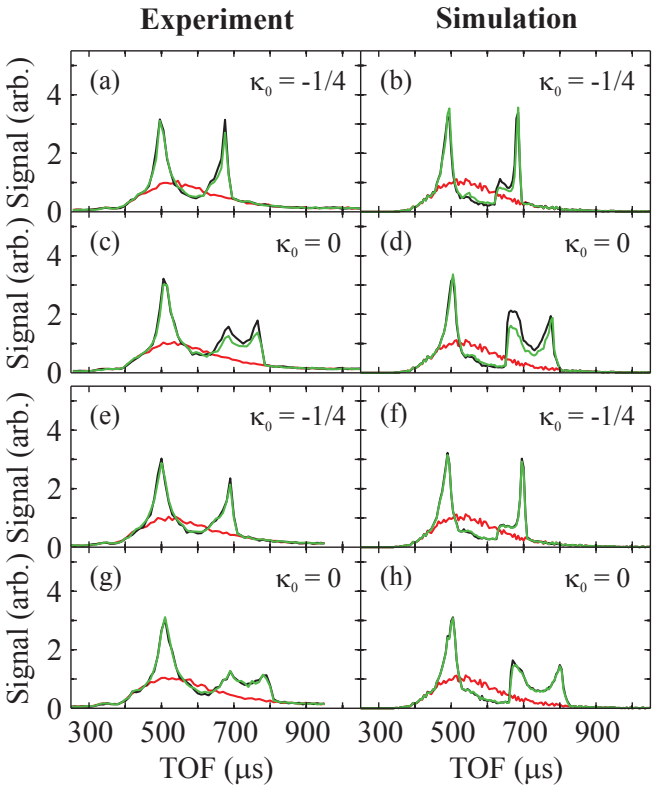

Figure 5.5: Experimental (left column) and simulated (right column) TOF profiles for Zeeman deceleration of H($1^2S_{1/2}$) from 500 m/s to 350 m/s (κ_0 = -1/4) and 240 m/s (κ_0 = 0) using coil I in (a)–(d) and coil XII in (e)–(h) at a current of -30 A to study transverse focusing effects. The colour code is the same as in Figure 5.3.

atom signal at κ_0 = -1/4 and 0 is observed when coil I is used for focusing (Figure 5.5). However, in contrast to the experiments with coil VI, there is no change in the signal intensity of the peak at 500 μs that can be assigned to accelerated hydrogen atoms. For coil XII, there is no noticeable change in the TOF traces. These effects can be understood in terms of the quadrupole magnetic fields in the transverse direction that are generated during the switching of a deceleration coil and the simultaneous operation of the focusing coil in a quasi-static mode, as illustrated in Figure 5.6 for focusing with coil VI. As the deceleration coils are successively pulsed, the position of the trapping minimum (enclosed by the blue contour lines) is shifted along the beam axis, in Figure 5.6 (e)→(h) from z = 136 mm to 158 mm. If current is applied to both coils V (or VII) and VI, the difference between the on-axis and off-axis magnetic fields, $\Delta B(r,z)$, is equal to 0.1 T (at r = 3 mm). For hydrogen atoms in low-field-seeking states, this magnetic field is already sufficient

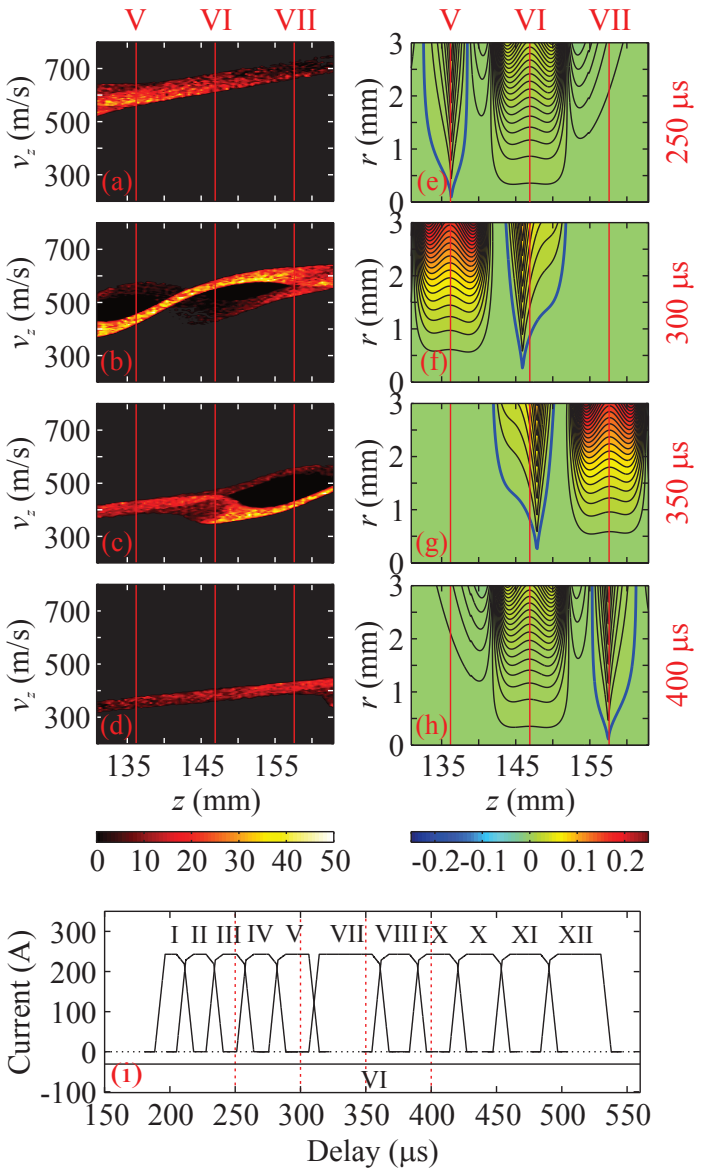

Figure 5.6: Left column (a)–(d): Snapshots of the simulated longitudinal particle velocities v_z along the beam axis z for Zeeman deceleration of H($1^2S_{1/2}$) at $\kappa_0 = 0$ using coil VI for transverse focusing. The snapshots are taken (a) 250 μs (during pulse III), (b) 300 μs (pulse V), (c) 350 μs (pulse VII) and (d) 400 μs (pulse IX) after the photolysis laser shot (times marked with dashed vertical lines in (i)). Only particles arriving in the detection region are plotted. Right column (e)–(h): Contour plots of the relative magnetic field $\Delta B(r,z) = B(r,z) - B(r = 0\ \text{mm}, z)$ (in T), where r is the transverse distance from the beam axis, given at the same times as in (a)–(d). The centre positions of the focusing coil and its neighbouring coils are indicated with red vertical lines. The extent of the focusing field is shown with blue contour lines. (i): Schematic current pulse sequences for the deceleration coils and the focusing coil. A current of -30 A is applied to coil VI for the entire duration of the deceleration pulse sequence (600 μs).

to confine particles with a transverse velocity of 35 m/s. Figure 5.6 also illustrates that the generation of transverse focusing fields is not restricted to neighbouring coils only. A small transverse magnetic trapping field of about 0.01 T – sufficiently high to confine hydrogen atoms with off-axis velocities of up to 11 m/s – is created even when the position of the focusing coil is further away from a deceleration coil, e.g. for coil III (as in (e)) or coil IX (as in (h)).

The additional transverse focusing fields at z = 136 mm in Figure 5.6 (f) and 158 mm in 5.6(g) stem from the switching of deceleration coils V and VII, respectively. The magnetic field in the centre of these coils is not seen by the decelerated particles, because each deceleration coil is turned off before the particles reach the coil centre in order to maintain longitudinal phase stability. However, the transverse magnetic fields in conjunction with coil VI are still present when the slowed particles pass through this region in the Zeeman decelerator.

As can be seen from Figure 5.6 (a), the magnetic focusing field generated by simultaneously switching focusing coil n and a deceleration coil $n-j$, where $j \geq 1$, has an effect on the fast-moving atoms only. At this time in the deceleration sequence, the slow atoms will not have reached the position of the quadrupole yet. Likewise, only the slow atoms will benefit from the quadrupole field between the focusing coil n and coils $n+j$ (Figure 5.6 (b)–(d)), since the fast atoms are already too far ahead in the Zeeman decelerator to be affected. In the case of coil I, there are no coils $n-j$; hence, when using I as the focusing coil, only the slow atoms can experience a focusing effect, and only an increase of the decelerated atom signal is observed. Likewise, there are no coils beyond coil XII, so that there is no transverse confinement for the slow atoms when this coil is used for focusing. In addition to that, the off-axis particles are already lost to the decelerator walls when reaching coil XII, so that the application of a focusing current to this coil has no effect at all.

Measurements in which the timing of the focusing coil is scanned relative to the start of the deceleration pulse sequence (Figure 5.7) further support these arguments. Here, the signal

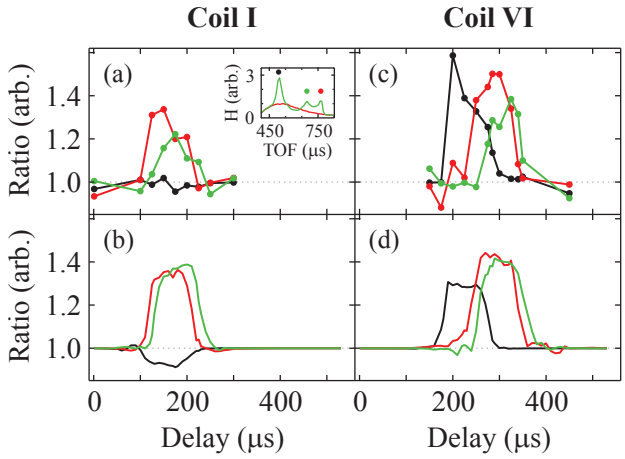

Figure 5.7: Scan of the trigger timing for the focusing coil with respect to the timing for the photolysis laser at $\kappa_0 = 0$ using coil I (left column) and coil VI (right column) for transverse focusing. In both experiments, the decelerator was pulsed at a current of 243 A and the focusing coil was switched at -30 A for a duration of 100 μs. (a) and (b): Experimentally observed change in signal intensity for three TOF peaks (510 μs, 670 μs, and 760 μs) upon pulsing of the focusing coil at different trigger delays between focusing coil and photolysis laser (dots). The solid lines are guides to the eye only. A reference TOF profile (no focusing current applied) is shown as an inset in (a). The TOF peaks used for the ratios are labeled with circles. The colour code of the circles is the same as in (a)-(d). (c) and (d): TOF signal ratios for the same settings obtained from particle trajectory simulations.

ratio was obtained from the intensity of three TOF peaks (marked with coloured dots in the inset of Figure 5.7) in toggling mode with and without focusing current. We observe a signal increase at earlier delay times for coil I than for coil VI, which is in accordance with the particle motion and the position of the coils inside the decelerator. We also see that the fast atoms are focused at earlier delays than the decelerated atoms, since they are further ahead in the decelerator, so that they experience the focusing fields at much earlier times. Both for coil I and coil VI, the peak of the partially decelerated atoms is increased at later delays than the peak that corresponds to the decelerated atoms. This may appear illogical at a first glance. However, as can be seen in Figure 5.1, the partially decelerated atoms have a lower initial velocity of 460 m/s, so that they are the last to move through the quadrupole focusing fields near coil I and coil VI, respectively. It is only in the last stages of the Zeeman decelerator that the partially decelerated atoms overtake the decelerated atoms due to their higher final velocity. The results from particle trajectory simulations

(Figure 5.7 (c) and (d)) are in excellent agreement with the experiment further supporting the conclusions that were drawn earlier.

Data at zero current for the focusing coil (Figure 5.5) show that both free flight through the focusing coil and Majorana spin-flip transitions do not have an impact on the experimental results. In this case, the focusing coil is not used for deceleration, so that there is an additional region of free flight for this coil. If free flight had any effect on the experimental results, the TOF profiles with coil VI held at zero current would show less signal than applying zero current to coil I or coil XII, because free flight in between two deceleration stages is more detrimental to the longitudinal phase space than at the beginning or at the end of the deceleration pulse sequence. The TOF traces in Figure 5.3 (coil VI) and Figure 5.5 (coils I and XII) look very similar when no current is applied for transverse confinement (green curves). Hence, we can rule out that the observed increase in signal intensity for a negative current to the focusing coil is merely due to a compensation of particle loss from free flight.

The potential influence of Majorana transitions on the shape of a TOF profile was described in Section 5.3.1. The use of a negative current for the focusing coils leads to the formation of quadrupole-like magnetic traps with a point of zero magnetic field along the beam axis. The resulting low magnetic field region does not substantially induce spin-flip transitions in the experiment. If Majorana transitions had a primary influence on these transverse focusing results, we would only be able to see these effects in the time-of-flight traces for coil VI. Assuming an equal distribution of quantum states after photolysis, spin flips in coil I would not cause a change in the quantum-state distribution. Likewise, coil XII is too close to the detection region to obtain a clear spatial separation of the high-field-seeking states that would cause a change in the TOF profile. The signal intensity of the decelerated atom peaks at 680 μs and 780 μs remains unchanged at zero focusing current confirming that Majorana losses are negligible. In any case, the good fit between experiment and simulations that do not include Majorana transitions, as shown in Figure 5.4, supports this argument.

5.4 Conclusions

Over the past decades, magnetic quadrupole fields have been commonly used to trap paramagnetic atoms, particularly in conjunction with laser cooling [11]. Quadrupole fields have also found applications in the area of Zeeman deceleration. The magnetic trapping of hydrogen and deuterium atoms after Zeeman deceleration was demonstrated by pulsing two solenoid coils in an anti-Helmholtz configuration at a current of 200 A [307, 308]. More recently, co-moving-trap Zeeman decelerators were developed in which the transverse confinement is either achieved using anti-Helmholtz coils [73, 74] or a magnetic quadrupole guide [62]. In comparison to the focusing experiments presented here, moving trap decelerators provide strong transverse confinement during the entire deceleration process. In the design from the Narevicius group [73, 74], transverse magnetic fields between 0.4 T and 1.2 T (at r = 5 mm) were generated using peak currents of up to 500 A. The quadrupole guide used by Trimeche et al. [62] was operated at 130 A, giving rise to a magnetic field of about 180 mT (at r = 0.6 mm). Moving-trap decelerators are advantageous for trapping experiments after deceleration, because virtually all particles with a transverse velocity component are captured. However, a large transverse velocity spread is usually not desired in collision experiments or spectroscopic applications.

In this Chapter, it was shown that the transverse acceptance in a Zeeman decelerator can be increased by applying a low current ($\leq$ 60 A) to one of twelve deceleration coils, provided that the current direction is opposite to the other coils. With only a minor change in the coil configuration, already a 40 % increase in the signal intensity on the beam axis was achieved. At the same time, it was demonstrated that the transverse focusing is much less effective when two adjacent coils carry currents in the same direction. This implies that optimum transverse focusing can be attained without having to generate strong transverse focusing fields on the entire length of the decelerator. The results suggest an alternative route towards attaining optimum transverse confinement, e.g. by inverting the current direction through every nth coil and pulsing it with a low, quasi-static current as described in this Chapter. Similarly, the use of inverted current pulses may be considered.

On the basis of simulations, I am convinced that more sophisticated focusing schemes will improve the transmission through the decelerator even further, and they can be used to tailor the height of the potential well in the transverse direction thus allowing for both trapping experiments and collision studies with the same device.

These results do not only indicate an increase in the overall number of particles at the end of the decelerator, but also a more effective focusing towards the beam axis. This may become useful in experiments in which beam overlap is of major importance, for example, in crossed-beam machines or in cold collision studies between decelerated molecules and laser-cooled ions which are spatially confined in a sub-millimeter volume inside an ion trap [217].

6 | Zeeman Deceleration of Light Metastable Atoms and Molecules

6.1 Introduction

Atoms and molecules in excited states are referred to as being 'metastable', when their tendency to return to the electronic ground state is strongly reduced, e.g. when electric dipole transitions to lower-lying states are formally forbidden. This results in natural lifetimes longer than 100 μs and thus allows for the study of metastables in time-of-flight experiments. In addition, atoms and molecules in these quantum states often possess one or more unpaired electron spins so that they become suitable systems of choice for Zeeman deceleration experiments. Comprehensive reviews on methods for the production and detection of metastable atoms and molecules are given by [248], Gay [245] and Hotop [309].

Radiative emission from metastable states is an important tool in astrophysics, e.g. to determine the temperature, density and chemical constituents of planetary atmospheres [231, 232]. Chemical reactions involving metastable species are often barrierless and exergonic, and are thus prevalent in diverse temperature and density regimes, where they are efficiently produced, e.g. by electron impact or charge transfer, such as in the Earth's upper atmosphere [228–230, 310], in the atmospheres of planets and their satellites [310] and in combustion and plasma processes [233, 234].

The experimental work described in this Chapter is primarily focused on two atoms in metastable states, N(^{2}D$_{3/2,5/2}$) and He(2^3S$_1$). In the Earth's upper atmosphere, N(^{2}D) and He(2^3S$_1$) are observed through their emission at 520 nm [311] and 1083 nm [312], respectively, with the N(^{2}D) emission – owing to the atom's high abundance – forming part of the visible aurora in the high-latitude regions of the Arctic and Antarctic. In this part of the atmosphere, these species are formed through collisions with photoelectrons and

participate in various (de-)excitation and ionisation cycles [313–315]. In this context, reactions with N(^{2}D) are of particular relevance, as they may be involved in the generation of other chemically active species like NO [314, 315], and there is strong evidence that N(^{2}D) also plays a significant role in the atmospheric chemistry of other planets [316, 317]. Furthermore, N(^{2}D) is an important partner in a number of chemical reactions relevant to air plasmas, including H_2O, NH_3 and O_2 [318, 319].

Table 6.1: Natural lifetimes and energies of metastable atoms and molecules relevant to this work. Values taken from [245] (and references therein) unless otherwise stated. Only excited states with lifetimes $\tau \geq 1$ ms are considered; the N($^2P_{1/2,3/2}$) state is omitted.

Metastable Species	Energy (eV)	Lifetime τ (s)	Primary Decay Process
H($2^2S_{1/2}$)	10.2 [246]	$122{\cdot}10^{-3}$ (T) [279]	2 x E1 to $1^2S_{1/2}$
$H_2(c^3\Pi_u)$	11.8	$1.02{\cdot}10^{-3}$ (E)	M1, E2 to $^3\Sigma_u^+$
He(2^3S_1)	19.8	7870 (E) [320]	M1 to 1^1S_0
He(2^1S_0)	20.6	$19.7{\cdot}10^{-3}$ (E)	2 x E1 to 1^1S_0
N($^2D_{5/2}$)	2.4 [246]	$1.52{\cdot}10^5$ (T) [321]	E2 to $^4S_{3/2}$
N($^2D_{3/2}$)	2.4 [246]	$6.25{\cdot}10^4$ (T) [321]	M1 to $^4S_{3/2}$
Ne(3^3P_2)	16.6	14.73 (E) [322]	M2 to 2^1S_0
Ne(3^3P_0)	16.7	430 (T)	M1 to 3^3P_1
$N_2(A^3\Sigma_u^+)$	6.2	1.27 for $\Sigma = 0$; 2.5 for $\Sigma = 1,-1$ (T) [323]	E1 to $X^1\Sigma_g^+$
Ar(4^3P_2)	11.5	38 (E)	M2 to 3^1S_0
Ar(4^3P_0)	11.7	44.9 (T)	M1 to 4^3P_1
Kr(5^3P_2)	9.9	39 (E) ; 28.3 (E) [324]	M2 to 4^1S_0
Kr(5^3P_0)	10.6	0.490 (T) [325]	M1 to 5^3P_1

E1 = electric dipole transitions, E2 = electric quadrupole transitions, M1 = magnetic dipole transitions , M2 = magnetic quadrupole transitions, E = experimental value, T = theoretical value, 2 x denotes two-photon transitions.

Originally, our experiments were aimed at the Zeeman deceleration of H_2 in the $c^3\Pi_u$ state, whose properties are still nearly unknown, even though ground-state molecular hy-

drogen belongs to one of the most well-understood systems from both experimental and theoretical perspectives. As the magnetic-moment-to-mass ratio of $H_2(c^3\Pi_u)$ is very similar to ground-state atomic hydrogen [326], it would have been an ideal target molecule for experiments with our 12-stage Zeeman decelerator. Unfortunately, we did not observe any evidence for metastable hydrogen molecule formation in our setup (see Section 6.2.1) and our experimental efforts were therefore directed to metastable He and N atoms. Nevertheless, over the course of this project, we were able to observe a whole range of different metastable species. Table 6.1 provides a list of energies and natural lifetimes of metastable atoms and molecules with potential relevance to this work. The properties of $H(2^2S_{1/2})$ are included owing to their relevance for the REMPI detection of ground-state atomic hydrogen.

6.2 Characterisation of the Metastable Source

This Section deals with the characterisation of the electron-impact source that was built as a part of this DPhil project. In the following, I will show that the system allows for the generation of a large range of metastable species, including metastable rare gas atoms and nitrogen molecules. I will also give a more detailed characterisation of the electron beam and provide evidence that metastable generation can be strongly increased upon application of a bias voltage to the pin. Through mixing with an appropriate carrier gas, this discharge-type mechanism can also be used to increase the production of metastable helium atoms (and possibly other metastable species), which are otherwise not affected by this process.

6.2.1 MCP Detection of Metastables

Owing to their high internal energy, many metastable atoms and molecules can be directly monitored through electron emission from an MCP detector, thus providing a more gen-

eral detection technique than, for example, laser techniques like REMPI. The detection of metastable atoms and molecules by Auger electron ejection from a metal-containing surface, such as an MCP detector, is possible if the particles' kinetic energy is above the work function Φ of the metal. For an MCP detector, $\Phi \approx 5.4$ eV (lead glass), so that all metastable species listed in Table 6.1, except for N(^{2}D), should induce such an emission signal. The mechanism responsible for electron emission involves the resonant ionisation of the metastable atom or molecule (RI), the subsequent neutralisation of the thus formed ion with an electron from the metal surface and the simultaneous ejection of another electron from the conduction band (Auger neutralisation, AN) [309].

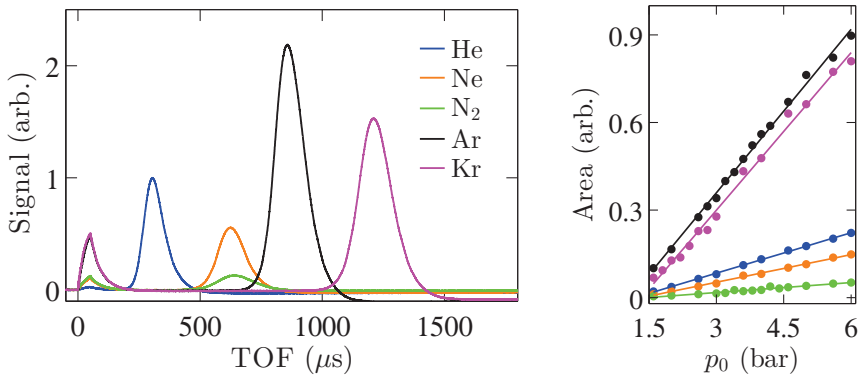

Figure 6.1: (a) TOF profiles of metastable rare gas atoms and molecular nitrogen (see legend, T_0 = 302 K and p_0 = 6.0 bar) from Auger electron detection on the MCPs (-1650 V). The peaks at early arrival time are from light emission during electron-impact excitation. Negative signal intensities are due to an artefact of the detection method (charge amplifier). The data are normalised to the metastable He signal intensity. (b) Change in integrated TOF signal as a function of source pressure; legend as in (a). Each data set is fitted with a linear regression. Pin grounded during the measurements.

Figure 6.1a shows time-of-flight (TOF) profiles of metastable rare gas atoms and molecular nitrogen obtained by electron-impact excitation and subsequent Auger electron detection on the MCPs. Here, the repeller and extractor plates (see Section 4.6) were set at constant voltages of 750 V and 500 V, respectively, to reject ions from impinging on the MCP surface. The total flight path between the excitation region and the detector is the same as in the REMPI measurements, i.e. the particles always pass through the Zeeman decelerator (not operated here) and the Wiley-McLaren-type ion-TOF setup before detection

(overall distance ≈ 500 mm). As discussed in Section 2.1, the measured beam velocities are in good agreement with theoretical estimates. Unfortunately, this type of measurement does not provide information about the individual metastable states generated during electron impact. However, it is very likely that particular states are predominantly produced during the excitation process [327]. In addition to that, the signal intensities for different species can hardly be compared directly even though they were acquired under similar source conditions (kinetic energy of 100 eV, Δt_e = 50 μs). Such an analysis would have to take into account the different cross sections for electron-impact excitation [280], the population ratios for different metastable states of one atom or molecule [327] and the individual metastable detection efficiencies of the MCPs. Other uncertainties arise from the transverse divergence of the supersonic beams during time-of-flight and the possible deflection of light metastables, such as He, by the electron beam [328].

The integrated TOF data for the same gases follow a linear dependence with respect to source pressure (Figure 6.1b) which can be rationalised through the larger number of atoms/molecules available for excitation towards higher pressures. However, the fitted lines have different slopes indicating that mechanisms like excitation and charge transfer may also be important for the excitation process.

Under similar conditions, no TOF signal from metastable H_2, HD and D_2 was observed on the MCPs (not shown), even though the electron-impact excitation cross sections to the $c^3\Pi_u$ state are comparable with those for the rare gases [329] and the excited-state energy should be more than sufficient to allow for Auger electron emission. It was also surprising to see that, except for an emission signal at early arrival times, there was not even a signal that could have been attributed to other metastable species, such as metastable H atoms produced via dissociative excitation [330]. State-selective laser detection of metastable H_2 using a (1+1) REMPI scheme via the $p^3\Sigma_g^+$ state (444.88 nm) or the $r^3\Pi_g$ state (441.35 nm) [331] was also attempted without success. Several reasons may be considered for the lack of signal, including a rather low electron beam current, the rapid collisional quenching of metastable H_2 by ground-state H_2 [332, 333], the deflection of metastables during electron impact (following similar arguments as for He [328, 334]) and

the population of many ro-vibrational levels, of which only a few are long-lived enough to be detected through TOF measurements [335–337].

6.2.1.1 Near-Threshold Excitation of Metastable Helium

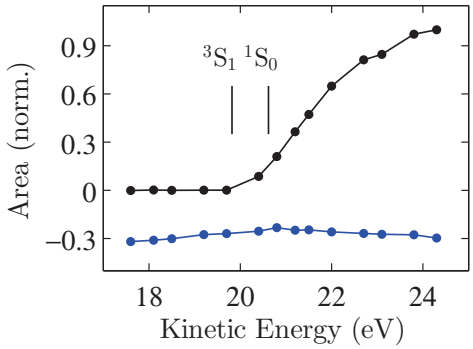

Figure 6.2: Electron-impact excitation of metastable helium atoms near threshold (T_0 = 300 K and p_0 = 6.0 bar). The black curve shows a normalised trace of the integrated MCP signal intensity as a function of kinetic energy for electron impact. The energetic thresholds for excitation into the metastable 2^3S_1 and 2^1S_0 states [246] are indicated. The blue curve shows the number of electrons measured at the pin in a control run after the threshold measurement (in units of 10^{10} electrons; U_{bias} = 5 V; pin grounded during threshold measurements). This curve is offset by -0.5 for reasons of visibility. The potentiometer settings for the kinetic energy were calibrated with a multimeter.

As detailed in Section 4.1.2, electron-impact excitation was typically carried out at a kinetic energy of 100 eV, as the electron emission currents under these conditions were much higher than at the energetic threshold. For metastable helium, a near-threshold measurement was done by scanning the electron kinetic energy over a short interval to avoid changes of the emission current (blue curve in Figure 6.2, signal optimisation at 21 eV). As can be seen from Figure 6.2, the integrated MCP signal intensity clearly increases just above the threshold for the metastable 2^3S_1 state, confirming that the triplet state is indeed formed by electron impact in this setup. The experimental data are in good agreement with the literature results [338–340]. However, owing to the comparatively low energy resolution for the filament (0.6 eV), we are unable to resolve the structure seen by other groups, in particular the dip at the threshold for the $^1S_0$ state between 20.3 eV and 21.0 eV.

6.2.2 Transition from Electron-Impact to Discharge-Type Excitation

To increase the number of metastables for Zeeman deceleration experiments, a positively biased metal pin was mounted on the valve body with the aim to focus electrons into the flight path of the supersonic beam. The exact location of the pin is indicated in Figure 4.2a. Experimental data in Figure 6.3a indeed show that more electrons are attracted to the pin as the bias voltage, U_{bias}, is turned up (black dots). The experimental results were compared to electron trajectory simulations in SIMION 8.0 (cf., Figure 4.7). Simulations were run for a total of $1{\cdot}10^5$ particles using a realistic experimental geometry (through import of CAD drawings) and voltages as specified in Table 4.1 (deflector voltages set to zero). In accordance with the experiment, electrons do not leave the filament region if the Wehnelt cylinder is negatively biased at -4.7 V. To compare with the experimental results, trajectories are simulated at different bias voltages and the electrons striking the metal pin are counted. The simulation output, shown as a red curve in Figure 6.3a, is normalised to the experimental data.

At a bias voltage of 200 V, the simulation predicts that about 88 % of the electrons hit the pin. In agreement with the experiment, the number of electrons at the pin increases at higher electric bias fields. However, the experimental electron current rises much more rapidly than suggested by the trajectory calculation, in particular at low U_{bias}. This indicates that there are deflection losses, e.g. due to surface patch fields and stray magnetic fields, which are not taken into account in the simulation. Rough estimates in SIMION (not shown) suggest that even small magnetic fields of less than 1 mT, e.g. from magnetised ferromagnetic components inside the pulsed valve, are sufficient to significantly deflect the electron beam. At the same time, the spatial spread of the electron beam at the valve exit is predicted *not* to change as a function of bias voltage. The distribution of the electron beam in the yz plane (at the valve orifice) is shown in the inset of Figure 6.3b at U_{bias} = 0 V. The electron beam is very narrow, with a width of about 2 mm in both the y and the z dimension. Compared to that, the spatial distribution at U_{bias} = 150 V is shifted by about 1 mm in the z direction, but the general shape is maintained (not shown).

The application of a bias voltage comes at the expense of a much broader electron kinetic energy distribution (see Figure 6.3b) than in the field-free case, from a simulated FWHM of 0.4 eV (same as SIMION input) at 0 V to about 20 eV at 150 V; the total number of electrons is nearly the same at both voltages. However, this broader kinetic energy distribution is not reflected in the properties of the supersonic beam, i.e. the measured beam velocities and temperatures are unchanged.

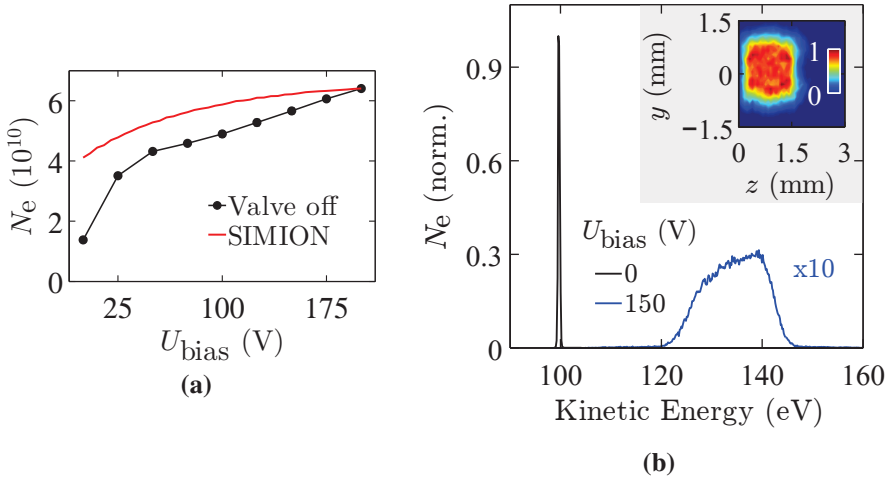

Figure 6.3: (a) Number of electrons per pulse, N_e, derived from a measurement of the electron current at the pin, as a function of bias voltage, U_{bias} (black dots). The pulsed valve is not operated. Results from a SIMION simulation (red curve) are normalised to the maximum of the experimental data. (b) Simulated kinetic energy distribution in the yz plane ($x = 0$, valve exit at $z = 0$ mm) for $U_{bias} = 0$ V and 150 V as indicated in the legend (150 V data scaled up by a factor of 10). The inset shows the spatial distribution of electrons at $U_{bias} = 0$ V in the same plane.

Even though the SIMION simulations predict that the spatial extent of the electron beam is unchanged in the excitation region, we *do* observe a huge increase in metastable production for certain gases if a bias voltage is applied during electron-impact excitation. Figure 6.4a shows that the MCP signal intensities for N_2, Ar and Kr linearly increase as a function of bias voltage, and the gain amounts to more than an order of magnitude at $U_{bias} = 200$ V as compared to $U_{bias} = 0$ V. There also seems to be a threshold for this process to happen, as indicated for N_2 in the inset to the figure. In contrast to that, the signal intensities for He and Ne remain unchanged throughout. The observed signal characteristics also correlate with higher electron currents at the pin (Figure 4.8a) and an increase

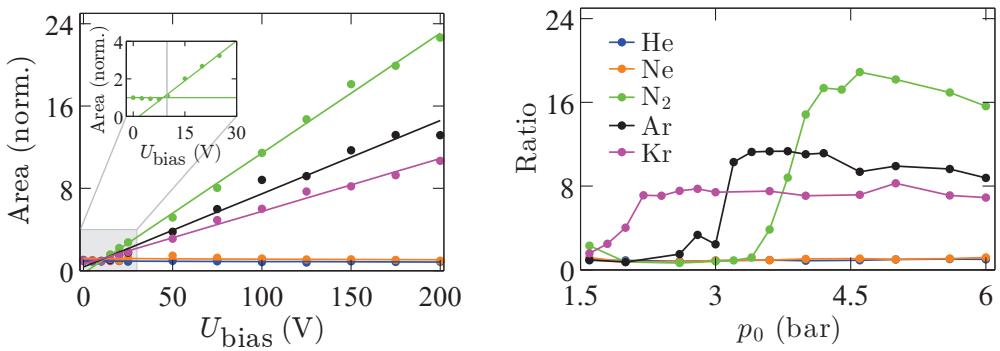

Figure 6.4: (a) Change of integrated MCP signal intensity as a function of bias voltage for different gases (same legend as in (b), T_0 = 301 K and p_0 = 5.6 bar) and linear fits. The onset of the signal increase for N_2 is shown in the inset; the N–N bond-dissociation energy (in eV) is marked with a grey vertical line. The MCP voltage was set to -1650 V for He and Ne and -1530 V for the other gases. Signals are normalised to the results obtained at U_{bias} = 0 V. (b) Ratio of the integrated MCP signal intensity with and without a 150 V bias voltage as a function of source pressure.

in light emission during the excitation process (recorded on the MCPs).

Figure 6.4b highlights the change of integrated MCP signals upon application of a 150 V bias voltage as a function of source pressure. Here, signals are shown as ratios with and without 150 V bias voltage to cancel out the pressure dependence at zero bias voltage (cf. Figure 6.1b). While there is no change in He and Ne ratios, the signals for N_2, Ar and Kr increase very suddenly at certain source pressures and remain, more or less, constant at higher pressures.

Both the threshold behaviour for the bias voltage and the step-like increase in signal at certain source pressures are strong indicators for an electrical breakdown that is typical of a gas discharge, i.e. the generation of an avalanche of charged particles initiated by an electrical current. In principle, there are three main criteria that determine the occurrence of a gas discharge: (1) an initial spark that liberates free electrons which can travel between the cathode and the anode, (2) a sufficient secondary-electron energy to release more electrons from the gas, and (3) a critical gas density (or pressure) to allow for sufficient electron-atom/molecule collisions so that more and more secondary electrons and

charged particles are created (avalanche process). In our case, condition (1) is fulfilled as soon as electrons from the electron gun reach the valve region. Then, the bias voltage applied to the pin only needs to be sufficiently high so that secondary electrons can be produced, i.e. U_{bias} needs to be above the ionisation threshold for the gas (Table 6.2). As highlighted in Figure 6.4a, this characteristic feature is indeed observed for Ar and Kr. In the case of N_2, the avalanche process is already initiated at lower bias voltages (inset in Figure 6.4a). At the time of writing, the exact cause for this is unclear. It may be related to the dissociation of the N–N bond, whose bond-dissociation energy is around 9.8 eV [341] .

The critical pressure for an electrical breakdown (condition (3)) can be estimated from Paschen's law, which describes the relationship between pressure, electrode separation d_{e} and applied voltage U_{crit} that must be met in order to initiate a gas breakdown, i.e. the sparking of an electrical discharge in a gas [342],

$$U_{\mathrm{crit}} = \frac{B p_0 d_{\mathrm{e}}}{\ln\left(A p_0 d_{\mathrm{e}}\right) - \ln\left(\ln\left(1 + 1/\gamma_{\mathrm{se}}\right)\right)}. \tag{6.1}$$

Here, A and B are the Paschen coefficients and γ_{se} is the second Townsend coefficient, i.e. the probability for secondary electron emission. As a first approximation, we assume that the pressure in the discharge region is similar to the source pressure, p_0, for the supersonic expansion. The second Townsend coefficient can be approximated (50 % accuracy) as [343]

$$\gamma_{\mathrm{se}} = \frac{0.016}{\mathrm{eV}} \left(IE - 2\Phi\right), \tag{6.2}$$

where IE is the ionisation energy of the gas and Φ is the work function of the cathode. Here, we use Φ = 2.6 eV, which is the work function of the yttria-coated iridium filament for the electron gun (see spec sheet from Kimball Physics). Paschen coefficients and ionisation energies for the gases relevant to this work are summarised in Table 6.2.

One characteristic of a Paschen curve is an asymptotic increase in the breakdown voltage. From Eq. 6.2, it can be obtained as

$$p(U_{\mathrm{crit}} \to \infty) = \frac{\ln(1+1/\gamma_{\mathrm{se}})}{A d_{\mathrm{e}}}. \tag{6.3}$$

Figure 6.5 illustrates Paschen curves and asymptotes for the gases used in the experiment. In this case, d_{e}, is used as a (constant) parameter and should not be interpreted as an 'electrode gap'. It was set to a value of 460 nm, so that the asymptote for Ar coincides with the experimentally observed, sudden increase in signal intensity (Figure 6.4b). Owing to the presence of an external electron source, the experimentally observed minimum of the breakdown voltage is much lower than in Figure 6.5. In the calculation, neither the inhomogeneous density distribution in the source region nor the inhomogeneous electric field at the pin are taken into account. Nevertheless, the relative positions of the asymptotes for the different gases, $p(\mathrm{Kr}) < p(\mathrm{Ar}) < p(\mathrm{N_2})$, are in remarkable agreement with the experimental results shown in Figure 6.4b. In addition to that, Paschen's law predicts that the critical pressure for an electrical breakdown in He and Ne is higher than the maximum pressure studied in the experiment, and thus provides a sound explanation for the lack of discharge characteristics seen for these gases. Figure 6.5 also highlights the expected discharge behaviour for H_2. As for He and Ne, the critical pressure is predicted to be very high, and probably not feasible with the present experimental setup.

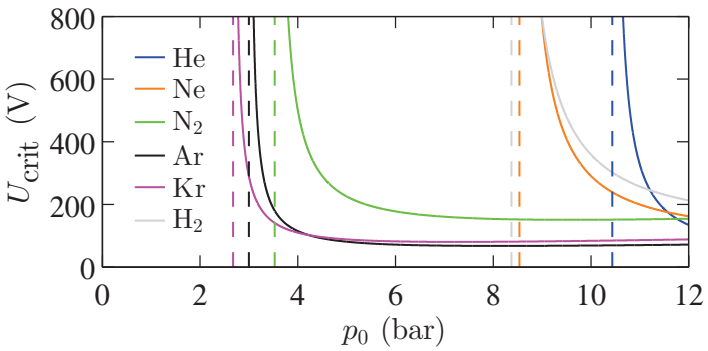

Figure 6.5: Paschen curves for the gases used in the experiment (solid lines). Dashed lines indicate the asymptotes at which $U_{\mathrm{crit}} \to \infty$. The value for d_{e} was set to 460 nm.

A more descriptive picture of the critical pressure required for an electrical breakdown in a gas may be obtained from the mean free path, l_f, i.e. the average distance travelled by a particle in between collisions. The mean free path is defined as $l_f = 1/(\sigma n_0) = 1/(\sqrt{2}\pi d_m^2 n_0)$ [344], where σ is the effective hard-sphere collision cross section, d_m is the molecular diameter and n_0 is the gas density in the source region (assuming that the discharge takes place very close to the valve exit). For a discharge to be efficient, a lot of collisions are required, so that we would expect l_f to be very small. Using the molecular diameters provided by McDaniel's book [344] and experimental conditions typical of the current experiments, the mean free path between collisions decreases in the order given by Table 6.2. The lowest values for l_f are calculated for Ar, Kr and N_2, which is again – albeit with a change of ordering – in very good agreement with the experimental observations.

Table 6.2: Mean free path, ionisation energy and Paschen coefficients for different gases. Molecular diameters for the calculation of the mean free path taken from McDaniel [344] and density obtained using the ideal gas law (p_0 = 5.6 bar, T_0 = 301 K).

Gas	He		Ne		H_2		Ar		N_2		Kr
l_f (nm)	35	>	25	>	22	>	13	>	12	>	10
IE (eV) [345]	24.6		21.6		15.4		15.8		15.6		14.0
A (Pa^{-1} m^{-1}) [342]	3		4		5.1		14		12		17
B (V Pa^{-1} m^{-1}) [342]	34		100		138.8		180		342		240

6.2.2.1 Implications for Metastable Nitrogen Production

The results discussed in the previous section provide strong evidence that the visible light emission highlighted in Figure 2.1 is due to a glow discharge in N_2 occuring at higher emission currents. However, the observed discharge mechanism does not only lead to an increased generation of metastable nitrogen molecules, but it also enhances the formation of N(^{2}D) atoms, as observed through an increase of the (2+1) REMPI signal at 269.97 nm (not shown). As the dynamics of a nitrogen discharge are utterly complex, it is not possible to pinpoint a specific mechanism for N(^{2}D) formation [346, 347]. How-

ever, electron-impact dissociation of N_2 [348] and dissociative recombination of N_2^+ [349] appear to be the most likely pathways.

Results from other studies indicate that the amount of ground-state nitrogen atoms ($^4S_{3/2}$), produced in a DC discharge, is more than two orders of magnitude higher as compared to N(^{2}D) [350, 351]. Since the ^{4}S state possesses a significant magnetic moment, it would also be an interesting system for Zeeman deceleration. The state-selective detection of ground-state atomic nitrogen could, for example, be attained in a (2+1) REMPI scheme via the $^4D_{7/2}$ state at 210.79 nm [352, 353][a]. On the other hand, it was found that the N(^{2}D) density in a discharge was significantly increased (^{4}S/^{2}D = 0.17) in N_2/He mixtures with a large excess of He, probably caused by energy transfer between metastable He and N_2 [350]. Supersonic beams of N_2/He mixtures will not have low-enough velocities for Zeeman deceleration in the current 12-coil setup, even if the valve body is cooled to liquid-nitrogen temperature. However, owing to the large excited-state energy of metastable Ne, similar energy transfer processes are expected to take place in N_2/Ne mixtures, and those experiments are therefore worth pursuing further.

6.2.2.2 Pathways to Increase the Formation of Helium in the Triplet State

The discharge mechanism laid out in Section 6.2.2 was also probed indirectly through measurements of different helium – carrier gas mixtures at a bias voltage of 150 V using state-selective REMPI detection of He(2^3S_1) (Section 4.1.2). As can be seen from Figure 6.6a, there is a sudden increase in signal intensity starting at a certain He/Ar and He/Kr mixing ratio. The measured signal for the gas mixture is even higher (by up to a factor of 6) than for pure He. A comparison with the results from Section 6.2.2 suggests that, at pressures $\geq$ 1.6 bar for Ar and $\geq$ 0.7 bar for Kr, a gas breakdown is initiated which releases an avalanche of secondary electrons, which in turn leads to an increased He(2^3S_1) signal. The critical pressure for the gas breakdown is lower than for the pure gases,

[a] The tuning range of the 56° BBO crystal (H atom experiments) is only 220.0 nm – 271.9 nm [354], so that we could not carry out this experiment.

because electronically excited He atoms can further promote the excitation and ionisation of the Ar and Kr gas particles.

The results for mixtures of He with Ne and H_2 further support these arguments. No discharge behaviour is observed for these gases. Instead, the integrated signal for He/Ne and He/H_2 mixtures decreases almost linearly as the He density in the mixture is lowered. This is in good agreement with other experimental results (Figure 6.1b) that show a linear dependence of the metastable signal on backing pressure, and this is generally what would be expected if we assume a linear dependence between metastable content and precursor gas density (black line in Figure 6.6a).

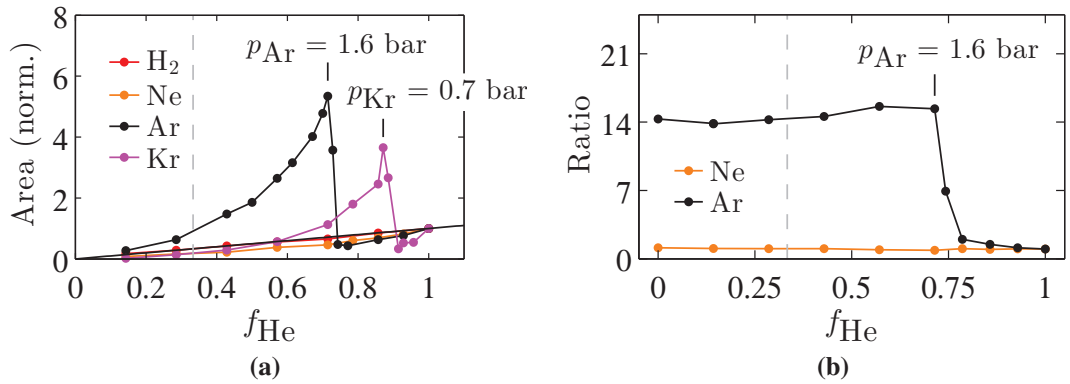

Figure 6.6: (a) Integrated He(2^3S_1) TOF signal intensity from (1+1) REMPI detection at 388.97 nm as a function of He fraction, f_{He}, in the initial gas mixture (see legend for carrier gas). The integrated signals for neat He beams (f_{He} = 1) are used for normalisation. U_{bias} = 150 V in all experiments. The black line indicates a linear decrease in signal intensity expected from a decrease in He concentration. (b) Ratio of the integrated MCP signal intensity with and without a 150 V bias voltage as a function of He concentration in the initial gas mixture. The He/Ar mixing ratio used in Zeeman deceleration experiments is indicated with a dashed grey line in both (a) and (b). Experimental conditions: T_0 = 302 K and p_0 = 5.6 bar, valve-to-electron gun trigger delay of 350 μs.

For He/Ar and He/Ne mixtures, we have also carried out TOF measurements using MCP detection. Figure 6.6b illustrates the ratio of the integrated MCP signal intensity with and without a 150 V bias voltage as a function of He content in the gas mixture. The results confirm the observations from the REMPI measurements, i.e. for the He/Ar mixture, a sudden increase in the signal ratio is observed at an Ar pressure of 1.6 bar, while there is

virtually no change in the signal ratio if Ne is used as a carrier gas. At Ar pressures above the 1.6 bar, the MCP signal ratio is constant, since the contributions from all metastable He and metastable Ar states are recorded simultaneously. It is thus also not possible to directly infer an increase in He(2^3S_1) flux from these measurements.

Owing to the high energy of He(2^3S_1) state (19.8 eV [246]), secondary electrons, released in Ar or Kr discharge processes, do not have sufficient energy to excite ground-state He atoms into a metastable level. However, He atoms in the metastable singlet state are very efficiently quenched into the metastable triplet state through collisions with thermal electrons [355]. As the cross section for the singlet-to-triplet conversion process is very high ($3{\cdot}10^{-14}$cm^2 [355]), this is probably the dominant process leading to the observed boost in He(2^3S_1) signal intensity. The results are also consistent with the generally high singlet-to-triplet He content observed for electron-impact sources, e.g. 2^1S_0:2^3S_1 = 7:1 for the source from Brutschy and Haberland [328]. In fact, this conversion process has been used in the past to ensure large triplet-to-singlet ratios in metastable He beams [356]. To confirm this mechanism, validation measurements could be carried out in which the signal intensity of He($^1S_0$) is determined, e.g. through a (1+1) REMPI via the 3^1P_1 state at 501.71 nm [297]. We should then observe a drop in signal intensity as soon as the discharge mechanism sets in.

The results in Figure 6.6a also illustrate that the He(2^3S_1) signal decreases nonlinearly as the Ar/Kr pressure in the mixture is increased. This process is not yet fully understood. It may be related to the deexcitation of He(2^3S_1) owing to the Penning ionisation of Ar/Kr [327] or it could be related to an increased transverse spreading of the beams due to lower beam velocities at higher carrier gas pressures.

He(2^3S_1) Zeeman deceleration experiments required a 1/3 He/Ar mixing ratio to attain an initial beam velocity of around 500 m/s. Under the experimental conditions chosen for the mixing ratio measurements in Figures 6.6a and 6.6b (p_0 = 5.6 bar), the signal enhancement from the discharge mechanism is only marginal (dashed grey line in Figures 6.6a and 6.6b). However, the signal gain can be easily increased by choosing a different

overall source pressure $p_0 = p_{Ar} + p_{He}$, e.g. p_{Ar} =2.5 bar and p_{He} =0.8 bar. To find optimum working conditions, the source pressure would have to be varied systematically at the chosen valve temperature. Unfortunately, we could not take full advantage of the discharge mechanism in the Zeeman deceleration experiments reported below, as we were not aware of the signal increase at the time these measurements were carried out.

6.2.3 Conclusions

To conclude, the application of a bias voltage to the pin *does* cause a very strong increase in metastable signal intensity when used for supersonic beams of N_2, Ar and Kr. However, the signal gain is *not* due to a focusing of the primary electron beam towards the centreline of the supersonic beam. Instead, a discharge-type process comes into play which leads to an increased formation of long- and short-lived excited-state species. Under the current experimental conditions, a gas breakdown cannot be induced in a pure supersonic beam of He atoms. However, as demonstrated above, the seeding in a carrier gas like Ar or Kr, which does show discharge behaviour under these experimental conditions, can significantly increase the formation of metastable He in the 2^3S_1 state through singlet-to-triplet conversion by secondary electrons.

The 1 mm diameter stainless steel pin used in the present setup generates a rather inhomogeneous field and was not designed with the purpose to create a discharge. It remains to be seen whether metastable production can be further increased by the use of a different anode material or a more homogeneous electric field, e.g. via a metal plate parallel to the electron gun. The combined electron-gun-discharge source produces not only more metastable species but also undesired ions and highly-excited species, and the signal intensities generally fluctuate more than with a normal electron-impact setup. It is thus important not only to improve metastable formation, but also to ensure the stable and reproducible operation of the source.

The injection seeding of a discharge with electrons – the opposite approach to what is

described here – has already been successfully used for the stable operation of an intense, pulsed metastable He source [299]. In retrospect, such a source would have probably been easier to construct and implement, and – considering the observed signal increase from the discharge mechanism – it may even be superior in terms of metastable flux. Nevertheless, it is not clear whether the Zeeman deceleration of He(2^3S_1) could actually be achieved using a more conventional discharge-type setup. In previous work with such a source [357], the metastable helium was entirely quenched upon dilution in a heavy carrier gas, possibly due to Penning ionisation processes. However, unless very low source temperatures are achieved (as in [66]), the seeding in a heavier carrier gas is a prerequisite for Zeeman deceleration experiments in order to decrease the initial velocity of the supersonic beam.

I hope that our findings can provide a more detailed understanding of the mechanisms that govern metastable formation in a combined electron-gun-discharge source, and may eventually lead to the development of even more intense sources of metastable atoms and molecules.

6.3 Zeeman Deceleration of Metastable Helium Atoms

The physical and chemical properties of metastable rare gas atoms are well-understood, as they have already been subject to numerous studies for many years. The advent of laser-cooling techniques has also enabled the cooling of metastable rare gases, including He(2^3S_1), down into the μK regime. A comprehensive review about the production and applications of metastable atoms in the field of ultracold atoms is given, for example, by Vassen et al. [358]. Even though we cannot reach μK temperatures with a Zeeman decelerator, we opted for He(2^3S_1), since its relatively high magnetic-moment-to-mass ratio and the comparably good signal intensities achieved make it a favourable test ground for Zeeman deceleration experiments in combination with our electron-impact source.

The experimental parameters used for Zeeman deceleration are similar to the previous studies on ground-state H atoms (Chapter 5). Here, all 12 deceleration coils are operated at a current of 243 A, resulting in rise and fall times of about 8 μs. Changes to the experimental setup used for H atom deceleration experiments are highlighted in Figure 4.1. To achieve supersonic beams with an initial velocity suitable for Zeeman deceleration, both cooling of the pulsed valve and seeding in Ar carrier gas is required. The state-selective detection of He(2^3S_1) is attained at the exit of the Zeeman decelerator using a (1+1) REMPI scheme at 388.97 nm. More details about the experimental settings are given in Section 4.1.2.

6.3.1 Phase-Space Matching

Compared to the Zeeman deceleration experiments with H atoms, the influence of the finite pulse duration for electron impact was one of the major questions to be addressed. While excimer laser photolysis of NH_3 typically generates H atoms in a time interval of about 10 ns, the pulse duration for an electron-impact source can be tuned over a wide range (Section 4.3.1), which offers the chance to completely fill the 6 D phase-space volume accepted by the Zeeman decelerator. However, it also introduces uncertainties arising from less well-defined source conditions, e.g. from the non-uniform pulse shape and the excitation in different parts of the initial gas pulse. In addition to that, the pulse duration for electron-impact excitation needs to be matched to the phase-space acceptance of the Zeeman decelerator to prevent the transmission of particles outside the accepted phase-space volume.

The effect of phase-space matching, i.e. the adjustment of the initial phase-space distribution of the beam to the phase-space acceptance of the decelerator, has already been investigated in the context of Stark deceleration and electrostatic trapping [268, 270, 359]. However, there has not been a systematic study on the width of the incoming particle distribution thus far. In discharge experiments with OH radicals, the use of longer pulse

durations also caused a broadening of the longitudinal velocity distribution and an increase in the measured rotational temperature of the OH beam, so that the group opted for very short excitation widths (2 μs) in general [360].

To characterise the system, Zeeman deceleration measurements were carried out at two different pulse durations for electron-impact excitation, 20 μs and 50 μs. Figure 6.7 contrasts the measured time-of-flight profiles (TOF) for Zeeman deceleration from an initial He(2^3S_1) velocity of 505 m/s to 590 m/s (top panel), 450 m/s (middle panel) and 390 m/s (bottom panel) and compares them with the output from 3 D particle trajectory simulations (Section 2.2.2). In this case, the time-of-flight is defined as the delay between the rising edge of the electron pulse and the detection laser beam.

The comparison with trajectory simulations suggests that the initial velocity distribution of the supersonic beam is centred at 520 m/s. Longitudinal and transverse temperatures of T_z = 0.7 K and T_r = 0.1 K are deduced from the shape of the TOF signal. The electron beam is assumed to have a 2 mm diameter; a value of 2.5 mm is chosen as the diameter of the detection laser beam. Several authors have calculated and experimentally demonstrated the deflection of metastable helium atoms in a electron impact transverse geometry [328, 334]. To account for such a deflection by the electron beam, the metastable He atoms are simulated with an additional off-axis velocity of 30 m/s. This value was not confirmed experimentally, but it tended to provide a better agreement with the experimental results.

Figure 6.7 clearly illustrates that the peak corresponding to the decelerated packet is shifted to later arrival times as the mean longitudinal acceleration, $\bar{a}_z/\bar{a}_{z,m}$, is set to more negative values, which is in accordance with the lower particle velocity. Compared to a pulse duration of 50 μs, the contrast between the decelerated and undecelerated parts of the beam is much more pronounced at the shorter, 20 μs pulse duration. This difference can be explained through a comparison with the longitudinal phase-space acceptance for Zeeman deceleration (see Section 3.2.1).

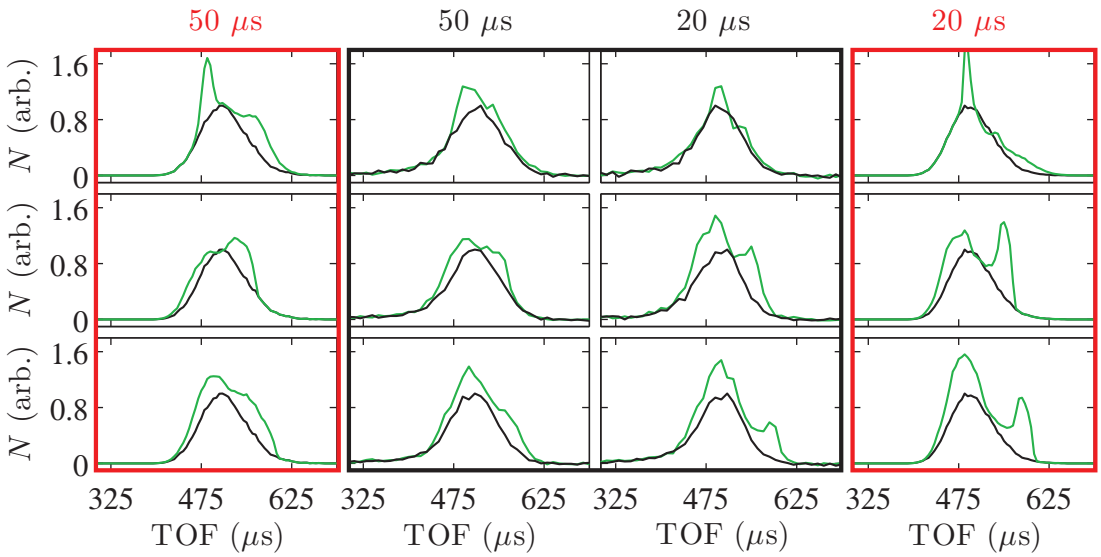

Figure 6.7: Experimental (black frame) and simulated (red frames) TOF traces for Zeeman deceleration/acceleration of He(2^3S_1) from 505 m/s to 590 m/s ($\bar{a}_z/\bar{a}_{z,m}$ = 1.0, top panel), 450 m/s ($\bar{a}_z/\bar{a}_{z,m}$ = -0.5, middle panel) and 390 m/s ($\bar{a}_z/\bar{a}_{z,m}$ = -1.0, bottom panel). Traces were taken on a two-shot basis (black traces: Zeeman decelerator off, green traces: Zeeman decelerator on) at pulse durations of 20 μs and 50 μs for the electron gun, as indicated above the figure. The black traces were used for normalisation. Here, $p_0 \approx 4.1$ bar, $T_0 = 143$ K.

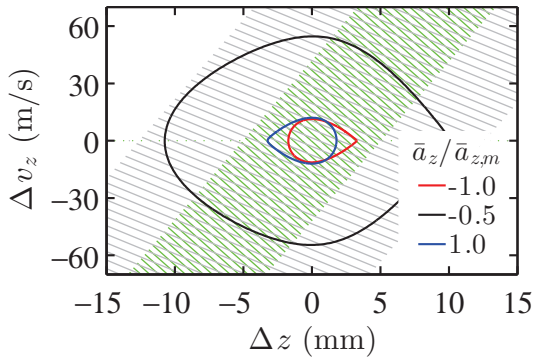

Figure 6.8: Separatrices in longitudinal phase space for the Zeeman deceleration of He($^3S_1$) at different mean longitudinal accelerations, $\bar{a}_z/\bar{a}_{z,m}$, as indicated in the legend. Green and grey hashes indicate the extent of the initial particle distributions expected for electron gun pulse durations of 20 μs and 50 μs after a flight time of 120 μs (approximate switch-on time for the first deceleration coil), respectively.

Figure 6.8 shows longitudinal separatrices, determined as outlined in Chapter 3, which would be expected for the chosen deceleration pulse sequences and compares them with the extent of the initial particle distributions, corresponding to electron gun pulse durations of 20 μs (green hashes) and 50 μs (grey hashes). The latter are shown at the

approximate switch-on time for the first deceleration coil, so that the distributions are tilted owing to free flight from the source region to the first deceleration coil. From the beam temperature, the longitudinal velocity distribution has a full-width-at-half maximum of about 87 m/s; the spatial spread should be approximately uniform (not shown in the figure). Figure 6.8 illustrates that the phase-space extent from a 50 μs electron pulse is much wider than the actual longitudinal acceptance of the Zeeman decelerator, especially at $|\bar{a}_z|/\bar{a}_{z,m} = 1.0$. While a long pulse duration ensures that virtually all particles in the phase-space region are addressed by the pulsed magnetic fields, it also causes the partial deceleration/acceleration of particles outside the accepted phase-space volume. As our Zeeman decelerator is relatively short, these particles can reach the detection region, causing an overall blurring of the decelerated signal (as seen in the TOF profiles in Figure 6.7), and a much broader velocity distribution than expected from phase-space calculations. These results show that, even though much higher metastable signal intensities can be achieved through longer pulse durations (cf. Figure 4.8b), the actual number of decelerated particles inside the phase-space volume is not increased any further. Both the peak positions and the peak shape of the TOF profiles obtained from trajectory simulations are in good agreement with the experimental results, and reflect the observed blurring of the signal at longer pulse durations. The effect of phase-space matching also becomes obvious when the incoupling time, i.e. the relative timing between electron-impact excitation and the beginning of the Zeeman deceleration sequence, is scanned (not shown). Experiments at even shorter pulse durations were not successful owing to very low signal intensities.

6.3.2 Experimental Limitations

Figure 6.9 shows an experimental and simulated TOF trace for the lowest velocity attained with the current setup. In this case, an initial velocity of 490 m/s was chosen for deceleration and a final velocity of 370 m/s was achieved, corresponding to a more than 40 % decrease of the particles' kinetic energy. The signal for the decelerated peak (at

610 μs, green trace) is clearly separated from the arrival times of the undecelerated beam (black trace). However, the attained signal intensity is rather low, because the selected velocity for deceleration is not in the centre of the initial velocity distribution (520 m/s). Again, the agreement with trajectory simulations is reasonable.

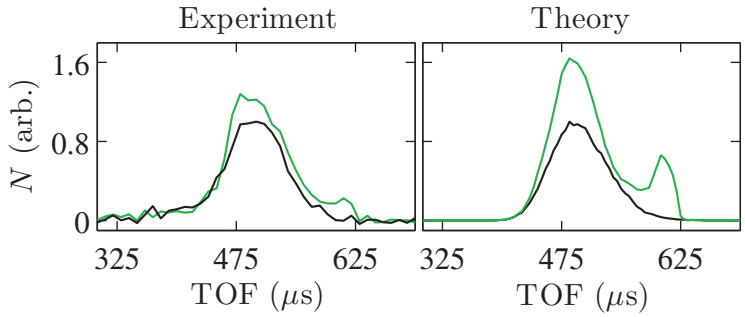

Figure 6.9: Experimental and simulated TOF traces for Zeeman deceleration of He(2^3S_1) from 490 m/s to 370 m/s ($\bar{a}_z/\bar{a}_{z,m}$ = -1.0). Colour code as in Figure 6.7. Traces were taken at a pulse duration of 20 μs for the electron gun. Here, p_0 = 5.4 bar, T_0 = 146 K.

In general, the level of agreement with trajectory simulations is not as good as for the H atom deceleration experiments. This is mainly due to the less well-defined characteristics of the initial supersonic beam, e.g. owing to the finite duration and the non-uniform shape of the electron-impact excitation pulse. Moreover, there are large uncertainties arising from the discharge-like excitation and the transverse geometry of the electron gun setup. In addition to that, the signals have a lot more noise, mainly due to the rather low metastable flux. Overall, the noise level arising from the instability of the electron impact source is not nearly as low as the shot-to-shot noise of the excimer laser for NH_3 photolysis.

6.3.3 Conclusions

The experiments presented here demonstrate that the velocity of He atoms in the 2^3S_1 can already be considerably reduced with a short 12-stage Zeeman decelerator. As far as we are aware, this is the first successful Zeeman deceleration experiment of metastable atomic helium. An extension of the existing setup to 30 deceleration stages would not

only allow for the Zeeman deceleration of He(2^3S_1) to an absolute standstill, but it would also give a lot more flexibility in terms of the source conditions, i.e. it would offer the possibility to work under less extreme demands for cooling and with different carrier gases.

Despite its current limitations, this work shows that a pulsed electron gun is a suitable source of metastable atoms and molecules for Zeeman deceleration. This source also has potential value for applications in collision experiments, for example, in Penning ionisation studies at high energy resolution, and possibly in trapping and laser cooling schemes.

7 | Magnetic Hexapole Focusing and Guiding after Zeeman Deceleration

This Chapter is concerned with two interrelated topics, magnetic hexapole focusing before Zeeman deceleration and the magnetic guiding of decelerated particles into an ion trap. The former is aimed at investigating further means of improving the transmission through the decelerator. The latter is a key step towards measuring quantum-state-selected and collision-energy-resolved ion-radical reaction rates. In both cases, I have devised approaches based on the use of permanent magnetic hexapoles in Halbach configuration. In the following, I will outline, discuss and evaluate these ideas using particle trajectory simulations. At the time of writing, three magnetic hexapoles in Halbach array configuration have been designed and constructed for us (see below), but they have not yet been used in the experiment.

7.1 Magnetic Hexapole Focusing

7.1.1 Introduction

As described in Chapter 5, transverse defocusing decreases the overall particle transmission through a Zeeman decelerator. Chapter 3 deals with improved deceleration switching schemes to address this problem. Here, I will assess the use of additional magnetic focusing devices to increase transverse confinement. For a long Zeeman decelerator, the phase-space model in Chapter 3 can be used to find the most efficient configuration of such focusing elements in terms of dimensions and sequence with respect to the deceleration coils. However, in the case of our short, 12-stage Zeeman decelerator, a single focusing element behind the skimmer should already be sufficient to improve the overall transmission, and this approach is explained below.

Good transverse focusing properties are obtained when the particles experience a linear restoring force towards the beam axis. In a magnetic field, the transverse force on an atom can be expressed as

$$F_r = -\frac{\mathrm{d}\left(\Delta E_{\mathrm{Z}}\right)}{\mathrm{d}r} = \mu \frac{\mathrm{d}B(r)}{\mathrm{d}r}, \tag{7.1}$$

where $\Delta E_{\mathrm{Z}} = -\mu B(r)$ is the Zeeman shift and $B(r)$ is the magnetic field in the transverse direction r. The magnetic dipole moment, $\mu = M_J g_J \mu_{\mathrm{B}}$, is the product of the Bohr magneton, μ_{B}, the projection of the total angular momentum J onto the local magnetic field axis, M_J, and the Landé factor, g_J. For particles in low-field-seeking states with $M_J > 0$, Eq. 7.1 implies that a linear restoring force is attained if $\mathrm{d}B(r)/\mathrm{d}r \propto r$, and thus $B(r) \propto r^2$. In an ideal $2n$-pole magnetic field, where $B(r) \propto r^{n-1}$, such a harmonic dependence is given for a hexapole, where $n = 3$.

Hexapole magnets have been used in atomic physics since the 1950s, and the first experiments were carried out by Friedburg and Paul [361, 362] using six conducting wires with currents in alternating directions. Only a few years later, the first configuration with electromagnets and iron pole tips was realised as well [363, 364]. Since then, hexapole magnets have found numerous applications, particularly in high energy physics for the production of highly polarized ions from atomic beams [365] and neutron focusing [366]. In atomic and molecular physics, magnetic hexapoles are used in ultracold atom experiments [367], atom lithography [368], surface scattering [369] and for quantum-state selection [370–372].

Permanent magnet designs provide strong transverse magnetic fields, but their use is restricted to specific atomic and molecular systems owing to the fixed magnetic field strength. Unfortunately, hexapole magnetic fields from current-carrying wires do not create sufficiently strong transverse forces to efficiently focus a supersonic beam unless very high currents are used. I have therefore opted for a permanent magnet hexapole design

based on a Halbach configuration. A Halbach array is a multi-segment, permanent magnet multipole design that was developed to reduce chromatic aberrations affecting the experimental performance of a standard multipole magnet [373, 374]. Hexapole focusing with Halbach arrays has already been used in various experiments [366, 375–381]. Recently, even a magnetic mirror based on a Halbach configuration has been demonstrated [382, 383].

Originally, we have decided to build a Halbach array to investigate whether such a permanent magnet design would be suitable for particle guiding after Zeeman deceleration (see Section 7.2 for further details). In the short term, I was interested to see whether Halbach magnets could also be used to focus particles into the Zeeman decelerator before the actual deceleration sequence is applied. In particular, the fabrication process of the arrays was a big unknown. Magnetic materials like NdFeB are known to demagnetise during the fabrication process and to chip easily; and we were by no means sure that a miniature Halbach design with dimensions similar to the deceleration coils was producible at all.

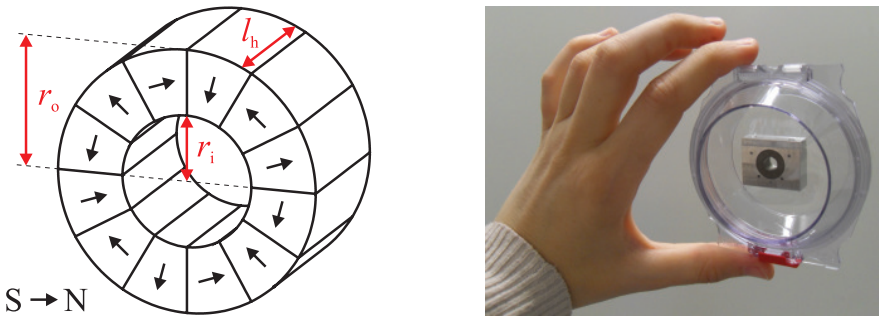

Figure 7.1: (a) Schematic drawing of a Halbach array in hexapole configuration. (b) Photograph of a Halbach array that was built for magnetic guiding and to study particle focusing into the decelerator. The Halbach segments (black colour) were potted into an aluminium housing of similar format as the coil blocks for the Zeeman decelerator.

The number of segments in a Halbach array is given by $S = m(2n)$, where n denotes the multipole order ($n = 3$ for a hexapole) and $m \in \mathbb{N}_{>0}$ [373]. For our setup, we chose $m = 2$ yielding a total number of $S = 12$ segments. Figure 7.1a shows a schematic representation of such a Halbach array in hexapole configuration. Our design is based on NdFeB magnets with a remanence $B_0 = 1.3$ T (N42SH). The dimensions of the Halbach array

(r_i = 3 mm, r_o = 6 mm, l_h = 7.1 mm) and its aluminium housing are matched to the size of the deceleration coils and the coil blocks, respectively. The Halbach array was built by Arnold Magnetic Technologies AG (local branch: Lupfig, Switzerland; project manager: Hansjörg Schmidlin) and potted into its aluminium housing to prevent shifts of array elements. Since the job had also been a novum for the manufacturer, we were provided with all three Halbach arrays that the company had made. A photograph of one of the assembled Halbach magnets is shown in Figure 7.1b. For focusing into the decelerator, the Halbach array will be located in between the skimmer and the decelerator, i.e. in the centre of the flange that holds the decelerator assembly. Positioning with a linear translation stage will allow for comparative studies with and without hexapole. All the mechanical parts for this have been purchased or built, and could be mounted at any time without having to detach the decelerator. If desired, the Halbach blocks can also be mounted onto the base plate of the Zeeman decelerator for other focusing experiments.

7.1.2 Magnetic Field of a Hexapole in Halbach Configuration

The magnetic field of the Halbach array was modelled in Radia 4.29 [384–386] and fit to the multipole expansion of the magnetic field to allow for an easier implementation in the trajectory programs, and to understand the physical concepts of multipole fields. Radia allows for three-dimensional magnetostatics simulations, so that it was possible to estimate the influence of fringe fields at the end of the multipole magnets as compared to the two-dimensional, analytical treatment by Halbach [373, 374].

In cylindrical coordinates, the multipole expansion of the magnetic field reads [387]

$$B_\phi(r,\phi) = B_0 \sum_{n=1}^{\infty} \left(b_n \cos(n\phi) + a_n \sin(n\phi)\right) \left(\frac{r}{r_i}\right)^{n-1}, \tag{7.2}$$

$$B_r(r,\phi) = B_0 \sum_{n=1}^{\infty} \left(-a_n \cos(n\phi) + b_n \sin(n\phi)\right) \left(\frac{r}{r_i}\right)^{n-1}, \tag{7.3}$$

where B_0 is the remanance, r_i is the inner radius of the multipole, b_n are the "normal" multipole coefficients and a_n are the "skew" coefficients. Owing to symmetry properties, the skew components in equations 7.2 and 7.3 vanish.

Higher harmonics, n', are given by $n' = n + \nu S$, where $\nu \in \mathbb{N}_{>0}$ [373]. In our case, it is sufficient to consider n = 3 and the first higher multipole term (ν = 1). As S = 12, n' = 15.

The results from Radia simulations (see below) suggest a significant contribution from edge effects requiring the introduction of an axial magnetic field component B_z and a scaling factor $A(z)$. Following the reasoning by Ackermann and Weiland [388], we obtain

$$B_\phi(r,\phi,z) = A(z)\,B_0 \sum_{n=3,15} b_n \cos(n\phi) \left(\frac{r}{r_i}\right)^{n-1} \tag{7.4}$$

$$B_r(r,\phi,z) = A(z)\,B_0 \sum_{n=3,15} b_n \sin(n\phi) \left(\frac{r}{r_i}\right)^{n-1} \tag{7.5}$$

$$B_z(r,\phi,z) = \frac{\mathrm{d}A(z)}{\mathrm{d}z} B_0 \sum_{n=3,15} b_n \sin(n\phi) \left(\frac{r^n}{n\,r_i^{n-1}}\right). \tag{7.6}$$

The normal multipole coefficients, b_3 and b_{15}, are found by fitting to the Radia simulation output in the centre of the hexapole (setting $A(z)$ = 1). For our configuration, b_3 = 0.86 and b_{15} = -0.11.

The scaling factor $A(z)$ is obtained by fitting to a Glaser function [389] of the form

$$A(z) = \frac{1}{((1+(z/a)^4)^2)}, \tag{7.7}$$

where $a = d/(\sqrt{(\sqrt{2}-1)})$ is a "specific" length and d is the full width at half maximum (FWHM) of the axial field distribution. The fit returned a value of d = 2.88 mm.

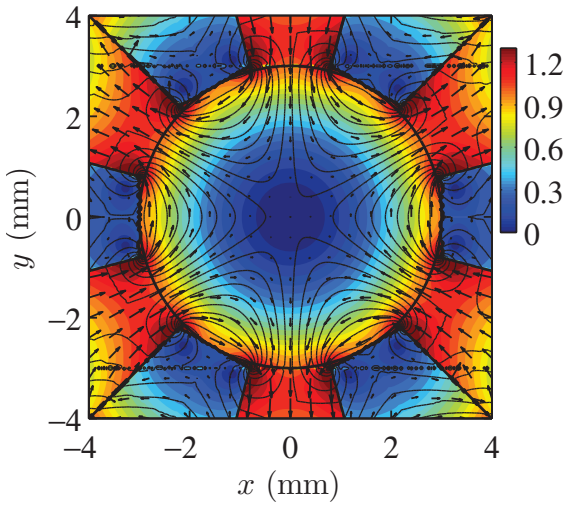

Figure 7.2: Density plot of the magnetic field magnitude B (in T) and flux lines (using B_ϕ) in the centre of a Halbach array in hexapole configuration (xy plane, see text for specifications), obtained from simulations in Radia. The 12 guide segments are framed.

Figures 7.2 and 7.3 illustrate that the output of the Radia simulations is in good agreement with the fit to Equations 7.5, 7.4 and 7.7, thus justifying the use of a multipole expansion. The results obtained in the centre of the Halbach array are also consistent with the two-dimensional, analytical solution by Halbach [373] (Figure 7.3) and with finite-element calculations (FEMM 4.2 [290], not shown) which provided a good cross check on the Radia output values.

7.1.3 Focal Length of a Magnetic Hexapole

Following the argumentats of Rossi [390], the focal length, f, of a magnetic lens can be written as

$$f = \frac{r_i m v_z^2}{F_{r,m} l_\mathrm{h}}. \tag{7.8}$$

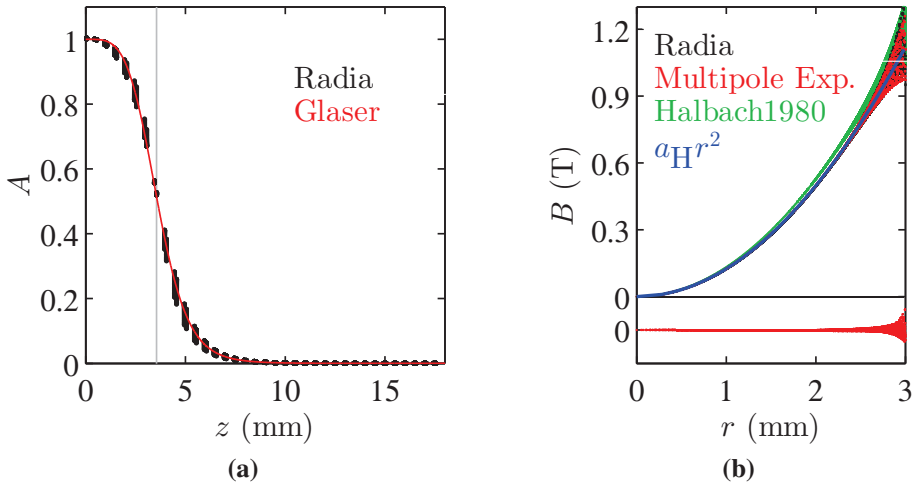

Figure 7.3: (a) Axial dependence of the Halbach magnetic field given in terms of the normalised coefficient $A(z)$. The output from the Radia simulation (black dots) and the fit to Eq. 7.7 (red curve) are shown. The outer boundary of the magnet in the z direction is indicated with a grey vertical line. (b) Transverse magnetic field in the centre of the Halbach array (at all angles ϕ). The output from Radia calculations is given by black dots. Results from a fit to the multipole expansion are represented by red dots. Residuals of the fit (in red colour) are vertically offset for clarity. The data are in close agreement with the two-dimensional, analytical solution to a Halbach array (green colour) [373] and they are well-approximated by a quadratic dependency to $a_H r^2$ (blue line; yielding $a_H = 0.12$ T/mm^2), where $a_H/2$ is the magnetic field curvature.

For an atom with mass m moving with a longitudinal velocity, v_z, in a magnetic field, the transverse force, F_r, is known from Eq. 7.1. Assuming an ideal hexapole magnet, where the magnitude of B does not depend on the angle ϕ, F_r can be expressed as $F_r = \mu\,(2a_H r)$, where $a_H/2$ is the magnetic field curvature. By fitting to the transverse magnetic field, we find $a_H = 0.12$ T/mm^2. This is close to the value for an ideal hexapole magnet ($a_H = 0.14$ T/mm^2), for which $a_H = B_0/r_i^2$. The maximum of the magnetic force, $F_{r,m}$, is found at the edges of the hexapole, so that $F_{r,m} = \mu\,(2a_H r_i)$. A detailed derivation of Eq. 7.8 can be found in Appendix 10.

For a given permanent magnet assembly, a_H is fixed, so that $f \propto m v_z^2/\mu$, i.e. the focal length will strongly depend on the magnetic-moment-to-mass ratio and the beam velocity and, hence, on the atomic or molecular system studied.

7.1.4 Transverse Phase-Space Acceptance of a Magnetic Hexapole

The implementation of a magnetic hexapole causes a rotation of the transverse phase-space acceptance thereby changing the transverse properties of the supersonic beam. The transverse acceptance of a hexapole magnet system can be estimated through one or several linear transformations [391] assuming that the transformation matrix $\mathbf{M}$ converts an existing, elliptical acceptance region $\sigma_\mathbf{1}$ into another elliptical region $\sigma_\mathbf{2}$, i.e.

$$\sigma_\mathbf{2} = \mathbf{M}\,\sigma_\mathbf{1}\,\mathbf{M}^T. \tag{7.9}$$

During this operation, phase-space acceptance is conserved owing to the unity determinant of $\mathbf{M}$. The transformation matrix for a low-field seeking particle in a magnetic hexapole, $\mathbf{M}_\mathrm{h}$, is obtained as

$$\mathbf{M}_\mathrm{h} = \begin{pmatrix} \cos(\xi l_\mathrm{h}) & \sin(\xi l_\mathrm{h})/\xi v \\ -\xi v \sin(\xi l_\mathrm{h}) & \cos(\xi l_\mathrm{h}) \end{pmatrix}, \tag{7.10}$$

where $\xi = \sqrt{2\mu a_\mathrm{H}/mv^2}$ is the hexapole strength parameter [392]. For a particle in a high-field seeking quantum state, the transformation matrix becomes

$$\mathbf{M}_\mathrm{h} = \begin{pmatrix} \cosh(\xi l_\mathrm{h}) & \sinh(\xi l_\mathrm{h})/\xi v \\ \xi v \sinh(\xi l_\mathrm{h}) & \cosh(\xi l_\mathrm{h}) \end{pmatrix}. \tag{7.11}$$

The matrix $\mathbf{M}$ can also be a linear combination of several operations, e.g. including a free-flight distance l_f in front ($\mathbf{M}_{\mathrm{f}_\mathbf{1}}$) and behind ($\mathbf{M}_{\mathrm{f}_\mathbf{2}}$) the hexapole with

$$\mathbf{M}_\mathrm{f} = \begin{pmatrix} 1 & l_\mathrm{f}/v \\ 0 & 1 \end{pmatrix}, \tag{7.12}$$

such that $\mathbf{M} = \mathbf{M}_{\mathrm{f_2}}\mathbf{M}_{\mathrm{h}}\mathbf{M}_{\mathrm{f_1}}$. By combining several hexapole matrices, this method can also be used to estimate the transverse phase-space rotation inside a multi-segment magnetic guide.

The elliptical acceptance region is given by

$$\sigma = \begin{pmatrix} \sigma_{11} & \sigma_{12} \\ \sigma_{12} & \sigma_{22} \end{pmatrix}. \tag{7.13}$$

For example,

$$\sigma_{\mathbf{1}} = \begin{pmatrix} (\Delta x)^2 & 0 \\ 0 & \sigma_{v_x}^2 \end{pmatrix}. \tag{7.14}$$

for the initial particle distribution in the x direction, where Δx and σ_{v_x} denote the position and velocity spread of the beam in that direction, respectively. The σ matrices can then be used to obtain the semi-axes and the tilt angle of the underlying ellipses.

7.1.5 Comparison with Trajectory Simulations

To validate analytical estimates for the transverse acceptance (Section 7.1.4) and the focal length (Section 7.1.3) of a Halbach hexapole magnet, three-dimensional particle trajectory simulations with and without magnetic focusing were carried out for ground-state H atoms, as the properties of the initial supersonic beam are well-understood, and an increase in the number of H atoms would be advantageous for Zeeman deceleration, magnetic guiding and subsequent studies of ion-radical reactions.

The implementation of the hexapole magnetic field in the simulations is straightforward, as it only requires adding of the hexapole magnetic field components and their gradients to the values for the deceleration coils (B_ϕ = 0 for a solenoid coil). In the program, the centre position of the magnetic hexapole (z_{H} = 71 mm) between the skimmer (orifice

at z = 49 mm) and the first deceleration coil (centre at z = 93 mm) is chosen to meet the (expected) experimental location. The estimated longitudinal and transverse temperatures of the beam are the same as in Chapter 5.

Figure 7.4 illustrates the rotation of the transverse phase space for H atoms in the low-field-seeking $M_F = 1$ state (see Figure 2.6a) upon hexapole focusing for longitudinal beam velocities centred at 500 m/s, 650 m/s and 800 m/s. In all cases, the extent of the simulated phase-space areas is in very good agreement with the analytical solution determined using transformation matrices (Section 7.1.4). While the tilt of the phase-space area is caused by free flight in front and behind the Halbach array, the hexapole field itself leads to a narrowing of the beam ellipse along one semi-axis and a spread in the other. As there are no dissipative forces, the phase-space area is conserved. As expected, this dispersion increases towards lower velocities, as the particles spend a longer time inside the hexapole and thus experience stronger transverse forces.

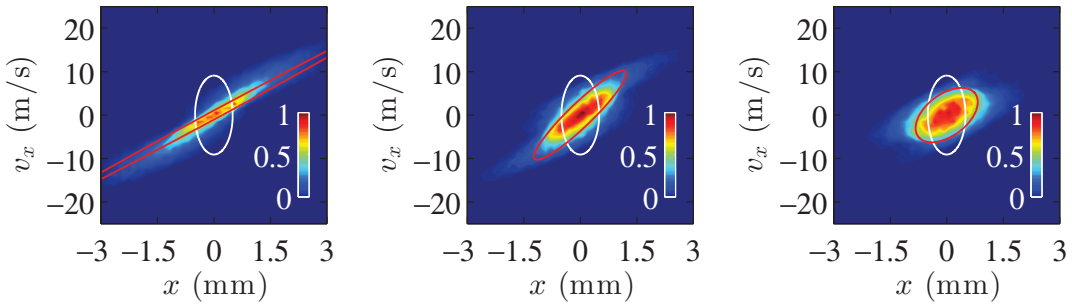

(a) $v_{z,m}$ = 500 m/s **(b)** $v_{z,m}$ = 650 m/s **(c)** $v_{z,m}$ = 800 m/s

Figure 7.4: Density plots of the simulated transverse phase space for H($1^2S_{1/2}$, $M_F = 1$) after the last deceleration coil (Zeeman decelerator not operated) upon hexapole focusing for three different longitudinal velocity distributions (arbitrary scale). The centre velocities of the distributions, $v_{z,m}$, are indicated in the subcaptions. The white and red ellipses denote the extent of the initial and final transverse phase-space region covered by the beam, respectively. The ellipses were calculated using the transformation matrices in Section 7.1.4.

Figure 7.5 shows the evolution of the density of simulated H atom trajectories ($M_F = 1$ state) along the x and z dimension under the same conditions as in Figure 7.4. The beam

expands in the transverse direction until it reaches the Halbach array[a]. Depending on the longitudinal beam velocity, the atoms are then focused to a different point further along the beam axis. As expected from Eq. 7.8, the density maximum (focal point) is shifted to larger longitudinal positions as the beam velocity is increased. The longitudinal and transverse distribution of particle positions and velocities and the finite length of the hexapole lead to chromic aberrations, i.e. a blurring of the focal point, especially at high particle velocities, where the focusing force is weak. The simulated focal lengths are approximately 30 % higher than the values obtained from the analytical solution (red dots and solid black curve in Figure 7.6). If both the Halbach array and the Zeeman decelerator are operated ($\bar{a}_z/\bar{a}_{z,m}$ = -1, blue dots in Figure 7.6), the focal lengths are increased even further. This is due to a reduction of the overall transverse force caused by the transversely defocusing magnetic fields outside the coils which affect most of the particles in the decelerator (Figure 3.1). Note that the focal lengths are shorter than the distance between the Halbach array and the exit of the decelerator ($z - z_\mathrm{H}$ = 139 mm).

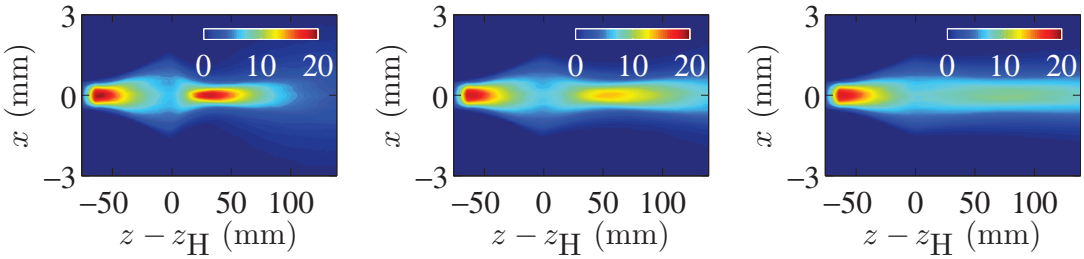

(a) $v_{z,m}$ = 500 m/s **(b)** $v_{z,m}$ = 650 m/s **(c)** $v_{z,m}$ = 800 m/s

Figure 7.5: Density of simulated H($1^2S_{1/2}$, M_F = 1) atom trajectories along the x and z dimension (all y positions) upon hexapole focusing (arbitrary scale) using three different longitudinal velocity distributions (simulation input as in Figure 7.4). The centre of the Halbach array (z_H = 71 mm) is set to zero.

For a full analysis, the particle velocities after deceleration must be considered separately. Figure 7.7a shows simulated longitudinal H atom velocity distributions after Zeeman deceleration from 500 m/s to 222 m/s (sum of the low-field-seeking states, $v_{z,m}$ = 500 m/s, $\bar{a}_z/\bar{a}_{z,m}$ = -1) including hexapole focusing at different remanences, B_0. In contrast to the

[a]Owing to the skimmer exclusion step in the program (Section 2.2.2), the beam spread is artificially reduced in front of the aperature of the skimmer.

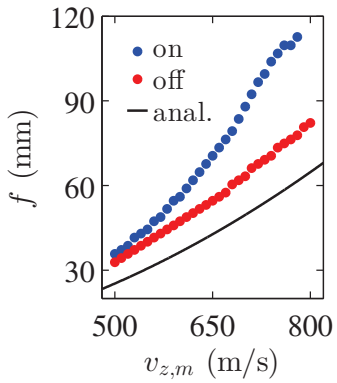

Figure 7.6: Focal length as a function of longitudinal H atom velocity (M_F = 1 state). The solid black curve is derived from Eq. 7.8. The blue (red) points are the maximum on-axis densities at $z > z_H$ obtained from particle trajectory simulations in which the Zeeman decelerator is (not) operated at $\bar{a}_z/\bar{a}_{z,m}$ = -1.

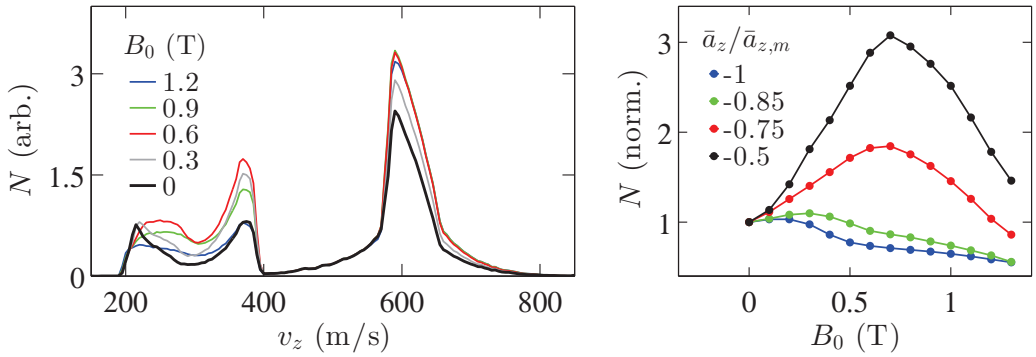

Figure 7.7: (a) Simulated longitudinal velocity distributions of H($1^2S_{1/2}$) after Zeeman deceleration from 500 m/s (sum of the low-field-seeking states, $v_{z,m}$ = 500 m/s, $\bar{a}_z/\bar{a}_{z,m}$ = -1) at different remanences, B_0, as indicated in the legend. The velocity distribution without Halbach focusing (black curve) is highlighted in bold. The number of particles is normalised to the maximum of the velocity distribution without Zeeman deceleration (same scaling as in Figure 7.8). (b) Simulated decelerated peak intensities for Zeeman deceleration of H($1^2S_{1/2}$) from 500 m/s to 389 m/s (-0.5), 316 m/s (-0.75), 288 m/s (-0.85) and 222 m/s (-1) as a function of remanence (normalised to B_0 = 0, low-field-seeking states only). Numbers in brackets denote the mean longitudinal acceleration $\bar{a}_z/\bar{a}_{z,m}$.

partially decelerated and undecelerated velocities, where the particle numbers increase under the influence of a hexapole magnetic field, the particle number for the decelerated peak is highest at B_0 = 0 – 0.3 T. At higher remanences, more (transversely focused and partially decelerated) particles at around 280 m/s are observed, which are outside of the

accepted phase-space volume for deceleration and would lead to a decrease of the energy resolution if used for collision experiments. In Figure 7.7b, the number of decelerated particles (same velocity as synchronous particle) is plotted as a function of remanence. While the particle numbers at high amounts of deceleration, i.e. $\bar{a}_z/\bar{a}_{z,m}$ = -0.85 (green dots) and -1 (blue dots), decrease as a function of B_0, they increase up to a remanence of B_0 = 0.7 T at lower values for $\bar{a}_z/\bar{a}_{z,m}$ (up to a factor of 3 for $\bar{a}_z/\bar{a}_{z,m}$ = -0.5). However, this increase is also partly due to an increased focusing of particles from the initial velocity distribution (cf. Figure 7.8a). The observed trends in Figure 7.7b can be understood in terms of a change in focal length as a function of v_z and B_0. When the focal length is much smaller than the length of the decelerator, i.e. at low velocities and high remanence, the particles are initially focused towards the beam axis, but diverge towards the walls of the decelerator afterwards. The overfocusing of low-velocity components at increasing remanence is also seen when the Zeeman decelerator is not switched (Figure 7.8a).

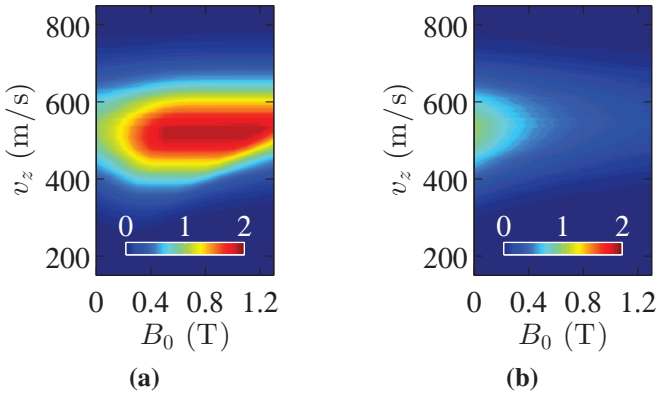

Figure 7.8: Simulated longitudinal velocity distributions of H($1^2S_{1/2}$) after the last deceleration coil (Zeeman decelerator not operated) as a function of remanence, B_0 for (a) all H atoms in low-field-seeking quantum states and (b) all H atoms in high-field-seeking quantum states. The initial distribution is centred at 500 m/s. The maximum of the velocity distribution at B_0 = 0 is assigned a value of 1.

Hexapole focusing also increases quantum-state selection, as demonstrated in Figure 7.8. Here, simulated longitudinal velocity distributions after the last deceleration coil (Zeeman decelerator not operated) are compared for both low- and high-field-seeking quantum states as a function of remanence. While the number of particles in low-field-seeking states increases significantly (up to a factor of 2 at 500 m/s), the number of particles

in high-field-seeking states drops. Owing to the short length of our Zeeman decelerator, quantum-state selection is not very efficient, so that additional state selection from hexapole focusing is beneficial. The (2+1) REMPI detection scheme employed here (Section 4.1.1) is not state-selective, but other detection methods, such as polarised fluorescence [393], may be used to experimentally demonstrate this effect.

7.1.6 Conclusions

While increased quantum-state selection from magnetic hexapole focusing is certainly beneficial for chemical reaction studies, the general applicability of this method for the Zeeman deceleration of ground-state H atoms is limited to low $\bar{a}_z/\bar{a}_{z,m}$, as the velocity dependence of the focal length causes an overfocusing of the low-velocity components. For low amounts of deceleration, a hexapole with a remanence of 0.7 T is predicted to yield the highest increase in the number of particles at the desired velocity. However, the hexapole focusing may also deteriorate the energy resolution of the decelerated beam. Since $f \propto m/\mu$, longer focal lengths will be obtained for paramagnetic species with a lower magnetic-moment-to-mass ratio. For metastable N atoms, the estimated focal lengths for initial velocities between 450 m/s and 650 m/s match very well with the dimensions of the experimental setup. Hexapole focusing would generally be useful for the characterisation of metastable He beams, since higher signal intensities than predicted by trajectory simulations would indicate a deflection of the He atoms upon electron impact (Section 6.2.1).

Magnetic focusing with several Halbach magnets in between deceleration coils, e.g. after every third solenoid coil, could prevent losses from overfocusing. In fact, the current design of the Halbach magnets already allows for experiments of this type, since the Halbach blocks can be mounted onto the base plate of the Zeeman decelerator (Figure 7.1b). However, changes in phase-space acceptance need to be carefully analysed and the increased heat load from longer coil switching times need to be considered. It would also be difficult to estimate the signal gain compared to the normal mode of operation,

since deceleration coils would have to be removed (or a second base plate added) and the magnetic field of the Halbach magnets cannot be varied *in situ*.

7.2 Magnetic Guiding after Zeeman Deceleration

7.2.1 Introduction

To determine accurate chemical reaction rates between Zeeman-decelerated atoms or molecules and trapped ions as a function of collision energy, it is necessary to filter out the carrier gas atoms and all other particles that are outside the phase-space volume accepted by the decelerator. For example, in H atom experiments, NH_3 precursor molecules, NH_2 molecules produced during photolysis, undecelerated or partially decelerated/accelerated H atoms (Figure 5.1) as well as Kr carrier gas atoms can be transmitted through the Zeeman decelerator and potentially corrupt the reaction rate measurements.

As the current Zeeman decelerator is rather short in length (13 cm), the different beam velocities after deceleration are not well-separated. Hence, the 700 μs opening time of a mechanical shutter, as used in the Stark decelerator-ion trap experiment in our laboratory [216], will not sharply isolate the decelerated beam packet only. Owing to its fast motion, a mechanical chopper wheel may be an alternative option. However, parts of the carrier gas pulse are likely to be transmitted if the amount of deceleration, $\bar{a}_z$, is low. A bent magnetic guide represents one possible way forward, as it would block the carrier gas atoms and act as a low-pass velocity filter for the decelerated particles. A possible setup for a combined Zeeman decelerator-ion trap experiment is illustrated in Figure 7.9.

Depending on the atomic or molecular system and the experimental conditions, there have been different approaches to achieve magnetic guiding. Magnetic hexapole fields generated from superconducting wires have been used to confine neutrons in the large-scale NESTOR storage ring [394]. There has also been a proposal for a storage ring based on alternating-gradient focusing (see Chapter 1) aiming to attain Bose-Einstein

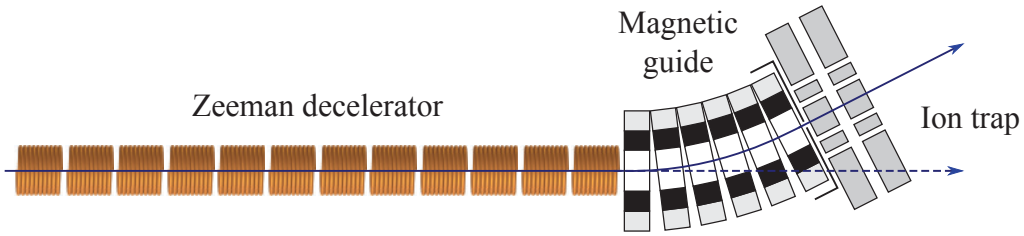

Figure 7.9: Schematic representation of a combined Zeeman decelerator-ion trap experiment including a bent magnetic guide to filter out the carrier and precursor gases and particles at higher longitudinal velocities; not to scale. Even though the magnetic field outside of a Halbach array drops quickly (Figure 7.3a), a mu-metal cup may be required to shield the ion trap from stray magnetic fields (indicated aperture between ion trap and guide).

condensation of ground-state hydrogen atoms in high-field-seeking quantum states [395]. Progress in the field of cold and ultracold atoms has triggered numerous ideas for guides based on microfabricated structures or wire geometries [396, 397], and some of these ideas have also been transferred to the macroscopic scale, e.g. by using a set of racetrack coils [398]. The magnetic transfer of ultracold atoms in between two trapping geometries (on the timescale of a few seconds) has been demonstrated by switching currents through a chain of anti-Helmholtz coils [399]. Bent magnetic guides based on permanent magnet assemblies have also been realised. Magnetic octupole setups were either used as a source of slow Li atoms [400, 401] or to filter out helium buffer-gas atoms from an effusive source of O_2 molecules [402]. Bent magnetic quadrupoles and hexapoles in Halbach configuration have proven to be efficient guides for Cs atoms [403] and metastable Ne atoms [404], respectively. However, none of these guides were specifically designed to allow for a variation of the guidable velocities.

The maximum guidable beam velocity, $v_{z,m}$, can be estimated by setting the transverse magnetic force F_r (see Eq. 7.1) equal to the centripetal force $F_c = m v_{z,m}^2/R$, where R is the bend radius and m is the particle mass. Rearranging to $v_{z,m}$ yields

$$v_{z,m} = \sqrt{\frac{\mu R}{m}\frac{\mathrm{d}B(r)}{\mathrm{d}r}}. \tag{7.15}$$

Equation 7.15 shows that the maximum guidable velocity is proportional to both the bend radius and the transverse magnetic field gradient. However, a variation of the bend radius is not practical in our case, as this would require a gradual change in the ion trap position, and the alignment of the cooling lasers, to ensure that the guided beam is aimed at the centre of the ion trap (Figure 7.9).

A magnetic guide made from current-carrying wires does allow for a change in the transverse magnetic field gradient, $\mathrm{d}B(r)/\mathrm{d}r$. However, this change is too small to enable the manipulation of beams in the supersonic flow regime unless very high currents are used. On the other hand, permanent magnets, e.g. in a hexapole configuration, provide large magnetic field gradients (see also Section 7.1) but the magnetic field is not tunable.

In the following, I will propose a scheme for a hybrid magnetic guide consisting of both permanent magnets and current-carrying wires which combines the benefits of both permanent magnets and electromagnetic guides, i.e. high magnetic field strengths and magnetic field tunability, respectively. Such a guide will allow for the efficient magnetic guiding of H atoms from zero up to the velocity of the initial supersonic beam ($\approx$ 500 m/s), and it will act as a strong filter for carrier gas atoms and H atoms at other, unwanted velocities. As a magnetic counterpart to an electrostatic velocity filter, such a guide could also provide an access route to slow paramagnetic atoms and molecules emerging from supersonic or effusive beam sources.

7.2.2 Hybrid Guide Configurations

The hybrid guide described here is based on the superposition of a magnetic hexapole field from a Halbach array[b] and a second magnetic field shape generated using current-carrying wires. Two wire configurations are considered here: (a) a hexapole design tailored to match the shape of the Halbach hexapole field ('two-hexapole configuration')

[b] A prototype permanent-magnet hexapole could also be made from bar magnets.

and (b) a configuration with two wire locations on opposite sides of the Halbach magnet ('deflection configuration').

To be consistent with the particle trajectory simulations described in Section 7.2.3, the magnetic fields components are calculated in cartesian coordinates (see Appendix 11 for coordinate transformations). The magnetic field of the Halbach array is calculated using Eq. 7.4–7.6, with the same dimensions as described previously (using $B_0 = 0.7$ T).

The magnetic field of each wire is approximated with the analytical solution of the Biot-Savart law for a long straight current-carrying wire. In this case, the magnetic field vector, $\vec{B}$, outside the wire is given by

$$\vec{B} = \begin{pmatrix} B_x \\ B_y \\ B_z \end{pmatrix} = \frac{\mu_0 I}{2\pi R_\mathrm{w}^2} \begin{pmatrix} -y \\ x \\ 0 \end{pmatrix}, \tag{7.16}$$

where μ_0 is the permeability of free space, I is the current through the wire and R_w is the distance to the centre of the wire. By adding the magnetic field components of different wires, which are mutually offset in the xy plane, various wire configurations can be attained. Sets of four wires are chosen to match the dimensions of a Halbach array segment, and a wire diameter $d_\mathrm{wire} = 450$ μm was used, because the same diameter was found to work reliably for the Zeeman deceleration coils.

7.2.2.1 Two-Hexapole Configuration

In the two-hexapole configuration, six sets of four wires are arranged inside the Halbach array and operated at the same current but in alternating current directions. In this way, the wires generate a magnetic hexapole field whose extent (Figure 7.10b) matches with that of the Halbach magnets (Figure 7.10a). Depending on the current direction, the application of a current then leads to an overall increase or decrease of the transverse magnetic field,

and thereby changes the magnetic field gradient $\mathrm{d}B(r)/\mathrm{d}r$. In Figure 7.10, this increase (decrease) is illustrated at currents of 500 A (-330 A). For I = -330 A, the opposing hexapole fields nearly cause a complete cancellation of the magnetic field magnitude in the transverse direction.

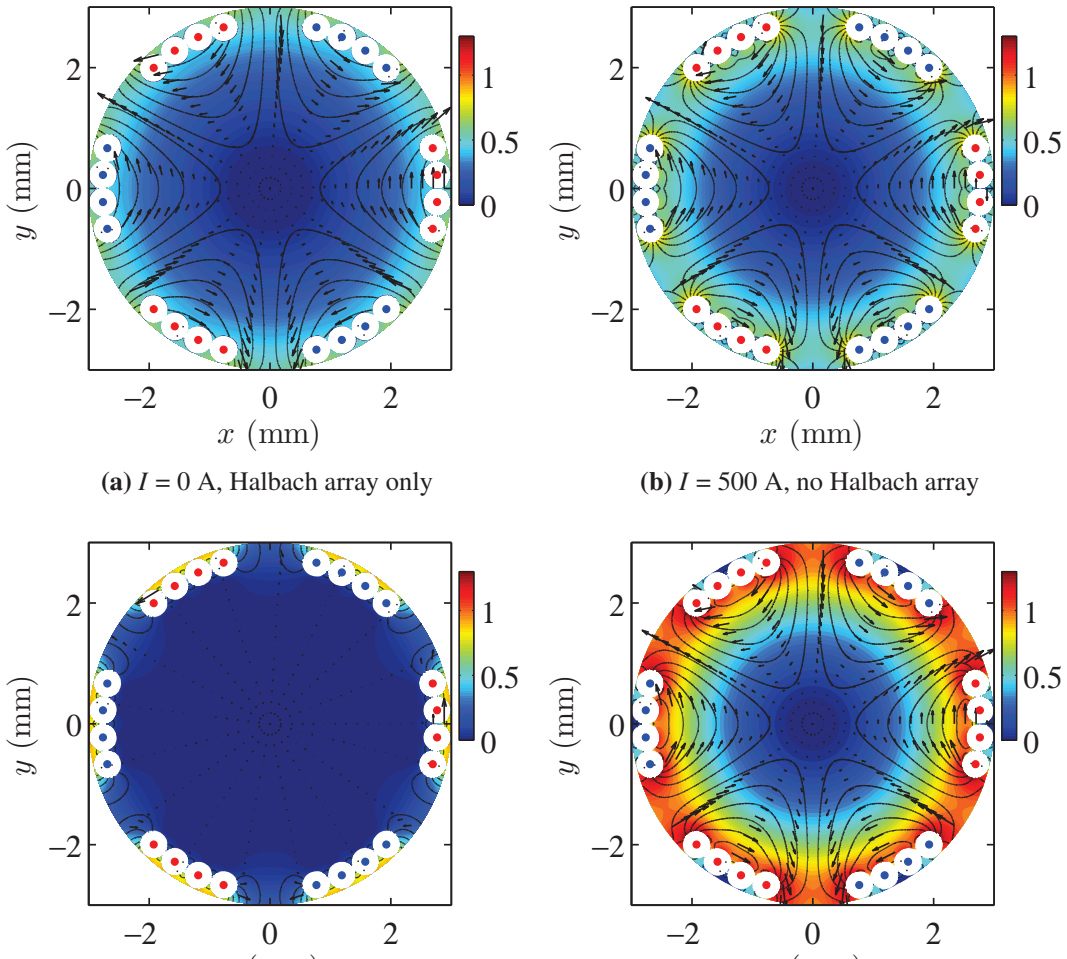

(a) I = 0 A, Halbach array only

(b) I = 500 A, no Halbach array

(c) I = -330 A

(d) I = 500 A

Figure 7.10: Two-hexapole configuration: density plot of the magnetic field magnitude B (in T) in the centre of a hybrid guide element and flux lines (using B_ϕ) at different currents through the wires. The position of the permanent magnet segments is as indicated in Figure 7.2. Wires (pointing into the plane) are shown as filled white circles. Red (blue) dots indicate that the current is directed towards (out of) the plane of projection. The current is assigned with a positive (negative) value if the superposition with the Halbach magnetic field results in an increase (decrease) of the transverse magnetic field.

Figure 7.11 shows that the resulting transverse magnetic field is well approximated by

a quadratic dependency on the transverse position, i.e. $B = a_{\mathrm{H}} r^2$. The parameter a_{H}, a measure of the magnetic field curvature, changes linearly with the current applied to the wires (inset of Figure 7.11a).

As the transverse magnetic field gradient for a magnetic hexapole depends on the off-axis particle position, i.e. $\mathrm{d}B(r)/\mathrm{d}r = 2a_{\mathrm{H}} r$ (cf. Section 7.1.3), it is difficult to assess the maximum guidable velocity for such a guide using Eq. 7.15. An upper estimate of $v_{z,m}$ can be obtained by setting $r = r_i - d_{\mathrm{wire}}$, as shown in Figure 7.11b. In the Figure, the lower and upper limits for a_{H} correlate with wire currents of -330 A and 500 A implying that the maximum guidable velocity for ground-state H atoms can be tuned between zero and roughly 900 m/s. Three-dimensional particle trajectory simulations (Section 7.2.3) imply that this guess clearly overestimates the true guidability for H atoms at different velocities.

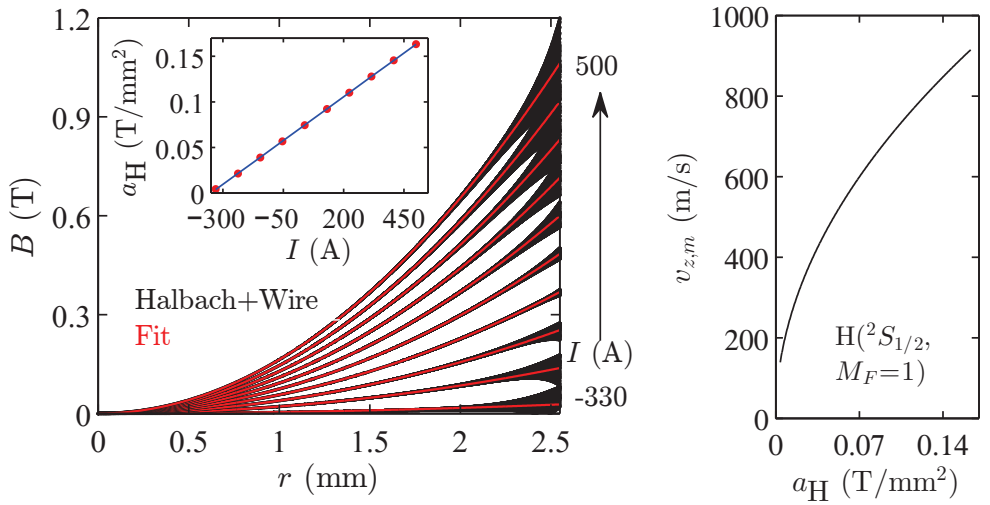

Figure 7.11: (a) Change of the transverse magnetic field of the hybrid guide (at all angles ϕ) as a function of current, I, applied to the wires (two-hexapole configuration). Results from the analytical solution are shown in black colour; quadratic fits to $B = a_{\mathrm{H}} r^2$ are indicated in red colour. The fitted a_{H} values are linearly dependent on the applied current (inset). (b) Upper estimate of the maximum guidable velocity for H($1^2\mathrm{S}_{1/2}$) as a function of a_{H} obtained using Eq. 7.15 and a bend radius of R = 180 mm.

7.2.2.2 Deflection Configuration

In the deflection configuration, two series of four wires – carrying the same current in the same direction – are placed on opposite sides of the Halbach array. This leads to an increase of the magnetic field strength B on the side of the Halbach magnets, where the flux lines of the Halbach magnets and the wires point in the same direction, while it causes a decrease in B on the other side. Depending on the current direction, a magnetic deflection field in the x (Figure 7.12a) or $-x$ direction (Figure 7.12c) is created which either increases or counteracts the centrifugal force on the particles inside a bent guide (Figures 7.12b and 7.12d).

Both the two-hexapole and the deflection configuration could be constructed straightforwardly by adaptation of the existing design for the Halbach arrays and they could be mounted onto a water-cooled aluminium base plate that is directly connected to the Zeeman decelerator. The deflection setup has advantages in terms of its practical implementation, i.e. less ohmic heating and lower mechanical complexity, especially with regard to misalignment between the wires and the Halbach array segments. Assuming 4x2 wires with a length of 60 mm each, the total length of wire (0.48 m) for the guide is less than one third of the wire length needed for a single deceleration coil. The resistance and, thus, the heat load for the guide will therefore be much less than for the Zeeman decelerator. Since the permanent magnet material (NdFeB) has a relatively high heat conductivity (6.4 W/mK, see spec sheet Arnold Magnetic Technologies AG[c]), the wires could be cooled directly via the Halbach housings. To minimise the rise and fall times of the currents for pulsing, the inductance could be reduced even further by operating each wire independently.

[c]For comparison, the thermal conductivity of the A-H77 epoxy glue for the deceleration coils is only 0.66 W/mK (see spec sheet from LewVac).

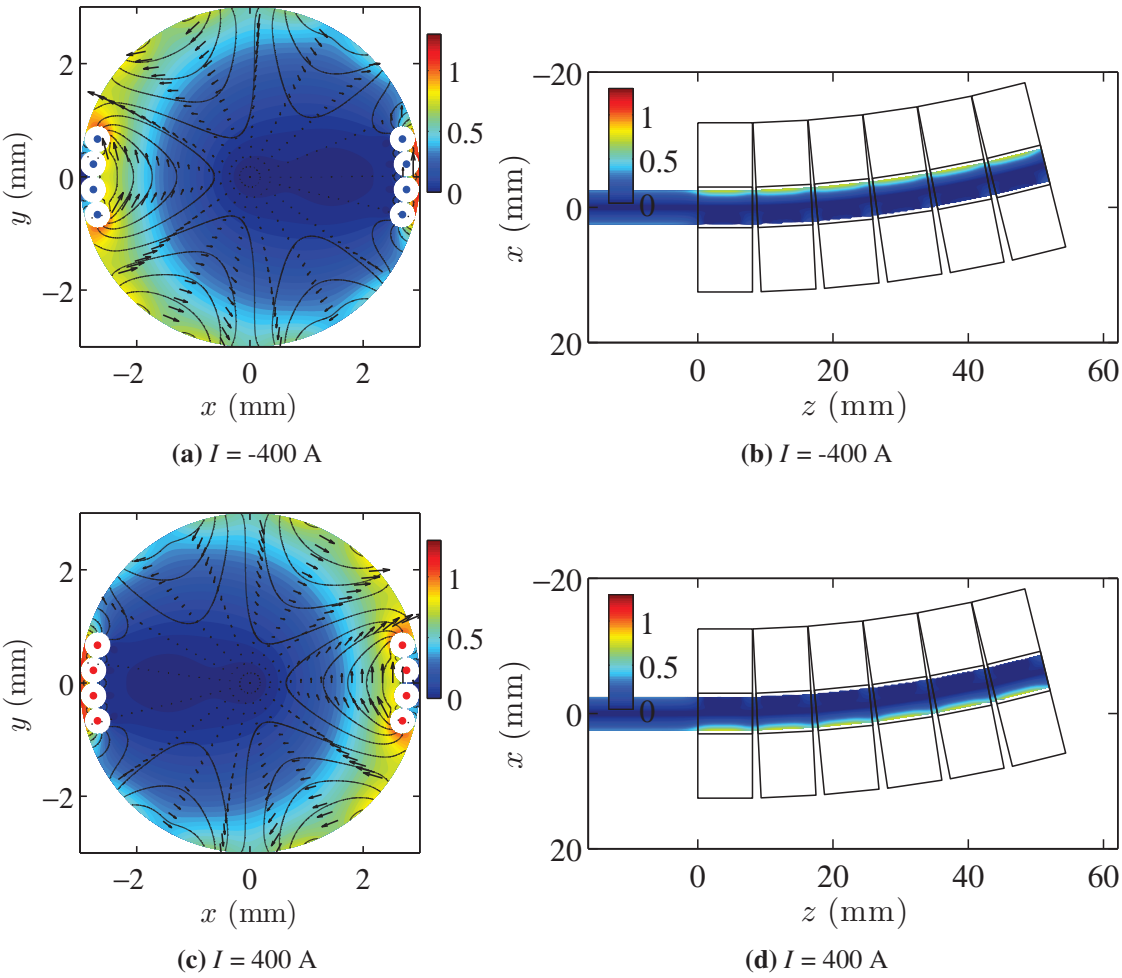

(a) I = -400 A **(b)** I = -400 A

(c) I = 400 A **(d)** I = 400 A

Figure 7.12: (a) and (c): Density plots of the magnetic field magnitude B (in T) in the centre of a hybrid guide element for the deflection configuration including flux lines (using B_ϕ). The current direction through the wires in (c) is reversed with respect to (a). The notation of the wires is the same as in Figure 7.10. (b) and (d): Cross-section view of B inside a bent guide (at $y = 0$, $R = 180$ mm, to scale) with six guide sections using the configurations in (a) and (c), respectively. The positions of the Halbach blocks is indicated to illustrate the physical arrangement.

7.2.3 Particle Trajectory Simulations

The basic concepts of the three-dimensional particle trajectory simulations for the Zeeman decelerator (Section 2.2.2) and the magnetic guide are similar, and the main differences arise from the more complex geometry of the guide. To allow for variations of the guide structure (number of segments, bent radius etc.), grids of the magnetic field components for the wires and the Halbach array are generated by rotation about the y-axis at the begin-

ning of each simulation. The influence of the exiting wires on the shape of the magnetic field was not considered and probably remains to be seen experimentally. As the bend radius is large (here: R = 180 mm), it is assumed that Eq. 7.16 is still a valid approximation for the magnetic vector field of the wires. Since the magnetic field is expressed in cartesian coordinates, trilinear interpolation [255] is required for the evaluation of the field components and partial derivatives. The program can propagate the positions and velocities of 100,000 particles (in each Zeeman substate of ground-state atomic hydrogen) at a time, and it can also process existing trajectory data from the Zeeman deceleration code. At each time step, particles are removed from the simulation if they are located outside the boundaries of the guide (inner diameter of 5.1 mm inside each guide section), given by the convex hull of points that mark the guide elements.

In an iterative process, the number of guide sections, the bend radius and the remanence of the Halbach magnets were varied to find a suitable geometry for the efficient, velocity-tunable magnetic guiding of H atoms in low-field-seeking quantum states after Zeeman deceleration. In the following, simulation results for a bent guide consisting of six Halbach arrays (R = 180 mm, B_0 = 0.7 T) and 6x4 or 2x4 wires in the two-hexapole and deflection configuration are shown (cf. geometry in Figures 7.12b and 7.12d).

7.2.4 Guiding Efficiency

7.2.4.1 Continuous Operation

To study the guiding efficiency of H atoms under continuous application of a current to the wires, trajectory simulations were run at different currents for fixed initial longitudinal velocities v_z (T_z = 0). A set position in front of the guide (z = -2 mm for all particles), a transverse temperature of 10 mK centred around v_r = 0, as in the simulations for the Zeeman decelerator, and a uniform transverse spread over the inner diameter of a guide section are assumed.

From the simulation results, the transmission of H atoms in the two low-field-seeking quantum states is obtained and shown in Figure 7.13 as a function of initial longitudinal velocity and wire current for both the two-hexapole configuration and the deflection configuration. The number of transmitted particles without a magnetic moment (< 3 %) and H atoms in high-field-seeking states (< 8 %) is negligible over the whole parameter range studied (not shown).

Figure 7.13 confirms that the maximum guidable velocity increases as the current through the wires is increased. The trends are similar for both wire configurations, with an advantage of the deflection configuration in terms of maximum transmission at different velocities. However, at a given current, there is a gradual increase in guidability as a function of initial v_z, which is due to the transverse distribution of positions and velocities inside the guide. For example, at a current of 200 A in the deflection configuration, the transmission is about 90 % for low-field-seeking particles with v_z = 250 m/s and 50 % for particles with v_z = 400 m/s; and the guidability falls below 10 % above a velocity of 600 m/s. This implies that a clear separation of similar particle velocities is difficult to achieve in a continuous mode of operation, and efforts to guide only the low-velocity tail would almost certainly result in a low particle transmission efficiency. A similar behaviour is expected for a guide setup in which the guided velocities are adjusted through a change in bend radius.

7.2.4.2 Pulsed Operation

As can be seen from Figure 7.13a, magnetic guiding at -400 A in the deflection configuration is inefficient for all but very low particle velocities (< 200 m/s) On the other hand, the transmission through the guide is predicted to be as high as 80 % above 0 A, and the initial longitudinal velocity – for which this maximum efficiency is reached – is gradually increased towards higher currents. Since the decelerated packet of H atoms is temporally offset from the other particles in the supersonic beam, operation of the guide in switched

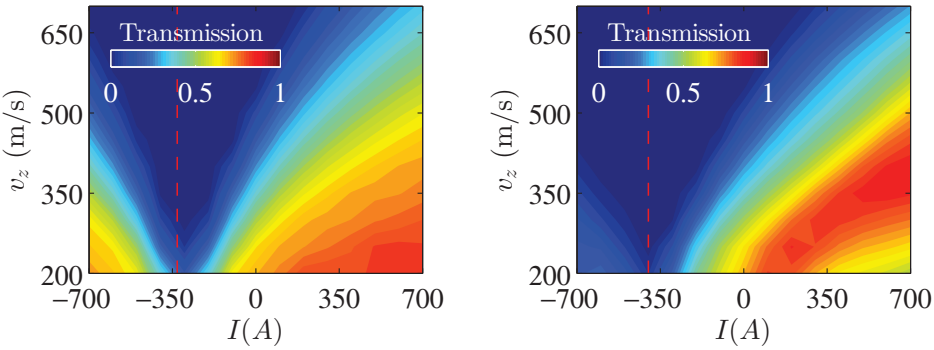

(a) Two-hexapole configuration **(b)** Deflection configuration

Figure 7.13: Density plot showing the transmission of H($1^2S_{1/2}$) in the two low-field-seeking quantum states as a function of initial longitudinal velocity, v_z and current applied to the wires, I. The guidability is given on a scale from 0 (no transmission) to 1 (all particles transmitted). The red dashed line denotes the current I_1 that is used for the simulation of the guiding efficiency in pulsed mode (see Section 7.2.4.2).

mode at two currents, I_1 and I_2, may significantly improve the velocity selection of the guide.

For this scheme, the guide would be switched to a current I_1, i.e. I_1 = -330 A for the two-hexapole configuration and I_1 = -400 A for the deflection configuration, at time t_1. Here, t_1 is defined as the arrival time of the first H atoms from the supersonic beam. The duration of current pulse 1, Δt_{I_1}, is scanned to find the optimum settings between efficient guidability for the decelerated particles and low transmission for particles at other velocities. The current is then switched to I_2, which shall be the lowest current required to achieve a high transmission of the decelerated beam. In this way, higher velocities are guided less efficiently and ohmic heating of the wires is minimised. The duration of the second current pulse, Δt_{I_2}, is determined by the time-of-flight of the decelerated particles through the guide (see also Figure 7.15b). Owing to the low inductance of the short wires, switching between the two currents should be almost instantaneous.

Operation of the guide in pulsed mode was simulated for a realistic supersonic beam of H atoms leaving the Zeeman decelerator at a longitudinal velocity of 220 m/s ($v_{z,0}$ = 500 m/s, $\bar{a}_z/\bar{a}_{z,m}$ = -1, beam characteristics as in Chapter 5). The distance between the end of the decelerator and the entrance of the guide was assumed to be 2 mm. Below, simulation

results are shown for magnetic guiding in the deflection configuration using I_1 = -400 A and I_2 = 150 A; t_1 = 260 μs after photolysis. Similar characteristics are observed for the two-hexapole configuration, but – as expected from Figure 7.13 – the guiding efficiency for the decelerated beam is lower.

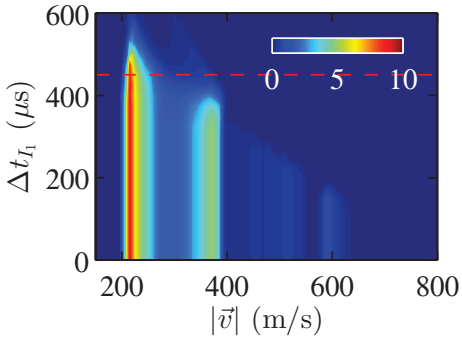

Figure 7.14: Density plot of Zeeman decelerated and guided H atom velocities $|\vec{v}|$ (low-field-seeking states only) as a function of pulse duration Δt_{I_1} in the deflection configuration; arbitrary scaling. The red dashed line highlights the velocity distribution at Δt_{I_1} = 450 μs used in Figure 7.15.

Figure 7.14 shows a density plot of the guided H atom velocities (low-field-seeking states only) as a function of the pulse duration Δt_{I_1}. Here, Δt_{I_1} = 0 μs corresponds to the case, where I_2 = 150 A at all times, whereas Δt_{I_1} = 600 μs illustrates the guiding efficiency at a constant current of -400 A. The overall transmission through the guide decreases the longer the pulse duration Δt_{I_1}, which is expected at -400 A (cf. Figure 7.13b). Even for Δt_{I_1} = 0 μs, the guiding efficiency for particle velocities above 400 m/s is low. However, under these conditions, not only the decelerated bunch of particles at 220 m/s, but also a packet moving at a velocity of 350 m/s is transmitted (50 % of the intensity). By increasing Δt_{I_1} to 450 μs, the guidability for this second packet is widely reduced, while the decelerated beam is still almost guided at unit efficiency ($\approx$ 87 %). This becomes even more apparent in Figure 7.15a, where the initial velocity distribution after Zeeman deceleration (upper panel) is compared to the velocity distribution after subsequent guiding (lower panel). None of the carrier gas particles are transmitted, and the guiding of particles in high-field-seeking states is several orders of magnitude smaller than for the decelerated particles.

Owing to the rotation of the beam inside the guide, the orientation of the velocity vectors is altered. For a typical supersonic beam, v_x and v_y are very small, so that $|\vec{v}| \approx v_z$. In contrast to that, the v_x component of the decelerated H atoms is narrowly centred around -60 m/s at the guide exit (v_y distribution unchanged), while the v_z distribution is shifted to a lower maximum value. Since the atoms do not experience a net acceleration or deceleration, the overall velocity distribution of the decelerated beam is the same before and after guiding (Figure 7.15a).

Due to the compact design of the guide, the flight time of the decelerated H atoms through the guide still remains relatively short (here: 250 μs). Nevertheless, the intensity of the TOF signal decreases by about a factor of three owing to the lack of focusing along the beam axis inside the guide (Figure 7.15b). For the study of cold-ion molecule reactions, the longitudinal beam spread is not an issue, because only the overall flux of decelerated particles through the ion trap matters. For other applications, a combination of the guide with a bunching scheme may be beneficial.

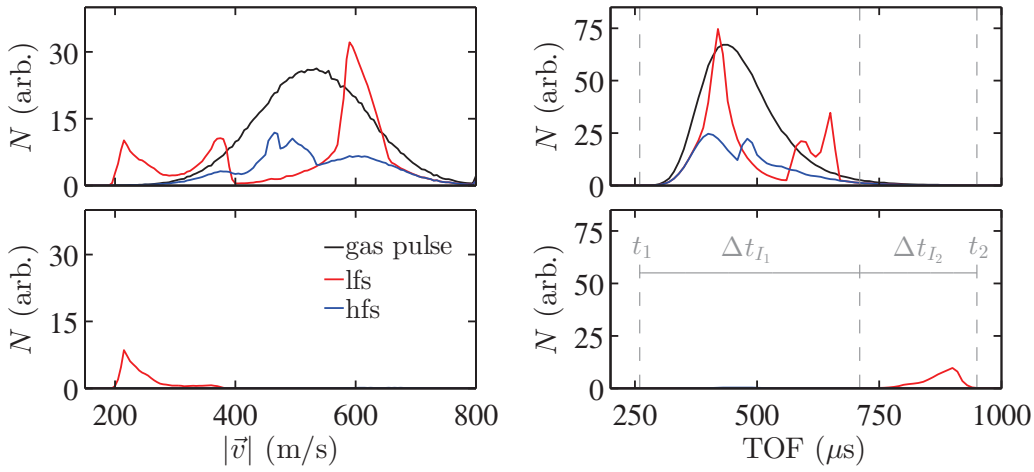

Figure 7.15: (a) Simulated velocity distribution of H($1^2S_{1/2}$) after Zeeman deceleration (upper panel) and after magnetic guiding in the deflection configuration ($\Delta t_{I_1} = 450$ μs, $\Delta t_{I_2} = 250$ μs) following Zeeman deceleration (lower panel); same scaling as in Figure 7.14. In the legend, 'lfs' ('hfs') denotes particles in low (high)-field-seeking quantum states and 'gas pulse' stands for particles whose motion is not influenced by a magnetic field. (b) Time-of-flight profiles for the same output data as in (a).

Figure 7.16 shows that the transverse distribution of the exiting, slow H atom beam (low-

field-seeking states only) is centred along the axis of the magnetic guide, with a half-width of less than 0.5 mm in either direction. Hence, in this case, the transverse extent of the guided beam is very well matched to the size of a typical Coulomb crystal in an ion trap (few hundred μm). Owing to its low velocity, the beam will rapidly diverge in the transverse direction and provisions must be made to minimise the spreading, e.g. through further transverse focusing and/or by placing the ion trap as close to the guide exit as possible.

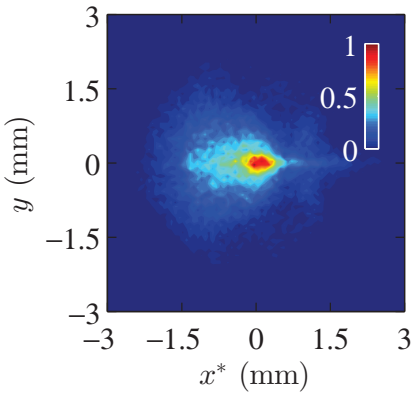

Figure 7.16: Density plot of the simulated transverse particle distribution of H($1^2S_{1/2}$) (at the guide exit; low-field-seeking states only) after Zeeman deceleration and magnetic guiding. The distribution is normalised and shown in the rotating frame of reference. Same settings as in Figure 7.15.

Further work is required to assess the transverse distribution of the guided particles for different final velocities after Zeeman deceleration, since the position of the exiting particles depends strongly on the switching times for the guide, the applied current and the longitudinal beam velocity. Owing to the higher centrifugal force, faster particles are horizontally offset with respect to the slower ones, and I am not convinced whether this effect can be compensated for solely by changing the applied guiding current. If there is a significant transverse offset, other means need to be found to match the guided beam to the position of the Coulomb crystal, e.g. via mechanical alignment or through a re-direction of the beam. With regard to an optimisation of the guiding scheme, it would also be interesting to look at different relative transverse positions (in the x direction) between the Zeeman decelerator and the magnetic guide, as this will influence particle transmission. Even though the length of the guide is very short compared to the bend radius, other trans-

verse dynamics, similar to those observed in molecular synchrotrons [405], may also have to be taken into account.

7.2.5 Other Applications

The proposed guide configurations could also be used for the magnetic velocity selection of effusive or supersonic beams. Such a bent guide would form the magnetic counterpart to the electric velocity filter developed by the Rempe group [34], i.e. it would reject all but the slowest paramagnetic particles from a given velocity distribution.

In the following, the operation of such a guide is demonstrated for the guide geometry presented above using a supersonic beam of ground-state H atoms, which has the same characteristics as the initial beam for Zeeman deceleration (see Section 7.2.4.2 and Chapter 5). The simulated 500 m/s supersonic beam (100,000 particles per Zeeman sublevel) is directed into the guide behind a skimmer (2 mm diameter), and all particles at the guide exit are considered in the analysis. The guide is operated at currents ranging from -400 A to 700 A, using either the two-hexapole or the deflection configuration. Here, the guide is used in a continuous mode, but in experiments, pulsing for the time-of-flight of the supersonic beam ($\approx 200\ \mu$s) would be sufficient.

Figure 7.17 shows that this scheme can indeed be used to selectively guide particles from the low-velocity tail of the initial particle velocity distribution. At zero current through the wires, the simulation predicts that the maximum of the velocity distribution is shifted to 350 m/s, with 10 % of the particles in low-field-seeking quantum states being transmitted. Depending on the current through the guide, the maximum of the velocity distribution can then be shifted to higher (currents with a positive sign) or lower values (currents with a negative sign). In addition to that, the number of transmitted carrier gas particles and particles in high-field-seeking states is several orders of magnitude lower than the initial number of particles, thus ensuring high quantum-state selectivity. However, as this scheme does not actively remove kinetic energy from the beam, the overall transmission

depends strongly on the initial particle velocity distribution. As shown in Figure 7.17b, the number of particles drops off towards lower velocities, even though most particles at these velocities are being guided. The figure also illustrates that the number of guided particles is very similar for the two-hexapole and the deflection configuration, but different currents are required to achieve the same velocity distribution (cf. Section 7.2.4.1).

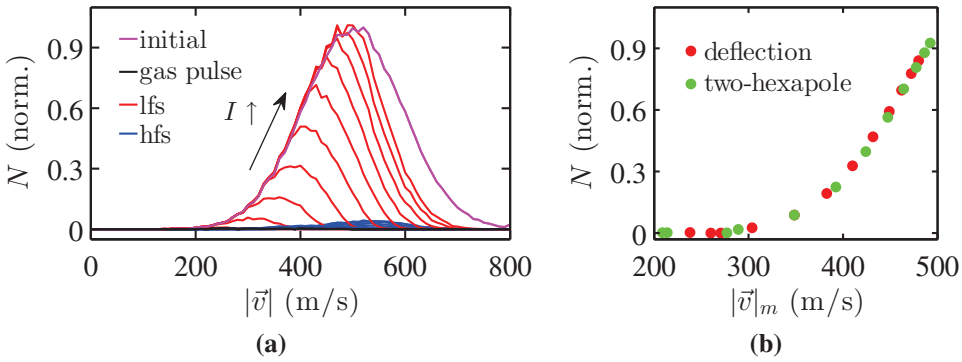

Figure 7.17: (a) Simulated velocity distributions after magnetic velocity selection in the deflection configuration at different wire currents assuming a supersonic beam of H($1^2S_{1/2}$) with an initial velocity distribution centered at 500 m/s. Curves are separately given for non-magnetic particles (black curve, always zero) and particles in low-field-seeking (lfs, red curves) and high-field-seeking quantum states (hfs, blue curves). The initial velocity distribution is shown for comparison (magenta curve). In the legend, 'lfs' ('hfs') denotes particles in low (high)-field-seeking quantum states, 'gas pulse' stands for particles whose motion is not influenced by a magnetic field and 'initial' marks the initial velocity distribution. (b) Normalised number of transmitted H atoms in low-field-seeking states as a function of most probable velocity, $|\vec{v}|_m$, after magnetic guiding of a 500 m/s supersonic beam of H atoms in the two-hexapole (green dots) and deflection configuration (red dots).

The above example illustrates that even undecelerated supersonic beams of H atoms can be magnetically guided, and this mode of operation may prove useful for the initial testing of the guide, as it does not rely on Zeeman deceleration. Likewise, a guide in this configuration would allow for preliminary collision-energy dependent ion-atom collision experiments, without the additional complexity of a Zeeman decelerator. Using different guide geometries (higher remanence for the Halbach segments, lower bend radii, more guide elements), the velocity-dependent guiding of numerous other paramagnetic species would be feasible. The guide could also be used in combination with buffer-gas-cooled sources, similar to pulsed electric guides [406]. If operated in a pulsed mode, such a

guide also presents an alternative way to produce a quantum-state-selected supersonic beam with a very narrow kinetic energy distribution.

7.2.6 Conclusions

As demonstrated through particle trajectory simulations with H atoms, a bent hybrid magnet design can provide a very efficient means to guide a selected particle velocity distribution, particularly in the switched mode of operation. In addition to that, it will ensure a high degree of quantum-state selection and a nearly complete removal of residual carrier gas, which is particularly important for a guide at the end of a short Zeeman decelerator such as in our laboratory.

In the case of a two-hexapole guide, the proposed guide increases the accessible range of transverse magnetic field gradients by a factor of two in comparison to a guide design made solely from current-carrying wires and operated at the same currents. Furthermore, guiding of a certain velocity range is already achieved at zero current through the wires, which is also useful for the initial characterisation of such an experimental setup.

As the guidable velocity range is determined by the remanence of the permanent magnet material and the bend radius, the geometry of a bent hydrid magnetic guide could be tailored to match the requirements for the velocity-selective guiding of a large number of different paramagnetic atoms and molecules.

In conclusion, the design of a magnetic guide/velocity selector discussed in this Chapter, together with the successful Zeeman deceleration experiments for ground-state hydrogen atoms and metastable helium atoms, and the improvements to decelerator transmission and acceptance shown experimentally with hydrogen atoms (Chapter 5) and in theory work (Chapter 3), point towards the future direction of this experiment, i.e. its application in collision experiments, particularly with ion traps. As discussed in Chapter 1, such experiments will remain highly challenging due to the densities of the interacting species. Nevertheless, the work described in this thesis

represents a significant advance towards the goal of studying the dynamics of low energy state-selected ion-radical collisions.

Bibliography

[1] Bethlem, H. L.; Meijer, G. *Int. Rev. Phys. Chem.* **2003**, *22*, 73.

[2] Doyle, J. M.; Friedrich, B.; Krems, R. V.; Masnou-Seeuws, F. *Eur. Phys. J. D* **2004**, *31*, 149.

[3] Schnell, M.; Meijer, G. *Angew. Chem. (int. edit.)* **2009**, *48*, 6010.

[4] Bell, M. T.; Softley, T. P. *Mol. Phys.* **2009**, *107*, 99.

[5] Carr, L. D.; DeMille, D.; Krems, R. V.; Ye, J. *New J. Phys.* **2009**, *11*, 055049.

[6] Krems, R.; Friedrich, B.; Stwalley, W. In *Cold Molecules: Theory, Experiment, Applications*; Krems, R., Friedrich, B., Stwalley, W., Eds.; Taylor & Francis, 2009.

[7] Dulieu, O.; Gabbanini, C. *Rep. Prog. Phys.* **2009**, *72*, 086401.

[8] van de Meerakker, S. Y. T.; Bethlem, H. L.; Vanhaecke, N.; Meijer, G. *Chem. Rev.* **2012**, *112*, 4828.

[9] Lemeshko, M.; Krems, R. V.; Doyle, J. M.; Kais, S. *Mol. Phys.* **2013**, *111*, 1648.

[10] Adams, C. S.; Riis, E. *Prog. Quant. Electron.* **1997**, *21*, 1.

[11] Phillips, W. D. *Rev. Mod. Phys.* **1998**, *70*, 721.

[12] Metcalf, H. J.; Straten, P. v. d. *Laser Cooling and Trapping*; Springer: New York, 1999.

[13] Kellerbauer, A.; Fritzsche, S. *J. Phys. Conf. Ser.* **2012**, *388*, 012023.

[14] Walter, C. W.; Gibson, N. D.; Matyas, D. J.; Crocker, C.; Dungan, K. A.; Matola, B. R.; Rohlén, J. *Phys. Rev. Lett.* **2014**, *113*, 063001.

[15] Shuman, E. S.; Barry, J. F.; DeMille, D. *Nature* **2010**, *467*, 820.

[16] Barry, J. F.; McCarron, D. J.; Norrgard, E. B.; Steinecker, M. H.; DeMille, D. *Nature* **2014**, *512*, 286.

[17] Hummon, M. T.; Yeo, M.; Stuhl, B. K.; Collopy, A. L.; Xia, Y.; Ye, J. *Phys. Rev. Lett.* **2013**, *110*, 143001.

[18] Tarbutt, M. R.; Sauer, B. E.; Hudson, J. J.; Hinds, E. A. *New J. Phys.* **2013**, *15*, 053034.

[19] Zhelyazkova, V.; Cournol, A.; Wall, T. E.; Matsushima, A.; Hudson, J. J.; Hinds, E. A.; Tarbutt, M. R.; Sauer, B. E. *Phys. Rev. A* **2014**, *89*, 053416.

[20] Nguyen, J. H. V.; Odom, B. *Phys. Rev. A* **2011**, *83*, 053404.

[21] Lien, C.-Y.; Seck, C. M.; Lin, Y.-W.; Nguyen, J. H.; Tabor, D. A.; Odom, B. C. *Nature Comm.* **2014**, *5:4783*, 1.

[22] Nguyen, J. H. V.; Viteri, C. R.; Hohenstein, E. G.; Sherrill, C. D.; Brown, K. R.; Odom, B. *New J. Phys.* **2011**, *13*, 063023.

[23] Hutson, J. M.; Soldàn, P. *Int. Rev. Phys. Chem.* **2006**, *25*, 497.

[24] Jones, K. M.; Tiesinga, E.; Lett, P. D.; Julienne, P. S. *Rev. Mod. Phys.* **2006**, *78*, 483.

[25] Köhler, T.; Góral, K.; Julienne, P. S. *Rev. Mod. Phys.* **2006**, *78*, 1311.

[26] Chin, C.; Grimm, R.; Julienne, P.; Tiesinga, E. *Rev. Mod. Phys.* **2010**, *82*, 1225.

[27] Ulmanis, J.; Deiglmayr, J.; Repp, M.; Wester, R.; Weidemüller, M. *Chem. Rev.* **2012**, *112*, 4890.

[28] Hutzler, N. R.; Lu, H.-I.; Doyle, J. M. *Chem. Rev.* **2012**, *112*, 4803.

[29] deCarvalho, R.; Doyle, J. M.; Friedrich, B.; Guillet, T.; Kim, J.; Patterson, D.; Weinstein, J. D. *Eur. Phys. J. D* **1999**, *7*, 289.

[30] Lu, H.-I.; Kozyryev, I.; Hemmerling, B.; Piskorski, J.; Doyle, J. M. *Phys. Rev. Lett.* **2014**, *112*, 113006.

[31] van Buuren, L. D.; Sommer, C.; Motsch, M.; Pohle, S.; Schenk, M.; Bayerl, J.; Pinkse, P. W. H.; Rempe, G. *Phys. Rev. Lett.* **2009**, *102*, 033001.

[32] Twyman, K. S.; Bell, M. T.; Heazlewood, B. R.; Softley, T. P. *J. Chem. Phys.* **2014**, *141*, 024308.

[33] Hansen, A.; Versolato, O.; Kłosowski, Ł.; Kristensen, S.; Gingell, A.; Schwarz, M.; Windberger, A.; Ullrich, J.; López-Urrutia, J. C.; Drewsen, M. *Nature* **2014**, *508*, 76.

[34] Rangwala, S. A.; Junglen, T.; Rieger, T.; Pinkse, P. W. H.; Rempe, G. *Phys. Rev. A* **2003**, *67*, 043406.

[35] Elioff, M. S.; Valentini, J. J.; Chandler, D. W. *Science* **2003**, *302*, 1940.

[36] Liu, N.-N.; Loesch, H. *Phys. Rev. Lett.* **2007**, *98*, 103002.

[37] Kay, J. J.; Kłos, J.; Alexander, M. H.; Strecker, K. E.; Chandler, D. W. *Phys. Rev. A* **2010**, *82*, 032709.

[38] Trottier, A.; Carty, D.; Wrede, E. *Mol. Phys.* **2011**, *109*, 725.

[39] Doherty, W. G.; Bell, M. T.; Softley, T. P.; Rowland, A.; Wrede, E.; Carty, D. *Phys. Chem. Chem. Phys.* **2011**, *13*, 8441.

[40] Dörner, R. et al. *Phys. Rev. Lett.* **1994**, *72*, 3166.

[41] Ghazarian, V.; Eloranta, J.; Apkarian, V. A. *Rev. Sci. Instrum.* **2002**, *73*, 3606.

[42] Gupta, M.; Herschbach, D. *J. Phys. Chem. A* **1999**, *103*, 10670.

[43] Strebel, M.; Stienkemeier, F.; Mudrich, M. *Phys. Rev. A* **2010**, *81*, 033409.

[44] Hogan, S. D.; Motsch, M.; Merkt, F. *Phys. Chem. Chem. Phys.* **2011**, *13*, 18705.

[45] Narevicius, E.; Raizen, M. G. *Chem. Rev.* **2012**, *112*, 4879.

[46] Bethlem, H. L.; Berden, G.; Meijer, G. *Phys. Rev. Lett.* **1999**, *83*, 1558.

[47] Bethlem, H. L.; Berden, G.; Crompvoets, F. M. H.; Jongma, R. T.; van Roij, A. J. A.; Meijer, G. *Nature* **2000**, *406*, 491.

[48] Heiner, C. E.; Carty, D.; Meijer, G.; Bethlem, H. L. *Nat. Phys.* **2007**, *3*, 115.

[49] Procter, S. R.; Yamakita, Y.; Merkt, F.; Softley, T. P. *Chem. Phys. Lett.* **2003**, *374*, 667.

[50] Vliegen, E.; Wörner, H. J.; Softley, T. P.; Merkt, F. *Phys. Rev. Lett.* **2004**, *92*, 033005.

[51] Fulton, R.; Bishop, A. I.; Barker, P. F. *Phys. Rev. Lett.* **2004**, *93*, 243004.

[52] Maher-McWilliams, C.; Douglas, P.; Barker, P. F. *Nat. Photon.* **2012**, *6*, 386.

[53] Enomoto, K.; Momose, T. *Phys. Rev. A* **2005**, *72*, 061403.

[54] Merz, S.; Vanhaecke, N.; Jäger, W.; Schnell, M.; Meijer, G. *Phys. Rev. A* **2012**, *85*, 063411.

[55] Chervenkov, S.; Wu, X.; Bayerl, J.; Rohlfes, A.; Gantner, T.; Zeppenfeld, M.; Rempe, G. *Phys. Rev. Lett.* **2014**, *112*, 013001.

[56] Summhammer, J.; Niel, L.; Rauch, H. *Z. Phys. B - Con. Mat.* **1986**, *62*, 269.

[57] Niel, L.; Rauch, H. *Z. Phys. B - Con. Mat.* **1989**, *74*, 133.

[58] Vanhaecke, N.; Meier, U.; Andrist, M.; Meier, B. H.; Merkt, F. *Phys. Rev. A* **2007**, *75*, 031402.

[59] Narevicius, E.; Libson, A.; Parthey, C. G.; Chavez, I.; Narevicius, J.; Even, U.; Raizen, M. G. *Phys. Rev. Lett.* **2008**, *100*, 093003.

[60] Hogan, S. D.; Sprecher, D.; Andrist, M.; Vanhaecke, N.; Merkt, F. *Phys. Rev. A* **2007**, *76*, 023412.

[61] Wiederkehr, A. W.; Motsch, M.; Hogan, S. D.; Andrist, M.; Schmutz, H.; Lambillotte, B.; Agner, J. A.; Merkt, F. *J. Chem. Phys.* **2011**, *135*, 214202.

[62] Trimeche, A.; Bera, M. N.; Cromières, J.-P.; Robert, J.; Vanhaecke, N. *Eur. Phys. J. D* **2011**, *65*, 263.

[63] Narevicius, E.; Libson, A.; Parthey, C. G.; Chavez, I.; Narevicius, J.; Even, U.; Raizen, M. G. *Phys. Rev. A* **2008**, *77*, 051401.

[64] Wiederkehr, A. W.; Schmutz, H.; Motsch, M.; Merkt, F. *Mol. Phys.* **2012**, *110*, 1807.

[65] Momose, T.; Liu, Y.; Zhou, S.; Djuricanin, P.; Carty, D. *Phys. Chem. Chem. Phys.* **2013**, *15*, 1772.

[66] Motsch, M.; Jansen, P.; Agner, J. A.; Schmutz, H.; Merkt, F. *Phys. Rev. A* **2014**, *89*, 043420.

[67] Phillips, W. D.; Metcalf, H. *Phys. Rev. Lett.* **1982**, *48*, 596.

[68] Meek, S. A.; Bethlem, H. L.; Conrad, H.; Meijer, G. *Phys. Rev. Lett.* **2008**, *100*, 153003.

[69] Meek, S. A.; Parsons, M. F.; Heyne, G.; Platschkowski, V.; Haak, H.; Meijer, G.; Osterwalder, A. *Rev. Sci. Instrum.* **2011**, *82*, 093108.

[70] Osterwalder, A.; Meek, S. A.; Hammer, G.; Haak, H.; Meijer, G. *Phys. Rev. A* **2010**, *81*, 051401.

[71] Hogan, S. D.; Allmendinger, P.; Saßmannshausen, H.; Schmutz, H.; Merkt, F. *Phys. Rev. Lett.* **2012**, *108*, 063008.

[72] Narevicius, E.; Parthey, C. G.; Libson, A.; Riedel, M. F.; Even, U.; Raizen, M. G. *New J. Phys.* **2007**, *9*, 96.

[73] Lavert-Ofir, E.; Gersten, S.; Henson, A. B.; Shani, I.; David, L.; Narevicius, J.; Narevicius, E. *New J. Phys.* **2011**, *13*, 103030.

[74] Lavert-Ofir, E.; David, L.; Henson, A. B.; Gersten, S.; Narevicius, J.; Narevicius, E. *Phys. Chem. Chem. Phys.* **2011**, *13*, 18948.

[75] Quintero-Pérez, M.; Jansen, P.; Wall, T. E.; van den Berg, J. E.; Hoekstra, S.; Bethlem, H. L. *Phys. Rev. Lett.* **2013**, *110*, 133003.

[76] Bulleid, N. E.; Hendricks, R. J.; Hinds, E. A.; Meek, S. A.; Meijer, G.; Osterwalder, A.; Tarbutt, M. R. *Phys. Rev. A* **2012**, *86*, 021404.

[77] Gilijamse, J. J.; Hoekstra, S.; van de Meerakker, S. Y. T.; Groenenboom, G. C.; Meijer, G. *Science* **2006**, *313*, 1617.

[78] van de Meerakker, S. Y. T.; Meijer, G. *Faraday Discuss.* **2009**, *142*, 113.

[79] Scharfenberg, L.; van de Meerakker, S. Y. T.; Meijer, G. *Phys. Chem. Chem. Phys.* **2011**, *13*, 8448.

[80] von Zastrow, A.; Onvlee, J.; Vogels, S. N.; Groenenboom, G. C.; van der Avoird, A.; van de Meerakker, S. Y. T. *Nat. Chem.* **2014**, *6*, 216.

[81] Bethlem, H. L.; van Roij, A. J. A.; Jongma, R. T.; Meijer, G. *Phys. Rev. Lett.* **2002**, *88*, 133003.

[82] Bethlem, H. L.; Tarbutt, M. R.; Küpper, J.; Carty, D.; Wohlfart, K.; Hinds, E. A.; Meijer, G. *J. Phys. B: At. Mol. Opt. Phys.* **2006**, *39*, 263.

[83] Tarbutt, M. R.; Bethlem, H. L.; Hudson, J. J.; Ryabov, V. L.; Ryzhov, V. A.; Sauer, B. E.; Meijer, G.; Hinds, E. A. *Phys. Rev. Lett.* **2004**, *92*, 173002.

[84] Wall, T. E.; Kanem, J. F.; Dyne, J. M.; Hudson, J. J.; Sauer, B. E.; Hinds, E. A.; Tarbutt, M. R. *Phys. Chem. Chem. Phys.* **2011**, *13*, 18991.

[85] Wohlfart, K.; Grätz, F.; Filsinger, F.; Haak, H.; Meijer, G.; Küpper, J. *Phys. Rev. A* **2008**, *77*, 031404.

[86] Wohlfart, K.; Filsinger, F.; Grätz, F.; Küpper, J.; Meijer, G. *Phys. Rev. A* **2008**, *78*, 033421.

[87] Tarbutt, M. R.; Hudson, J. J.; Sauer, B. E.; Hinds, E. A. *Faraday Discuss.* **2009**, *142*, 37.

[88] Crompvoets, F. M. H.; Jongma, R. T.; Bethlem, H. L.; van Roij, A. J. A.; Meijer, G. *Phys. Rev. Lett.* **2002**, *89*, 093004.

[89] Heiner, C. E.; Bethlem, H. L.; Meijer, G. *Phys. Chem. Chem. Phys.* **2006**, *8*, 2666.

[90] Willitsch, S. *Int. Rev. Phys. Chem.* **2012**, *31*, 175.

[91] Staanum, P. F.; Højbjerre, K.; Skyt, P. S.; Hansen, A. K.; Drewsen, M. *Nat. Phys.* **2010**, *6*, 271.

[92] Schneider, T.; Roth, B.; Duncker, H.; Ernsting, I.; Schiller, S. *Nat. Phys.* **2010**, *6*, 275.

[93] Tong, X.; Winney, A. H.; Willitsch, S. *Phys. Rev. Lett.* **2010**, *105*, 143001.

[94] Tong, X.; Wild, D.; Willitsch, S. *Phys. Rev. A* **2011**, *83*, 023415.

[95] Wester, R. *J. Phys. B: At. Mol. Opt. Phys.* **2009**, *42*, 154001.

[96] Härter, A.; Hecker Denschlag, J. *Contemp. Phys.* **2014**, *55*, 33.

[97] Willitsch, S. *P. Int. Sch. Phys., Course 189: Ion Traps for Tomorrows Applications*; IOS Press, 2014.

[98] Rellergert, W. G.; Sullivan, S. T.; Schowalter, S. J.; Kotochigova, S.; Chen, K.; Hudson, E. R. *Nature* **2013**, *495*, 490.

[99] Tokunaga, S.; Skomorowski, W.; Żuchowski, P.; Moszynski, R.; Hutson, J.; Hinds, E.; Tarbutt, M. *Eur. Phys. J. D* **2011**, *65*, 141.

[100] Tscherbul, T. V.; Kłos, J.; Dalgarno, A.; Zygelman, B.; Pavlovic, Z.; Hummon, M. T.; Lu, H.-I.; Tsikata, E.; Doyle, J. M. *Phys. Rev. A* **2010**, *82*, 042718.

[101] Żuchowski, P. S.; Hutson, J. M. *Phys. Chem. Chem. Phys.* **2011**, *13*, 3669.

[102] Skomorowski, W.; González-Martínez, M. L.; Moszynski, R.; Hutson, J. M. *Phys. Chem. Chem. Phys.* **2011**, *13*, 19077.

[103] González-Martínez, M. L.; Hutson, J. M. *Phys. Rev. Lett.* **2013**, *111*, 203004.

[104] Ketterle, W.; Druten, N. V. In *Advances In Atomic, Molecular, and Optical Physics*; Bederson, B., Walther, H., Eds.; Advances In Atomic, Molecular, and Optical Physics; Academic Press, 1996; Vol. 37; pp 181 – 236.

[105] Stuhl, B. K.; Hummon, M. T.; Yeo, M.; Quéméner, G.; Bohn, J. L.; Ye, J. *Nature* **2012**, *492*, 396.

[106] Quintero-Pérez, M.; Wall, T. E.; Hoekstra, S.; Bethlem, H. L. *J. Mol. Spectrosc.* **2014**, *300*, 112.

[107] Marx, S.; Adu Smith, D.; Abel, M. J.; Zehentbauer, T.; Meijer, G.; Santambrogio, G. *Phys. Rev. Lett.* **2013**, *111*, 243007.

[108] Zeppenfeld, M.; Englert, B. G. U.; Glöckner, R.; Prehn, A.; Mielenz, M.; Sommer, C.; van Buuren, L. D.; Motsch, M.; Rempe, G. *Nature* **2012**, *491*, 570.

[109] van de Meerakker, S. Y. T.; Jongma, R. T.; Bethlem, H. L.; Meijer, G. *Phys. Rev. A* **2001**, *64*, 041401.

[110] Jung, S.; Tiemann, E.; Lisdat, C. *Phys. Rev. A* **2006**, *74*, 040701.

[111] Rennick, J., C. Lam, J.; Doherty, G., W. Softley, P., T. *Phys. Rev. Lett.* **2014**, *112*, 023002.

[112] Riedel, J.; Hoekstra, S.; Jäger, W.; Gilijamse, J. J.; van de Meerakker, S. Y. T.; Meijer, G. *Eur. Phys. J. D* **2011**, *65*, 161.

[113] Brouard, M.; Parker, D. H.; van de Meerakker, S. Y. T. *Chem. Soc. Rev.* **2014**, *43*, 7279.

[114] Smalley, R. E.; Wharton, L.; Levy, D. H. *Acc. Chem. Res.* **1977**, *10*, 139.

[115] Levy, D. H. *Annu. Rev. Phys. Chem.* **1980**, *31*, 197.

[116] Levy, D. H. *Science* **1981**, *214*, 263.

[117] van Veldhoven, J.; Küpper, J.; Bethlem, H. L.; Sartakov, B.; van Roij, A. J. A.; Meijer, G. *Eur. Phys. J. D* **2004**, *31*, 337.

[118] Hudson, E. R.; Lewandowski, H. J.; Sawyer, B. C.; Ye, J. *Phys. Rev. Lett.* **2006**, *96*, 143004.

[119] van de Meerakker, S. Y. T.; Vanhaecke, N.; van der Loo, M. P. J.; Groenenboom, G. C.; Meijer, G. *Phys. Rev. Lett.* **2005**, *95*, 013003.

[120] Gilijamse, J. J.; Hoekstra, S.; Meek, S. A.; Metsälä, M.; van de Meerakker, S. Y. T.; Meijer, G.; Groenenboom, G. C. *J. Chem. Phys.* **2007**, *127*, 221102.

[121] Blokland, J. H.; Riedel, J.; Putzke, S.; Sartakov, B. G.; Groenenboom, G. C.; Meijer, G. *J. Chem. Phys.* **2011**, *135*, 114201.

[122] Kirste, M.; Wang, X.; Meijer, G.; Gubbels, K. B.; van der Avoird, A.; Groenenboom, G. C.; van de Meerakker, S. Y. T. *J. Chem. Phys.* **2012**, *137*, 101102.

[123] Campbell, W. C.; Groenenboom, G. C.; Lu, H.-I.; Tsikata, E.; Doyle, J. M. *Phys. Rev. Lett.* **2008**, *100*, 083003.

[124] Hoekstra, S.; Gilijamse, J. J.; Sartakov, B. G.; Vanhaecke, N.; Scharfenberg, L.; van de Meerakker, S. Y. T.; Meijer, G. *Phys. Rev. Lett.* **2007**, *98*, 133001.

[125] Vanhaecke, N.; Dulieu, O. *Mol. Phys.* **2007**, *105*, 1723.

[126] Tsikata, E.; Campbell, W. C.; Hummon, M. T.; Lu, H.-I.; Doyle, J. M. *New J. Phys.* **2010**, *12*, 065028.

[127] Hogan, S. D.; Seiler, C.; Merkt, F. *Phys. Rev. Lett.* **2009**, *103*, 123001.

[128] Seiler, C.; Hogan, S. D.; Schmutz, H.; Agner, J. A.; Merkt, F. *Phys. Rev. Lett.* **2011**, *106*, 073003.

[129] Ubachs, W. M. G.; Steimle, T. *J. Mol. Spectrosc.* **2014**, *300*, 1.

[130] The ACME Collaboration, et al. *Science* **2014**, *343*, 269.

[131] Hudson, J. J.; Kara, D. M.; Smallman, I. J.; Sauer, B. E.; Tarbutt, M. R.; Hinds, E. A. *Nature* **2011**, *473*, 493.

[132] Loh, H.; Cossel, K. C.; Grau, M. C.; Ni, K.-K.; Meyer, E. R.; Bohn, J. L.; Ye, J.; Cornell, E. A. *Science* **2013**, *342*, 1220.

[133] Kozlov, M. G.; Labzowsky, L. N. *J. Phys. B: At. Mol. Opt. Phys.* **1995**, *28*, 1933.

[134] DeMille, D.; Cahn, S. B.; Murphree, D.; Rahmlow, D. A.; Kozlov, M. G. *Phys. Rev. Lett.* **2008**, *100*, 023003.

[135] Isaev, T. A.; Hoekstra, S.; Berger, R. *Phys. Rev. A* **2010**, *82*, 052521.

[136] van den Berg, J.; Turkesteen, S.; Prinsen, E.; Hoekstra, S. *Eur. Phys. J. D* **2012**, *66*, 1.

[137] Borschevsky, A.; Iliaš, M.; Dzuba, V. A.; Beloy, K.; Flambaum, V. V.; Schwerdtfeger, P. *Phys. Rev. A* **2012**, *86*, 050501.

[138] van den Berg, J.; Mathavan, S.; Meinema, C.; Nauta, J.; Nijbroek, T.; Jungmann, K.; Bethlem, H.; Hoekstra, S. *J. Mol. Spectrosc.* **2014**, *300*, 22.

[139] Quack, M. *Angew. Chem. (int. edit.)* **2002**, *41*, 4618.

[140] Darquié, B.; Stoeffler, C.; Shelkovnikov, A.; Daussy, C.; Amy-Klein, A.; Chardonnet, C.; Zrig, S.; Guy, L.; Crassous, J.; Soulard, P.; Asselin, P.; Huet, T. R.; Schwerdtfeger, P.; Bast, R.; Saue, T. *Chirality* **2010**, *22*, 870.

[141] Patterson, D.; Doyle, J. M. *Mol. Phys.* **2012**, *110*, 1757.

[142] Patterson, D.; Schnell, M.; Doyle, J. M. *Nature* **2013**, *497*, 475.

[143] Shubert, V. A.; Schmitz, D.; Patterson, D.; Doyle, J. M.; Schnell, M. *Angew. Chem. (int. edit.)* **2014**, *53*, 1152.

[144] Schnell, M.; Küpper, J. *Faraday Discuss.* **2011**, *150*, 33.

[145] Webb, J. K.; Flambaum, V. V.; Churchill, C. W.; Drinkwater, M. J.; Barrow, J. D. *Phys. Rev. Lett.* **1999**, *82*, 884.

[146] Uzan, J.-P. *Rev. Mod. Phys.* **2003**, *75*, 403.

[147] Chin, C.; Flambaum, V. V.; Kozlov, M. G. *New J. Phys.* **2009**, *11*, 055048.

[148] Kozlov, M. G.; Levshakov, S. A. *Ann. Phys.-Berlin* **2013**, *525*, 452.

[149] Jansen, P.; Bethlem, H. L.; Ubachs, W. *J. Chem. Phys.* **2014**, *140*, 010901.

[150] Rosenband, T. et al. *Science* **2008**, *319*, 1808.

[151] Bagdonaite, J.; Jansen, P.; Henkel, C.; Bethlem, H. L.; Menten, K. M.; Ubachs, W. *Science* **2013**, *339*, 46.

[152] Bethlem, H. L.; Kajita, M.; Sartakov, B.; Meijer, G.; Ubachs, W. *Eur. Phys. J. Spec. Top.* **2008**, *163*, 55.

[153] Santamaria, L.; Sarno, V. D.; Ricciardi, I.; Mosca, S.; Rosa, M. D.; Santambrogio, G.; Maddaloni, P.; Natale, P. D. *J. Mol. Spectrosc.* **2014**, *300*, 116.

[154] Libson, A.; Bannerman, S.; Clark, R.; Mazur, T.; Raizen, M. *Hyperfine Interact.* **2012**, *212*, 203.

[155] Cassidy, D. B.; Hogan, S. D. *Int. J. Mod. Phys. Conf. Ser.* **2014**, *30*, 1460259.

[156] Stuhl, B. K.; Hummon, M. T.; Ye, J. *Annu. Rev. Phys. Chem.* **2014**, *65*, 501.

[157] Quéméner, G.; Julienne, P. S. *Chem. Rev.* **2012**, *112*, 4949.

[158] Scharfenberg, L.; Kłos, J.; Dagdigian, P. J.; Alexander, M. H.; Meijer, G.; van de Meerakker, S. Y. T. *Phys. Chem. Chem. Phys.* **2010**, *12*, 10660.

[159] Kirste, M.; Scharfenberg, L.; Kłos, J.; Lique, F.; Alexander, M. H.; Meijer, G.; van de Meerakker, S. Y. T. *Phys. Rev. A* **2010**, *82*, 042717.

[160] Scharfenberg, L.; Gubbels, K.; Kirste, M.; Groenenboom, G.; van der Avoird, A.; Meijer, G.; van de Meerakker, S. *Eur. Phys. J. D* **2011**, *65*, 189.

[161] Kirste, M.; Wang, X.; Schewe, H. C.; Meijer, G.; Liu, K.; van der Avoird, A.; Janssen, L. M. C.; Gubbels, K. B.; Groenenboom, G. C.; van de Meerakker, S. Y. T. *Science* **2012**, *338*, 1060.

[162] Onvlee, J.; Vogels, S. N.; Zastrow, A. v.; Parker, D. H.; van de Meerakker, S. Y. T. *Phys. Chem. Chem. Phys.* **2014**, *16*, 15768.

[163] Strebel, M.; Müller, T.-O.; Ruff, B.; Stienkemeier, F.; Mudrich, M. *Phys. Rev. A* **2012**, *86*, 062711.

[164] Gubbels, K. B.; van de Meerakker, S. Y. T.; Groenenboom, G. C.; Meijer, G.; van der Avoird, A. *J. Chem. Phys.* **2012**, *136*, 074301.

[165] Schutte, A.; Bassi, D.; Tommasini, F.; Scoles, G. *Phys. Rev. Lett.* **1972**, *29*, 979.

[166] Wei, Q.; Lyuksyutov, I.; Herschbach, D. *J. Chem. Phys.* **2012**, *137*, 054202.

[167] Shagam, Y.; Narevicius, E. *J. Phys. Chem. C* **2013**, *117*, 22454.

[168] Henson, A. B.; Gersten, S.; Shagam, Y.; Narevicius, J.; Narevicius, E. *Science* **2012**, *338*, 234.

[169] Lavert-Ofir, E.; Shagam, Y.; Henson, A. B.; Gersten, S.; Kłos, J.; Żuchowski, P. S.; Narevicius, J.; Narevicius, E. *Nat. Chem.* **2014**, *6*, 332.

[170] Jankunas, J.; Bertsche, B.; Jachymski, K.; Hapka, M.; Osterwalder, A. *J. Chem. Phys.* **2014**, *140*, 244302.

[171] Jankunas, J.; Bertsche, B.; Osterwalder, A. *J. Phys. Chem. A* **2014**, *118*, 3875.

[172] Zieger, P. C.; van de Meerakker, S. Y. T.; Heiner, C. E.; Bethlem, H. L.; van Roij, A. J. A.; Meijer, G. *Phys. Rev. Lett.* **2010**, *105*, 173001.

[173] Zieger, P. C.; Eyles, C. J.; Meerakker, S. Y. T. v. d.; van Roij, A. J. A.; Bethlem, H. L.; Meijer, G. *Z. Phys. Chem.* **2013**, *227*, 1605.

[174] Campbell, W. C.; Tsikata, E.; Lu, H.-I.; van Buuren, L. D.; Doyle, J. M. *Phys. Rev. Lett.* **2007**, *98*, 213001.

[175] Campbell, W. C.; Tscherbul, T. V.; Lu, H.-I.; Tsikata, E.; Krems, R. V.; Doyle, J. M. *Phys. Rev. Lett.* **2009**, *102*, 013003.

[176] Hummon, M. T.; Campbell, W. C.; Lu, H.-I.; Tsikata, E.; Wang, Y.; Doyle, J. M. *Phys. Rev. A* **2008**, *78*, 050702.

[177] Hummon, M. T.; Tscherbul, T. V.; Kłos, J.; Lu, H.-I.; Tsikata, E.; Campbell, W. C.; Dalgarno, A.; Doyle, J. M. *Phys. Rev. Lett.* **2011**, *106*, 053201.

[178] Lu, M.-J.; Weinstein, J. D. *New J. Phys.* **2009**, *11*, 055015.

[179] Singh, V.; Hardman, K. S.; Tariq, N.; Lu, M.-J.; Ellis, A.; Morrison, M. J.; Weinstein, J. D. *Phys. Rev. Lett.* **2012**, *108*, 203201.

[180] Sawyer, B. C.; Stuhl, B. K.; Wang, D.; Yeo, M.; Ye, J. *Phys. Rev. Lett.* **2008**, *101*, 203203.

[181] Pavlovic, Z.; Tscherbul, T. V.; Sadeghpour, H. R.; Groenenboom, G. C.; Dalgarno, A. *J. Phys. Chem. A* **2009**, *113*, 14670.

[182] Tscherbul, T. V.; Pavlovic, Z.; Sadeghpour, H. R.; Côté, R.; Dalgarno, A. *Phys. Rev. A* **2010**, *82*, 022704.

[183] Sawyer, B. C.; Stuhl, B. K.; Yeo, M.; Tscherbul, T. V.; Hummon, M. T.; Xia, Y.; Kłos, J.; Patterson, D.; Doyle, J. M.; Ye, J. *Phys. Chem. Chem. Phys.* **2011**, *13*, 19059.

[184] Parazzoli, L. P.; Fitch, N. J.; Żuchowski, P. S.; Hutson, J. M.; Lewandowski, H. J. *Phys. Rev. Lett.* **2011**, *106*, 193201.

[185] Wynar, R.; Freeland, R. S.; Han, D. J.; Ryu, C.; Heinzen, D. J. *Science* **2000**, *287*, 1016.

[186] Mukaiyama, T.; Abo-Shaeer, J. R.; Xu, K.; Chin, J. K.; Ketterle, W. *Phys. Rev. Lett.* **2004**, *92*, 180402.

[187] Staanum, P.; Kraft, S. D.; Lange, J.; Wester, R.; Weidemüller, M. *Phys. Rev. Lett.* **2006**, *96*, 023201.

[188] Zahzam, N.; Vogt, T.; Mudrich, M.; Comparat, D.; Pillet, P. *Phys. Rev. Lett.* **2006**, *96*, 023202.

[189] Hudson, E. R.; Gilfoy, N. B.; Kotochigova, S.; Sage, J. M.; DeMille, D. *Phys. Rev. Lett.* **2008**, *100*, 203201.

[190] Deiglmayr, J.; Repp, M.; Wester, R.; Dulieu, O.; Weidemüller, M. *Phys. Chem. Chem. Phys.* **2011**, *13*, 19101.

[191] Deiglmayr, J.; Repp, M.; Grochola, A.; Dulieu, O.; Wester, R.; Weidemüller, M. *J. Phys. Conf. Ser.* **2011**, *264*, 012014.

[192] Kraemer, T.; Mark, M.; Waldburger, P.; Danzl, J. G.; Chin, C.; Engeser, B.; Lange, A. D.; Pilch, K.; Jaakkola, A.; Nägerl, H.-C.; Grimm, R. *Nature* **2006**, *440*, 315.

[193] Chin, C.; Kraemer, T.; Mark, M.; Herbig, J.; Waldburger, P.; Nägerl, H.-C.; Grimm, R. *Phys. Rev. Lett.* **2005**, *94*, 123201.

[194] Ospelkaus, S.; Ni, K.-K.; Wang, D.; Miranda, M. H. G. d.; Neyenhuis, B.; Quéméner, G.; Julienne, P. S.; Bohn, J. L.; Jin, D. S.; Ye, J. *Science* **2010**, *327*, 853.

[195] Ni, K.-K.; Ospelkaus, S.; Wang, D.; Quéméner, G.; Neyenhuis, B.; Miranda, M. H. G. d.; Bohn, J. L.; Ye, J.; Jin, D. S. *Nature* **2010**, *464*, 1324.

[196] de Miranda, M. H. G.; Chotia, A.; Neyenhuis, B.; Wang, D.; Quéméner, G.; Ospelkaus, S.; Bohn, J. L.; Ye, J.; Jin, D. S. *Nat. Phys.* **2011**, *7*, 502.

[197] Krems, R. V. *Int. Rev. Phys. Chem.* **2005**, *24*, 99.

[198] Krems, R. V. *Phys. Chem. Chem. Phys.* **2008**, *10*, 4079.

[199] Grätz, F.; Engelhart, D. P.; Wagner, R. J. V.; Haak, H.; Meijer, G.; Wodtke, A. M.; Schäfer, T. *Phys. Chem. Chem. Phys.* **2013**, *15*, 14951.

[200] Drewsen, M.; Jensen, I.; Lindballe, J.; Nissen, N.; Martinussen, R.; Mortensen, A.; Staanum, P.; Voigt, D. *Int. J. Mass Spectrom.* **2003**, *229*, 83.

[201] Willitsch, S.; Bell, M. T.; Gingell, A. D.; Softley, T. P. *Phys. Chem. Chem. Phys.* **2008**, *10*, 7200.

[202] Drewsen, M.; Mortensen, A.; Martinussen, R.; Staanum, P.; Sørensen, J. L. *Phys. Rev. Lett.* **2004**, *93*, 243201.

[203] Schowalter, S. J.; Chen, K.; Rellergert, W. G.; Sullivan, S. T.; Hudson, E. R. *Rev. Sci. Instrum.* **2012**, *83*, 043103.

[204] Schneider, C.; Schowalter, S. J.; Chen, K.; Sullivan, S. T.; Hudson, E. R. *Phys. Rev. Applied* **2014**, *2*, 034013.

[205] Crick, D. R.; Ohadi, H.; Bhatti, I.; Thompson, R. C.; Segal, D. M. *Opt. Express* **2008**, *16*, 2351.

[206] Mølhave, K.; Drewsen, M. *Phys. Rev. A* **2000**, *62*, 011401.

[207] Baba, T.; Waki, I. *J. Chem. Phys.* **2002**, *116*, 1858.

[208] Drewsen, M.; Hornekær, L.; Kjærgaard, N.; Mølhave, K.; Thommesen, A.-M.; Videsen, Z.; Mortensen, A.; Jensen, F. *AIP Conf. Proc.* **2002**, *606*, 135.

[209] Blythe, P.; Roth, B.; Fröhlich, U.; Wenz, H.; Schiller, S. *Phys. Rev. Lett.* **2005**, *95*, 183002.

[210] Roth, B.; Daerr, H.; Blythe, P.; Patacchini, L.; Schiller, S. *J. Phys. B: At. Mol. Opt. Phys.* **2006**, *39*, 1241.

[211] Roth, B.; Wenz, H.; Daerr, H.; Schiller, S. *Phys. Rev. A* **2006**, *73*, 042712.

[212] Roth, B.; Offenberg, D.; Zhang, C. B.; Schiller, S. *Phys. Rev. A* **2008**, *78*, 042709.

[213] Staanum, P. F.; Højbjerre, K.; Wester, R.; Drewsen, M. *Phys. Rev. Lett.* **2008**, *100*, 243003.

[214] Hansen, A. K.; Sørensen, M. A.; Staanum, P. F.; Drewsen, M. *Angew. Chem. (int. edit.)* **2012**, *51*, 7960.

[215] Willitsch, S.; Bell, M. T.; Gingell, A. D.; Procter, S. R.; Softley, T. P. *Phys. Rev. Lett.* **2008**, *100*, 043203.

[216] Bell, M. T. Cold chemistry in the gas phase using velocity selection and molecular deceleration. Ph.D. thesis, University of Oxford, 2008.

[217] Bell, M. T.; Gingell, A. D.; Oldham, J. M.; Softley, T. P.; Willitsch, S. *Faraday Discuss.* **2009**, *142*, 73.

[218] Gingell, A. D. Applications of Coulomb crystals in cold chemistry. Ph.D. thesis, University of Oxford, 2010.

[219] Gingell, A. D.; Bell, M. T.; Oldham, J. M.; Softley, T. P.; Harvey, J. N. *J. Chem. Phys.* **2010**, *133*, 194302.

[220] Okada, K.; Suganuma, T.; Furukawa, T.; Takayanagi, T.; Wada, M.; Schuessler, H. A. *Phys. Rev. A* **2013**, *87*, 043427.

[221] Harper, L. D. Stark deceleration and reactivity of polyatomic molecules and ions at low temperatures. Ph.D. thesis, University of Oxford, 2013.

[222] Twyman, K. Electrostatic extraction of buffer-gas-cooled beams for studying ion-molecule chemistry at low temperatures. Ph.D. thesis, University of Oxford, 2014.

[223] Chang, Y.-P.; Długołęcki, K.; Küpper, J.; Rösch, D.; Wild, D.; Willitsch, S. *Science* **2013**, *342*, 98.

[224] Anicich, V. G. *JPL-Publication-03-19, JPL TRS 1992+*; Jet Propulsion Laboratory: Pasadena, CA, USA, 2003.

[225] Snow, T. P.; Bierbaum, V. M. *Annu. Rev. Anal. Chem.* **2008**, *1*, 229.

[226] Oka, T. *Chem. Rev.* **2013**, *113*, 8738.

[227] Borodi, G.; Luca, A.; Gerlich, D. *Int. J. Mass Spectrom.* **2009**, *280*, 218.

[228] Zipf, E. C. *Can. J. Chemistry* **1969**, *47*, 1863.

[229] Takayanagi, K.; Itikawa, Y. *Space Sci. Rev.* **1970**, *11*, 380.

[230] Chakrabarti, S. *J. Atmos. Sol.-Terr. Phys.* **1998**, *60*, 1403.

[231] Galand, M.; Chakrabarti, S. In *Atmospheres in the Solar System: Comparative Aeronomy*; Mendillo, M., Nagy, A., Waite, J., Eds.; American Geophysical Union, 2013; Chapter I.4, pp 55 – 76.

[232] Kim, S.; Lee, Y.; Kim, Y. *Planet. Space Sci.* **2001**, *49*, 117.

[233] Baulch, D. L.; Bowman, C. T.; Cobos, C. J.; Cox, R. A.; Just, T.; Kerr, J. A.; Pilling, M. J.; Stocker, D.; Troe, J.; Tsang, W.; Walker, R. W.; Warnatz, J. *J. Phys. Chem. Ref. Data* **2005**, *34*, 757.

[234] Herron, J.; Green, D. *Plasma Chem. Plasma P.* **2001**, *21*, 459.

[235] Miller, D. R. In *Atomic and Molecular Beam Methods*; Scoles, G., Ed.; Oxford University Press: New York, 1988; Vol. 1; Chapter 2, pp 14 – 53.

[236] Morse, M. D. In *Atomic, Molecular, and Optical Physics: Atoms and Molecules*; Dunning, F., Hulet, R. G., Eds.; Experimental Methods in the Physical Sciences; Academic Press, 1996; Vol. 29, Part B; pp 21 – 47.

[237] Lubman, D. M.; Rettner, C. T.; Zare, R. N. *J. Phys. Chem.* **1982**, *86*, 1129.

[238] Toennies, J. P.; Winkelmann, K. *J. Chem. Phys.* **1977**, *66*, 3965.

[239] Ashkenas, H.; Sherman, F. S. In *Rarefied Gas Dynamics: Proceedings of the 4th International Symposium on Rarefied Gas Dynamics*; de Leeuw, J. H., Ed.; Advances in Applied Mechanics, Suppl. 3; Academic Press: New York, 1966; Vol. II; Chapter 7, pp 84 – 105.

[240] Oman, R. A.; Bogan, A.; Weiser, C. H.; C. H. Li, G. *Grumman Research Department Report RE-166*; 1963.

[241] Anderson, J. B.; Andres, R. P.; Fenn, J. B. In *Advances in Chemical Physics*; Ross, J., Ed.; Adv. Chem. Phys.: Molecular Beams; Wiley, 1966; Vol. 10; Chapter 8, pp 275 – 317.

[242] Liepmann, H. W.; Roshko, A. In *Elements of Gasdynamics*; Roshko, A., Ed.; Calcit Aeronautical Series; Wiley: New York, 1957; Chapter 2, pp 39 – 61.

[243] Christen, W.; Rademann, K. *Phys. Rev. A* **2008**, *77*, 012702.

[244] Haberland, H.; Buck, U.; Tolle, M. *Rev. Sci. Instrum.* **1985**, *56*, 1712.

[245] Gay, T. J. In *Atomic, Molecular, and Optical Physics: Atoms and Molecules*; Dunning, F., Hulet, R. G., Eds.; Experimental Methods in the Physical Sciences; Academic Press, 1996; Vol. 29, Part B; pp 95 – 114.

[246] Kramida, A.; Ralchenko, Y.; Reader, J.; and NIST ASD Team, NIST Atomic Spectra Database (Version 5.1). [Online]. Available: http://physics.nist.gov/asd [2014, June 5], 2013.

[247] Misakian, M.; Mumma, M. J. *Rev. Sci. Instrum.* **1974**, *45*, 296.

[248] Trajmar, S.; Nickel, J. In *Advances In Atomic, Molecular, and Optical Physics*; Bates, D., Bederson, B., Eds.; Advances In Atomic, Molecular, and Optical Physics; Academic Press, 1992; Vol. 30; pp 45 – 103.

[249] Reis, V. H.; Fenn, J. B. *J. Chem. Phys.* **1963**, *39*, 3240.

[250] Koplitz, B.; Xu, Z.; Wittig, C. *Chem. Phys. Lett.* **1987**, *137*, 505.

[251] Salathé, Y. Optimizing Zeeman Deceleration of Atomic Hydrogen by Evolutionary Algorithms. B.Sc. thesis, ETH Zurich, 2009.

[252] Wiederkehr, A. W. Multistage Zeeman deceleration of atoms and molecules. Ph.D. thesis, ETH Zürich, 2012.

[253] Matsumoto, M.; Nishimura, T. *ACM Trans. Model. Comput. Simul.* **1998**, *8*, 3.

[254] Bergeman, T.; Erez, G.; Metcalf, H. J. *Phys. Rev. A* **1987**, *35*, 1535.

[255] Kang, H. R. *Computational Color Technology*; SPIE Press: Bellingham, Washington USA, 2006; Chapter 9, pp 151–159.

[256] Weinreich, G.; Hughes, V. W. *Phys. Rev.* **1954**, *95*, 1451.

[257] Radford, H. E.; Evenson, K. M. *Phys. Rev.* **1968**, *168*, 70.

[258] Drake, C. W.; Hughes, V. W.; Lurio, A.; White, J. A. *Phys. Rev.* **1958**, *112*, 1627.

[259] Beltrán-López, V.; Rangel G., J.; González-Nucamendi, A.; Jiménez-Mier, J.; Fuentes-Maya, A. *Phys. Rev. A* **1989**, *39*, 58.

[260] Feynman, R.; Leighton, R.; Sands, M. *The Feynman Lectures on Physics*, 6th ed.; The Feynman Lectures on Physics; Pearson/Addison-Wesley: Reading, Massachusetts, 1963; Vol. III; Chapter 12, p 1 = 16.

[261] Cohen-Tannoudji, C.; Diu, B.; Laloë, F. *Quantum Mechanics*; Hermann, Wiley: Paris, 1977; Vol. II; Chapter XII, pp 1232 – 1245.

[262] Verlet, L. *Phys. Rev.* **1967**, *159*, 98.

[263] Swope, W. C.; Andersen, H. C.; Berens, P. H.; Wilson, K. R. *J. Chem. Phys.* **1982**, *76*, 637.

[264] National Geophysical Data Center, Magnetic Field Calculators, Magnetic Field. [Online]. Available: `http://www.ngdc.noaa.gov/geomag-web` [2014, October 12].

[265] McMillan, E. M. *Phys. Rev.* **1945**, *68*, 143–144.

[266] Veksler, V. *J. Phys.* **1945**, *9*, 153–158.

[267] Bethlem, H. L.; Berden, G.; van Roij, A. J. A.; Crompvoets, F. M. H.; Meijer, G. *Phys. Rev. Lett.* **2000**, *84*, 5744.

[268] Bethlem, H. L.; Crompvoets, F. M. H.; Jongma, R. T.; van de Meerakker, S. Y. T.; Meijer, G. *Phys. Rev. A* **2002**, *65*, 053416.

[269] van de Meerakker, S. Y. T.; Vanhaecke, N.; Bethlem, H. L.; Meijer, G. *Phys. Rev. A* **2006**, *73*, 023401.

[270] van de Meerakker, S. Y. T.; Vanhaecke, N.; Bethlem, H. L.; Meijer, G. *Phys. Rev. A* **2005**, *71*, 053409.

[271] Scharfenberg, L.; Haak, H.; Meijer, G.; van de Meerakker, S. Y. T. *Phys. Rev. A* **2009**, *79*, 023410.

[272] Wiederkehr, A. W.; Hogan, S. D.; Merkt, F. *Phys. Rev. A* **2010**, *82*, 043428.

[273] Hogan, S. D.; Wiederkehr, A. W.; Andrist, M.; Schmutz, H.; Merkt, F. *J. Phys. B: At. Mol. Opt. Phys.* **2008**, *41*, 081005.

[274] TURBOVAC SL 700, Wide-Range Turbomolecular Pump with Integrated or External Frequency Converter, Operating Instructions. Oerlikon Leybold Vacuum GmbH: Cologne, Germany, 2008.

[275] TURBOVAC, Turbomolecular pumps with grease-lubricated bearings, Operating Instructions. Leybold Vacuum GmbH: Cologne, Germany, 2005.

[276] Cheng, B.-M.; Lu, H.-C.; Chen, H.-K.; Bahou, M.; Lee, Y.-P.; Mebel, A. M.; Lee, L. C.; Liang, M.-C.; Yung, Y. L. *Astrophys. J.* **2006**, *647*, 1535.

[277] Bethe, H. A.; Salpeter, E. E. *Quantum Mechanics of One- and Two-Electron Atoms*; Springer: Berlin, 1957; Chapter IV, pp 258, 284 – 288.

[278] Oed, A. *Phys. Lett. A* **1973**, *45*, 25.

[279] Chluba, J.; Sunyaev, R. A. *Astron. Astrophys.* **2008**, *480*, 629.

[280] Fabrikant, I.; Shpenik, O.; Snegursky, A.; Zavilopulo, A. *Phys. Rep.* **1988**, *159*, 1.

[281] Dunning, F. B.; Stebbings, R. F. *Phys. Rev. Lett.* **1974**, *32*, 1286.

[282] Campargue, R. *J. Phys. Chem.* **1984**, *88*, 4466.

[283] Even, U.; Jortner, J.; Noy, D.; Lavie, N.; Cossart-Magos, C. *J. Chem. Phys.* **2000**, *112*, 8068.

[284] Irimia, D.; Dobrikov, D.; Kortekaas, R.; Voet, H.; van den Ende, D. A.; Groen, W. A.; Janssen, M. H. M. *Rev. Sci. Instrum.* **2009**, *80*, 113303.

[285] Yan, B.; Claus, P. F. H.; van Oorschot, B. G. M.; Gerritsen, L.; Eppink, A. T. J. B.; van de Meerakker, S. Y. T.; Parker, D. H. *Rev. Sci. Instrum.* **2013**, *84*, 023102.

[286] Murray, A. J.; Hammond, P. *Rev. Sci. Instrum.* **1999**, *70*, 1939.

[287] Seamans, J. F.; Kimura, W. D. *Rev. Sci. Instrum.* **1993**, *64*, 460.

[288] Parthey, C. G. Pulsed Magnetic Slowing of Supersonic Beams. M.Sc. thesis, University of Texas at Austin, 2007.

[289] Haq, S. U. A Study on Insulation Problems in Drive Fed Medium Voltage Induction Motors. Ph.D. thesis, University of Waterloo, 2007.

[290] Meeker, D. C. Finite Element Method Magnetics (Version 4.2). [Online]. Available: `http://www.femm.info` [2014, Aug 2], 2010.

[291] Dimov, S. S.; Cai, J. Y.; Lipson, R. H. *J. Chem. Phys.* **1994**, *101*, 10313.

[292] Raptis, C. A.; Pratt, S. T. *J. Chem. Phys.* **2001**, *115*, 2483.

[293] Quanta-Ray PDL-3, Pulsed Dye Laser, Instruction Manual. Spectra-Physics: Mountain View, CA; Darmstadt, Germany, 1989.

[294] Foot, C. J. *Atomic Physics*; Oxford Master Series in Physics; Oxford University Press, 2005; Chapter 7, pp 142 – 143.

[295] Downey, S. W.; Hozack, R. S. *Opt. Lett.* **1989**, *14*, 15.

[296] Redman, S. A.; Chung, C.; Rosser, K. N.; Ashfold, M. N. R. *Phys. Chem. Chem. Phys.* **1999**, *1*, 1415.

[297] Haberland, H.; Oschwald, M.; Broad, J. T. *J. Phys. B: At. Mol. Opt. Phys.* **1987**, *20*, 3367.

[298] Haberland, H.; Oschwald, M. *J. Phys. B: At. Mol. Opt. Phys.* **1988**, *21*, 1183.

[299] Halfmann, T.; Koensgen, J.; Bergmann, K. *Meas. Sci. Technol.* **2000**, *11*, 1510.

[300] Halfmann, T.; Rickes, T.; Vitanov, N. V.; Bergmann, K. *Opt. Comm.* **2003**, *220*, 353.

[301] Clouthier, D. J.; Karolczak, J. *Rev. Sci. Instrum.* **1990**, *61*, 1607.

[302] Wiley, W. C.; McLaren, I. H. *Rev. Sci. Instrum.* **1955**, *26*, 1150.

[303] Haynes, W. *CRC Handbook of Chemistry and Physics, 95th Ed.*; Taylor & Francis, 2014-2015.

[304] Wall, T. E.; Tokunaga, S. K.; Hinds, E. A.; Tarbutt, M. R. *Phys. Rev. A* **2010**, *81*, 033414.

[305] Meek, S. A.; Santambrogio, G.; Sartakov, B. G.; Conrad, H.; Meijer, G. *Phys. Rev. A* **2011**, *83*, 033413.

[306] Sawyer, B. C.; Stuhl, B. K.; Lev, B. L.; Ye, J.; Hudson, E. R. *Eur. Phys. J. D* **2008**, *48*, 197.

[307] Hogan, S. D.; Wiederkehr, A. W.; Schmutz, H.; Merkt, F. *Phys. Rev. Lett.* **2008**, *101*, 143001.

[308] Wiederkehr, A. W.; Hogan, S. D.; Lambillotte, B.; Andrist, M.; Schmutz, H.; Agner, J.; Salathé, Y.; Merkt, F. *Phys. Rev. A* **2010**, *81*, 021402.

[309] Hotop, H. In *Atomic, Molecular, and Optical Physics: Atoms and Molecules*; Dunning, F., Hulet, R. G., Eds.; Experimental Methods in the Physical Sciences; Academic Press, 1996; Vol. 29, Part B; pp 191 – 215.

[310] Wayne, R. P. *Chemistry of Atmospheres*, 3rd ed.; Oxford University Press: Oxford, 2000; Chapter 6, 8, pp 481 – 524, 561 – 650.

[311] Rees, M. H.; Romick, G. J. *J. Geophys. Res. - Space* **1985**, *90*, 9871.

[312] Bishop, J.; Link, R. *J. Geophys. Res. - Space* **1999**, *104*, 17157.

[313] Rundel, R. D.; Stebbings, R. F. *J. Geophys. Res. - Space* **1974**, *79*, 681.

[314] Frederick, J. E.; Rusch, D. W. *J. Geophys. Res.* **1977**, *82*, 3509.

[315] Torr, D.; Torr, M. *J. Atmos. Terr. Phys.* **1979**, *41*, 797.

[316] Bakalian, F. *Icarus* **2006**, *183*, 69.

[317] Imanaka, H.; Smith, M. A. *P. Natl. Acad. Sci. USA* **2010**, *107*, 12423.

[318] Donovan, R. J.; Husain, D. *Chem. Rev.* **1970**, *70*, 489.

[319] Herron, J. T. *J. Phys. Chem. Ref. Data* **1999**, *28*, 1453.

[320] Hodgman, S. S.; Dall, R. G.; Byron, L. J.; Baldwin, K. G. H.; Buckman, S. J.; Truscott, A. G. *Phys. Rev. Lett.* **2009**, *103*, 053002.

[321] Wiese, W. L.; Fuhr, J. R. *J. Phys. Chem. Ref. Data* **2007**, *36*, 1287.

[322] Zinner, M.; Spoden, P.; Kraemer, T.; Birkl, G.; Ertmer, W. *Phys. Rev. A* **2003**, *67*, 010501.

[323] Shemansky, D. E. *J. Chem. Phys.* **1969**, *51*, 689.

[324] Lefers, J.; Miller, N.; Rupke, D.; Tong, D.; Walhout, M. *Phys. Rev. A* **2002**, *66*, 012507.

[325] Mishra, A. P.; Balasubramanian, T. *J. Quant. Spectrosc. Ra.* **2001**, *69*, 769.

[326] Lichten, W. *Phys. Rev.* **1962**, *126*, 1020.

[327] Siska, P. E. *Rev. Mod. Phys.* **1993**, *65*, 337.

[328] Brutschy, B.; Haberland, H. *J. Phys. E: Sci. Instrum.* **1977**, *10*, 90.

[329] Yoon, J.-S.; Song, M.-Y.; Han, J.-M.; Hwang, S. H.; Chang, W.-S.; Lee, B.; Itikawa, Y. *J. Phys. Chem. Ref. Data* **2008**, *37*, 913.

[330] Misakian, M.; Zorn, J. C. *Phys. Rev. A* **1972**, *6*, 2180.

[331] Eyler, E. E.; Pipkin, F. M. *Phys. Rev. A* **1983**, *27*, 2462.

[332] Tischer, H.; Phelps, A. *Chem. Phys. Lett.* **1985**, *117*, 550.

[333] Wedding, A. B.; Phelps, A. V. *J. Chem. Phys.* **1988**, *89*, 2965.

[334] Tommasi, O.; Bertuccelli, G.; Francesconi, M.; Giammanco, F.; Romanini, D.; Strumia, F. *J. Phys. D: Appl. Phys.* **1992**, *25*, 1408.

[335] Chiu, L.-Y. C.; Bhattacharyya, D. K. *J. Chem. Phys.* **1979**, *70*, 4376.

[336] Bhattacharyya, S.; Bhattacharyya, D. K. *J. Phys. Chem.* **1993**, *97*, 4899.

[337] Berg, C.; Ottinger, C. *J. Chem. Phys.* **1994**, *100*, 8746.

[338] Schulz, G. J.; Fox, R. E. *Phys. Rev.* **1957**, *106*, 1179.

[339] Holt, H. K.; Krotkov, R. *Phys. Rev.* **1966**, *144*, 82.

[340] Johnston, A. R.; Burrow, P. D. *J. Phys. B: At. Mol. Opt. Phys.* **1983**, *16*, 613.

[341] Darwent, B. *Bond dissociation energies in simple molecules*; NSRDS-NBS; U.S. National Bureau of Standards, 1970; Vol. 31.

[342] Nasser, E. In *Fundamentals of Gaseous Ionization and Plasma Electronics*; Brown, S. E., Ed.; Wiley Series in Plasma Physics; Wiley: New York, 1971; pp 203; 245 – 248.

[343] Raizer, Y. P. *Gas Discharge Physics*; Springer: New York, 1997.

[344] McDaniel, W. In *Collision Phenomena in Ionized Gases*; Brown, S. E., Ed.; Wiley Series in Plasma Physics; Wiley: New York, 1964; pp 35; 38 – 39.

[345] Lias, S. G. *Ionization Energy Evaluation*; NIST Chemistry WebBook, NIST Standard Reference Database 69; National Institute of Standards and Technology: Gaithersburg MD, 20899, 2014.

[346] Guerra, V.; Tatarova, E.; Ferreira, C. *Vacuum* **2002**, *69*, 171.

[347] Tsyganov, D.; Pancheshnyi, S. *Plasma Sources Sci. T.* **2012**, *21*, 065010.

[348] Cosby, P. C. *J. Chem. Phys.* **1993**, *98*, 9544.

[349] Peterson, J. R.; Le Padellec, A.; Danared, H.; Dunn, G. H.; Larsson, M.; Larson, A.; Peverall, R.; Strömholm, C.; Rosén, S.; af Ugglas, M.; van der Zande, W. J. *J. Chem. Phys.* **1998**, *108*, 1978.

[350] Foner, S. N.; Hudson, R. L. *J. Chem. Phys.* **1962**, *37*, 1662.

[351] Lin, C.-L.; Kaufman, F. *J. Chem. Phys.* **1971**, *55*, 3760.

[352] Omidvar, K. *Phys. Rev. A* **1980**, *22*, 1576.

[353] Omidvar, K. *Phys. Rev. A* **1984**, *30*, 2805.

[354] MOPO-FDO, FDO-900, Frequency Doubler Option, User's Manual. Spectra-Physics: Mountain View, CA, 1996.

[355] Phelps, A. V. *Phys. Rev.* **1955**, *99*, 1307.

[356] Schmeltekopf, A. L.; Fehsenfeld, F. C. *J. Chem. Phys.* **1970**, *53*, 3173.

[357] Raunhardt, M. Generation and spectroscopy of atoms and molecules in metastable states. Ph.D. thesis, ETH Zürich, 2009.

[358] Vassen, W.; Cohen-Tannoudji, C.; Leduc, M.; Boiron, D.; Westbrook, C. I.; Truscott, A.; Baldwin, K.; Birkl, G.; Cancio, P.; Trippenbach, M. *Rev. Mod. Phys.* **2012**, *84*, 175.

[359] Hudson, E. R.; Bochinski, J. R.; Lewandowski, H. J.; Sawyer, B. C.; Ye, J. *Eur. Phys. J. D* **2004**, *31*, 351.

[360] Hudson, E. R. Experiments on Cold Molecules Produced via Stark Deceleration. Ph.D. thesis, University of Colorado, 2006.

[361] Friedburg, H. *Z. Phys. A - Hadron Nucl.* **1951**, *130*, 493.

[362] Friedburg, H.; Paul, W. *Naturwissenschaften* **1951**, *38*, 159.

[363] Lemonick, A.; Pipkin, F. M. *Phys. Rev.* **1954**, *95*, 1356.

[364] Lemonick, A.; Pipkin, F. M.; Hamilton, D. R. *Rev. Sci. Instrum.* **1955**, *26*, 1112.

[365] Haeberli, W. *Ann. Rev. Nucl. Sci.* **1967**, *17*, 373.

[366] Oku, T.; Yamada, S.; Sasao, H.; ichi Suzuki, J.; Shinohara, T.; Hirota, K.; Ikeda, K.; Tsuzaki, T.; Kiyanagi, Y.; Furusaka, M.; Shimizu, H. M. *Physica B* **2006**, *385*, 1225.

[367] Woestenenk, G. R.; Thomsen, J. W.; Rijnbach, M. v.; Straten, P. v. d.; Niehaus, A. *Rev. Sci. Instrum.* **2001**, *72*, 3842.

[368] Meschede, D.; Metcalf, H. *J. Phys. D: Appl. Phys.* **2003**, *36*, 17.

[369] Jardine, A. P.; Dworski, S.; Fouquet, P.; Alexandrowicz, G.; Riley, D. J.; Lee, G. Y. H.; Ellis, J.; Allison, W. *Science* **2004**, *304*, 1790.

[370] Kurahashi, M.; Yamauchi, Y. *Phys. Rev. A* **2008**, *78*, 022708.

[371] Watanabe, D.; Ohoyama, H.; Matsumura, T.; Kasai, T. *Eur. Phys. J. D* **2006**, *38*, 219.

[372] Kravchuk, T.; Reznikov, M.; Tichonov, P.; Avidor, N.; Meir, Y.; Bekkerman, A.; Alexandrowicz, G. *Science* **2011**, *331*, 319.

[373] Halbach, K. *Nucl. Instrum. Methods* **1980**, *169*, 1.

[374] Halbach, K. *Nucl. Instrum. Methods* **1981**, *187*, 109.

[375] Schiemenz, P.; Ross, A.; Graw, G. *Nucl. Instrum. Meth. A* **1991**, *305*, 15.

[376] Kaenders, W. G.; Lison, F.; Richter, A.; Wynands, R.; Meschede, D. *Nature* **1995**, *375*, 214.

[377] Kaenders, W. G.; Lison, F.; Müller, I.; Richter, A.; Wynands, R.; Meschede, D. *Phys. Rev. A* **1996**, *54*, 5067.

[378] Szczerba, D.; van Buuren, L. D.; van den Brand, J. F. J.; Bulten, H. J.; Ferro-Luzzi, M.; Klous, S.; Kolster, H.; Lang, J.; Mul, F.; Poolman, H. R.; Simani, M. C. *Nucl. Instrum. Meth. A* **2000**, *455*, 769.

[379] Dworski, S.; Alexandrowicz, G.; Fouquet, P.; Jardine, A. P.; Allison, W.; Ellis, J. *Rev. Sci. Instrum.* **2004**, *75*, 1963.

[380] Chaustowski, R.; Leung, V.; Baldwin, K. *Appl. Phys. B - Lasers O.* **2007**, *86*, 491.

[381] Sun, L. T.; Zhao, H. W.; Zhang, Z. M.; Wang, H.; Ma, B. H.; Zhang, X. Z.; Li, X. X.; Feng, Y. C.; Li, J. Y.; Guo, X. H.; Shang, Y.; Zhao, H. Y. *Rev. Sci. Instrum.* **2007**, *78*, 053302.

[382] Gardner, J.; Castillo-Garza, R.; Raizen, M. G. *J. Chem. Phys.* **2013**, *139*, 096103.

[383] Mazur, T. R.; Klappauf, B.; Raizen, M. G. *Nat. Phys.* **2014**, *10*, 601.

[384] Chavanne, J. Radia (Version 4.29). [Online]. Available: http://www.esrf.eu/Accelerators/Groups/InsertionDevices/Software/Radia [2014, Aug 2], 2009.

[385] Elleaume, P.; Chubar, O.; Chavanne, J. *Proc. IEEE, PAC-97* **1997**, *3*, 3509.

[386] Chubar, O.; Elleaume, P.; Chavanne, J. *J. Synchrotron Radiat.* **1998**, *5*, 481.

[387] Rossbach, J.; Schmüser, P. *Conf.Proc.* **1993**, *C9209071*, 17.

[388] Ackermann, W.; Weiland, T. *Proc. IEEE, PAC-05* **2005**, 4036.

[389] Glaser, W. *Z. Phys. A - Hadron Nucl.* **1941**, *117*, 285.

[390] Rossi, M. Atomlithographie, Hauptseminar Ultrakalte Atome und Atomoptik. [Online]. Available: http://www.plasmatod.de/hs2k/atomlithographie_2.html [2014, July 24], SS 2000.

[391] Zhang, W. Z.; Schmelzbach, P. A.; Singy, D.; Grüebler, W. *Nucl. Instrum. Meth. A* **1985**, *240*, 229.

[392] Grüebler, E. *AIP Conf. Proc.* **1982**, *80*, 53.

[393] Rakitzis, T. P. *Chem. Phys. Chem.* **2004**, *5*, 1489.

[394] Kügler, K.-J.; Moritz, K.; Paul, W.; Trinks, U. *Nucl. Instrum. Methods* **1985**, *228*, 240.

[395] Thompson, D.; Lovelace, R. V. E.; Lee, D. M. *J. Opt. Soc. Am. B* **1989**, *6*, 2227.

[396] Folman, R.; Krüger, P.; Schmiedmayer, J.; Denschlag, J.; Henkel, C. In *Advances In Atomic, Molecular, and Optical Physics*; Bederson, B., Walther, H., Eds.; Advances In Atomic, Molecular, and Optical Physics; Academic Press, 2002; Vol. 48; pp 263 – 356.

[397] Fortágh, J.; Zimmermann, C. *Rev. Mod. Phys.* **2007**, *79*, 235.

[398] Tonyushkin, A.; Prentiss, M. *J. Appl. Phys.* **2010**, *108*, 094904.

[399] Greiner, M.; Bloch, I.; Hänsch, T. W.; Esslinger, T. *Phys. Rev. A* **2001**, *63*, 031401.

[400] Ghaffari, B.; Gerton, J. M.; McAlexander, W. I.; Strecker, K. E.; Homan, D. M.; Hulet, R. G. *Phys. Rev. A* **1999**, *60*, 3878.

[401] Hulet, R.; Strecker, K.; Gerton, J.; Mcalexander, W.; Bradley, C.; Tollett, J.; Sackett, C.; Ghaffari, B.; Moss, S. Method and apparatus for magnetically guiding neutral particles. 2003.

[402] Patterson, D.; Doyle, J. M. *J. Chem. Phys.* **2007**, *126*, 154307.

[403] Goepfert, A.; Lison, F.; Schütze, R.; Wynands, R.; Haubrich, D.; Meschede, D. *Appl. Phys. B - Lasers O.* **1999**, *69*, 217.

[404] Beardmore, J. P.; Palmer, A. J.; Kuiper, K. C.; Sang, R. T. *Rev. Sci. Instrum.* **2009**, *80*, 073105.

[405] Heiner, C. E.; Meijer, G.; Bethlem, H. L. *Phys. Rev. A* **2008**, *78*, 030702.

[406] Sommer, C.; Motsch, M.; Chervenkov, S.; van Buuren, L. D.; Zeppenfeld, M.; Pinkse, P. W. H.; Rempe, G. *Phys. Rev. A* **2010**, *82*, 013410.

[407] Furlani, E. P. In *Permanent Magnet and Electromechanical Devices: Materials, Analysis, and Applications*; Mayergoyz, I., Ed.; Academic Press Series in Electromagnetism; Academic Press, 2001.

8 | Electrical Connections to Decelerator

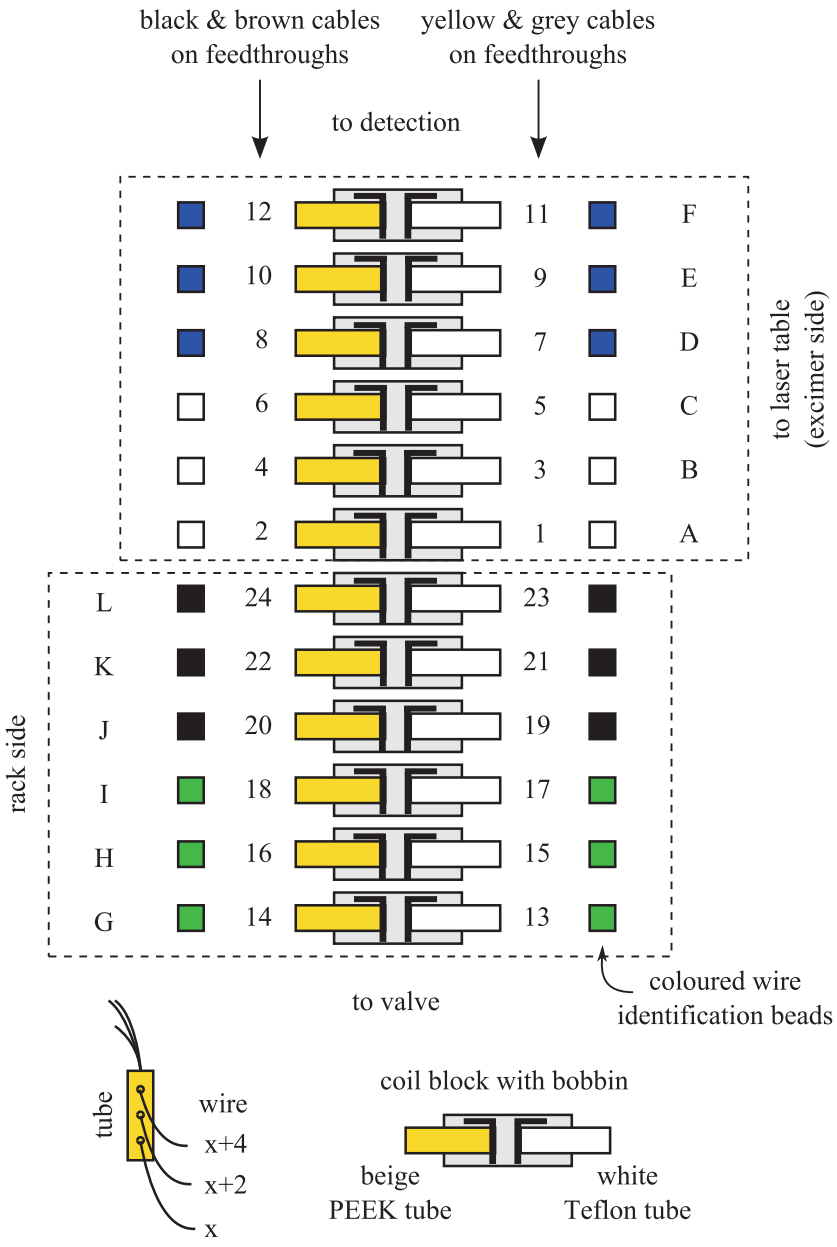

A-L: thick cable (= "coil") labels
1-24: wire labels (only on feedthroughs)

Figure 8.1

9 | Trigger Sequences and Data Acquisition

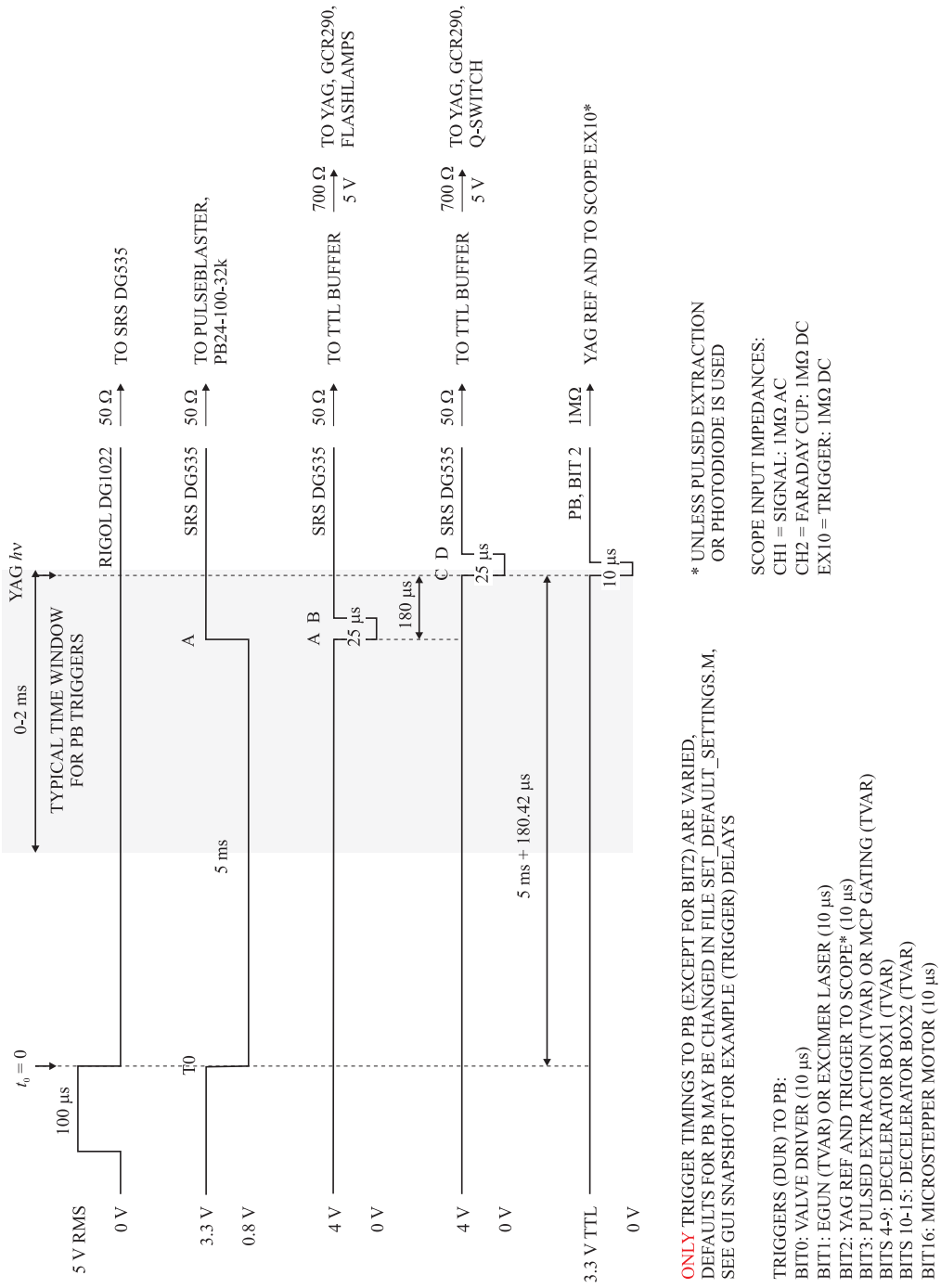

Figure 9.1

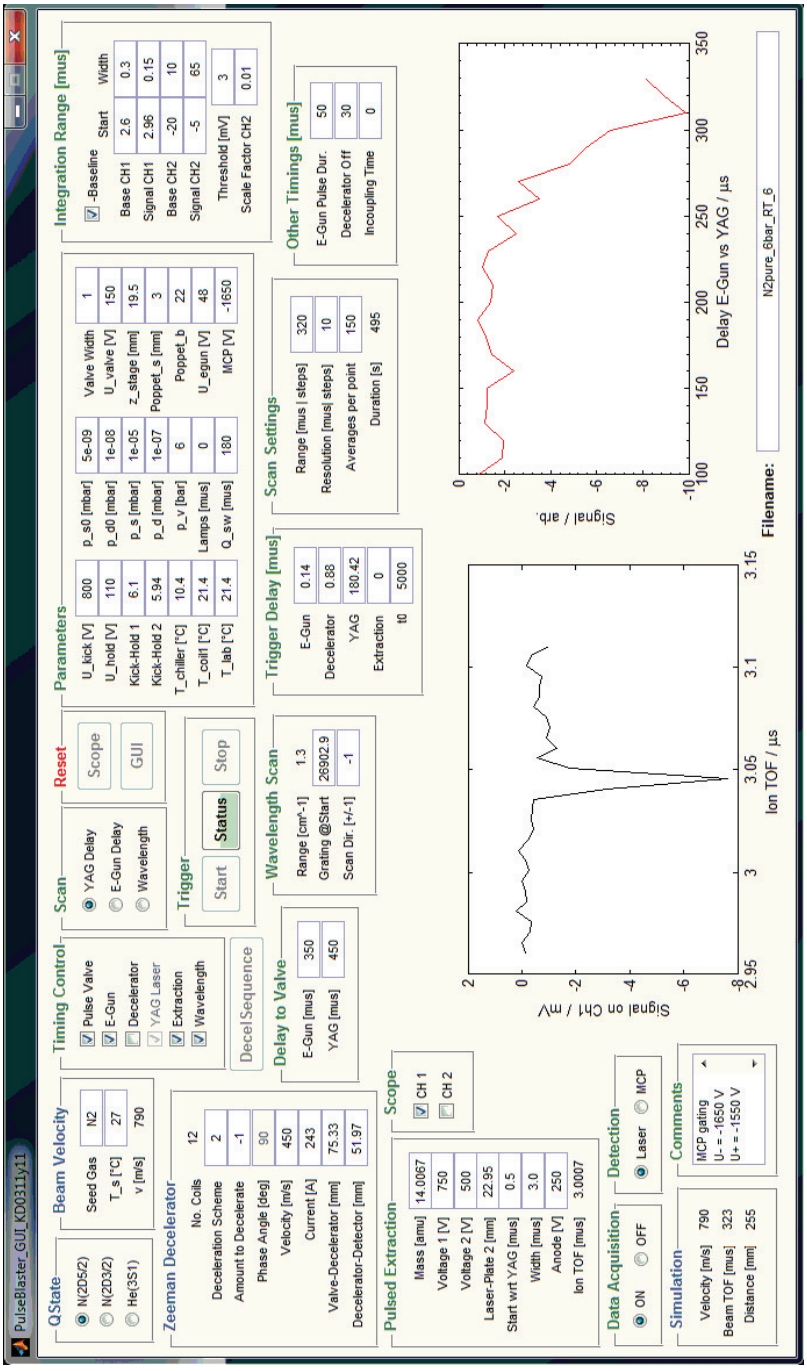

Figure 9.2: Graphical user interface for the experiment, here: settings for N(^{2}D).

10 | Focal Length of a Magnetic Lens

In the following, Eq. 7.8 shall be derived.

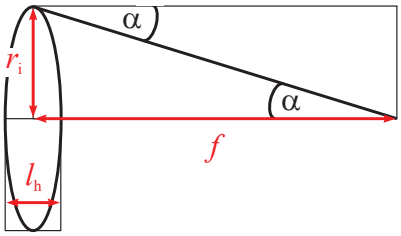

Figure 10.1

Using a thin-lens approximation [390], the angle α in Figure 10.1 can be approximated as

$$\alpha \approx \tan(\alpha) = \frac{r_i}{f}, \tag{10.1}$$

where f is the focal length and r_i is the radius of the lens. Further, α can be considered as the ratio between the momentum change Δp and the momentum, p, i.e. $\alpha = \Delta p/p$. We can assume that $\Delta p = F_{r,m}\Delta t = F_{r,m} l_\mathrm{h}/v_z$ and $p \approx m v_z$, where $F_{r,m}$ is the maximum transverse force in a magnetic field, Δt is the duration of the force, l_h is the thickness of the lens, v_z is the longitudinal particle velocity and m is the particle mass. Hence,

$$\alpha = \frac{F_{r,m} l_\mathrm{h}}{m v_z^2}. \tag{10.2}$$

Setting Eq. 10.1 equal to Eq. 10.2 and rearranging to f yields

$$f = \frac{r_i m v_z^2}{F_{r,m} l_\mathrm{h}}. \tag{10.3}$$

11 | Useful Coordinate Transformations

Below, I have summarised a few recurring coordinate transformations between cartesian and cylindrical coordinates with relevance to this thesis, as can be found in Appendix A of Furlani's book [407] [a].

11.1 Cylindrical to Cartesian Coordinates

$$x = r\cos(\phi), \qquad y = r\sin(\phi), \qquad z = z \tag{11.1}$$

$$B_x = B_r\cos(\phi) - B_\phi\sin(\phi) \tag{11.2}$$

$$B_y = B_r\sin(\phi) + B_\phi\cos(\phi) \tag{11.3}$$

$$B_z = B_z \tag{11.4}$$

11.2 Cartesian to Cylindrical Coordinates

$$r = \sqrt{x^2+y^2}, \qquad \phi = \arctan\left(\frac{y}{x}\right), \qquad z = z \tag{11.5}$$

$$B_r = B_x\cos(\phi) + B_y\sin(\phi) \tag{11.6}$$

$$B_\phi = -B_x\sin(\phi) + B_y\cos(\phi) \tag{11.7}$$

$$B_z = B_z \tag{11.8}$$

[a] Equation 11.3 in the book contains an error (page 492).

Und als er auf die Höhe des Bergrückens kam,
siehe,
da lag das andere Meer vor ihm ausgebreitet:
und er stand still und schwieg lange.
Die Nacht aber war kalt in dieser Höhe
und klar und hellgestirnt.

(Friedrich Nietzsche – Also sprach Zarathustra)